iTi Conference on Turbulence X

July 23 – 26, 2023 | Bertinoro, Italy

Book of Abstracts

ALMA MATER STUDIORUM
UNIVERSITÀ DI BOLOGNA

TECHNISCHE
UNIVERSITÄT
DARMSTADT

CARL
VON
OSSIETZKY
universität OLDENBURG

KTH
VETENSKAP
OCH KONST

iTi CONFERENCE ON TURBULENCE X
July 23 - 26, 2023 | Bertinoro, Italy

Editors:

Ramis Örlü
Linné FLOW Centre
KTH Engineering Mechanics
Stockholm, Sweden

Alessandro Talamelli
Department of Industrial Engineering
Università di Bologna
Forlì, Italy

Joachim Peinke
Institute of Physics
University of Oldenburg
Oldenburg, Germany

Martin Oberlack
Department of Mechanical Engineering
TU Darmstadt
Darmstadt, Germany

iTi Conference on Turbulence X

July 23 - 26, 2023 | Bertinoro, Italy

time	Sunday (23rd of July)
19:00	Welcome buffet - Registration

time	Monday (24th of July)
08.30	Registration and Introductory remarks
	Session 1 – Turbulence Theory I – Chair: Martin Oberlack
9:00	**Invited talk** *CICLoPE – a Discriminating Facility for Wall-Bounded Turbulence and Recent Lessons from Experiments-Asymptotics-Computation*. **Hassan Nagib** (Illinois Institute of Technology, USA) *page 3*
9:30	*A newly established laboratory and theoretical framework for non-equilibrium turbulence studies.* **C. M. Velte**, A. Hodzic, H. Abitan, P. J. Olesen, M. Schiødt, S. L. Ribergaard, Y. Zhang *page 4*
9:50	*Multiscale dynamics in turbulent wakes.* **N. Biswas**, O. R. H. Buxton *page 6*
10:10	*Linear Amplification of Large Scale Structures in Adverse Pressure Gradient Turbulent Boundary Layers through Resolvent Analysis*. **S. Gomez**, B. McKeon *page 8*
10:30	*The role of laminar/turbulent interface on energy transfer between scales in by-pass transition*. **G. Papadakis**, H. Yao *page 10*
	Coffee break (10:50 -11:20)

time	Monday (24th of July)
	Session 2 – Coherent Structures – Chair: Jonathan Morrison
11:20	*Contribution of large-scale coherent structures to budgets of turbulent kinetic energy in turbulent pipe flow*. A. Shahirpour, **J. Sesterhenn** *page 12*
11:40	*Decay and formation of secondary motions in a turbulent channel flow*. **A. Andreolli**, N. Hutchins, B. Frohnapfel, D. Gatti *page 14*
12:00	*On the origins of dual hairpin vortex arrangement in the wake of oscillating foils*. **S. Verma**, A. Hemmati *page 16*
12:20	*Conditional analysis of local energy cascade in isotropic turbulence*. H. Yao, M. Schnaubelt, A. Szalay, P.K. Yeung, T. A. Zaki, **C. Meneveau** *page 18*
	Lunch (12:40 – 13:40)
	Session 3 – Wall Turbulence I – Chair: Hassan Nagib
13:40	**Invited talk** *Modeling wall-bounded turbulent flows: a search for structure in chaos.* **Dennice Gayme** (Johns Hopkins University, USA) page *20*
14:10	*A tool for efficient application of the QSQH theory of modulation of near-wall turbulence.* **Y. Yang**,S. I. Chernyshenko *page 21*
14:30	*Spectral analysis of the inter-scale transport mechanisms of energy-containing eddies in turbulent boundary layers*. **A. Matas**, E. Kannadasan, C. Atkinson, J. Soria *page 23*
14:50	*Convection velocities of a turbulent boundary layer subjected to pressure gradients and curvature*. **P. Manovski**, M. Giacobello, C. M. de Silva, N. Hutchins, I. Marusic *page 25*
15.10	*Law of the wake and scaling of the mean velocity profile in turbulent pipe flow.* **G. Bellani**, A. Talamelli *page 27*
15:30	*Coupling anisotropic fiber tracking with instantaneous volumetric flow field in turbulent channel flows*. G. C. A. Caridi, V. Giurgiu, M. Alipour, M. De Paoli, **A. Soldati** *page 29*
15:50 – 17:00	**Poster session I and Coffee break**

time	Monday (24th of July)
	Session 4 – Flow Control – Chair: Ivan Marusic
17:00	*Vorticity transport mechanism in a turbulent channel flow controlled using streamwise travelling waves.* M. Umair, **S. Tardu** *page 30*
17:20	*Crossflow-oscillating plasma jets in a turbulent channel flow*. L. d'Amato , E. Amico, G. Cafiero, G. Iuso, **J. Serpieri** *page 32*
17:40	*Boundary layer modification with travelling surface waves generated by kagome lattices*. **I. Fumarola**, Z. Soltani, M. Santer, J. Morrison *page 34*
18:00	*On the wave-induced Stokes sublayer and drag reduction in the turbulent wind*. **A. Cimarelli**, F. Romoli, E. Stalio *page 36*
18:20	*Investigations into spatio-temporal interactions in rough wall-bounded turbulence using reduced order modelling*. **B. Viggiano**, D. F. Gayme *page 38*

time	Tuesday (25th of July)
	Session 5 – Experiments – Chair: Joachim Peinke
8:30	**Invited talk** *Energy cascades in axisymmetric turbulent wakes*. **Martin Obligado** (Université Grenoble Alpes, France) *page 40*
9:00	*Event-based imaging for visualization and measurement of turbulent flows*. **C. Willert**, J. Klinner *page 42*
9:20	*Effects of anisotropy on the geometry of tracer particle trajectories in turbulent flows*. **Y. Hengster**, M. Lellep, J. Weigel, M. Bross, J. Bosbach, D. Schanz, A. Schröder, F. Huhn, M. Novara, D. Garaboa Paz, C. Kähler, and M. Linkmann *page 44*
9:40	*Augmenting PIV temporal resolution via semi-Lagrangian estimation of velocity fluctuations*. M. Vocke, R. Kapulla, C. Morton, **R. Martinuzzi** *page 46*
10:00	*Inertial Particles in Turbulence under Minimum Gravity*. F. Cabrera, K. Cardin, L. Chevillard, R. Volk, N. Plihon, M. Bourgoin, **R. B. Cal** *page 48*
	Coffee break (10:20 -10:50)
	Session 6 – Turbulence Theory II – Chair: Joe Klewicki
10:50	*Not all Clear Air Turbulence is Kolmogorov - The fine-scale nature of atmospheric turbulence*. **A. Dörnbrack**, P. Rodriguez Imazio, P. D. Mininni *page 49*
11:10	*Symmetries in Second Moment Turbulence Modeling.* **F. C. Putz**, M. Oberlack *page 51*
11:30	*Isotropy, super-isotropy and a finite dimensional eigenvalue problem from the Lundgren hierarchy of turbulence*. **S. Görtz**, J. Conrad, M. Oberlack *page 53*
11:50	*Self-similarity and the physical mechanism of the direct cascade in two-dimensional turbulence*. **R. O. Grigoriev**, D. Zhigunov, M. Reynoso *page 54*
12:10	*New insights in wall-bounded turbulence*. **S. Hoyas**, M. Oberlack *page 55*
	Lunch (12:30-13:30)

time	Tuesday (25th of July)
	Session 7 – Roughness – Chair: Bharath Ganapathisubramani
13:30	**Invited talk**: *Turbulent flows over heterogeneous rough walls*. **Bettina Frohnapfel** (KIT, Germany) *page 57*
14:00	*Assessment of different methods for drag penalty predictions in rough-wall boundary layers*. **T. Medjnoun**, M. A. Ferreira, R. Reinartz, B. Nugroho, J. P. Monty, N. Hutchins, B. Ganapathisubramani *page 58*
14.20	*On the instantaneous characteristics of ridge-type induced secondary motions*. **K. Schäfer**, B. Frohnapfel, D. Gatti *page 60*
14:40	*Wall pressure fluctuations in the CICLoPE facility*. **G. Dacome**, W. J. Baars, A. Talamelli, L. Lazzarini, G. Bellani *page 62*
15:00	*Flexible fibers in turbulent channel flow*. **C. Marchioli**, D. Di Giusto *page 64*
15:20 – 16:20	**Poster session II and Coffee break**
	Session 8 – Numerical Methods – Chair: Davide Gatti
16:20	*Evaluation of Turbulence Models in Unsteady Separated Flows*. C. Y. MacDougall, **U. Piomelli**, F. Ambrogi *page 66*
16:40	*Computationally efficient prediction of turbulence statistics using a Bayesian hierarchical multifidelity model*. S. Rezaeiravesh, T. Mukha, **P. Schlatter** *page 68*
16:00	*A multi-timescale wall model for LES and applications to non-equilibrium channel flows.* **M. Fowler**, T. A. Zaki, C. Meneveau *page 70*
17:20	*Physics-Informed Minimal Error Simulation Methods for Turbulent Flow Predictions*. **S. Heinz** *page 72*
18:00	**Conference dinner (BUS)**

time	Wednesday (26th of July)
	Session 9 – Free Shear Flows – Chair: Martin Obligado
8:30 9:00 9:20 9:40 10:00	**Invited talk**: *Towards a clearer understanding of jet and propeller noise: time-frequency analysis and stochastic models*. **Roberto Camussi** (University Roma Tre, Italy) *page 74* *The near– and intermediate–wakes of cylinders under the influence of freestream turbulence*. **L. Li**, R. J. Hearst *page 75* *Spatial evolution of the turbulent/turbulent interface geometry and turbulent momentum entrainment*. **J. G. Chen**, O. R. H. Buxton *page 77* *The beauty of active grids and their infinite possibilities of turbulence generation*. **L. Neuhaus**, M. Hölling, M. Wächter, J. Peinke *page 79* *Comparing hot-wire measurements and particle image velocimetry of turbulence fields generated by a flapping active grid*. **I. Neunaber**, M. Asadi, L. Li, R. J. Hearst *page 81*
	Coffee break (10:20-10:50)
	Session 10 – Thermal Convection – Chair: Roberto Camussi
10:50 11:10 11:30 11:50 12:10	*Study of dust devils in a large-scale laboratory experiment*. **R. du Puits**, C. Kaestner *page 83* *Effect of coherent fluctuation in stellar convection viewed from the non-equilibrium turbulence effect*. **N. Yokoi**, Y. Masada, T. Takiwaki *page 85* *Estimation of boundary layer turbulence through non-intrusive sensing of wall-temperature fluctuations*. **F. Foroozan**, A. Ianiro, S. Discetti, W. J. Baars *page 87* *Enstrophy budgets in a turbulent temporal plume*. **L. Campana**, M. van Reeuwijk, E. De Angelis *page 89* *New Insights on Buoyancy Driven Turbulence*. **K. Bhaganagar** *page 91*
	Lunch (12:30-13:30)

time	Wednesday (26th of July)
	Session 11 –Wall Turbulence II – Chair: Alessandro Talamelli
13:30	*Detailing history and non-equilibrium effects in adverse pressure gradient turbulent boundary layers*. **S. Romero**, S. Zimmerman, J. Philip, J. Klewicki *page 93*
13:50	*Statistical characteristics of three velocity components in pipe flow at high Reynolds number*. **M. Ono**, N. Furuichi, Y. Tsuji *page 95*
14.10	*Effects of spanwise mean pressure gradient on rotating plane Couette flow*. **O. Iida**, T. Kanda *page 97*
14:30	*Turbulence in spatially accelerating turbulent boundary layers*. **M. Falcone**, S. He *page 99*
14:50	Closing remarks

Posters

iTi Conference on Turbulence X

July 23 - 26, 2023 | Bertinoro, Italy

ORAL PRESENTATION

CICLoPE a Discriminating Facility for Wall-Bounded Turbulence and Recent Lessons from Experiments-Asymptotics-Computation

Hassan M. Nagib
Illinois Tech (IIT), Chicago, IL 60616, USA

and

Peter A. Monkewitz
Swiss Federal Institute of Technology Lausanne (EPFL), CH-1015 Lausanne, Switzerland

Utilizing the three-pronged approach of experimental measurements, computational results (DNS) and matched asymptotic analysis, we have reexamined the three canonical wall-bounded turbulent flows of pipe, channel and zero pressure gradient boundary layer. Detailed and systematic study confirmed the non-universality of the Kármán 'constant' (κ) reported in 2008 by *Nagib, H. M. & Chauhan, K. A. "Variations of von Kármán coefficient in canonical flows." Phys. Fluids 20, 101518.* The new matching approach also revealed an inner-outer overlap consisting of a superposition of log-law and a linear term, see P. Monkewitz and H. Nagib "*The hunt for the Kármán 'constant' Revisited" Submitted to J. Fluid Mech., (2023)*. A similar linear term was suggested by Afzal & Yajnik, *J. Fluid Mech.* (1973 & 1970) and Luchini (2017) *Phys. Rev. Lett. 118, 224501*. In our results, we find that the coefficients of both terms are dependent on the pressure gradient of the flow. A new and robust method is devised to simultaneously determine the coefficients of the log and linear terms, in pressure driven flows at currently accessible Reynolds numbers, and *yields κ's which are consistent with the κ's deduced from the Reynolds number dependence of centerline velocities*.

A newly established laboratory and theoretical framework for non-equilibrium turbulence studies

Clara M. Velte[1], Azur Hodžić[1], Haim Abitan[1], Peder J. Olesen[1], Martin Schiødt[1], Simon L. Ribergaard[1] and Yisheng Zhang[1]

[1] Dept. of Civil and Mechanical Engineering, Technical University of Denmark, Kgs. Lyngby, Denmark

key-words: Non-equilibrium turbulence, Experiments, Theory

Abstract: The cornerstone assumption of equilibrium of the small and intermediate scales in the classical view of turbulence (K41 - the combined efforts of Kolmogorov, Batchelor and Richardson) is under ever increased scrutiny. Although the theory based models do appear to apply well to some flows, there exist many important flows that are problematic for K41-based turbulence models. In particular, it is interesting to note that the most challenging applications appear to have one thing in common - rapid changes of the flow in the mean in time and/or space.

It is thus interesting to investigate what the potential bounds of validity of the classical K41 view of turbulence are, if any. And if the K41-view does indeed break down, what are the mechanisms that lead to non-equilibrium turbulence behavior (local vs. nonlocal)? Does the non-linear energy exchange between scales divert from the classically assumed Richardson cascade? And is the constancy of the spectral flux across the inertial range interrupted?

The experimental facility: To try to answer these questions, a new facility for studying non-equilibrium turbulence in a controlled setting has been established at the Department of Civil and Mechanical Engineering at the Technical University of Denmark, see Figure 1. The experiments are challenging and have required in-house development of optical solutions, including improved high-power LEDs, in-house designed Scheimpflug camera mounts and dedicated optics to improve laser based light budgets.

The round turbulent jet has been chosen as the test bed for several reasons, among the central ones being that the jet is near equilibrium when stationary and that it can be pushed out of equilibrium in a practical, reproducible and arbitrary manner. The scales are also sufficiently large and slow that the smallest relevant (dissipative) scales can be resolved. Further, the global development of the jet can be measured since the round turbulent jet evolves over practical distances.

Although we are pushing the limits for what can be measured with currently available technology, the experiments had to be divided up into two separate ones: Direct measurement of the full and instantaneous dissipation rate are carried out to quantify the degree of non-equilibrium of the modulated jet flow. And global measurements of the jet in four dimensions are used to decompose the energetic and inertial range of the flow field into waves to analyze whether non-stationarity triggers different (non-local) non-linear interactions than the classical Richardson cascade, see e.g. Figure 2. Both experiments are based on particle tracking velocimetry (PTV). The two jets for the two separate experiments can be seen in Figure 3.

Theory framework: Equally important as the physical lab facilities is the developed theoretical framework that enables robust analysis of the acquired measurements. Since we do not benefit from periodicity in all four dimensions, the proper orthogonal decomposition (POD) is implemented rather than Fourier modes [1]. We have developed tools that enable POD to be applied to e.g. non-stationary flows (PhasePOD) [2], Lagrangian particle trajectories (ParticlePOD) [3] and using the dissipation rate based POD modes as a basis rather than the classical turbulent kinetic energy based POD (DissipationPOD) [4].

The rationale behind the experiments, the theoretical methods developed to analyze the measurements and initial results will be discussed. More details of the individual setups, optical developments and analysis method developments will be further detailed in separate contributions of other group members of the DTU Turbulence Research Laboratory during the meeting.

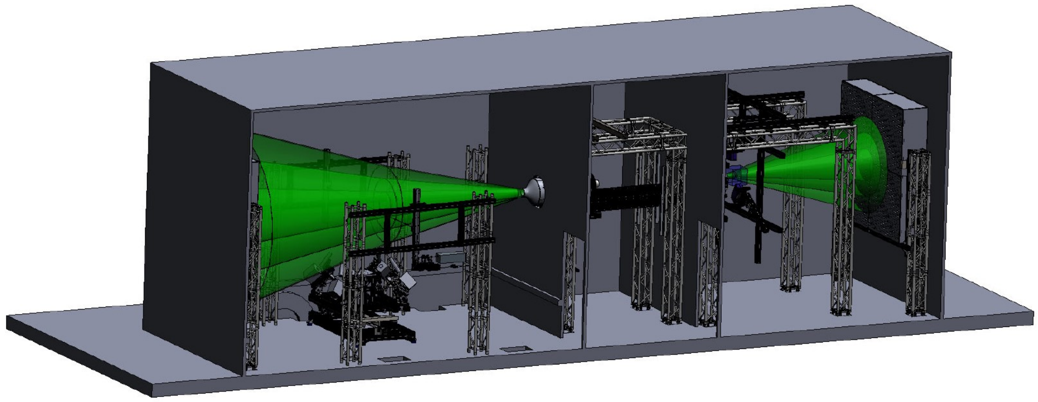

Figure 1: *Left test cell: Direct measurements of the instantaneous dissipation rate. Middle cell: Control room. Right cell: Global measurements of the four-dimensional turbulent jet dynamics.*

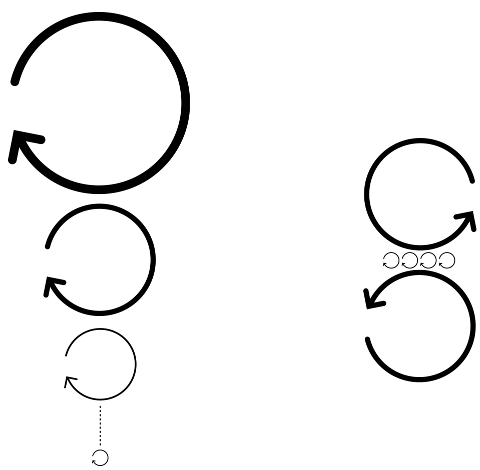

Figure 2: *(Left) Local interactions (Richardson cascade) vs. (Right) example of non-local interactions.*

Figure 3: *Left jet: Large jet for producing large and slow scales for measurement of the instantaneous dissipation rate. Right jet: Small jet for producing a flow that can be measured globally to study modal interactions.*

References

[1] Hodžić, A., Olesen, P. J., and Velte, C. M., (2023), On the Discrepancies between POD and Fourier Modes on Aperiodic Domains, *arXiv:2207.02550 [physics.flu-dyn].*

[2] Zhang, Y., Hodžić, A., Evrard, F., Van Wachem, B., and Velte, C. M., (2023), Phase proper orthogonal decomposition of non-stationary turbulent flow, *arXiv:2301.10462 [physics.flu-dyn].*

[3] Schiødt, M., Hodžić, A., Evrard, F., Hausmann, M., van Wachem, B., and Velte, C. M., (2022), Characterizing Lagrangian particle dynamics in decaying homogeneous isotropic turbulence using proper orthogonal decomposition, *Physics of Fluids, 34(6), [063303].*

[4] Olesen, P. J., Hodžić, A., Andersen, S. J., Sørensen, N. N., and Velte, C. M., (2023), Dissipation-optimized Proper Orthogonal Decomposition, , *Physics of Fluids, 35(1), [015131].*

Multiscale dynamics in turbulent wakes

Neelakash Biswas [1], Oliver R. H. Buxton [2]

[1] Department of Aeronautics, Imperial College London, London, UK

key-words: Wakes, Multiscale Flows

Abstract:
Real life flows are often multiscale in nature, where multiple length/time scales can be present simultaneously. The simplest possible example of such a flow is two cylinders of different diameters placed side by side in a way they produce individual vortex streets of different characteristic frequencies. On the other hand a more complicated example could be a wind turbine where multiple length/time scales are shed into the flow from the blades, nacelle, tower etc. A schematic of the first example is shown in fig. 1(a) where the larger cylinder (called the main cylinder) is accompanied by a smaller cylinder (called the control rod). In such a multiscale system, apart from the sheddings from the two cylinders (denoted by f_m and f_c), new frequencies are observed which correspond to the addition and subtraction of the two shedding frequencies ($f_c \pm f_m$) (see fig. 1(b)). The origin of these frequencies can be understood by studying the energy budgets for each of the various coherent modes, which was developed by Baj and Buxton [2017]. The coherent energy budget ($\tilde{k}_l$) equation can be represented in a symbolic form as

$$\frac{\partial \tilde{k}_l}{\partial t} = -\tilde{C}_l + \tilde{P}_l - \hat{P}_l + \left(\tilde{T}_l^{+} - \tilde{T}_l^{-}\right) - \tilde{\epsilon}_l + \tilde{D}_l \tag{1}$$

In equation 1, the source terms on the right hand side consists of convection ($\bar{C}_l$), production from mean flow ($\tilde{P}_l$), production of stochastic turbulent kinetic energy ($\hat{P}_l$), triadic energy production ($\tilde{T}_l^{+} - \tilde{T}_l^{-}$), dissipation ($\tilde{\epsilon}_l$) and diffusion ($\tilde{D}_l$). The sheddings of the two cylinders were found to be energised by the mean flow (through the $\tilde{P}_l$ term), however, the two new frequencies were found to be formed through non-linear interaction (through the $\tilde{T}_l^{+} - \tilde{T}_l^{-}$ term) between the sheddings of the two wake generating bodies [Biswas et al., 2022]. For a wind turbine the scenario becomes much more complex due to inherent three-dimensionality and the presence of many more coherent structures, simultaneously. We conducted Particle Image Velocimetry (PIV) experiments on a small-scale wind turbine consisting of a nacelle and a tower, mimicking a real scale wind turbine. Fig. 2 shows instantaneous vorticity fields at two different planes for tip speed ratio $\lambda = 6$ ($\lambda = \omega R/U_\infty$, where R is the turbine radius, ω is the rotational speed, and U_∞ is the free stream velocity). An array of tip vortices could be seen along the outer edge of the wake ($y/D \approx 0.5$, $z/D \approx \pm 0.5$). The flow field behind the tower, however, is more turbulent and chaotic due to the interaction between the tip vortices and the tower's vortex shedding. Frequency spectra are obtained at the points shown by the + signs and shown in fig. 3(a-b) and fig. 3(c-d) for the xy and xz planes respectively. A number of frequencies could be observed in different regions of the flow, including the blade passing frequency ($3f_r$), rotor frequency (f_r) and their harmonics, nacelle shedding frequency (f_n), wake meandering frequency (f_{wm}) etc. Understanding the energy exchanges to and from these frequencies can be critical in developing a better understanding of the spatio-temporal development of wind-turbine wakes. Fig. 4 shows the energy budget terms for f_r, $3f_r$ and their harmonics. The different sectors correspond to the different terms in equation 1. The radial lengths of the sectors represent the relative contribution of the different terms in logarithmic scale and the red and blue colors represent loss and gain of energy respectively. Note that some of the modes are energised by the mean flow while some are entirely energised by non-linearity, a scenario qualitatively similar to that observed in the simplified example containing two cylinders (fig. 1(a)). In addition, there are also some modes which are energised by both production from mean flow and non-linearity and some solely due to convection.

References

P. Baj and O. R. Buxton. Interscale energy transfer in the merger of wakes of a multiscale array of rectangular cylinders. *Physical Review Fluids*, 2(11):114607, 2017.

N. Biswas, M. M. Cicolin, and O. R. Buxton. Energy exchanges in the flow past a cylinder with a leeward control rod. *Journal of Fluid Mechanics*, 941:A36, 2022.

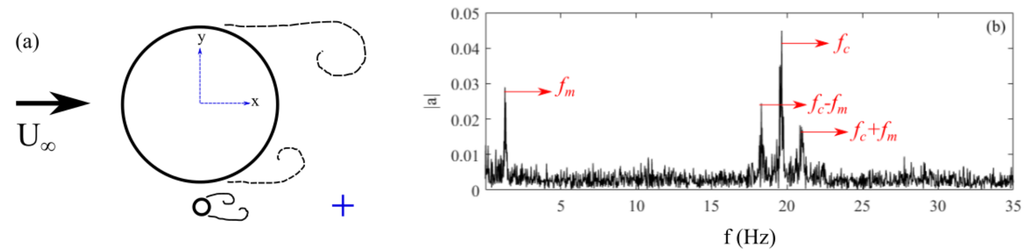

Figure 1: (a) Schematic of a multiscale system consisting of a main cylinder and a control rod. (b) Frequency spectrum obtained at the point shown by $+$ sign.

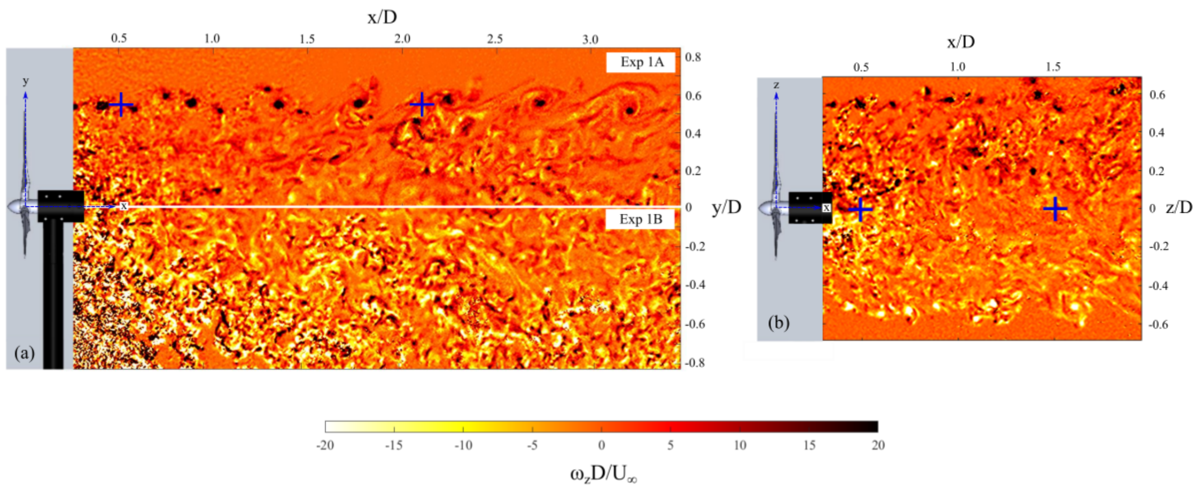

Figure 2: Instantaneous vorticity field of a wind turbine wake in (a) the $xy(z = 0)$ plane and (b) the $xz(y = 0)$ plane for $\lambda = 6$. For sub figure (a), the top $(y > 0)$ and bottom $(y < 0)$ parts of the field of view correspond to two non-synchronous experiments.

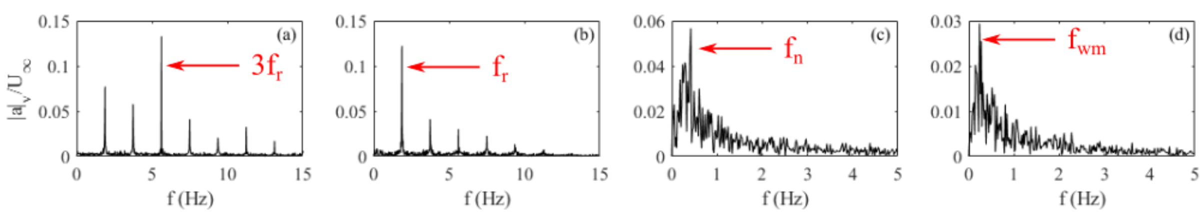

Figure 3: (a-b) Frequency spectra obtained at the points shown by $+$ sign in fig. 2(a). Sub figures (c-d) show the same for fig. 2(b).

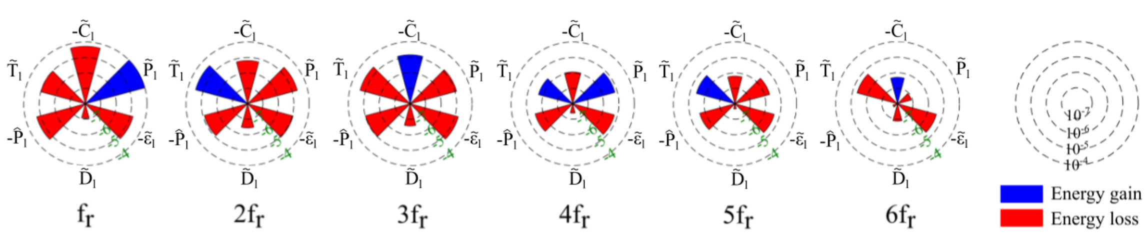

Figure 4: Different energy budget terms for the frequencies f_r - $6f_r$. A red sector denotes loss of energy while a blue sector denotes gain of energy. The dashed lines represent magnitudes of energy in logarithmic scale as shown in the right most sub figure. $\tilde{T}_l^+ - \tilde{T}_l^-$ is represented in short by $\tilde{T}_l$.

Linear Amplification of Large Scale Structures in Adverse Pressure Gradient Turbulent Boundary Layers through Resolvent Analysis

S. Gomez [1], B. McKeon [1,2]

[1] GALCIT, California Institute of Technology, Pasadena, United States of America
[2] Mechanical Engineering, Stanford University, Palo Alto, United States of America

Key-words: Fundamentals, Turbulent Boundary Layers, Scaling Laws, Mathematical Methods

Abstract:
An understanding of the physical mechanisms that support turbulence in turbulent boundary layers (TBL) with adverse pressure gradients (APG) can better aid modelling and control efforts in realistic aerodynamic applications. The resolvent analysis framework identifies an equation-based scale-dependent decomposition of the Navier-Stokes operator, linearized about the mean flow field [1]. The outputs of this analysis are two orthonormal bases that represent the most amplified forcing modes and their corresponding response modes, each ranked by their respective linear gain. This linear analysis has been shown to predict key features of energetic motions in shear driven turbulence. We exploit biglobal resolvent analysis to account for nonparallel effects in the TBL and parameterize the analysis with only a spanwise wavenumber, k_z, and temporal frequency, ω. As such, the biglobal forcing and response modes are resolved in the streamwise and wall-normal directions. Due to the large computational costs of the matrix operations in resolvent analysis, methods will be discussed that can efficiently compute the linear amplification and enable the parameter sweeps required for this study.

The results from biglobal resolvent analysis are used to compare the linear amplification of the flat plate APGTBL at low Reynolds number, obtained using mean flow fields from a database of large eddy simulations [2], with the LES statistics. The domain of interest is $40\delta_{99}$ long in each dataset. The four mean flow fields have increasing APG strength, measured by the Clauser parameter, β. From a sweep over k_z and ω, a near wall peak and a secondary large-scale outer-layer peak are identified from the linear amplification and leading response mode in the APGTBL, as illustrated in figure 1. The secondary peak becomes more amplified with increasing APG strength. In contrast, the linear amplification of the zero pressure gradient TBL exhibits only the near wall peak for the same Reynolds number. The behavior of the linear amplification is shown to be consistent with observations in APGTBL simulations, where the premultiplied streamwise energy spectra identify large-scale outer-layer peaks that become energized with increased APG strength [3] and a secondary peak in the streamwise fluctuations [2]. The linear amplification in the outer region is then explained with scaling arguments and implications for modeling the APGTBL are discussed.

References

[1] McKeon B. J., Sharma A. S., (2010), A critical-layer framework for turbulent pipe flow, *Journal of Fluid Mechanics, vol. 658, pp. 336-382*

[2] Vinuesa, R. Bobke, A. Örlü, R., Schlatter, P. (2016), On determining characteristic length scales in pressure-gradient turbulent boundary layers, *Physics of Fluids, vol. 28, pp. 055101*

[3] Lee, J. H. (2017), Large-scale motions in turbulent boundary layers subjected to adverse pressure gradients, *Journal of Fluid Mechanics, vol. 810, pp. 323-361*

The support by the U.S. Office of Naval Research through grants N00014-17-1-2307 and N00014-17-1-3022 is gratefully acknowledged.

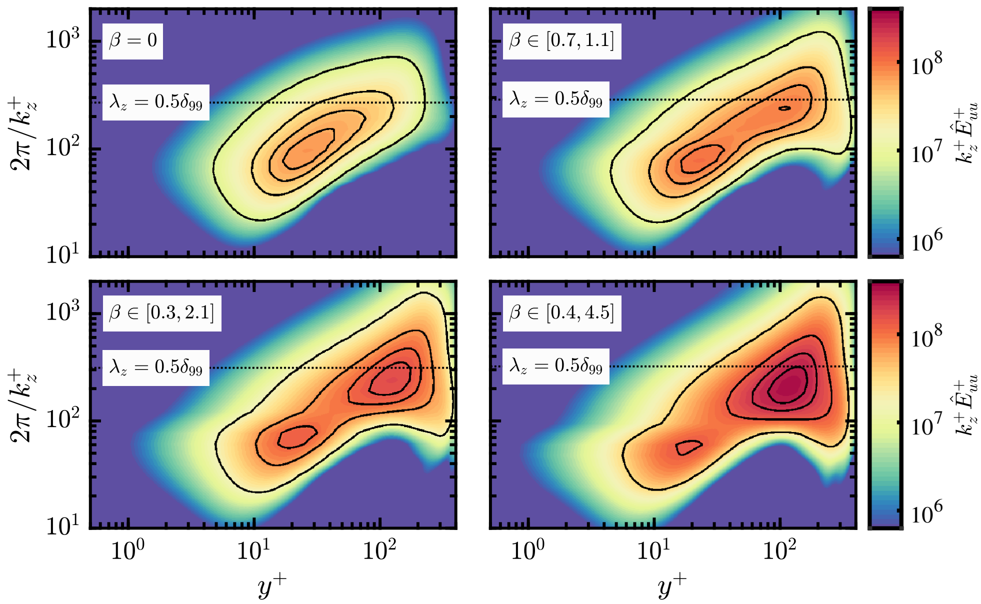

Figure 1: *Contours of the modeled premultiplied streamwise kinetic energy,* $k_z E_{uu}(x, y) = k_z \int_0^\infty \sigma_1(k_z, \omega)^2 |\psi_{u,1}(x, y; k_z, \omega)|^2 d\omega$*, where* σ_1 *and* ψ_1 *are the leading singular value and response mode, respectively, plotted at the streamwise location where the friction Reynolds number is equal to* 537*. APG strength is denoted by the largest* β *in the range. Inner scaled variables are denoted with* + *superscripts.*

The role of laminar/turbulent interface on energy transfer between scales in bypass transition

G. Papadakis [1], H. Yao[1]

[1] Dept of Aeronautics, Imperial College London, SW7 2AZ, UK

key-words: Bypass transition, interscale energy transfer, laminar-turbulent interface, conditional averaging

Abstract:
We investigate the role of laminar/turbulent interface in the interscale energy transfer in a boundary layer undergoing bypass transition, with the aid of the Karman-Howarth-Monin-Hill (KHMH) equation. A local binary indicator function, $\tau(X, Y, Z)$, is used to detect the interface and employed subsequently to define two-point intermittencies. These intermittencies are used to perform conditional averaging and decompose the energy fluxes into different components that depend on the local conditions at the two points used to define the flux; the points are both within a laminar region (LL events) or a turbulent spot (TT evens) or straddle the laminar/turbulent interface (LT or TL events). The flux terms are evaluated numerically directly in the scale space because conditional averaging does not commute with the spatial derivative operator.

We find that the inverse cascade in the streamwise direction reported in [1] arises due to events across the downstream or upstream interfaces of a turbulent spot. However, the three-dimensional energy flux maps reveal significant differences between these two regions: in the downstream interface, inverse cascade is stronger and dominant over a larger range of streamwise and spanwise separations, see figure 1. We explain this finding by considering a propagating spot of simplified shape as it crosses a fixed streamwise location.

We derive also the conditionally-averaged KHMH equation, thus generalising similar equations for single-point statistics to two-point statistics. We compare the three-dimensional maps of the conditionally-averaged production and total energy flux within turbulent spots against the maps of standard-averaged quantities within the fully turbulent region. The results indicate remarkable dynamical similarities between turbulent spots and the fully turbulent region for two-point statistics. This has been known only for single-point quantities, but the present work demonstrates that the similarity extends to two-point quantities as well.

The conditional averaging approach for two-point statistics that we propose can be applied to other flow configurations that exhibit sharp interfaces, such as wakes and jets, where a turbulent/non-turbulent interface separates the irrotational and vortical regions. The approach can be use to answer important questions, for example, do the conditionally-averaged two-point statistics exhibit self-similarity? How does this develop as the jet/wake expands?

References

[1] H. Yao, J.-P. Mollicone, and G. Papadakis. Analysis of interscale energy transfer in a boundary layer undergoing bypass transition. *Journal of Fluid Mechanics*, 941:A14, 2022.

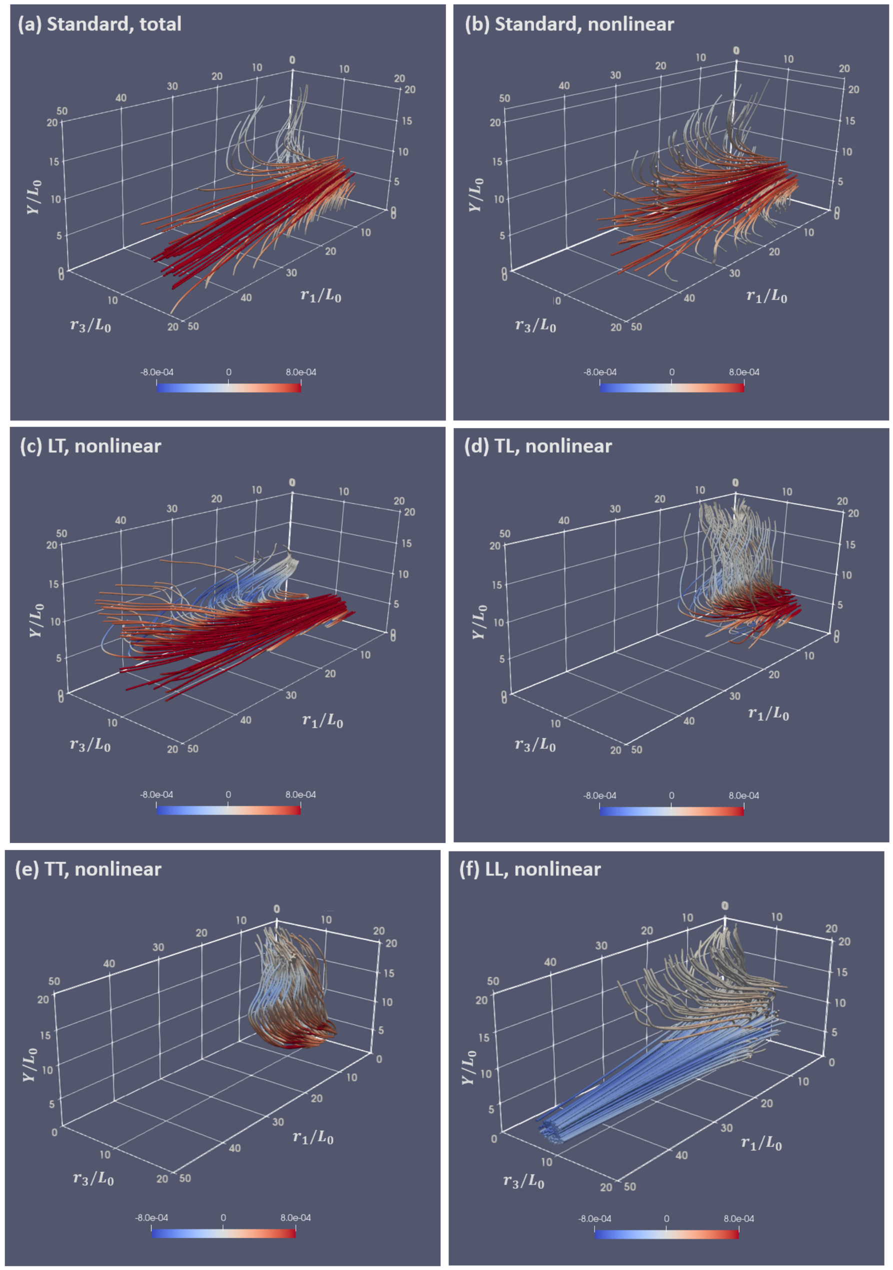

Figure 1: Stream-tubes of (a) the total flux vector $(\phi_{r_1}, \phi_{r_3}, \phi_{s_2})$, (b) the standard-averaged non-linear flux vector $\left(\phi^F_{r_1}, \phi^F_{r_3}, \phi^F_{s_2}\right)$, and the conditionally-averaged vectors (c) $\left(\phi^{F\,(LT)}_{r_1}, \phi^{F\,(LT)}_{r_3}, \phi^{F\,(LT)}_{s_2}\right)$, (d) $\left(\phi^{F\,(TL)}_{r_1}, \phi^{F\,(TL)}_{r_3}, \phi^{F\,(TL)}_{s_2}\right)$, (e) $\left(\phi^{F\,(TT)}_{r_1}, \phi^{F\,(TT)}_{r_3}, \phi^{F\,(TT)}_{s_2}\right)$ and (f) $\left(\phi^{F\,(LL)}_{r_1}, \phi^{F\,(LL)}_{r_3}, \phi^{F\,(LL)}_{s_2}\right)$ at $TR2$. The plots are generated by placing a sphere of radius $5L_0$ at point $(r_1, r_3, Y) = (5L_0, 10L_0, 3L_0)$ and tracing the stream-tubes crossing the sphere. The stream-tubes are coloured according to the sign of the first component i.e. ϕ_{r_1}, $\phi^F_{r_1}$, $\phi^{F\,(LT)}_{r_1}$, $\phi^{F\,(TL)}_{r_1}$, $\phi^{F\,(TT)}_{r_1}$ and $\phi^{F\,(LL)}_{r_1}$ (red for positive, blue for negative, thus indicating inverse or forward cascade in the r_1 direction respectively). The colour bars also refer to the value of the first component (the min/max values are the same to facilitate comparison).

Contribution of large-scale coherent structures to budgets of turbulent kinetic energy in turbulent pipe flow

A. Shahirpour[1] and J. Sesterhenn[1]

[1] Lehrstuhl für Technische Mechanik und Strömungsmechanik, Universität Bayreuth, Bayreuth, Germany

key-words: Large-scale coherent structures, dynamic mode decomposition

Abstract:
Large-scale coherent structures are known to dominate the nature of wall-bounded turbulent flows and have major contributions to transport properties. One of the key aspects which contributes to a deeper understanding of dynamics of such structures, is to clarify what they feed on and how their regeneration mechanism works. Aiming at answering these questions, we investigate and quantify contribution of large-scale structures to streamwise and azimuthal energy spectra and to production and dissipation of turbulent kinetic energy.

In order to analyse the kinematic properties of the structures in the absence of smaller scale structures and instabilities, data driven methods are potential candidates. Since interaction between the modes are to be studied, the implemented decomposition should not impose orthogonality in subspaces where the modes are detected. On the other hand, given the transport dominated nature of structures, standard decomposition methods such as Dynamic Mode Decomposition (DMD) will fail to reconstruct a reduced-order model of the flow with a minimal number of modes. The same fact will lead to inaccurate estimation of decay rates and frequencies for such motions.

To overcome the mentioned obstacle, we have developed a Characteristic Dynamic Mode Decomposition (CDMD) [1] and have addressed how the subspaces can be identified to capture transport dominated structures (Sesterhenn & Shahirpour 2019[1]). Hereby, a temporal sequence of state vectors from DNS or time-resolved measurements, are transformed such that persistent dynamical modes are found on a hypersurface traveling along its normal in space and time on a moving frame of reference. A subset of the spatio-temporal modes is selected so that their reconstruction optimally represents the spectral peak in premultiplied energy spectra in physical space. The latter modes form a subspace which accommodates large-scale features of the flow. DMD spectrum, mode coefficients and kinetic energy of the modes are then used to detect further subspaces interacting with each other and with the coherent structures.

Reconstruction of each subspace along the normal to the hypersurface and transforming them back to physical space gives the low rank model of the flow [Figures 1-4]. Once the coherent and incoherent parts of the flow are extracted in the corresponding subspaces, their contributions to energy spectrum, turbulent kinetic energy production, viscous dissipation, viscous diffusion and turbulent velocity diffusion are determined.

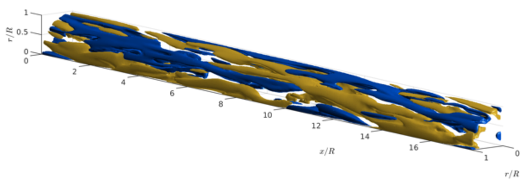

Figure 1: *Full-field. Iso surfaces of streamwise velocity component. (*<U> ± 0.1 U_b *)*

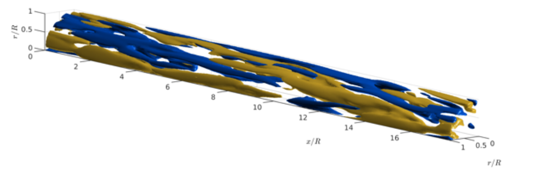

Figure 2: *Subspace 1 using 4 CDMD modes*

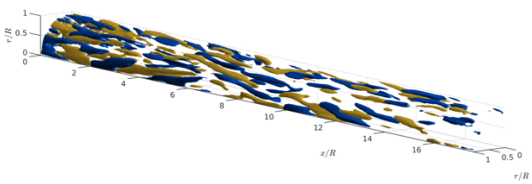

Figure 3: *Subspace 2.*

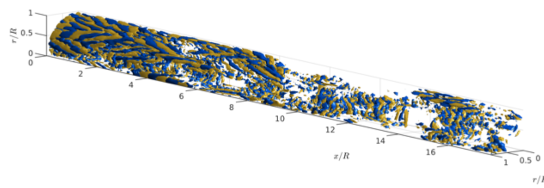

Figure 4: *Subspace 3.*

References

[1] Sesterhenn J. and Shahirpour A., (2019), A characteristic dynamic mode decomposition, *Journal of theoretical and computational fluid dynamics, vol. 33, pp. 281-305*

Decay and formation of secondary motions in a turbulent channel flow

A. Andreolli[1,2], N. Hutchins[2], B. Frohnapfel[1] and D. Gatti[1]

[1] Institute of Fluid Mechanics (ISTM), Karlsruhe Institute of Technology, 76131 Karlsruhe, Germany
[2] Department of Mechanical Engineering, University of Melbourne, Victoria 3010, Australia

key-words: Secondary motions, Simulation

Abstract:

Of the many scales of motion that compose wall-bounded turbulence, those scaling with the channel half-height h (or equivalently the boundary layer thickness δ, depending on the flow configuration) appear to be naturally amplified by the flow [1, 2]; this is in line with the prediction of Townsend [3] that a specific range of motions with spanwise wavelengths of order δ and smaller than 4δ should be able to self-sustain longer than any other scale. To shed light on the subject, we numerically investigate the time scales needed for the decay and formation of flow patterns of different sizes produced by a lateral wall shear stress variation. The statistically evolving setting explored here permits the analysis of the physical mechanisms driving the transient state.

Streamwise-elongated strips of width s of smooth or rough wall alternating in the spanwise direction are modelled through a spanwise slip length [4] applied to the walls of a turbulent channel flow. This configuration is known to produce secondary motions of spanwise period $2s$ [5]. With this numerical setup, we first produce a set of statistically steady simulations at a friction Reynolds number $Re_\tau = 180$ with values of s/h ranging from 0.125 to 3 (in addition to a simulation with smooth walls); these are used to spectrally identify the secondary motions, which mainly excite the streamwise-invariant Fourier mode of spanwise wavelength $2s$, as well as its shorter spanwise harmonics. As can be seen from figure 1, the relative magnitude of the harmonics with respect to the dominant mode increases with increasing s; motions with larger spanwise wavelength λ_z have a larger wall-normal extent, with the notable exception of the harmonic $\lambda_z/h = 6$ for the $s/h = 3$ case being confined at the wall. This exception reinforces the conjecture of Townsend that the flow favours a specific range of scales of size $\sim 1\,h$.

Having identified the Fourier modes that mainly contribute to the secondary motions, their evolution in time is tracked and ensemble-averaged across multiple statistically instationary simulations. For instance, to study the decay of a secondary motion of given spanwise period, the initial condition is picked from the steady simulation with the corresponding roughness pattern; the spanwise alternating slip is then deactivated and the flow evolves in presence of smooth walls. This is repeated for a set of statistically independent initial conditions referring to the same steady state, so that the time evolution of the secondary motion can be ensemble-averaged. Preliminary results are shown in figure 2, plotting the ensemble-averaged time evolution of the norm of the dominant Fourier mode of the secondary motions for selected values of s. The duration of the transient increases with increasing s and appears to saturate around a value of $1\,h/u_\tau$ (where u_τ is the friction velocity) for high enough values of s. Once again, this deviation from the monotonic behaviour constitutes evidence in favour of Townsend's conjecture.

Finally, statistics of the initial fields conditioned on the duration of the resulting transient are collected in an attempt to explain the fluctuations in its duration. Moreover, we compute the ensemble-averaged budget equation [6] for the mean streamwise vorticity of the flow, so to shed light on which physical mechanisms drive the formation of secondary flows.

References

[1] Illingworth S. J., (2020), Streamwise-constant large-scale structures in Couette and Poiseuille flows, *Journal of Fluid Mechanics, vol. 889, A13.*

[2] Reynolds R.T., Hayden P., Castro I.P. & Robins A.G. (2007), Spanwise variations in nominally two-dimensional rough-wall boundary layers, *Experiments in Fluids, vol. 42, pp. 311-320.*

[3] Townsend A. A., (1976): *The structure of turbulent shear flow*, 2nd edn., Cambridge University Press, page 331.

[4] Neuhauser J., Schäfer K., Gatti D. & Frohnapfel B. (2022), Simulation of turbulent flow over roughness strips, *Journal of Fluid Mechanics, vol. 945, A14.*

[5] Chung D., Monty J.P. & Hutchins N. (2018), Similarity and structure of wall turbulence with lateral wall shear stress variations, *Journal of Fluid Mechanics, vol. 847, pp. 591-613.*

[6] Türk S., Daschiel G., Stroh A., Hasegawa Y. & Frohnapfel B. (2014), Turbulent flow over superhydrophobic surfaces with streamwise grooves, *Journal of Fluid Mechanics, vol. 747, pp. 186-217.*

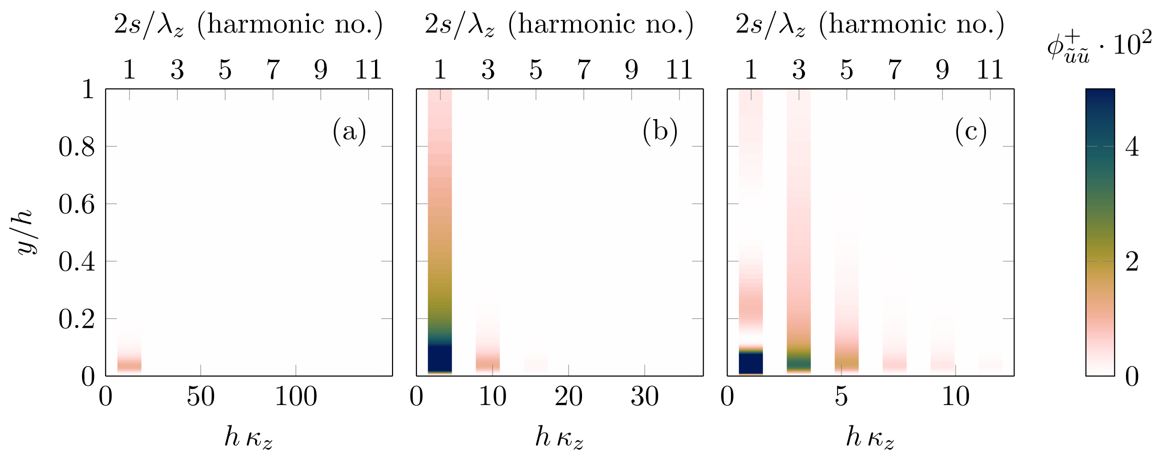

Figure 1: power spectral density $\phi^+_{\tilde{u}\tilde{u}}(y, \kappa_z)$ (colour; no premultiplication) of the streamwise component of the time, streamwise and phase averaged dispersive motion at a steady state, scaled in viscous units as indicated by the superscript $(\cdot)^+$; $s/h = 0.25$ (a), $s/h = 1$ (b), $s/h = 3$ (c). The spanwise mean is removed from the signal prior to the Fourier transform; κ_z represents the spanwise wavenumber and λ_z the corresponding wavelength, y the wall-normal distance.

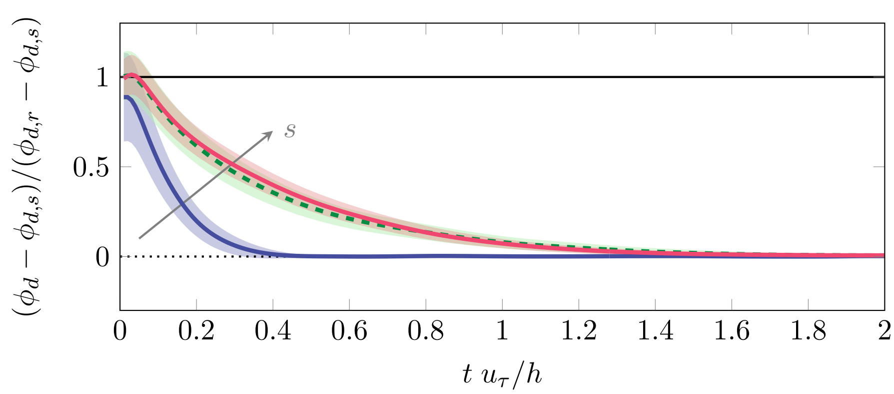

Figure 2: ensemble-averaged time-evolving power spectral density ϕ_d on the dominant mode (streamwise-invariant, $\lambda_z = 2s$) at the wall ($y^+ = 7$) of the streamwise component of decaying dispersive motions; $s/h = 0.25$ (blue), $s/h = 1$ (green, dashed), $s/h = 3$ (red). The shaded areas indicate 99.7% confidence intervals. The value of ϕ_d is rescaled with $\phi_{d,r}$ and $\phi_{d,s}$, that is the expected values of ϕ_d at the beginning and at the end of the transient respectively.

On the origins of dual hairpin vortex arrangement in the wake of oscillating foils

Suyash Verma[1] and Arman Hemmati[1]

[1] Department of Mechanical Engineering, University of Alberta, Edmonton, Canada

key-words: Unsteady wakes, Vortex instabilities, Secondary vortex, Oscillating foil, turbulent wake

Abstract:

Three-dimensional wake transition behind an oscillating foil with combined heaving and pitching motion is numerically evaluated at a range of chord-based Strouhal number ($0.32 \leq St_c \leq 0.64$) and phase offset ($90^\circ \leq \phi \leq 270^\circ$), at $Re = 8000$. The range of ϕ coincides with a transition of kinematics from heave- to pitch-dominated motion. The association of spanwise instabilities on the leading edge vortex (LEV) and the growth of secondary hairpin structures was established recently at $St_c = 0.32$ [2]. Particularly, the heave-dominated motion at $\phi = 90^\circ$ and 180° exhibited the growth of large-scale spanwise hairpin structures in the wake, whose origins were attributed to an elliptic or core instability mechanism of an unequal strength counter-rotating roller pair [1, 3]. This mechanism promoted a core vorticity outflux from either the weak secondary LEV or an evolving trailing edge structure (TEV) that paired with the primary LEV [2].

It was evident that for the range of ϕ and St_c(=0.32) assessed above, the primary LEV does not encounter a strong strain field intensity from the streamwise hairpin legs. Thus, it fails to reveal dominant vortex dislocation features and LEV bending, while advecting downstream [2]. Further, the evolution of rib pairs in the wake was only governed by the elongation and tearing of secondary hairpin heads due to shear straining in the braid region [5]. Here, we expand on the effect of increasing St_c, which highlights an additional novel mechanism that promotes the growth of a supplementary hairpin and rib system. These dominant large scale structures evolve in conjunction with the secondary hairpin arrangement discussed at $St_c = 0.32$. The supplementary hairpin system forms through the substantial bending of the primary LEV, which occur due to a strong strain field intensity of pre-existing hairpins. These structures further possess an increased circulation strength at higher St_c. The evolution mechanism is initially characterized by a dual arch configuration of primary LEV (noticeable at St_c >0.40), which transforms into a spanwise configuration of horseshoe vortical structures. The continued elongation and straining of horseshoe legs creates an additional hairpin, followed by a rib pair, that co-exist and elongate with the rib pairs characterized at lower St_c. Analysis of frequency signature and growth rates associated with the individual hairpin and rib systems is still under evaluation, which will quantitatively characterize the onset of three-dimensional transition to turbulence in oscillating shear flows.

References

[1] Leweke, T., Le Dizès, S., & Williamson, C. H. K. (2016). Dynamics and Instabilities of Vortex Pairs. *Annual Review of Fluid Mechanics.*

[2] Verma, S. & Hemmati, A. (2022) Implications of spanwise wake instability on formation of secondary structures behind oscillating foils. *Proceedings of 12th International Symposium on Turbulence and Shear Flow Phenomena (TSFP12)*, Osaka, Japan.

[3] Verma, S. & Hemmati, A. (2021a).Evolution of wake structures behind oscillating hydrofoils with combined heaving and pitching motion. *Journal of Fluid Mechanics* 927, A23.

[4] Verma, S. & Hemmati, A. (2021b). Asymmetry in wake of oscillating foils with combined pitching and heaving motion. In *Progress in Turbulence IX (ed. R. Örlü, A. Talamelli, J. Peinke & M. Oberlack),* pp. 97–102. Springer International Publishing.

[5] R. Mittal and S. Balachandar (1995). Generation of Streamwise Vortical Structures in Bluff Body Wakes. *Physical Review Letters* , 75, 1300.

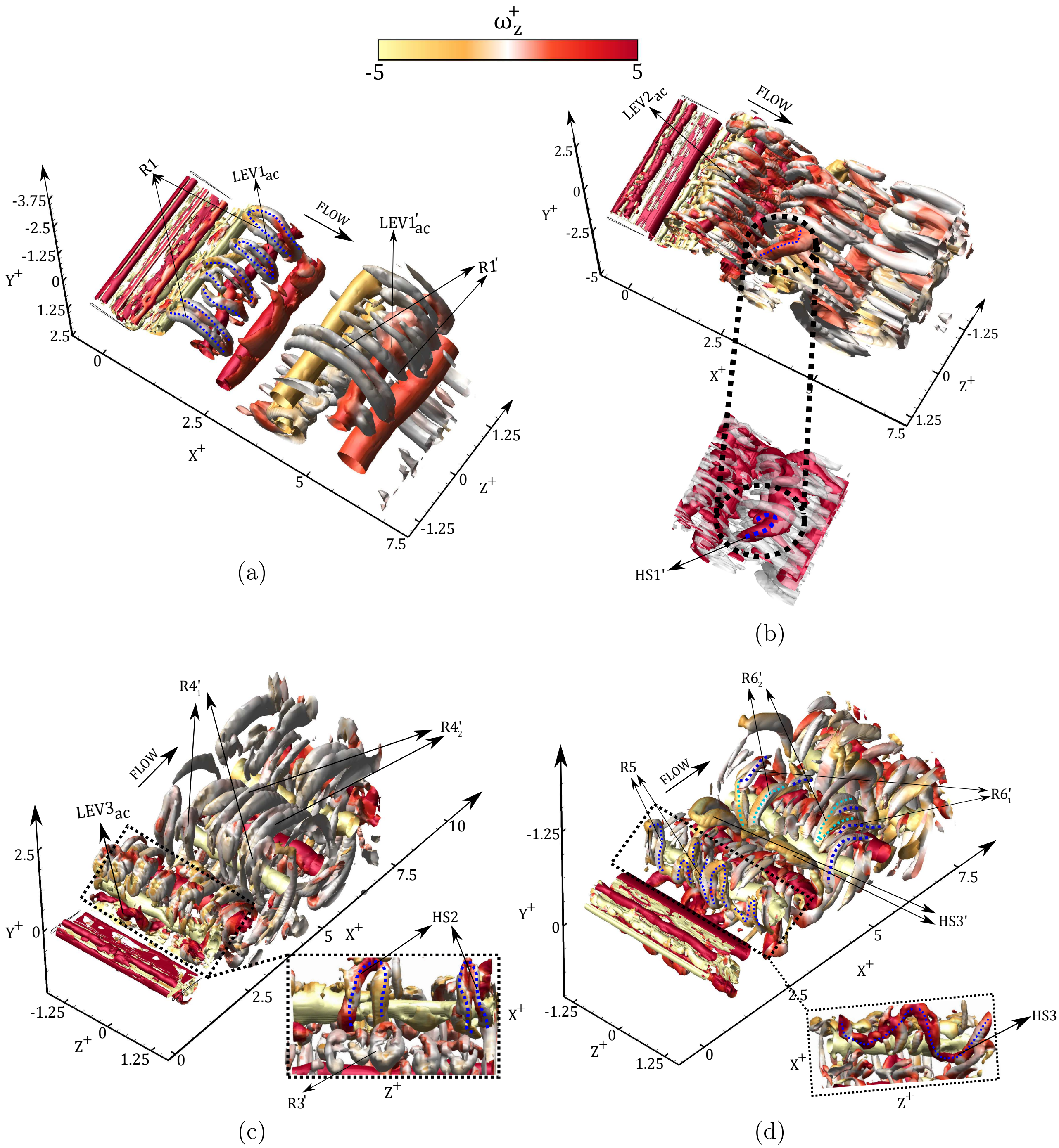

Figure 1: *Vortical structures (identified using λ_2-criterion) in the wake at ϕ =90° and (a)St_c =0.32, (b)St_c =0.40, (c)St_c =0.48 and (d)St_c =0.56. Wake at St_c =0.32 is characterized by single system of ribs ($R1$ or $R1'$) from two consecutive shedding cycle. Increasing St_c to 0.40 depicts bending of primary roller to form a horseshoe structure marked $HS1'$. This structure evolves along with preexisting ribs. At St_c =0.48 and 0.56, a horseshoe arrangement evolving via primary LEV bending, and dual rib system is observed in the downstream wake.*

Conditional analysis of local energy cascade in isotropic turbulence

H. Yao[1], M. Schnaubelt[1], A. Szalay[1], P.K. Yeung[2], T.A Zaki[1] and C. Meneveau[1]

[1] Johns Hopkins University, Baltimore MD, USA
[2] Georgia Institute of Technology, Atlanta GA, USA

Key-words: Energy Cascade, Isotropic Turbulence

Abstract:

The Karman-Howarth-Monin-Hill (KHMH) equation [1] is applied for analyzing spatial subsets of DNS data from homogeneous isotropic turbulence at Taylor-scale Reynolds number = 1300, to characterize local forward and inverse energy cascades statistically. The local cascade rate is computed at any given physical location and is identified using a spherical surface integration in length-scale space of the triple velocity difference term appearing in the KHMH equation. Under global averaging, this term is related to the mean rate of dissipation by a factor of $-4/5$ as in the classic formulation of the 4/5th law. When evaluated using conditional averaging based on the locally averaged dissipation rate ϵ_r, our results show that it equals the locally averaged dissipation rate, representing a conditionally averaged version of the $-4/3$ law. The result confirms Kolmogorov's refined similarity hypothesis [2] (KRSH) for these particular conditional statistics.

We further explore the reverse conditioning of terms in the KHMH equation based on the local cascade rate. Dimensional reasoning would imply that the conditional averaged dissipation should equal the prescribed value of the cascade rate. However, results show that when conditioning on the cascade rate, significant disagreements with the 'inverse -4/3 law' are obtained. We trace the discrepancy to the conditional averages of the unsteady and pressure contributions appearing in the KHMH. For this analysis we use data at lower Reynolds number $Re_\lambda = 430$, for which the entire time evolution is available.

To further improve our understanding of the energy cascade process, we explore the relationship between the local cascade rate and the filtered strain and rotation rates. Using joint conditional averaging of the local cascade rate based on both strain-rate and rotation rate square magnitude (see figure 1), we find strong positive correlation with the rate of strain at large scales, as expected. We also detect locally inverse cascade events in which the conditionally averaged cascade rate is negative. However, such events only occur when both the large-scale rotation rate is unusually strong and the strain rate is very weak. Comparisons are shown with the spatial filtering approach commonly used in Large Eddy Simulations, in which the cascade rate is usually called the subgrid-scale (SGS) rate of dissipation. We find that the joint conditional averaging yields significantly weaker trends of inverse cascade (negative conditionally averaged SGS dissipation or backscatter). Results shed new light onto the cascade process in isotropic turbulence

For these analyses, we use recent updates made to the JHTDB (Johns Hopkins Turbulence Databases [3]) data access and analysis tools. JHTDB has been operating for over a decade and has led to hundreds of peer-reviewed articles on turbulence. A new set of data access tools based on Jupyter notebooks has been developed that enable direct access to subsets of the data continuing the "virtual sensors" concept. The new notebooks provide fast and stable operation on the existing turbulence data sets while enabling user-programmable, server-side computations. To date, the new data access tools have been tested on the high Reynolds number, forced isotropic turbulence data set at a Taylor microscope Reynolds number of $Re_\lambda = 1,300$ [4].

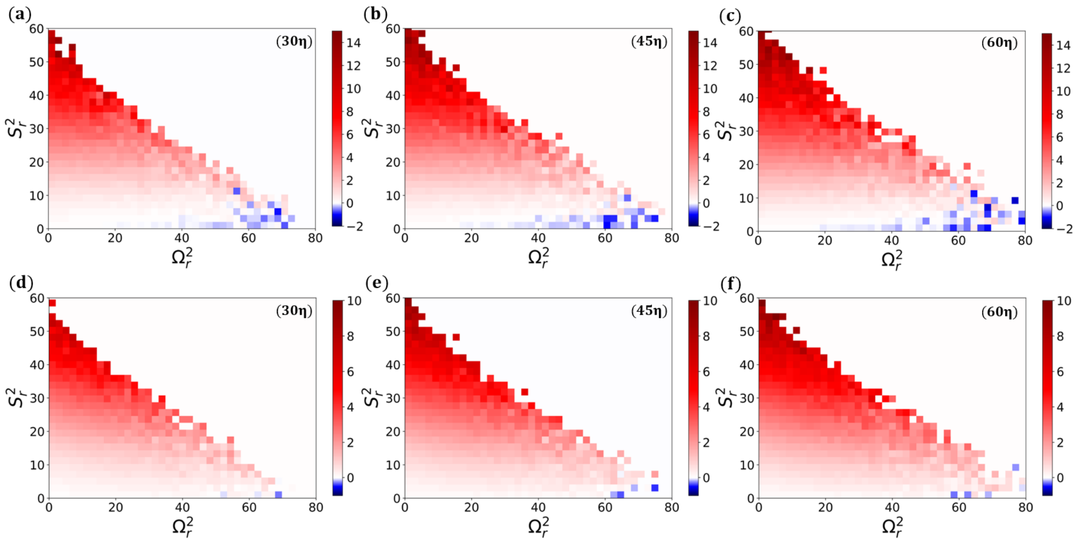

Figure 1: Conditional average of cascade rates at three different scales, conditioned on square strain-rate and rotation rate spherically filtered at those scales. Panels (a), (b), (c) correspond to the cascade rate based on velocity increments according to the KHMH equation, $\langle F_r | S_r^2, \Omega_r^2 \rangle$ while (d), (e), (f) show the subgrid-scale "dissipation" in the filtering approach, $\langle \Pi_r | S_r^2, \Omega_r^2 \rangle$. The three scales are $r = 30\eta, 45\eta, 60\eta$, where η is the Kolmogorov scale. The red region represents positive F_r, i.e., local forward energy cascade.The blue region represents negative F_r, i.e., local inverse energy cascade.

Acknowledgements: This work is supported by the National Science Foundation, grant CSSI-2103874. We also thank the entire JHTDB team for their sustained efforts.

References

[1] Hill R.J. (2002), Exact second-order structure-function relationships, *J. Fluid Mech.*, vol. 468, pp. 317-326

[2] Kolmogorov, A. N. (1962), A refinement of previous hypotheses concerning the local structure of turbulence in a viscous incompressible fluid at high Reynolds number. *J. Fluid Mech.*, vol. 13, pp. 82-85.

[3] Li, Y., Perlman, E., Wan, M., Yang, Y., Meneveau, C., Burns, R., Chen, S., Szalay, A. and Eyink, G., (2008). A public turbulence database cluster and applications to study Lagrangian evolution of velocity increments in turbulence. *J. Turbulence*, vol. 9, p. N31.

[4] Yeung, P. K. and Zhai, X. M. and Sreenivasan, K. R., (2015). Extreme events in computational turbulence. *Proc. Nat. Acad. Sci.*, vol. 112, pp. 12633-12638.

Modeling wall-bounded turbulent flows: a search for structure in chaos

Dennice F. Gayme[1]

[1] Department of Mechanical Engineering, Johns Hopkins University, Baltimore, MD, USA

key-words: Wall-bounded turbulence, coherent structures, spanwise heterogeneous roughness

Abstract:
The prevalence of streamwise coherent motions and their role in energy growth, momentum transfer and the self-sustaining processes underlying wall-bounded turbulent flow has motivated the development of reduced order representations that emphasize streamwise coherent motion. In the restricted nonlinear (RNL) modeling framework this emphasis takes the form of a decomposition of the flow dynamics into a large-scale streamwise constant mean flow and perturbations about this mean. Order reduction is achieved through a restriction of the nonlinear interactions to those contributing to the large-scale mean. This approach has proven successful in generating self-sustaining turbulent activity with low order statistics and structural features consistent with moderate Reynolds number wall-bounded turbulence at vastly reduced computational costs. In this talk we discuss the relationship between RNL scale interactions and turbulent energy transport. We then employ a RNL Large Eddy Simulation (RNL-LES) model to investigate interactions between large- and small-scale motions in flow over strip-type roughness. In particular, we exploit the simplified RNL setting to highlight the role of large- and small-scale motions in the generation of secondary flow and their relationship to large-scale meandering.

A tool for efficient application of the QSQH theory of modulation of near-wall turbulence

Y. Yang and S. Chernyshenko

Department of Aeronautics, Imperial College London, London, UK

key-words: Near-wall turbulence, Scale interactions

Abstract:
The Quasi-Steady-Quasi-Homogeneous (QSQH) theory of scale interaction in near-wall turbulence (see[1] and references therein) predicts, with various degree of accuracy, the near-wall turbulent flow properties related to the modulation of the flow in the buffer layer by the large-scale motions. It also gives a theoretical derivation of the predictive inner-outer model of turbulent statistics [2] and explicit expressions for the superposition and modulation coefficients in that model. However, using the QSQH theory requires a substantial amount of analytic work. We will present a publicly available computational tool that makes application of the theory easy.

In a nutshell, the QSQH theory presumes that the near-wall turbulence adjusts itself to the large-scale component of the wall friction. It replaces the friction velocity u_τ with the large-scale friction velocity $u_{\tau_L}(t,x,z)$ in the classical formula $u = u_\tau u^+(t^+,x^+,y^+,z^+)$. Here, $t^+ = tu_\tau^2/\nu$, $(x^+,y^+z^+) = (x,y,z)u_\tau/\nu$, $u_\tau = \sqrt{\overline{\tau}/\rho}$, and all symbols have their traditional meaning. The large-scale friction velocity $u_{\tau_L}(t,x,z) = \sqrt{\tau_L(t,x,z)/\rho}$, where $\tau_L(t,x,z)$ is the large-scale component of the wall friction, which can be obtained by applying a large-scale filter to the total wall friction. The classical formula is thus replaced by

$$u = u_{\tau_L}\tilde{u}(\tilde{t},\tilde{x},\tilde{y},\tilde{z}), \quad \tilde{t} = tu_{\tau_L}^2/\nu,\ (\tilde{x},\tilde{y},\tilde{z}) = (x,y,z)u_{\tau_L}/\nu. \tag{1}$$

The classical formulation implies that $u^+(t^+,x^+,y^+,z^+)$ is universal, that is that its statistical properties are the same for all flows satisfying a certain set of conditions, including a high Reynolds number and a smooth wall. Instead, the QSQH theory implies that under the same conditions $\tilde{u}(\tilde{t},\tilde{x},\tilde{y},\tilde{z})$ is universal. Since the large-scale motions propeties are not universal in wall (that is $^+$) units, predictions based on (1) and the classical universality differ.

Universality of $\tilde{u}(\tilde{t},\tilde{x},\tilde{y},\tilde{z})$ allows to make predictions of any property of a flow, which we will call a target flow, given a limited information on this flow and a complete information on another flow, which we will call the base flow. This can be done in two steps. First, the large-scale filter is applied to the base flow wall friction, giving u_{τ_L} of that flow. Then (1) is used to find the universal $\tilde{u}(\tilde{t},\tilde{x},\tilde{y},\tilde{z})$. In the second step, the same large-scale filter is applied to the skin friction field of the target flow to obtain u_{τ_L} of the target flow, and then the target flow statistics are obtained from (1) with the target flow u_{τ_L} and the universal $\tilde{u}(\tilde{t},\tilde{x},\tilde{y},\tilde{z})$ from the base flow.

The large-scale wall friction varies with time and space both in magnitude and direction, and (1) has to be modified to take into account the direction fluctuations. This is particularly important for predictions related to the spanwise velocity [1]. Our tool uses the 3D formulation of [1]. We use the channel flow at $Re_\tau = 5200$ [3] (data obtained from the JHTDB at `http://turbulence.pha.jhu.edu`) as the base flow. The large-scale filter is a Fourier cut-off filter with the cut-offs in wall-parallel directions. The first step was done separately. The tool database contains two universal velocity fields based on two pairs of Fourier cut-offs, allowing users to test the effects of the choice of the filter on the predictions by the tool. The user should supply a representative snapshot of the skin friction of the target flow. The output of the tool is a file containing a large number of samples of the (vector) velocity field as a function of the wall-normal coordinate. Then the user can calculate the desired statistics of the target flow by a straightforward averaging of these data. Examples of the use of the tool will be presented.

References

[1] Chernyshenko S., (2021), Extension of QSQH theory of scale interaction in near-wall turbulence to all velocity components, *Journal of Fluid Mechanics*, vol. 916, pp. A52

[2] Mathis R., Hutchins N. and Marusic I (2011). A predictive inner-outer model for streamwise turbulence statistics in wall-bounded flows. *Journal of Fluid Mechanics, vol. 681, pp. 537-566.*

[3] Lee M., and Moser, R. D., (2015), Direct numerical simulation of turbulent channel flow up to $Re_\tau \approx 5200$, *Journal of Fluid Mechanics, vol. 774, pp. 395-415*

Spectral analysis of the inter-scale transport mechanisms of energy-containing eddies in turbulent boundary layers

Antonio Matas [1], E. Kannadasan [1] C. Atkinson [1] and J. Soria [1]

[1] Department of Mechanical and Aerospace Engineering, Monash University, Melbourne, Australia

key-words: turbulence simulation, turbulent boundary layers, turbulent flows

Abstract:
Turbulent wall-bounded flows can be interpreted as a cluster of recurrent patterns of energy-containing eddies (energy-eddies) [1]. These energy-eddies carry most of the momentum and kinetic energy and are considered to be the elementary structures capable of explaining how momentum and kinetic energy redistribute in wall-bounded turbulence. Understanding the dynamics of the energy-eddies, their precise origin and their interactions has attracted immense interest and posed a significant challenge for many years. The current consensus on energy-eddies in the near-wall region is that they are involved in a temporal self-sustaining cycle, which describes the interaction between the streaks and vortices [2, 3, 4]. In the present work, we study the inter-scale energy transfer in incompressible zero-pressure-gradient turbulent boundary layers (ZPG-TBL) by examining the turbulent kinetic energy (TKE) and the Reynolds shear stress transport using the spectral spanwise decomposition introduced by [5] for plane Couette flows. Our aim is to get insight into the inter-scale energy transfer and its association with the self-sustaining cycle of energy-eddies in boundary layers. A preliminary analysis is carried out using the direct numerical simulation (DNS) database of the ZPG-TBL in [6] with a Reynolds number based on momentum thickness reaching up to $Re_\theta \approx 4000$. From the spectral analysis of the TKE transport we observe the separation between energy-eddies and cascading eddies at $\lambda_z \approx 3y$ and we capture the inverse energy cascade that takes place in the near-wall region in agreement with previous studies in channels [7, 8] and boundary layers [9]. Our preliminary study reveals that more DNS fields are required to conduct the spectral analysis of the inter-scale energy transport. We have resumed the TBL-DNS and 3 eddy-turnovers are being collected weekly. We will report results based on the extended DNS database.

References

[1] Richardson, L.F, (1922): *Weather Prediction by Numerical Process*, Cambridge University Press

[2] Hamilton J.M., Kim J., Waleffe F., (1995), Regeneration mechanisms of near-wall turbulence structures, *J. Fluid Mech., vol. 287, pp. 317–348*

[3] Waleffe F., (1997), On a self-sustaining process in shear flows, *Phys. Fluids, vol. 9, pp. 883-900*

[4] Jimenez J., (1999), The autonomous cycle of near-wall turbulence, *J. Fluid Mech., vol. 389, pp. 335–359*

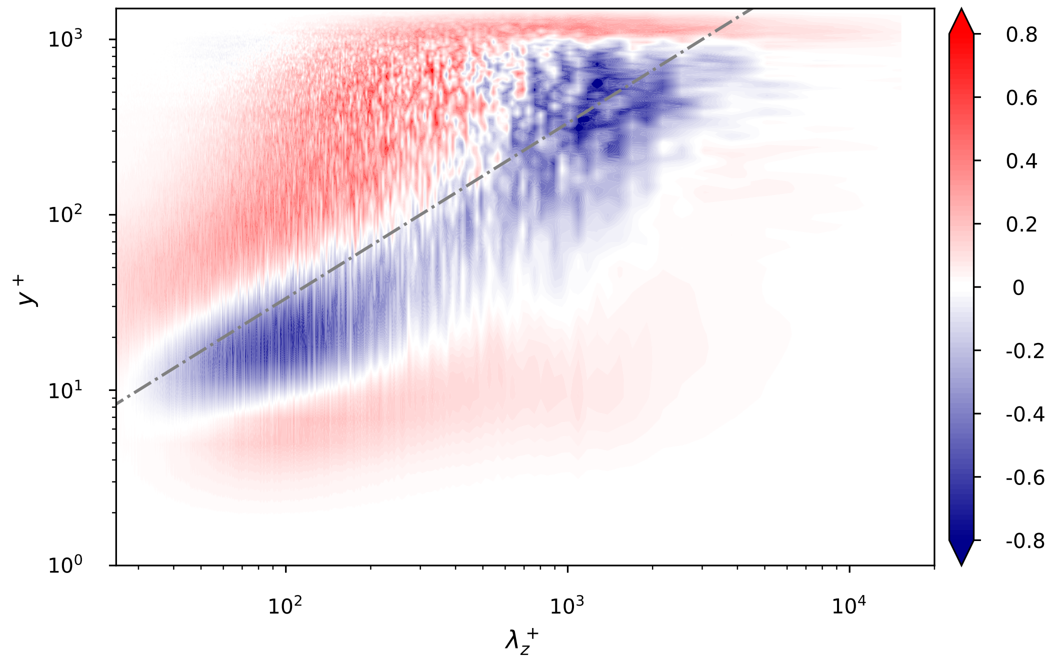

Figure 1: *Pre-multiplied spanwise spectra of the TKE transport as function of the wall-distance at* $Re_\theta = 3450$ *normalized by the maximum value. Red represents energy gain and blue energy lost. The dashed line is at* $\lambda_z^+ = 3y^+$.

[5] Kawata T., Alfredsson, P.H., (2018), Inverse interscale transport of the Reynolds shear stress in plane Couette turbulence, *Phys. Rev. Lett., vol. 120, 244501*

[6] Kitsios V., Atkinson C., Sillero J., Borrell G., Gungor A.G., Jimenez J., Soria J., (2016), Direct numerical simulation of a self-similar adverse pressure gradient turbulent boundary layer, *Intl J. Heat Fluid Flow, vol. 61, 129-136*

[7] Cho M., Hwang Y., Choi H., (2018), Scale interactions and spectral energy transfer in turbulent channel flow, *J. Fluid Mech., vol. 854, pp. 474–504*

[8] Lee M., Moser R.D., (2019), Spectral analysis of the budget equation in turbulent channel flows at high reynolds number, *J. Fluid Mech., vol. 860, 886-938*

[9] Chan C.I., Schlatter P., Chin R.C., (2021), Interscale transport mechanisms in turbulent boundary layers, *J. Fluid Mech., vol. 921, A13*

Convection velocities of a turbulent boundary layer subjected to pressure gradients and curvature

Peter Manovski [1,2], M. Giacobello [1], C.M. de Silva [3], N. Hutchins [2] and I. Marusic [2]

[1] Platforms, Defence Science and Technology Group, Melbourne, Australia
[2] Department of Mechanical Engineering, University of Melbourne, Melbourne, Australia
[3] School of Mechanical and Manufacturing Engineering, University of New South Wales, Sydney, Australia

key-words: Turbulent Boundary Layer, Convection Velocity, Pressure Gradient

Abstract:

Research into the effects of pressure gradients on turbulent boundary layers (TBL) has endured for decades. These studies are typically conducted over flat plates with downstream blockage or over simple ramp geometries to provide a constant pressure gradient. However, in real world applications, such as aerodynamic vehicles, the TBL is typically subjected to varying pressure gradients and a changing curvature. In an effort to study these effects, the TBL over an axisymmetric body of revolution geometry has been measured using high-speed PIV. Specifically, the aim is to study how the large-scale motions develop and evolve along the geometry. Ultimately, a better understanding of the mechanisms can lead to improved vehicle performance.

The geometry used in this study is shown in figure 1, together with the measured axial pressure distribution and TBL measurement locations. Here, U_∞ is the incoming free-stream velocity, x is the axial direction, z is the vertical direction, L (= 2 m) is the hull length, and C_p is the coefficient of pressure. All tests were conducted in a large wind tunnel with the model tested at zero incidence and a freestream velocity of 28.8 m/s. The TBL parameters are summarised in table 1. Using a slender laser sheet, the high-speed PIV as described in [1], enabled near time-resolved repetition rates (up to 80 kHz) with time series and spatial data from which scale (or frequency) dependent convection velocities were determined. At each wall height the phase angle of the cross spectrum between streamwise separated locations was used to determine the scale-dependent convection velocities. Further, as per [2], the gradient from a linear fit of the phase across a range of streamwise locations was used to increase the accuracy of the measurement.

In figure 2, the convection velocity normalised by the local mean streamwise velocity (U_c/U_m) is presented as a function of wavelength and wall distance (where $^+$ indicates normalisation by inner viscous units). At $x/L = 0.449$, where the pressure gradient is nominally zero, the results appear qualitatively consistent with the literature. At $x/L = 0.650$ and 0.700, the pressure gradient is favourable, similar contour results are shown, except for slightly faster convection velocities for the very large wavelengths ($\lambda_x/\delta > 3$). These higher levels also extend further into the outer layer. At $x/L = 0.800$, the adverse pressure gradient and increased curvature results in a marked increase in the convection velocities for all wavelengths, across the entire TBL. The full paper will present further analysis and insights into the flow physics.

measurement location	x/L	0.449	0.650	0.700	0.800
friction velocity (via Clauser chart)	U_τ [m/s]	1.19	1.20	1.28	1.15
boundary layer thickness	δ [mm]	12.82	17.23	17.60	21.05
friction Re	$Re_\tau = U_\tau \delta_{99}/\nu$	1038	1415	1438	1612
Clauser pressure gradient parameter	$\beta = \delta^*/\tau_w(\mathrm{d}P/\mathrm{d}x)$	-0.001	-0.25	-0.47	0.56
curvature parameter	$\delta_{99}/\mathrm{radius}(a)$	0.10	0.14	0.14	0.17

Table 1: *Boundary layer parameters at the axial measurement locations.*

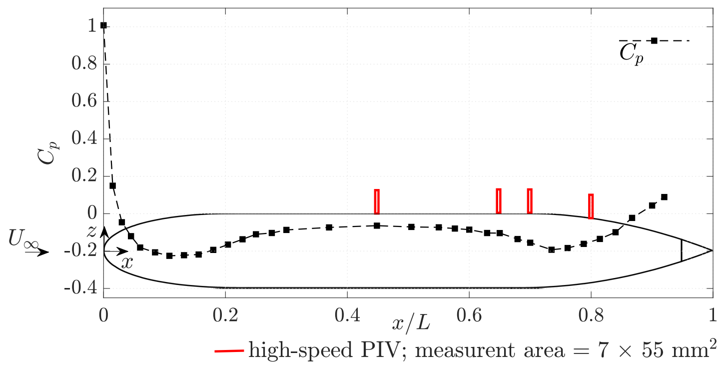

Figure 1: *The body of revolution geometry, pressure distribution and measurement locations.*

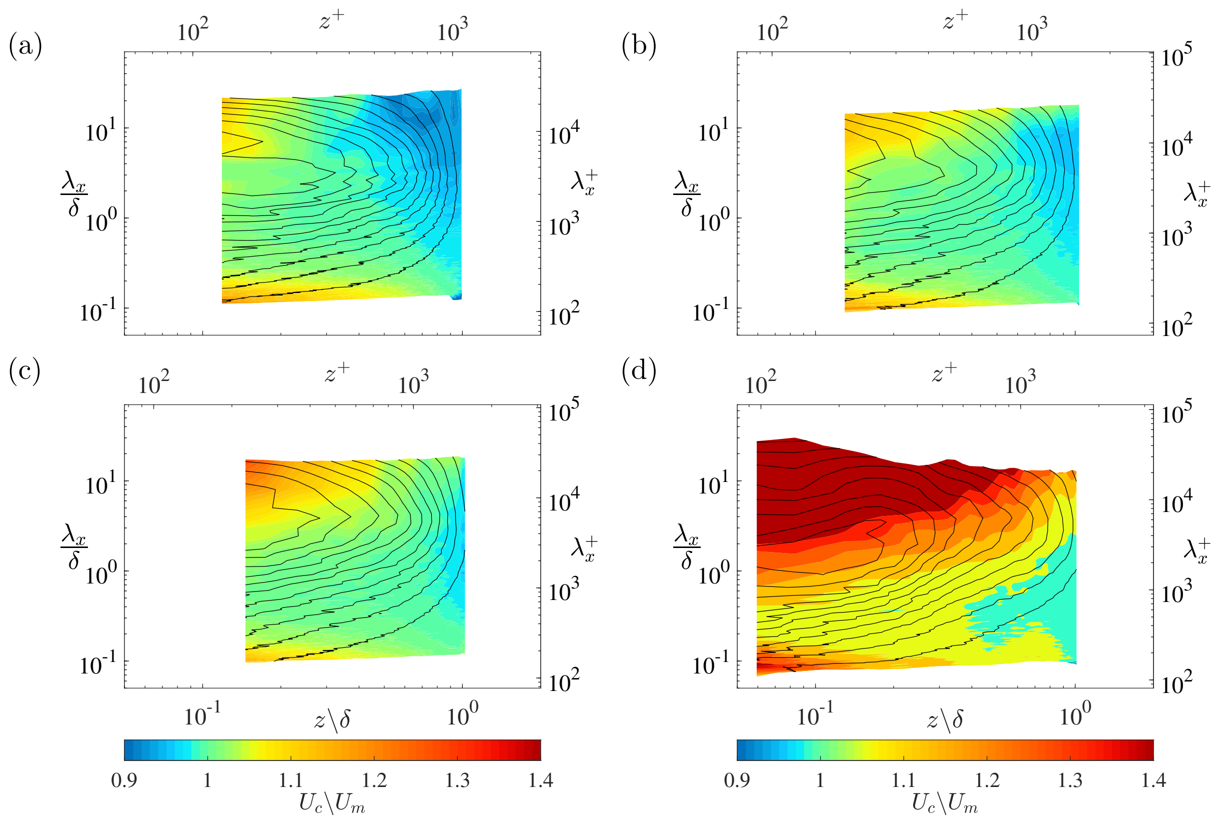

Figure 2: *Convection velocity normalised by the mean streamwise velocity (U_c/U_m) as a function of wavelength and wall distance. Black iso-lines of pre-multiplied spectra, $k_x\Phi_{uu}(k_x)/U_\tau^2$, where k_x is the streamwise wavenumber. At axial locations of x/L = 0.449 (a), x/L = 0.650 (b), x/L = 0.700 (c), and x/L = 0.800 (d).*

References

[1] Manovski, P., Gulotta, P., Giacobello, M., de Silva, C., Hutchins, N., and Marusic, I., (2020): High-Speed PIV Measurements of a Turbulent Boundary Layer at 80 kHz, *Proceedings of 22nd Australasian Fluid Mechanics Conference*, Brisbane, Australia.

[2] Prigent, S.L., Salze, É., and Bailly, C., (2022): Wall Pressure Spectra and Convection: Two-Dimensional Analysis Under Mean Pressure Gradients, *AIAA Journal, vol. 60.*

Law of the wake and scaling of the mean velocity profile in turbulent pipe flow

Gabriele Bellani [1,2], Alessandro Talamelli [1,2]

[1] Dipartimento di Ingegneria Industriale, Università di Bologna, Forlì, Italia
[2] CIRI Aerospace, Università di Bologna, Bologna, Italia

key-words: Turbulence, Pipe flow, high-Reynolds number

Abstract:
Despite decades of research, the advent of modern high-Reynolds number facilities [1], [2], [3], of numerical simulations at increasingly high-Reynolds number [4] [5] and attempts to determine a universal velocity profile for pipe flow are object of present research (see e.g. [8]), the asymptotic scaling of the mean velocity profiles in wall-bounded flow remains to a large extent and unsolved problem. Questions such the universality of the Von-kármán constant in the log-law, the bounds of the logarithmic region, and the minimum Reynolds number needed to observe a well-developed logarithmic region are still debated, due to a relatively large scatter in reported experimental and numerical data.

The discrepancies observed in different experimental and numerical studies can be attributed to several factors. Insufficient Reynolds number or limited accuracy are among the most crucial issues. Another issue is the sensitivity of the parameters to the methodology used to extract the quantities of interest such as, for example, the slope of the logarithmic region (i.e. the so called Von Kármán constant). Recently Luchini [7] suggested that first-order corrections to the log-law are needed to compensate the influence of pressure gradient in parallel flows such as Pipe and Duct flow. Luchini further pointed out [9] the importance of isolating the so called law of the wake from the Reynolds-invariant part of the velocity profile. The law of the wake is typically estimated from empirical data by subtracting a pre-determined log-law. However, if the log-law is to be estimated, the law of the wake must be determined without a priori assumptions on the inner part. This can be done using an iterative procedure based on the subtraction of two datasets obtained at different Reynolds numbers. This was shown in [9]. However, this analysis was applied mainly to low-Reynolds number data and only to a limited extent to experimental data at higher Reynolds number. No results for the wake function were explicitly reported for experimental data.

In this paper we apply this methodology to mean velocity profiles of turbulent pipe flow ranging between 9900 ¡ Re_τ ¡ 40000. The velocity profiles have been acquired in the Long Pipe CICLoPE by hot-wire anemometry (see fig. 1). We report the law of the wake obtained by applying the procedure reported in [9] from 4 different pairs of Reynolds number, using the higher Reynolds number case as a reference (see fig. 1). We compare the results with those obtained from DNS and we report the sensitivity of this procedure to experimental uncertainty. Finally, we investigate the influence of the law of the wake on the extraction of the fitting parameteres in the log region for various Reynolds numbers.

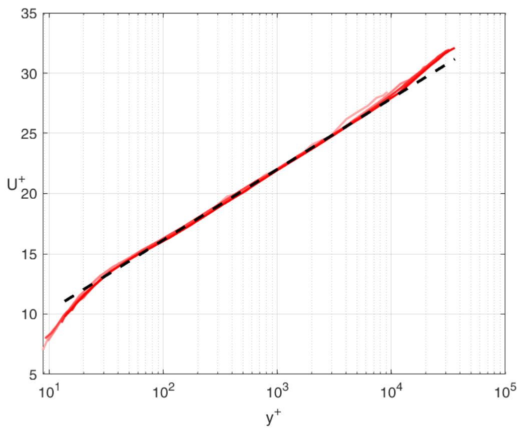

Figure 1: *Inner-scaled mean velocity profiles at Re_τ=9900, 22000, 32000, 35000, 39000, from from light to dark red, respectively. The dotted line is the log-law with κ=0.392 and B=4.4.*

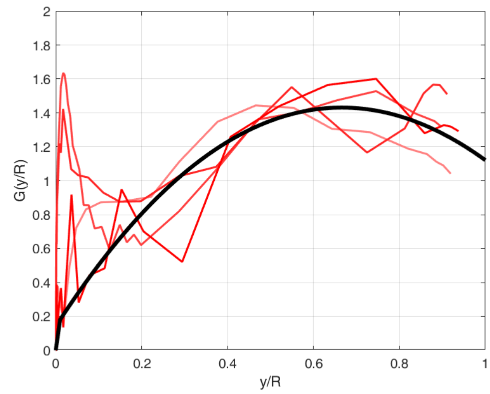

Figure 2: *Law of the Wake estimated using the iterative method reported in [Luchini] The red lines represent the wake law estimated from data at Re_τ=9900, 22000, 32000, 35000 using Re_tau=39000 as a reference dataset. The dark thick line is a polynomial fit to all datsets*

References

[1] Furuichi, N. and Terao, Y. and Wada, Y. and Tsuji, Y. (2015), Friction factor and mean velocity profile for pipe flow at high Reynolds num- bers, *Phys. Fluids 27 (9), 095108.*

[2] Zagarola, M. V. and Smits, A. J., (1998), Mean-flow scaling of turbulent pipe flow, *J. Fluid Mech. 373, 33–79.*

[3] Orlü, R. and Fiorini, T.and Segalini, A. and Bellani, G. and Talamelli, A. and Alfredsson, P. H., (2017), Reynolds stress scaling in pipe flow tur- bulence - first results from CICLoPE, *Trans. R. Soc. A 375, 20160187.*

[4] Pirozzoli, S. and Romero, J. and Fatica, M. and Verzicco, R. and Orlandi, P., (2021), Reynolds number trends in turbulent pipe flow: a DNS perspective, *J. of Fluid Mech., vol. 926 1–20.*

[5] Tao, J. and Rezaeiravesh, S. and Schlatter, P. and Hussain, F., (2023), Direct numerical simulations of turbulent pipe flow up to $Re_\tau \approx 5200$, *J. of Fluid Mech. vol.956 A18 1-18.*

[6] Nagib, and H. M. Monkewitz, and P. A. Mascotelli, and L. Fiorini, T. and Bellani, G. and Zheng, X. and Talamelli, A. (2017), Centerline Kármán "Constant" Revisited And Contrasted To Log-layer Karman Constant At CICLoPE, *in 10th International Symposium on Turbulence and Shear Flow Phenomena (TSFP10), Chicago, USA, July, 2017.*

[7] Luchini, P. (2017), Universality of the Turbulent Velocity Profile, *PRL. vol.118 224501.*

[8] Cantwell, B. J. (2019), A universal velocity profile for smooth wall pipe flow, *J. of Fluid Mech. 834–874.*

[9] Luchini, P. (2018), Structure and interpolation of the turbulent velocity profile in parallel flow, *European J Mech - B Fluids 71, 15–34.*

Coupling anisotropic fiber tracking with instantaneous volumetric flow field in turbulent channel flows

G. C. A. Caridi [1], V. Giurgiu [1], M. Alipour [2], M. De Paoli[3] and A. Soldati [1,4]

[1] Institute of Fluid Mechanics and Heat Transfer, TU Wien, 1060 Vienna, Austria
[2] Dep. of Mech. Eng. and Material Science, Yale University, New Haven, CT, USA
[3] Physics of Fluids Group, University of Twente, 7500AE Enschede, The Netherlands
[4] Polytechnic Department, University of Udine, 33100 Udine, Italy

key-words: anisotropic fiber, tracking, 3D PIV

Abstract:
Time-resolved and instantaneous volumetric measurements are coupled with Lagragian tracking of anisotropic curved fibers in the TU Wien Turbulent Water Channel. The experiments are conducted at friction Reynolds number ranging from 180 to 720 in the viscous wall region and in the channel center. The length of the fiber (1.2mm) is comparable to the Kolmogorovlength scales (0.3-0.8 mm). An established technique of fibre reconstruction and tracking is employed (Alipour et al., 2021). The latter allows the definition of the fibre containing plane and tracking its change in orientation, as shown in the example of one fiber reconstruction (Figure1). In the current experiment the optical magnification is improved achieving higher 3D reconstruction resolution (up to 100 voxel per fibre length), which in return, enables measurements of the spinning rate with lower uncertainty. Figure 2 shows an example of the coupling between the fiber reconstruction and instantaneous volumetric flow field. Full rotation rate tensor of small slender fibers is captured with velocity gradient tensor of the flow which allows the determination of statistical and instantaneous velocity and rotational slip between the fiber and the flow structures (laden). As results, the different behaviors of the fibers in terms of transnational and rotational motion in different regions of the channel are correlated to the homogeneous turbulent structures in the center of the channel and to the coherent structures within the viscous wall region, i.e., hairpin packets and transverse and longitudinal vortices.

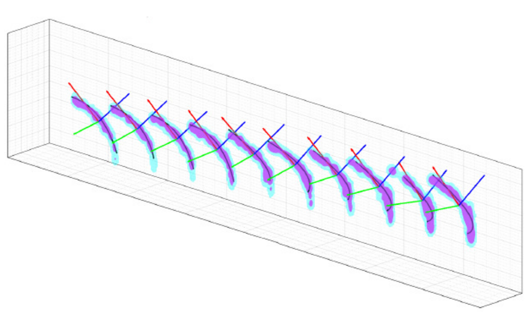

Figure 1: *3D reconstruction of a fiber trajectory with istantaneous orientation of the fiber's reference system.*

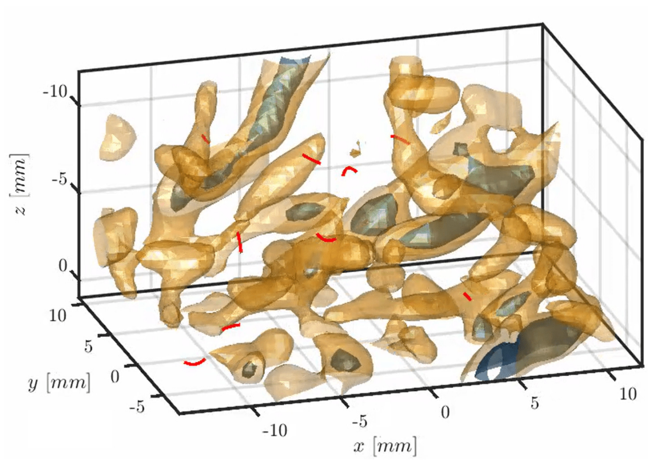

Figure 2: *3D visualization of the vortical structures at $Re_\tau = 720$ coupled with fiber reconstruction (red lines). Isosurfaces correspond at $\lambda_2 = -1000$ (blue) and -300 (yellow).*

Alipour M., De Paoli M., Ghaemi S. and Soldati A. (2021). Long non-axisymmetric fibres in turbulent channel flow. Journal of Fluid Mechanics, 916, A3.

Vorticity transport mechanism in a turbulent channel flow controlled using streamwise travelling waves

Mohammad Umair and Sedat Tardu

Grenoble Alpes University, Laboratoire LEGI, Domaine Universitaire, CS 40700, 38058 Grenoble Cedex 9, France

key-words: Drag reduction, Streamwise travelling waves, Direct numerical simulations

Abstract:

Transverse wall oscillation techniques have received an unprecedented amount of attention from the turbulence control community owing to its extraordinary capability of producing drag reduction margin as large as 60% [1-3]. Despite the continuous efforts in investigating the various captivating features of transverse wall oscillations techniques in the last few decades, the mechanism responsible for the observed drag reduction is still far from being fully understood. In the present work, we conducted few direct simulations of a plane turbulent channel flow controlled by streamwise travelling waves of spanwise wall velocity of amplitudes ranging from 0.15 to 1.25 (in outer units) at fixed frequency and wavenumber at friction Reynolds number 180. The resulting analyses show that the forcing acts primarily on the spanwise turbulent vorticity that is linked to the fluctuating shear stress at the wall, almost entirely attenuating it for the large amplitude cases (figure 1), while the effect on the other two components is subordinate. To strengthen this point, we performed numerical experiments, where the streamwise fluctuating velocity, and consequently the spanwise vorticity is artificially suppressed next to the wall. The anisotropic invariant maps show striking resemblance for large amplitude STW actuation and artificially forced cases. The quasi-streamwise vortices (QSVs), which play a key role in the regeneration mechanism, are pushed away from the wall, resulting in their weakened signature at the wall (figure 2). The shift (Δd_s) in QSVs can be roughly related to the drag reduction margin using the model proposed by [4]. There are direct terms in the vorticity transport equations that are directly related to the travelling wave characteristics and that play a direct role in the large drag reducing cases. Detailed analyses of various structural features are also provided, which includes the response of the near-wall streaks and shear layers of spanwise fluctuating velocity field.

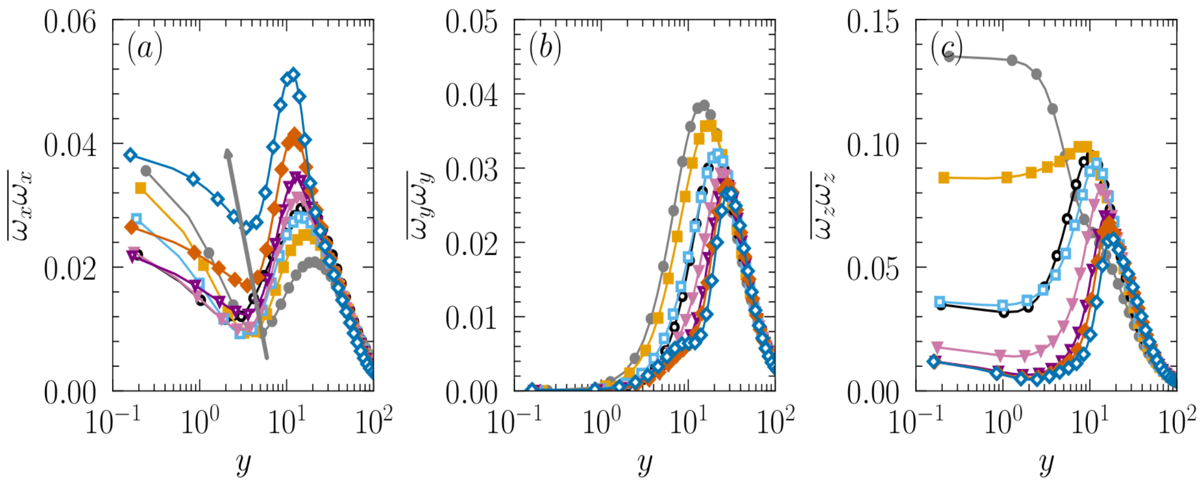

Figure 1: Turbulent (a) streamwise, (b) wall-normal and (c) spanwise enstrophy component, respectively. Scaling is based on the friction velocity of the controlled flow.

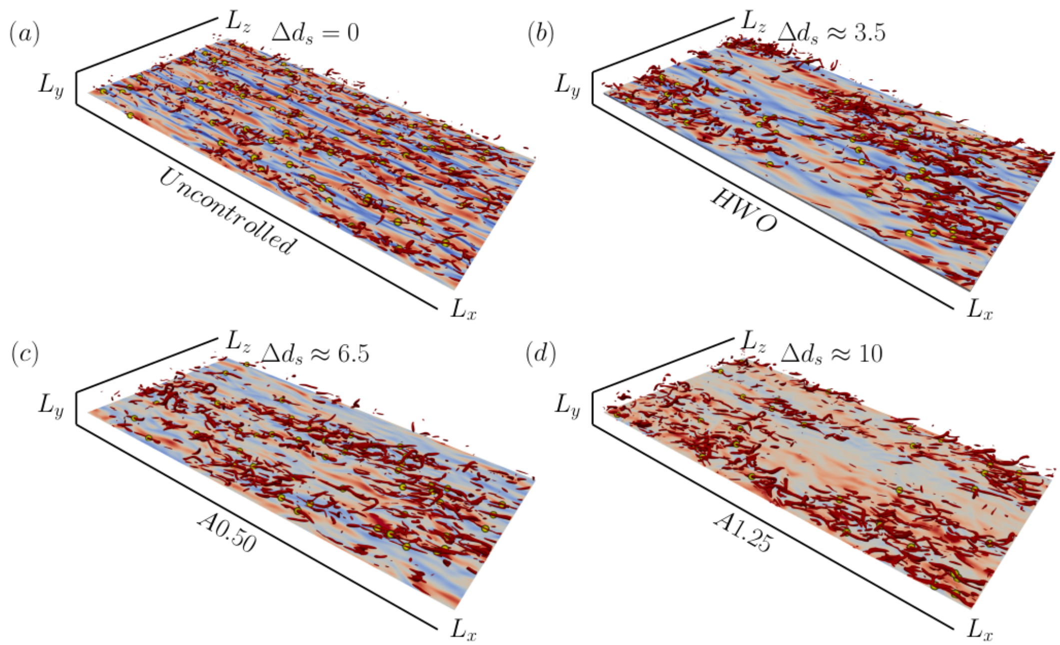

Figure 2: Quasi-streamwise vortical structures along with the instantaneous streamwise fluctuating velocity field (red: positive; blue: negative) on a wall parallel plane at $y^+=15$ for (a) uncontrolled, (b) homogeneous wall oscillation (HWO) at optimal forcing, (c) A0.50 and (d) A1.25 case, respectively. Scaling is based on the friction velocity of the controlled flow.

References

[1] Umair M., Tardu S. and Doche O., (2022), Reynolds stresses transport in a turbulent channel flow subjected to streamwise travelling waves, *Phys. Review Fluids, vol. 7 Issue 5 pp. 054601.*

[2] Quadrio M., Ricco P. and Claudio V., (2009): Streamwise-travelling waves of spanwise wall velocity for turbulent drag reduction, *J. Fluid Mechanics, vol. 627, pp. 161-178.*

[3] Quadrio M. and Ricco P., (2011): The laminar generalized Stokes layer and turbulent drag reduction, *J. Fluid Mechanics, vol. 667, pp. 135-157.*

[4] Orlandi P. and Jiménez J., (1994): On the generation of turbulent wall friction, *Phys. Fluids, vol. 6(2), pp. 634-341.*

Crossflow-oscillating plasma jets in a turbulent channel flow

L. d'Amato[1], E. Amico[1], G. Cafiero [1], G. Iuso [1], J. Serpieri [1]

[1] Department of Mechanical and Aerospace Engineering, Politecnico di Torino, Turin, Italy

key-words: Active flow control, Drag reduction, Plasma actuators

Abstract:

In recent efforts, dielectric-barrier-discharge plasma actuators (PA) have been considered as plausible flow actuators to induce a Stokes-like wall flow capable of reducing the friction drag (e.g. [3, 6, 5]) given their simplified technological embodiment compared to mechanical or piezo-electric devices (e.g. [1, 4, 7]). In this study, an array of PAs was built and installed in a channel flow facility. It was designed and fabricated to induce a wall jet oscillating along the opposite crossflow directions.

The measurements were performed in a ducted flow facility (0.42 m x 0.035 m x 10 m, in width, height and length) operated at friction Reynolds numbers (Re_τ) ranging between $200 \leq Re_\tau \leq 400$. A total of 14 pressure taps are installed in the channel walls every 0.20 m along the streamwise direction. These pressure taps are connected to a piezo-electric pressure transducer (DSA) operated at 20 Hz and set to acquire for 300 s. The flow actuator hereby considered features an array of seven DBD PAs with the electrodes aligned with the streamwise direction. Every actuator featured one exposed electrode connected to the ground and two encapsulated electrodes, one per side of the exposed electrode, each connected to a high voltage (HV) source. A schematic of the actuator installed in the channel is shown in figure 1(a). The HV amplifiers were switched on/off to modulate the plasma jets leading to the wished crossflow-oscillating forcing. The modulation frequency was varied around the literature-deemed-optimal non-dimensional period of $T^+ = 100$ (where the + labeled units are non dimensionalised with inner-layer scales) (e.g. [2]). A schematic of the voltage-modulation functions is shown in figure 1(b). The crossflow spacing of the actuators was $\Delta z = 20$ mm ($\Delta z^+ = 350$ for the reference Reynolds number flow).

The friction Reynolds number of $Re_\tau = 300$ was chosen as reference flow. The actuator was supplied with a peak-to-peak voltage signal at 8 kV_{pp} and three different modulation frequencies were considered corresponding to the non dimensional periods of: $T^+ = 50$, 80 and 100. The measured differential pressure Dp, shown in figure 2, retrieves rather similar behaviors for all the three frequencies, where, for comparison, the reference unforced flow is measured and reported too. Moving along the streamwise direction as the flow undergoes actuation, the slope of the differential pressure decreases whereas, moving downstream of the actuation region, the slope recovers to the unforced value. Such behaviour of the pressure trend is thought to be initially caused by the downwash motions of higher-momentum fluid needed to comply with mass continuity and induced crossflow momentum. On the other side, at more downstream stations, the beneficial effect of the performed actuation is likely overcoming this negative (drag enhancing) effect and a lower pressure drop is reported for the actuated flow.

The final contribution will discuss the effects of the variation of other actuation parameters as the supplied voltage (i.e. the induced body force), the actuators' crossflow spacing (and for the various jets strengths) as well as the flow Reynolds number. For these parameters, sub-optimal (compared to the available literature) actuation was also performed. A quantitative measurement campaign is also underway and it will allow to inspect the flow topology and modifications due to the applied actuation. It will help understanding the opposite effect on the measured flow pressure observed at the upstream and downstream actuation region here only conjectured upon. Finally, the actuator consumed power will also be reported thus leading to efficacy/efficiency maps of the actuation parameter space.

References

[1] F. Auteri, A. Baron, M. Belan, G. Campanardi, and M. Quadrio. *Physics of Fluids*, 22(11), 2010.

[2] K.-S. Choi and M. Graham. Drag reduction of turbulent pipe flows by circular-wall oscillation. *Physics of Fluids*, 10(1):7–9, 1998.

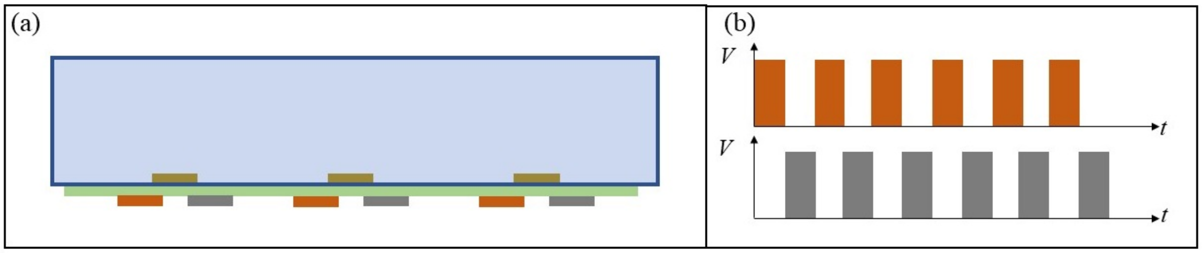

Figure 1: *(a) Schematics of the setup as seen in a crossflow plane (not to scale): operated electrodes in orange and grey, exposed electrode in yellow and dielectric in light green; (b) Voltage-modulation functions for the two exposed electrodes, color coded as the electrodes of (a).*

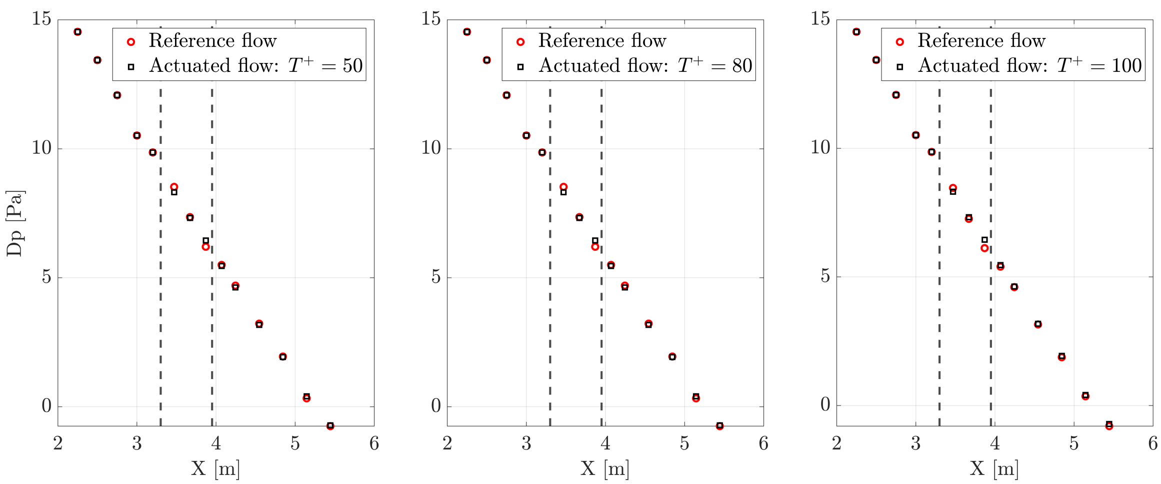

Figure 2: *Measured differential pressure for three actuated flows: $T^+ = 50$, 80 and 100 and for the reference unforced flow. The dashed vertical lines at station x =3.30 m and x =3.95 m represent the upstream and downstream boundaries of the actuated region.*

[3] K.-S. Choi, T. Jukes, and R. Whalley. *Philosophical Transactions of the Royal Society A: Mathematical, Physical and Engineering Sciences*, 369(1940):1443–1458, 2011.

[4] D. Gatti, A. Güttler, B. Frohnapfel, and C. Tropea. *Experiments in Fluids*, 56(5):110, 2015.

[5] M. T. Hehner, D. Gatti, P. Mattern, M. Kotsonis, and J. Kriegseis. Beat-frequency-operated dielectric barrier discharge plasma actuators for virtual wall oscillations. *AIAA Journal*, 59(2):763–767, 2021.

[6] O. Mahfoze and S. Laizet. *International Journal of Heat and Fluid Flow*, 66:83–94, 2017.

[7] I. Marusic, D. Chandran, A. Rouhi, M. K. Fu, D. Wine, B. Holloway, D. Chung, and A. J. Smits. An energy-efficient pathway to turbulent drag reduction. *Nature Communications*, 12(1):1–8, 2021.

Boundary layer modification with travelling surface waves generated by kagome lattices

I. Fumarola [1], Z. Soltani, [1] M. Santer [1] and J. Morrison [1]

[1] Department of Aeronautics, Imperial College, London, UK

key-words: Turbulent boundary layer, flow control, simultaneous PIV, DIC

Abstract:
Simulations and experiments have demonstrated that skin friction drag reduction greater than 40% can be achieved by moving wall with different types of motion, such as oscillating walls or spanwise waves travelling in the streamwise direction [1]. Both drag and power reductions at $Re_\tau = 12,800$ have also been demonstrated experimentally [3] using surface waves generated by a system of oscillating plates, each of length $O(\delta)$. Systematic experiments are required to understand the fundamental mechanisms at high Reynolds numbers. Here we present an experiment on a new surface for control, based on a kagome lattice. The surface is able to generate spanwise travelling waves, of variable waveform (e.g. square or sinusoid) at different amplitudes and frequencies over a wide range of wave speeds. The present work focuses on simultaneous measurements of both the flow field and of the surface deformation by combining Particle Image Velocimetry (PIV) with Digital Image Correlation (DIC) allowing identification of those configurations that show a potential for drag reduction. The potential for transients in surface motion to provide temporal reductions in surface drag depends on the time constants associated with the relaxation of the turbulence towards some long-time average. How this happens can be assessed by new ideas such as resolvent analysis, either linear or nonlinear. The key fundamental question is therefore what is the relative importance of linear, fast and nonlinear, slow mechanics when the wall forcing is applied at high Reynolds numbers?

The model comprises a flat plate, with a modified super-elliptic leading edge, resting on the floor of the wind tunnel with a 1 m of active surface starting 2.4 m downstream of the leading edge. The active surface consists of a black silicone skin glued onto a kagome lattice structure, figure 2., which is actuated along its spanwise corridors by a pneumatic mechanism. It comprises six tiles (modules) with continuous waveforms for about 10δ in the streamwise direction. Therefore, the boundary layer has not fully adjusted to the surface-wave condition. The active surface over a longer fetch has previously been used [2], showing a maximum drag reduction of 21.5% at $Re_\tau = 1125$.

The present experiment focuses on simultaneous measurements of surface deformation and flow field using respectively planar PIV and stereo DIC. Both techniques are based on the correlation of image pairs. PIV captures the motion of the seeding particles in a narrow area illuminated by the laser sheet, while with DIC, it is the motion of random dots painted on the surface illuminated by a diffuse light that generates a speckle pattern. The implementation of simultaneous PIV and DIC is a relatively new approach for fluid-structure interaction problems. Figure 1 shows the setup of the current experiment which adopts a three-colour scheme to avoid any interference between images. The PIV is carried out on a horizontal plane 2.5 mm above the surface, corresponding to $y^+ = 30$ at $Re_\tau = 1129$, approximately. Figure 3 shows typical results from a single tile of active surface 300 mm x 100 mm.

Results of time-resolved PIV synchronised with DIC for the six-tile configuration will be presented for a range of actuation parameters and travelling-wave direction. Measurements also include hot-wire anemometry and oil film interferometry to measure the turbulent boundary layer and of the skin friction. Future developments include extending the active surface up to 3 m for measurements in an equilibrium boundary layer at $Re_\tau \approx 8000$.

References

[1] P. Ricco, M. Skote, M. A. Leschziner (2021), A review of turbulent skin-friction drag reduction by near-wall transverse forcing, *Progress in Aerospace Sciences*, vol. 123, 100713.

[2] J. Bird, M. Santer, J.F. Morrison, (2018), Experimental control of turbulent boundary layers with in-plane travelling waves, *Flow, Turbulence and Combustion, vol. 100, 1015-1035.*

[3] I. Marusic, D. Chandran, A. Rouhi, M. K. Fu, D. Wine, B. Holloway D. Chung, A. J. Smits, (2021), An energy-efficient pathway to turbulent drag reduction, *Nature Communications, vol. 12(1), 1-8.*

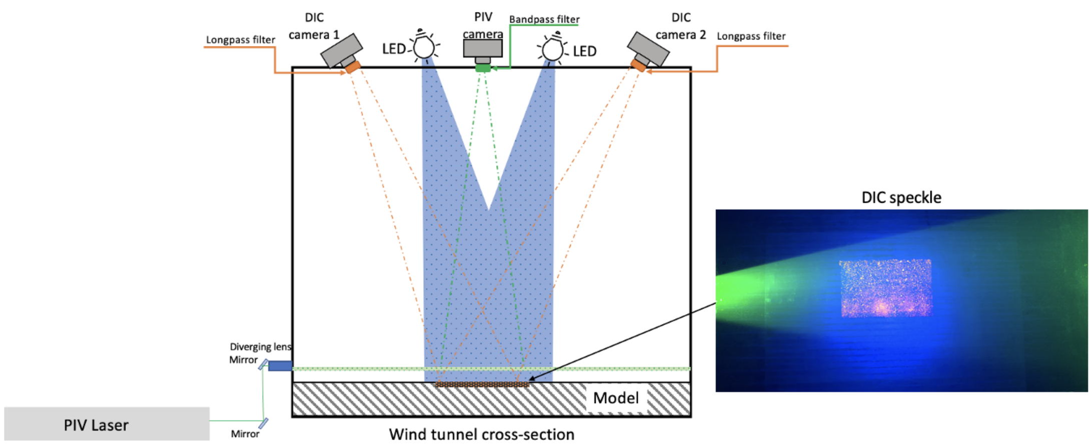

Figure 1: Schematic of the experiment in cross-section. Top: DIC and PIV cameras with filters and the blue LED light. Side: green PIV laser with optics. The dash lines indicate the field of views of the cameras. Model surface painted in fluorescent orange.

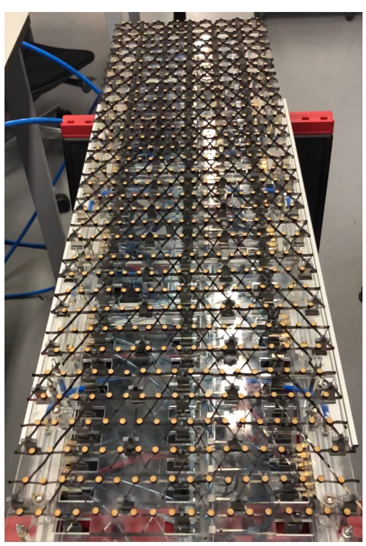

Figure 2: Active surface without silicone skin (six tiles).

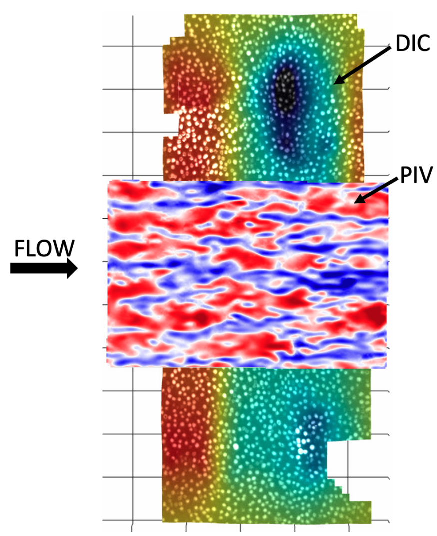

Figure 3: Instantaneous image of surface DIC and planar PIV at $y^+ = 30$ at $Re_\tau = 1129$ (single tile).

On the wave-induced Stokes sublayer and drag reduction in the turbulent wind

A. Cimarelli, F. Romoli and E. Stalio

DIEF, University of Modena and Reggio Emilia, 41125 Modena, Italy

Key-words: Wind waves, Turbulent drag

Abstract:
Surface fluxes of momentum and energy through the ocean-atmosphere interface are of primary importance for the characterization of geophysical flows and climate formation mechanisms. The presence of a somewhat compliant water surface gives rise to complex nonlinear interaction mechanisms between the atmospheric boundary layer and the wave field developed in response to the turbulent wind forcing itself [1]. These interactions determine the flux of momentum and energy trough the air-sea interface thus representing a fundamental process for the climate behaviour. However, the physical mechanisms behind the wind-wave interactions still lack a sufficiently general and complete theory [2]. The main reason is the multiplicity of complex phenomena involved and the lack of suitable experimental and numerical data. In order to address the latter issue, we performed a Direct Numerical Simulation of the wind-wave interaction problem in the flow settings of a two-phase open channel driven by a constant pressure gradient where the wind is turbulent and the water is almost quiescent [3]. To the author' knowledge, the simulation represents one of the very first attempts to get the fully-coupled solution of the wind-wave problem based on first principles and on realistic values of the fluid properties of air and water. The simulation reveals an interesting water wave pattern, see figure 1(a). It consists of waves at very low steepness and elevation ($S = 7.3 \cdot 10^{-4}$ and $\delta_w^+ = 0.3$) propagating at an angle $\gamma = 38.6°$ in the upwind direction with a phase speed $\mathbf{c}^+ = (\mathbf{10}, \mathbf{8})$. Despite the small size of the water wave pattern, its effect on the turbulent wind is far from being negligible, see figure 1(b). A significant reduction of drag is indeed observed. The origin of drag reduction is associated with the presence of a wave-induced Stokes sublayer. The picture is the following. The oblique wave pattern is found to induce periodically distributed pressure gradients in the spanwise direction thus leading to a flow pattern oscillating in the spanwise direction, see figure 2. Such type of modulation gives rise to a weakening of the self-sustaining processes of turbulence in the very near-interface region and, hence, to drag reduction. It is remarkable the significant effect on the turbulent wind despite the very small thickness of the Stokes layer $\ell_s^+ \approx 2$ and the very weak intensity of the associated spanwise motion $|w|_{max}^+ \approx 10^{-3}$. The details of the processes involved and the related strong repercussions for climate science will be presented at the conference meeting.

References

[1] Sullivan P.P. and McWilliams J.C., (2010), Dynamics of winds and currents coupled to surface waves, *Ann. Rev. Fluid Mech., vol. 42, pp. 19-42*

[2] Ayet A. and Chapron B., (2021), The dynamical coupling of wind-waves and atmospheric turbulence: a review of theoretical and phenomenological models, *Bound.-Lay. Meteorol., pp. 1-33*

[3] Cimarelli A., Romoli F. and Stalio E., (2023), On wind-wave interaction phenomena at low Reynolds numbers, *J. Fluid Mech., vol. 956, A13*

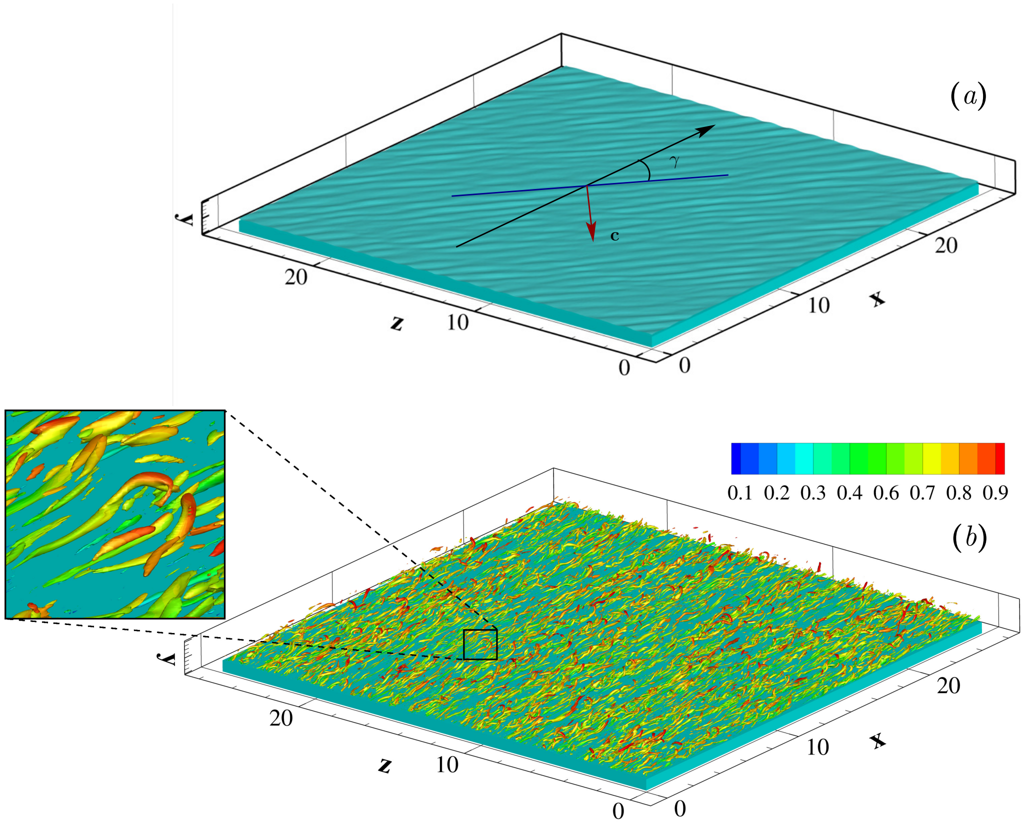

Figure 1: (a) Instantaneous water-wave pattern. The vertical wave length has been expanded by a factor 80 for readability reasons. The black arrow denotes the wind direction, the blue line the dominant wave alignment with γ the angle with respect to the wind direction and the red arrow indicates the phase speed $\mathbf{c}$. (b) Instantaneous vortex pattern in the turbulent wind boundary layer shown by means of an iso-surface of $\lambda_2 = -3$ colored with the streamwise velocity intensity.

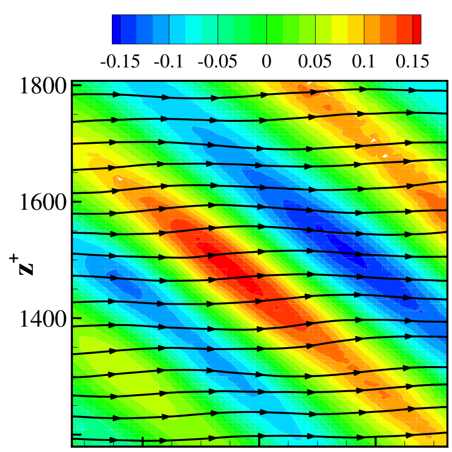

Figure 2: Wave-induced Stokes sublayer: isocontours of the instantaneous wave elevation $\eta^+(x, z)$ and velocity field streamlines zoomed in a portion of the flow domain for readability reasons.

Investigations into spatio-temporal interactions in rough wall-bounded turbulence using reduced order modeling

Bianca Viggiano [1] and Dennice F. Gayme[1]

[1] Mechanical Engineering Department, Johns Hopkins University, Baltimore, MD, USA

key-words: Wall-bounded turbulence, reduced-order modeling, riblets

Abstract:
Installing microgroves on a surface (riblets) subjected to a turbulent flow is known to alter the skin-friction drag. The ability of these structures to reduce drag in particular, has motivated a large body of work studying the mechanisms associated with drag reduction, and its breakdown. While the drag reduction mechanism is well understood, its breakdown and how this varies with Reynolds number is not fully understood. Achieving the desired understanding is challenging using conventional approaches as full-scale modeling of drag over microgrooves remains a computationally expensive undertaking due to the increased resolution required to capture the details of the flow at the surface. Modesti *et al.* [1] sought to gain insight at lower computational costs by employing a minimal channel, which was shown to accurately reproduce flow features upto a certain channel height. Resolvant analysis provides another approach to analyze the dominant flow features and provide insight into how key structures interact [2]. The restricted nonlinear (RNL) model has also been applied as a low order simulation and analysis method for these flows [3]. The RNL model decomposes the flow field into large scales (assocaited with a streamwise constant mean) and small scales (perturbations about that mean). The reduction of computation arises from the restriction of nonlinear interactions of the perturbations to only those contributing to the mean flow [4]. One advantage of the RNL model is it enables study of the time evolution of a simplified flow field in a full cross flow domain, therefore providing a means to capture both the statistical and dynamic flow features.

RNL simulations have been show to agree well with direct numerical simulation (DNS) and experimental data for turbulent flows over both smooth and rough walls [3] at moderate Reynolds numbers. However, the small number of streamwise scales supporting the flow in the traditional RNL framework is inadequate to describe the larger number of scales and scale interactions in high Reynolds number flows. The recently introduced augmented RNL (ARNL) model [3] extends the RNL paradigm to include additional scale interactions through the systematic inclusion of intermediate scales following the approach in Marston *et al.* [5]. In this work we look to exploit the greatly decreased computation costs of the ARNL model to perform simulations of higher Reynolds number turbulent flows over riblets of varying geometries to characterize the physics of both drag reduction and drag increase in these flows. The resulting simulated flow fields are compared to DNS of flow over riblets at moderate and high Reynolds numbers. The instantaneous streamwise velocity of the ARNL simulation over blade riblets at $Re_\tau = 550$ is presented in figure 1. The snapshot shows realistic cross-stream structures of turbulence within the domain. Figure 2 provides a comparison of the Reynolds shear stress $\langle uv \rangle$ for the ARNL modeled flow and DNS data of García-Mayoral and Jiménez [6]. Three different riblet spacings of $s^+ = 12$, 20 and 33 ($\ell_g^+ = 7.2$, 12.4 and 20.4, respectively) show very good agreement with the fully resolved DNS.

Additional analysis to be included in the presentation is the analytical decomposition of the mean velocity using methods provided in Endrikat *et al.* [7], which will enable us to further characterize the physics associated with the drag alteration due to the rough wall. This analysis will be performed at $Re_\tau = 395, 550$ and 1000.

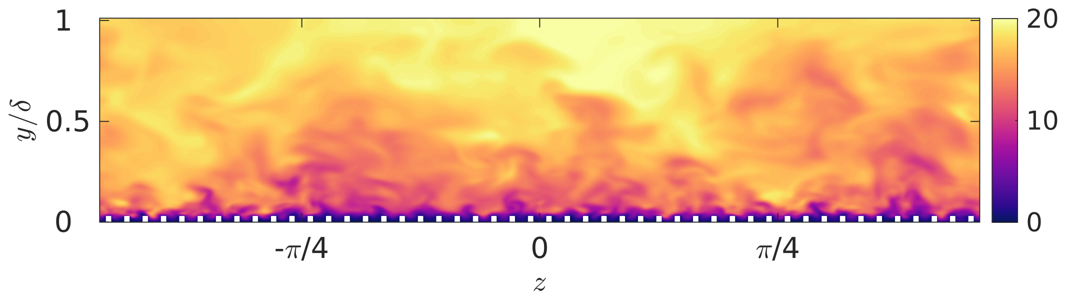

Figure 1: Instantaneous snapshot of streamwise velocity in the $y - z$ plane for $Re_\tau = 550$ of the ARNL model.

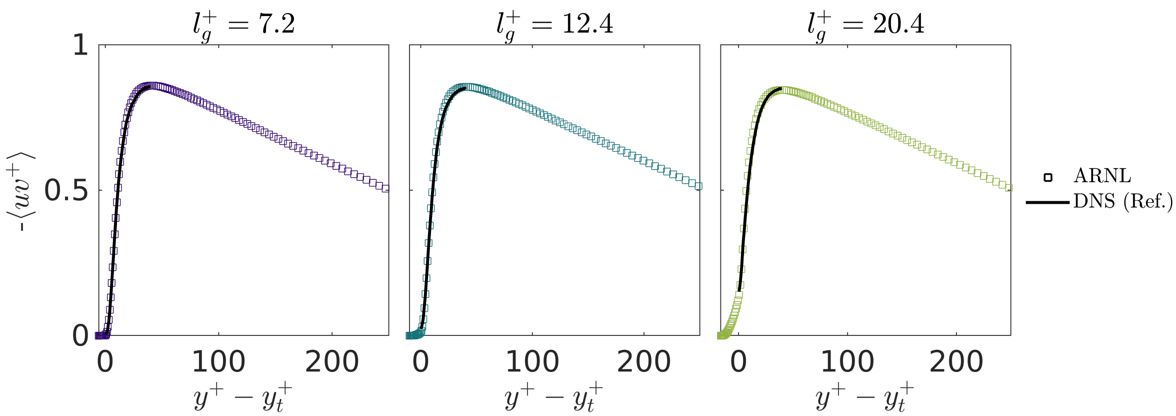

Figure 2: Comparisons of the Reynolds shear stress as a function of wall normal location, y, of the ARNL model to DNS [6] of riblets at $Re_\tau = 550$ for the same spacings of $s^+ = 12$, 20 and 33. y_t denotes the riblet tip height for ease of comparison

References

[1] D. Modesti, S. Endrikat, N. Hutchins and D. Chung, (2021): Dispersive stresses in turbulent flow over riblets, Journal of Fluid Mechanics 917, A55.

[2] C. Andrew and M. Luhar, (2020): Resolvent Analysis for Turbulent Channel Flow with Riblets, AIAA Journal 58.1, pp. 589-599.

[3] B. A. Minnick, (2022): A Restricted Nonlinear Approach to Momentum and Scalar Mixing in Wall-Turbulence Johns Hopkins University, Dissertation.

[4] D. F. Gayme, and B. A. Minnick, (2019): Coherent structure-based approach to modeling wall turbulence, Physical Review Fluids 4.11 : pp. 110505.

[5] J. B. Marston, G. P. Chini and S. M. Tobias, (2016): Generalized Quasilinear Approximation: Application to Zonal Jets., Phys. Rev. Lett., 116, 214501.

[6] R. García-Mayoral and J. Jiménez, (2012): Scaling of turbulent structures in riblet channels up to $\mathrm{Re}_\tau \approx 550$, Physics of Fluids, 24 (10) 105101.

[7] S. Endrikat, D. Modesti, R. García-Mayoral, N. Hutchins and D. Chung, (2021): Influence of riblet shapes on the occurrence of Kelvin–Helmholtz rollers, Journal of Fluid Mechanics, 913.

Energy cascades in axisymmetric turbulent wakes

M. Obligado [1]

[1] LEGI, Grenoble, France

key-words: Axisymmetric turbulent wakes, free-shear flows, energy cascade

Abstract:

Within a worldwide effort to increase alternative energies generation, the study of the flow downstream one or several turbines has received widespread attention. Despite this growing interest, many recent advances in the modelling of turbulent flows have not yet been adapted to such studies [1]. They concern the understanding of the inner structure of turbulence: the energy cascade. This parameter sets how energy is transferred among large to small scales and how the energy of the flow is dissipated. This complicated phenomenon has been found to ultimately set important properties of turbulent wakes, such as their velocity deficit and how they spread on the streamwise direction [2, 3, 4].

The theory that allows to predict the far-wake streamwise scalings of the centreline wake deficit u_0 and the wake width δ has been developed by Townsend and George [5, 6]. It relies on a set of hypotheses that includes the axisymmetry and self-preservation of different averaged quantities of the flow and a scaling for the turbulent kinetic energy dissipation rate ε. The latter is usually modelled according to the Richardson-Kolmogorov cascade. In this way, the well-known predictions for the streamwise evolution (along x) for u_0 and δ are obtained. The centreline velocity deficit is found to scale as $u_0(x) = AU_\infty \left((x - x_0)/\theta\right)^{-2/3}$. On the other hand, the wake width evolves as $\delta(x) = B\theta \left((x - x_0)/\theta\right)^{1/3}$, where θ is the momentum thickness, U_∞ the incoming freestream velocity, A and B are dimensionless constants and x_0 a virtual origin.

Despite the widespread use of these scalings, it has recently been found that the Richardson-Kolmogorov phenomenology [5, 6] is not the only one relevant for wind energy applications. Indeed, over the last years, a new type of energy cascade has been reported in a number of turbulent flows, including axisymmetric turbulent wakes [1]. The so-called non-equilibrium energy cascade can be identified via anomalous scalings of the dissipation constant C_ε, that is defined as $C_\varepsilon = \varepsilon L/u'^3$, with L the integral length scale of the flow and u' the rms value of the fluctuations of the streamwise velocity. Moreover, it has been proven that the Townsend-George theory predicts different streamwise scalings depending on the nature of the energy cascade. For instance, the non-equilibrium predictions are $u_0(x) = AU_\infty \left((x - x_0)/L_b\right)^{-1} (\theta/L_b)^2$ and $\delta(x) = B\sqrt{L_b(x - x_0)}$, where L_b is the square root of the area $\mathcal{A}$ of the generator.

While the presence of non-equilibrium streamwise scalings for u_0 and δ has been reported in the wakes of bluff [3, 4] (see figure 1-left) and slender bodies [7], its relevance for wind energy applications remains an open question. One of the main difficulties of such studies is that they require experiments in wind tunnels that are large enough to allow testing realistic scaled turbines far enough downstream to disentangle the nature of the streamwise scalings. Furthermore, experimental data accessible from field measurements is still somewhat limited, and relevant quantities from the theory, such as $\varepsilon(x)$, are not accessible.

In this work, we propose a wind tunnel study about the spatial development of the turbulent wake of a scaled wind turbine. We report data from the large wind tunnel at Oldenburg University, that has a test section with a length of 30 m and a square cross section of $3 \times 3\,\mathrm{m}^2$. The scaled wind turbine consisted on a single three-bladed horizontal axis model (of type MoWiTO 0.6, see [8], see figure 1-right) with a rotor diameter D of 58 cm. During tests, the rotor was controlled to optimise the power output for a given blade pitch angle and incoming velocity. An array consisting of 16 single hot-wire probes was used to scan the wake at hub height between $x/D = 1$ and $x/D = 32$ in steps of $1D$. In the spanwise direction y, the probes cover a range from $y/D = -1.91$ to $y/D = 1.04$. The turbine was tested under several different working conditions, including different freestream velocities and tip speed ratios. Both laminar and turbulent inflows were studied, the first consisting on an empty test section (i.e. only the scaled turbine and the hot-wire probes were placed on it) and the second in passive-grid-generated turbulence.

The first part of the presentation will be devoted to the deduction of the two sets of scalings using the Townsend-George theory. Moreover, current evidence of non-equilibrium turbulence in the wake of slender and bluff bodies will be presented. Finally, the aforementioned experimental setup and other works from the literature will be discussed in order to asses the relevance and consequences of the presence of a different energy cascade in the wake of single and multiple wind turbines.

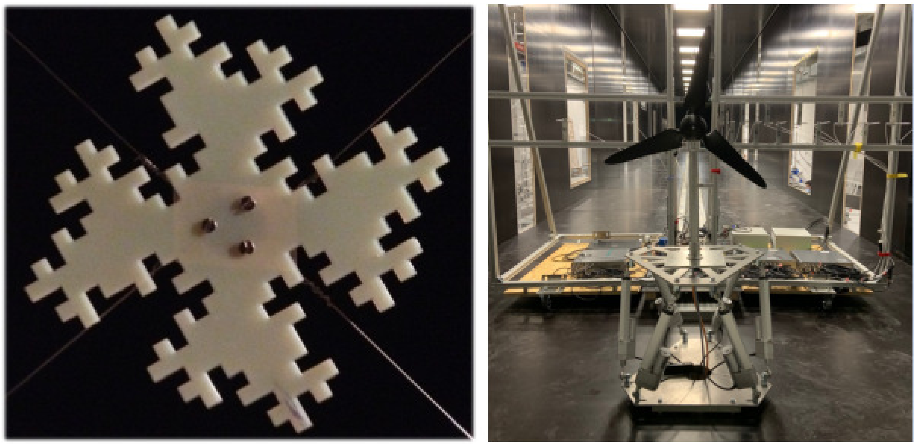

Figure 1: Different wake generators: bluff body with irregular peripheries (left) and scaled wind turbine (right).

References

[1] Vassilicos J. C., (2015), Dissipation in turbulent flows., *Annual Review of Fluid Mechanics, vol. 47, pp. 95-114*

[2] Dairay T., Obligado M. and Vassilicos J. C., (2014), Non-equilibrium scaling laws in axisymmetric turbulent wakes., *Journal of Fluid Mechanics, vol. 781, pp. 166-195*

[3] Obligado M., Dairay T. and Vassilicos J. C., (2011), Nonequilibrium scalings of turbulent wakes., *Physical Review Fluids, vol. 1*

[4] Nedić, J., Vassilicos J.C., and Ganapathisubramani B., (2013), Axisymmetric turbulent wakes with new nonequilibrium similarity scalings., *Physical review letters, vol. 111*

[5] George W., (1989), Self-preservation of turbulent flows and its relation to initial conditions and coherent structures

[6] Townsend A. A., (1949), The fully developed turbulent wake of a circular cylinder

[7] Ortiz-Tarin, J.L., Nidhan, S. and Sarkar, S., (2021), High-Reynolds-number wake of a slender body., *Journal of Fluid Mechanics, vol. 918*

[8] Neunaber I., Peinke J. and Obligado M., (2021), Investigation of the dissipation in the wake of a wind turbine array., *Wind Energy Science, 2021, 13*

Event-based imaging for visualization and measurement of turbulent flows

Christian Willert [1], J. Klinner [1]

[1] DLR Institute of Propulsion Technology, German Aerospace Center, Köln, Germany

Key-words: experiment, turbulent boundary layer, event-based imaging, particle tracking velocimetry, PIV

Abstract:
Event-based vision (EBV), dynamic vision sensing (DVS) or neuromorphic imaging describe a rather new sub-field within computer vision, differing considerably from classical frame-based imaging (Gallego et al., 2022). Event cameras only record contrast changes ("events") within the scene, either going from dark to bright (positive event) or bright-to-dark (negative event). As the pixels "fire" independently an asynchronous stream of *events* results that consist of pixel coordinates, a time stamp and a binary contrast change signal. Static areas in the imaged scene provide no information; intensity data is essentially not available. At the same time, event cameras feature a very high dynamic range (>110 dB) and are considerably more sensitive than conventional CCD/CMOS cameras.

In the context of particle imaging, narrow event streaks are produced in the space-time domain and can be processed to provide 3D-3C particle tracking velocimetry (PTV) data.The recently introduced event-based imaging velocimetry (EBIV) technique combines EBV and light sheet illumination to provide time-resolved, planar (2D-2C) velocity fields (Willert and Klinner, 2022; Willert, 2023)). In this work we apply EBIV to obtain time-resolved velocity profiles of a turbulent boundary layer (TBL) in analogy to the profile-PIV technique (Willert, 2015). The latter has been used to simultaneously provide detailed velocity statistics and time-resolved data of turbulent flows (see eg. Willert et al., 2017). The field of view is generally illuminated by a high-speed pulsed laser that is collimated into a narrow light sheet.

Fig. 2 presents exemplary velocity statistics obtained with EBIV at the 1m wind tunnel of the DLR Institute of Aerodynamics and Flow Technology (Göttingen) with $U_\infty = 5.2$ m/s, $\mathrm{Re}_\tau = 520$ using the setup shown in Fig. 1(a). A viscous scale of $\nu/u_\tau = 67\,\mu$m and an image magnification of 84 pixel/mm results in a resolution of 5.7 pixel per viscous unit. The data was processed using a multiple-frame, cross-correlation based PIV algorithm but can also be handled by 2D particle tracking algorithms. The described system is capable of providing data quality on par with currently used, considerably more expensive, high-speed PIV hardware and is currently suitable for measurements up to 10 m/s on a field of view of 50 mm.

A second EBIV configuration (c.f. Fig. 1(b)) captured the flow in the viscous sublayer of the TBL using a thin wall-parallel light sheet of <1 mm thickness and a set of three synchronized event-cameras. The ultimate aim of this setup is to estimate the unsteady wall shear stress field through triangulation of the recorded particle tracks which will be addressed in the proposed contribution. The dynamics of the near wall flow can already be visualized in the raw event data for which two examples are shown in Fig. 3, although the static imagery can only partially reveal the true particle motion.

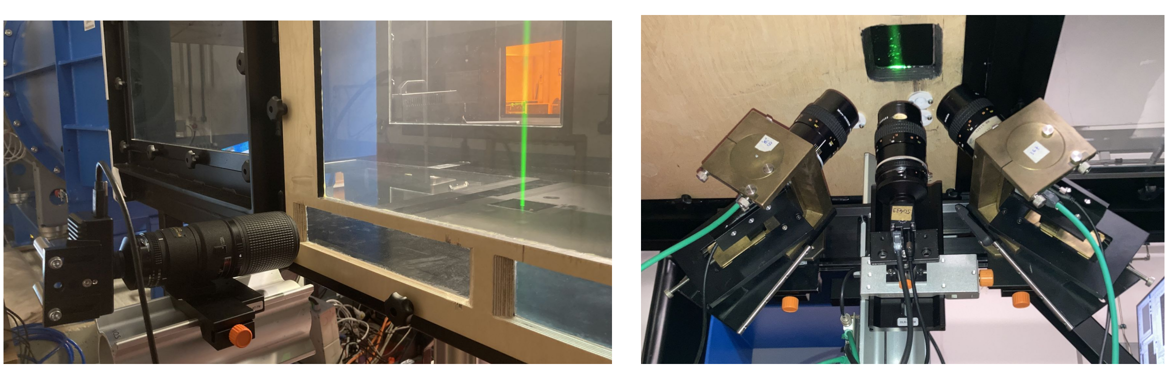

(a) (b)

Figure 1: *(a): velocity profile measurement setup using an event-camera; (b): triple-event camera setup for particle tracking in the viscous and buffer layers of a TBL.*

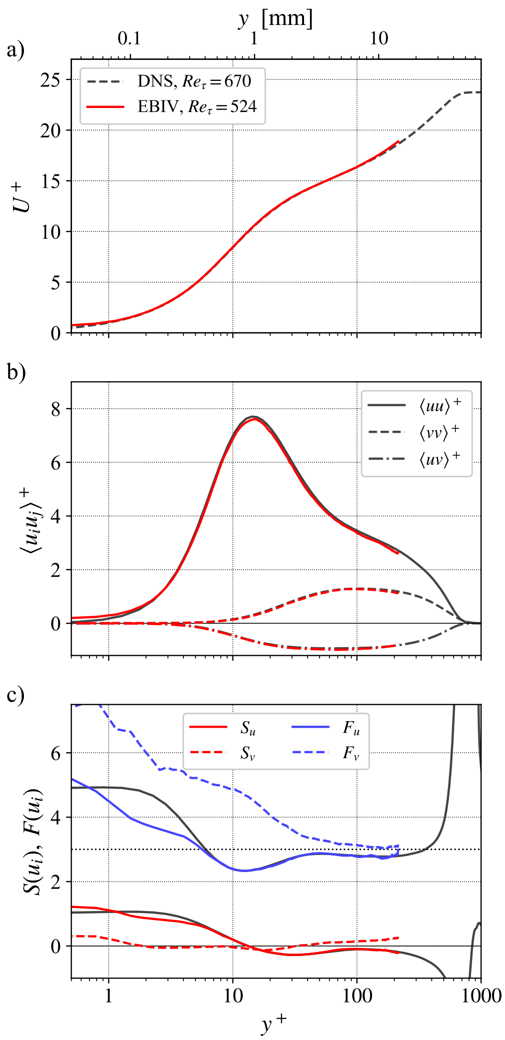

Figure 2: *Velocity statistics obtained with EBIV, using three records of 10 s duration (raw data ≈3GB), compared to DNS data of similar Reynolds number by Schlatter and Örlü (2010).*

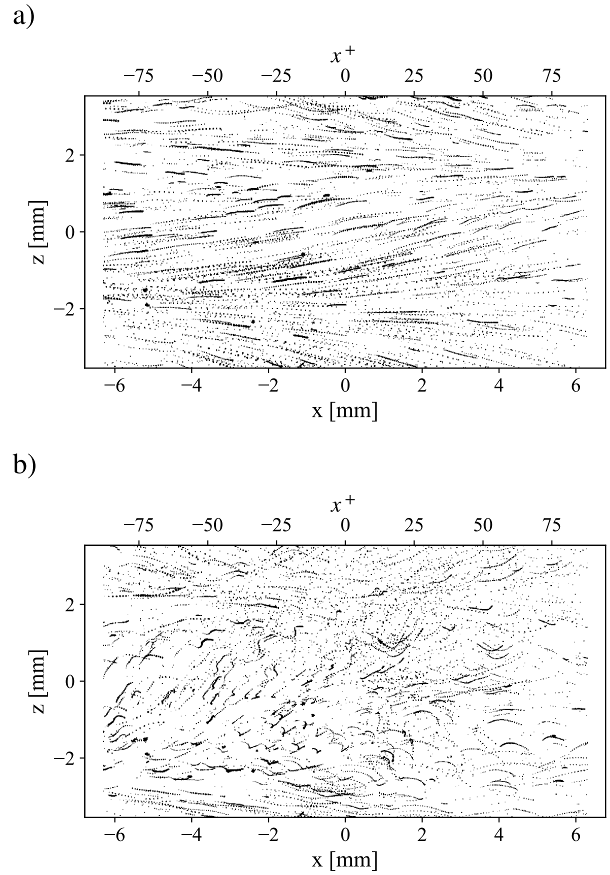

Figure 3: *Visualizations of the near wall flow ($y^+ < 8$) with mean flow left-to-right; (a) sweep event at $z = -2$ mm, (b) streaklines produced by a reverse flow event near the lower center (particles briefly moving upstream, best observed if animated).*

References

Gallego G, Delbrück T, Orchard G, Bartolozzi C, Taba B, Censi A, Leutenegger S, Davison AJ, Conradt J, Daniilidis K, and Scaramuzza D (2022) Event-based vision: A survey. *IEEE Transactions on Pattern Analysis and Machine Intelligence* 44:154–180

Schlatter P and Örlü R (2010) Assessment of direct numerical simulation data of turbulent boundary layers. *Journal of Fluid Mechanics* 659:116–126

Willert C (2015) High-speed particle image velocimetry for the efficient measurement of turbulence statistics. *Experiments in Fluids* 56:17

Willert C (2023) Event-based imaging velocimetry using pulsed illumination. *Experiments in Fluids* (under review)

Willert C and Klinner J (2022) Event-based imaging velocimetry: An assessment of event-based cameras for the measurement of fluid flows. *Experiments in Fluids* 63:101

Willert C, Soria J, Stanislas M, Klinner J, Amili O, Eisfelder M, Cuvier C, Bellani G, Fiorini T, and Talamelli A (2017) Near-wall statistics of a turbulent pipe flow at shear Reynolds numbers up to 40 000. *Journal of Fluid Mechanics* 826

Effects of anisotropy on the geometry of tracer particle trajectories in turbulent flows

Y. Hengster [1], M. Lellep [2], J. Weigel [3], M. Bross [4,5], J. Bosbach [6], D. Schanz [6], A. Schröder [6,7], F. Huhn [6], M. Novara [6], D. Garaboa Paz [8], C. Kähler [5], and M. Linkmann [1]

[1] School of Mathematics and Maxwell Institute for Mathematical Science, University of Edinburgh, UK
[2] SUPA, School of Physics and Astronomy, University of Edinburgh, UK
[3] Department for Physics and Astronomy, University of Heidelberg, Germany
[4] Fluids Research Department, Applied Research Laboratory (ARL), Pennsylvania State University, USA
[5] Institute of Fluid Mechanics and Aerodynamics, Universität der Bundeswehr München, Germany
[6] German Aerospace Center (DLR), Inst. of Aerodynamics and Flow Technology, Göttingen, Germany
[7] Brandenburgische Technische Universität (BTU), Cottbus-Senftenberg, Germany
[8] Group of Non-linear Physics, University of Santiago de Compostela, Spain

key-words: Fundamentals, Experiment

Abstract:

Using curvature and torsion to describe Lagrangian trajectories gives a full description of these as well as an insight into small and large time scales as temporal derivatives up to order 3 are involved. One might expect that the statistics of these properties depend on the geometry of the flow. Therefore, we calculated curvature and torsion probability density functions (PDFs) for Lagrangian trajectories obtained from experimental data using the Shake-the-Box algorithm. We analyse three datasets, turbulent von Kármán flow, Rayleigh-Bénard convection and a zero-pressure-gradient (ZPG) boundary layer over a flat plate, see fig. 1 for visualisations. The results for the von Kármán flow compare well with experimental results for the curvature PDF [1] and numerical simulation of homogeneous and isotropic turbulence for the torsion PDF [2]. For Rayleigh-Bénard convection, the power law tails found agree with those measured for von Kármán flow. Results for the logarithmic layer within the boundary layer differ. To detect and quantify the effect of anisotropy either resulting from a mean flow or large-scale coherent motions on the geometry or tracer particle trajectories, we introduce the curvature vector. We connect its statistics with those of velocity fluctuations and demonstrate that strong large-scale motion in a given spatial direction results in meandering rather than helical trajectories. For the turbulent boundary layer, this is commensurate with the current understanding of turbulent superstructure [3, 4].

This work received funding from Priority Programme SPP 1881 "Turbulent Superstructures" of the Deutsche Forschungsgemeinschaft (DFG, grant numbers LI3694/1, KA1808/21, BO5544/1 and SCHR1165/5). Yasmin Hengster was also supported by MAC-MIGS Centre for Doctoral training at the University of Edinburgh and Heriot-Watt University through EPSRC grant EP/S023291/1. We acknowledge funding from the European High-Performance Infrastructures in Turbulence (EuHIT) consortium for the DTrack measurement campaign at the von Kármán flow facility GTF3 and the support of the staff at MPIDS in Göttingen, in particular Eberhard Bodenschatz.

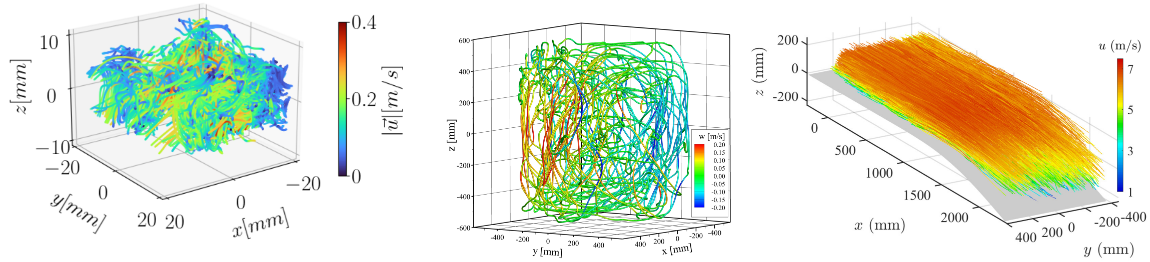

Figure 1: *(Left) Visualisation of a subset of tracer particle trajectories in von Kármán flow at Taylor-scale Reynolds number $Re_\lambda = 270$. The colour bar indicates the absolute value of the velocity. (Middle) Visualisation of a single long tracer particle trajectory in Rayleigh-Bénard convection at Rayeigh number $Ra = 1.53 \cdot 10^9$. The colour bar indicates the vertical component of the velocity. (Right) Visualisation of a subset of tracer particle trajectories within a turbulent boundary layer at friction Reynolds number $Re_\tau = 2295$, coloured with stream-wise velocity. The ZPG region analysed here extends from $x = 0$mm until $x = 1000$mm.*

References

[1] Xu, H., Ouellette, N. and Bodenschatz, E., (2007), Curvature of Lagrangian Trajectories in Turbulence, *Phys. Rev. Lett., vol. 98, 050201*

[2] Scagliarini, A., (2011), Geometric properties of particle trajectories in turbulent flows, *J. Turbul., vol. 12, N25*

[3] Hutchins, N. and Marusic, I., (2007), Evidence of very long meandering features in the logarithmic region of turbulent boundary layers, *J. Fluid Mech., vol. 579, pp. 1-28*

[4] Kevin, K., Monty, J. and Hutchins, N., (2019), The meandering behaviour of large-scale structures in turbulent boundary layers, *J. Fluid Mech., vol. 865, pp. R1*

Augmenting PIV temporal resolution via semi-Lagrangian estimation of velocity fluctuations

Maegan Vocke[1], Ralf Kapulla[2], Chris Morton[3], Robert Martinuzzi[1]

[1] University of Calgary, Department of Mechanical and Manufacturing Engineering, Calgary, Canada
[2] Paul Scherrer Institute, Villigen, Switzerland
[3] McMaster University, Department of Mechanical Engineering, Hamilton, Canada

key-words: Turbulence, Particle Image Velocimetry, Rapid Distortion Theory, Nyquist Frequency

Abstract:

Turbulent flows require high-frequency, high-resolution data to characterize the wide range of spatiotemporal scales. The evolution of turbulent fluctuations is due to the dynamic coupling of the spatial and temporal flow scales. The behaviour can be described using the local covariance between velocity fluctuations resolved in space and time. While Particle Image Velocimetry (PIV) is an attractive technique allowing spatiotemporal measurements, suitable resolution of both temporal and spatial scales remains challenging. We present here a strategy for augmenting the temporal resolution of PIV measurements beyond the Nyquist limit.

We have recently demonstrated the ability of an advection-based flow reconstruction technique to increase the temporal resolution of turbulent flow fields [1]. The model is developed through a linearization of the Navier-Stokes equations, decoupling the linear and non-linear terms to provide a relation for the transport of turbulent fluctuations. Under the assumption of Rapid Distortion Theory (RDT) the nonlinear interactions are neglected, thus, the governing equation reduces to a non-homogeneous material derivative. The quasilinear approximation is then used to predict the forward and backward evolution of the fluctuations based on two successive flow measurements. This is achieved numerically using a modified semi-Lagrangian technique.

The performance is quantified using a benchmark DNS dataset of a turbulent plane jet with $Re = 10,000$ and a sampling rate f_s. The technique is assessed by comparing the reconstructed velocity fields and the ground truth data for a range of sub-sampling factor $S^* = f_s/f_n$, where the DNS data is re-sampled at $fn < fs$. The spectra of the raw DNS and reconstructed flow with $S^* = 50$ and 150 for the u'- and w'- components of velocity are displayed in Figure 1. The method successfully recovers spectral information up to two orders of magnitude beyond the Nyquist criterion. The present investigation extends upon [1] to improve the prediction of small-scale fluctuations and consider the model's applicability towards inhomogeneous turbulence. Higher-order temporal weighting schemes are explored to improve the convergence between the backward and forward estimate. The quasilinear approximation under RDT selectively removes triadic interactions, which suppresses certain mode interactions from the system dynamics [2]. This minimizes energy paths leading towards dissipation, as the fluctuations are limited to interactions with the mean flow. Extensions are discussed to approximate the triadic interactions and model the energy transfer between small-scale modes.

References

[1] M. Vocke, R. Kapulla, C. Morton, M. Klein, and R. J. Martinuzzi, "Advection-based temporal reconstruction technique for turbulent velocity fields," *Physics of Fluids*, vol. 35, no. 1, p. 015123, 2023.

[2] J. Marston and S. Tobias, "Recent developments in theories of inhomogeneous and anisotropic turbulence," *Annual Review of Fluid Mechanics*, vol. 55, no. 1, pp. 351–375, 2023.

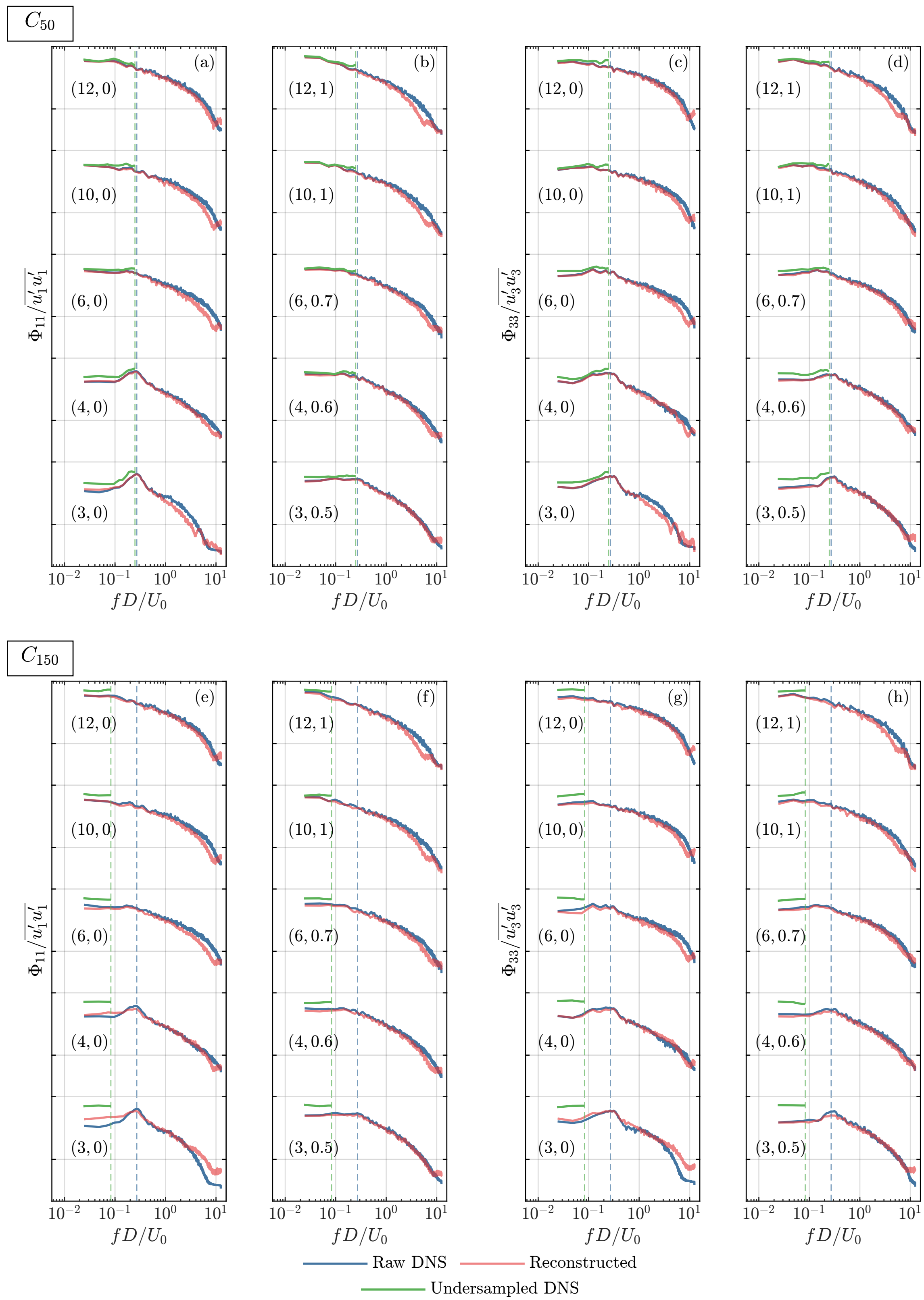

Figure 1: Comparison of the DNS and reconstructed PSD with C_{50} (a-d) and C_{150} (e-h) along the jet centreline (a,c,e,g) and shear layer (b,d,f,h), for velocity components (a-b,e-f) u'- and (c-d,g-h) w'- components of velocity. The blue and green dashed lines correspond to the fundamental frequency of the jet, f_v and the Nyquist frequency, f_N of the under-sampled data set.

Inertial Particles in Turbulence under Minimum Gravity

F. Cabrera[1], K. Cardin[1], L. Chevillard[2], R. Volk[2], N. Plihon[2],
M. Bourgoin[2] and Raúl Bayoán Cal[1]

[1] Dept. Mechanical and Materials Engineering, Portland State University, Portland, OR, USA
[2] Laboratorie de Physique, École Normale Supérieure de Lyon, Lyon, France

key-words: Experiments, Particle Tracking Velocimetry, Inertial Particles, Turbulence

Abstract:
The dynamics of inertial particles in turbulent flows is composed of several physical ingredients that are entangled by gravity; namely particle settling and particle-turbulence couplings. Thus the study of particle-laden turbulent flows in a microgravity environment disentangles these effects and allows to successfully measure particle-turbulence couplings effects, independently of gravity effects. To achieve this a dedicated experimental device that produces nearly homogeneous and isotropic turbulence (HIT) through the interaction of 8 water jets in a cylindrical water tank was designed. Particularly, particle trajectories inside the tank are measured using a 3-camera PTV system. The experimental device was conceived to fit in the Dryden Drop Tower at Portland State University, which provides 2.1 seconds of microgravity. Experimental results on the Lagrangian dynamics of particles in microgravity will be presented.

The micro-gravity experiments will be performed in the Dryden Drop Tower facility, located at the Center for Engineering, Science and Technology at Portland State University (see Fig. 1). The tower has a height of 31.1 m with a free fall distance of 22.2 m, where gravity values of $10^{-3}g_0$ (g_0 = 9.8 m/s^2) are achieved for approximately 2 s. The experiment, mounted on a rig, falls freely inside a drag shield that takes the form of a 56 × 40 × 81 cm^3 rectangular prism, guided by two 'non-contact' stainless steel cables that run the length of the tower. Two steel fins rigidly mounted to the drag shield pass through two 1.1 m long permanent magnets at the lower level of the tower. The relative motion between the fins and parallel magnetic fields generate eddy currents in the fins that resist motion and decelerate the drag shield before it comes to rest on foam pads (i.e. eddy current braking). Limited by the latter, the maximum weight of the experiment is approximately 45 kg. The deceleration mechanism leads to a peak and average decelerations of 15 g_0 and 8.5 g_0, respectively. Furthermore, a touch-screen computer permits safe, single-operator control of the primarily automated tower functions which allows for a short automated retrieval time of 5 min that permits repetitive realisations in the same day. Sample trajectories are provided in figure 2.

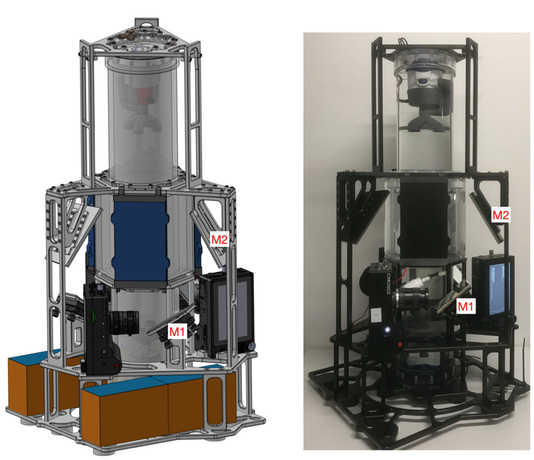

Figure 1: *Test rig dropped in drop tower.*

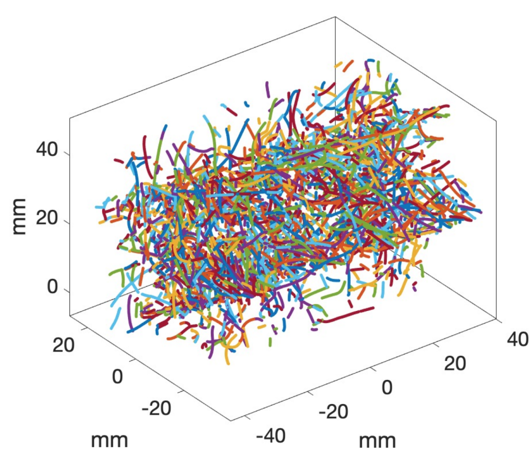

Figure 2: *Sample trajectories of tracers.*

Not all Clear Air Turbulence is Kolmogorov The fine-scale nature of atmospheric turbulence

Andreas Dörnbrack [1], Paola Rodriguez Imazio [2,3], and Pablo D Mininni [4,5]

[1] DLR Oberpfaffenhofen, Institut für Physik der Atmosphäre, 82234 Oberpfaffenhofen, Germany

[2] Consejo Nacional de Investigaciones Científicas y Técnicas, Buenos Aires, Argentina

[3] Servicio Meteorológico Nacional, Dorrego 4019, 1428 Buenos Aires, Argentina

[4] Universidad de Buenos Aires, Facultad de Ciencias Exactas y Naturales, Departamento de Física. Ciudad Universitaria, 1428 Buenos Aires, Argentina

[5] CONICET - Universidad de Buenos Aires, Instituto de Física del Plasma (INFIP). Ciudad Universitaria, 1428 Buenos Aires, Argentina

key-words: Clear-Air turbulence, Scaling laws

Abstract:

Clear air turbulence (CAT) is a common phenomenon in the upper troposphere and lower stratosphere, often triggered by the instability of internal gravity waves or by strong wind shear. Here, we analyze a strong CAT event experienced by the German High-Altitude Long-Range research aircraft (HALO) during the Southern Hemisphere Transport, Dynamics, and Chemistry (SOUTHTRAC) campaign [1]. HALO encountered CAT leeward of the southern Andes Mountains, where tropospheric airflow favored vertically propagating mountain waves that were refracted southeastward into the core of tropopause jet [2].

Turbulence is quantified using spectral quantities and structure functions computed from in situ 100 Hz flight level data, see Figure 1. The detected CAT region exhibits strong patchiness, characterized by separated bursts in turbulent kinetic energy and energy dissipation rate. The high-resolution in situ observations reveal different turbulent scaling within each patch, in both spectra and structure functions, and following Monin and Yaglom's conversion law. One patch follows power laws with exponents -1.71 ± 0.06, -1.771 ± 0.006, and -1.56 ± 0.05 for the velocity components w, v, and u respectively, while another patch has exponents -2.17 ± 0.12, -2.50 ± 0.08, and -1.92 ± 0.09. These patches are mediated by a third patch with less clear scaling. While the patches can deviate from Kolmogorov scaling due to the anisotropy of the airflow, they still display evidence of CAT with enhanced energy dissipation rates.

References

[1] Rapp, M., B. Kaifler, A. Dörnbrack, S. Gisinger, T. Mixa, R. Reichert, N. Kaifler, S. Knobloch, R. Eckert, N. Wildmann, A. Giez, L. Krasauskas, P. Preusse, M Geldenhuys, W. Woiwode, F. Friedl-Vallon, B.-M. Sinnhuber, A. de la Torre, P. Alexander, J. L. Hormaechea, D. Janches, M. Garhammer, J. L. Chau, J. F. Conte, P. Hoor, and A. Engel, (2021) SOUTHTRAC-GW: An airborne field campaign to explore gravity wave dynamics at the world's strongest hotspot. *Bulletin of the American Meteorological Society*, **102**, E871-E893. `https://journals.ametsoc.org/view/journals/bams/102/4/BAMS-D-20-0034.1.xml`

[2] Rodriguez Imazio, P., Mininni, P. D., Godoy, A., Rivaben, N., and Dörnbrack, A. (2023) Not all clear air turbulence is Kolmogorov - The fine-scale nature of atmospheric turbulence. *Journal of Geophysical Research: Atmospheres*, **128**, e2022JD037491. `https://doi.org/10.1029/2022JD037491`

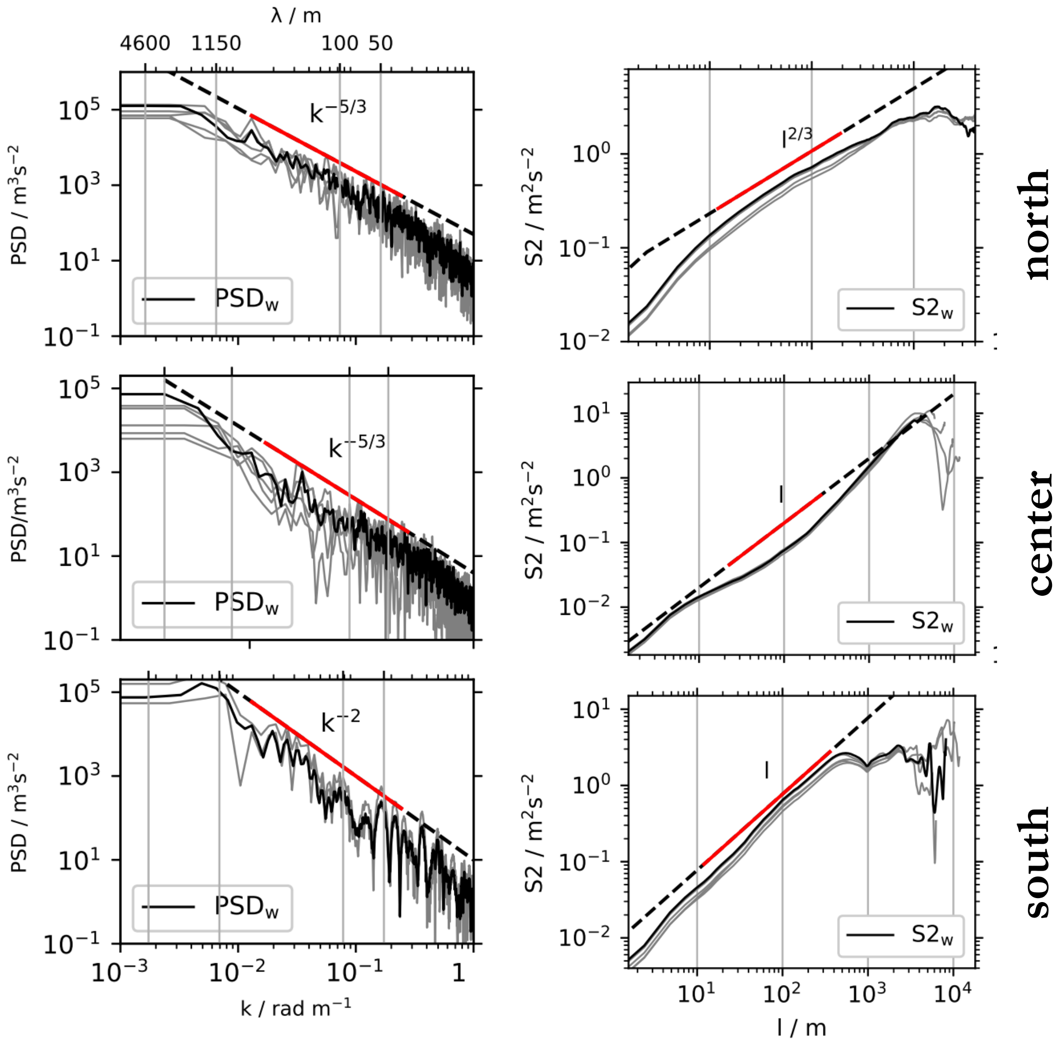

Figure 1: *Left column: Power spectral density PSD_w of the vertical wind component w as analyzed from the HALO in situ data for the three turbulent patches, respectively. Inertial range scaling is shown as a reference in gray dashed lines on each panel. Red solid lines denote the extension of the inertial range used for the calculation of the spectral indices α_w. Right column: Second-order structure functions $S2_w$ for vertical velocity w on the turbulent sublegs calculated using 4, 6, 8, 10, and 16 km lengths. As an example, for the sublegs of 4 km, S2 is computed in subsets of 4 km, and averaged over all subsets. Inertial range scaling laws inferred from spectral indices are shown as a reference in dotted gray lines. Scaling laws calculated from a best fit in the sub-inertial range are plotted using black solid lines, along with the obtained values.*

Symmetries in Second Moment Turbulence Modeling

F. Putz [1] and M. Oberlack [1,2]

[1] Chair of Fluid Dynamics, Technische Universität Darmstadt, Darmstadt, Germany
[2] Centre for Computational Engineering, Technische Universität Darmstadt, Darmstadt, Germany

key-words: Turbulence Modeling, Symmetries

Abstract:
Attempts to model turbulence date back to the late 19th century, with notable works by Boussinesq [1] and Reynolds [10]. Many turbulence models have since emerged, including eddy viscosity, Reynolds stress, and combinations of both. However, their limitations often stem from missing symmetries, as seen in Prandtl's mixing-length model [9]. Efforts to generalize turbulence models by removing explicit spatial dependencies are thus at the same time efforts to include more symmetries into the turbulence model.

Symmetries are known to most as geometrical properties, e.g. rotation applied to a circle. In this context, symmetries are variable transformations that leave a given equation form invariant. The symmetries of the incompressible Navier-Stokes equation, first calculated by Bytev [2], include time and pressure translation, rotation, generalized Galilean transformation, and scaling. The time and pressure translation prohibits the explicit use of the variables, e.g. pressure only occurs under a gradient. Rotational symmetry is closely related to correct tensorial notation and the scaling symmetry ensures dimensional accuracy. The generalized Galilean symmetry allows for the transformation of independent variables under constant acceleration.

Turbulence models based on the Boussinesq assumption, such as zero- and one-equation models, require a flow-dependent turbulent length scale, which can compromise Galilean symmetry if it's a function of spatial coordinates. Two-equation models address this issue by introducing a second scale-providing variable, but still have more symmetries than the exact Navier-Stokes equation, being invariant under constant rotations [6].

In the late 1940s and early 1950s, turbulence models known as Reynolds stress models (RSMs) were developed. These models solve the transport equation for Reynolds stresses, are thus called second-order closure models, and avoid the Boussinesq approximation. Depending on the modeling of the unclosed terms in the transport equation, most have the same symmetries as the exact Navier-Stokes equations and are hence more general than two-equation models. Of particular note is the work of Donaldson and Rosenbaum, who applied the invariant modeling method to RSMs as early as 1969 [3]. The goal was to include all symmetries so that the model could be applied to a wide range of flows.

Recently, new symmetries that occur in the infinite set of multi-point correlation equations (MPCE) and in other exact statistical descriptions of turbulence such as the Lundgren probability density function hierarchy have been found [7, 11]. These are dubbed statistical symmetries, as they only occur in the statistical descriptions of turbulence and have been linked with intermittency and non-Gaussianity - critical properties of turbulence [11].

All turbulence models covered so far are not invariant under these statistical symmetries. Only recently, a barebone invariant Reynolds stress model and an extension to two-equation models into three-equation models that are then invariant have been proposed [5, 4].

We show very concretely how a Reynolds stress model can be developed from all the symmetries known so far, and further we also give a recently developed model. With the symmetries thus available, we show that many classical but, in particular, also the latest near-wall turbulent scaling laws [8] can be reproduced with the new model, which exhibit clearly intermittent behavior.

References

[1] J. Boussinesq. *Essai sur la théorie des eaux courantes*. Paris: Imprimerie Nationale, 1877. XXII, 680.

[2] V. O. Bytev. "Group properties of the Navier-Stokes equations". In: *Numerical Methods of the Solid Medium* 3.3 (1972), pp. 13–17. ISSN: 0201-8268.

[3] C. Donaldson and H. Rosenbaum. "Calculation of Turbulent, Shear Flows Through Closure of the Reynolds Equations by Invariant Modeling". In: *NASA Special Publication*. Vol. 216. 1969, p. 231. URL: `https://ui.adsabs.harvard.edu/abs/1969NASSP.216..231D`.

[4] D. Klingenberg and M. Oberlack. "Statistically invariant eddy viscosity models". In: *Physics of Fluids* 34.5 (May 2022), p. 055114. DOI: `10.1063/5.0090988`.

[5] D. Klingenberg, M. Oberlack, and D. Pluemacher. "Symmetries and turbulence modeling". In: *Physics of Fluids* 32.2 (Feb. 2020), p. 025108. DOI: `10.1063/1.5141165`.

[6] M. Oberlack. "A unified approach for symmetries in plane parallel turbulent shear flows". In: *J. Fluid Mech.* 427 (Jan. 25, 2001), pp. 299–328. ISSN: 0022-1120, 1469-7645. DOI: `10.1017/S0022112000002408`.

[7] M. Oberlack and A. Rosteck. "New statistical symmetries of the multi-point equations and its importance for turbulent scaling laws". In: *Discrete & Continuous Dynamical Systems - S* 3.3 (2010), pp. 451–471. DOI: `10.3934/dcdss.2010.3.451`.

[8] M. Oberlack et al. "Turbulence Statistics of Arbitrary Moments of Wall-Bounded Shear Flows: A Symmetry Approach". In: *Physical Review Letters* 128.2 (Jan. 2022), p. 024502. DOI: `10.1103/physrevlett.128.024502`.

[9] L. Prandtl. "7. Bericht über Untersuchungen zur ausgebildeten Turbulenz". In: *ZAMM - Journal of Applied Mathematics and Mechanics / Zeitschrift für Angewandte Mathematik und Mechanik* 5.2 (1925), pp. 136–139. DOI: `10.1002/zamm.19250050212`.

[10] O. Reynolds. "On the dynamical theory of incompressible viscous fluids and the determination of the criterion". In: *Philosophical Transactions of the Royal Society of London. (A.)* 186 (Dec. 1895), pp. 123–164. DOI: `10.1098/rsta.1895.0004`.

[11] M. Wacławczyk et al. "Statistical symmetries of the Lundgren-Monin-Novikov hierarchy". In: 90.1 (July 2014), p. 013022. DOI: `10.1103/physreve.90.013022`.

Isotropy, super-isotropy and a finite dimensional eigenvalue problem from the Lundgren hierarchy of turbulence

S. Görtz [1,2], J. Conrad [1] and M. Oberlack [1,2]

[1] Chair of Fluid Dynamics, Technische Universität Darmstadt, Germany
[2] Graduate School of Computational Engineering, Technische Universität Darmstadt, Germany

key-words: Fundamentals, HIT, statistical description, probability density functions

Abstract:
Our modern understanding of turbulence is focused on its statistical behavior. We therefore analyze Lundgren's [1] infinite but linear multi-point hierarchy of probability density functions (PDF). The problem of homogeneous isotropic tubulence (HIT) is revisited as an (quasi)exact solution of the LMN hierarchy. This hierarchy emerges directly from the Navier Stokes equations, with the PDF defined as follows: Any averaged function Q of the (statistical) physical velocities ${}_1\vec{u}, \ldots, {}_n\vec{u}$ at points ${}_1\vec{x}, \ldots, {}_n\vec{x}$ can be described via the integration of the n-point PDF ${}_nf$ over the sample space velocities ${}_1\vec{v}, \ldots, {}_n\vec{v}$

$$\langle Q({}_1\vec{u}, \ldots, {}_n\vec{u})\rangle = \int_{\mathbb{R}^{3n}} Q({}_1\vec{v}, \ldots, {}_n\vec{v})\, {}_nf\,(t, {}_1\vec{x}, {}_1\vec{v}, \ldots\, {}_n\vec{x}, {}_n\vec{v})\, \mathrm{d}_1\vec{v} \ldots \mathrm{d}_n\vec{v} \tag{1}$$

To account for the physical properties of HIT, we introduce spherical coordinates and obtain a dimensional reduction in the two-point case $n = 2$. We further extend the concept of isotropy for PDFs to higher order which naturally leads to super-isotropy. This leads to a further dimensional reduction, since each of the PDFs then only depends on time t, the spherical radius r, the radial sample space velocity component v^r and the absolute value of the sample space velocity components orthogonal to the radial comoponent, i.e. $\left(v^\perp\right)^2 = \left(v^\theta\right)^2 + \left(v^\phi\right)^2$. Since the resulting reduced super-isotropic PDF hierarchy is still linear, we formulate an ansatz of superposed products for the PDF, reading

$${}_nf = \sum_{m=1}^{\infty} \prod_{k=1}^{n} {}_kh\left(t,\, {}_kr,\, {}_kv^r,\, {}_kv^\perp;\, \lambda_m\right) \tag{2}$$

The superposition of eigenfunctions with eigenvalues λ_m is necessary since it takes into account the statistical coupling of processes on different scales. For a solution to have the proper character of a probability density function, the Lundgren hierarchy comes with a number of side conditions [2]. These conditions are consequently reduced for the case of super-isotropy. Applying the permutation condition on (2) greatly simplifies the hierarchy of equations, since it yields the same functional form for all ${}_kh$. With this simplification, the initially infinite dimensional hierarchy is reduced to a *single* but *non-linear integro-differential* equation. The resulting equation together with the associated side conditions forms an eigenvalue problem for the eigenvalues λ_m, since the eigenfunctions have to be superposed in order to fulfill all side and boundary conditions, such as ${}_nf$ decaying to zero for ${}_k\vec{v} \to \pm\infty$.
We further give an outlook on approaches to obtain a solution. We state that the dimensionally reduced system admits additional symmetries, which allow further insight into new scaling laws and the underlying turbulence physics.

References

[1] Lundgren T. S., (1967), Distribution Functions in the Statistical Theory of Turbulence, *Phys. Fluids, vol. 10, pp. 969-975.*

[2] Hosokawa I., (2006), Monin-Lundgren hierarchy versus the Hopf equation in the statistical theory of turbulence, *Phys. Rev. E, vol. 73, pp. 067301.*

Coherent structures and the direct cascade in two-dimensional turbulence

R. O. Grigoriev [1], D. Zhigunov [1] and M. Reynoso [1]

[1] School of Physics, Georgia Institute of Technology, Atlanta, USA

key-words: Turbulent Cascades, Coherent Structures

Abstract:
Its multiscale nature is both a distinguishing feature of fluid turbulence, giving it a rather unique flavor, and a key difficulty making both analysis and simulation of turbulent flows challenging. Multiple scales arise due various physical mechanisms transferring energy and helicity in three dimensions (3D) or energy and enstrophy in two dimensions (2D) between different scales. Existing theories of turbulent cascades due to Richardson and Kolmogorov in 3D and Kraichnan, Leith, and Batchelor in 2D [1, 2, 3] are statistical in nature and mostly agnostic of the specific physical mechanisms responsible for the inter-scale transfer. As a result, in practice, one finds deviations from their predictions, especially in the presence of pronounced coherent structures at large scales. These deviations are the most severe for the direct cascade in 2D, where KLB theory predicts the energy density to scale as $E(k) \propto k^{-\alpha}$ with a universal, integral exponent $\alpha = 3$, while numerical and experimental studies find non-universal, fractal scaling exponents ranging from less than 3 to more than 5.

We describe a mechanism of the direct 'cascade' in 2D turbulence which explains when the scaling predicted by the KLB theory holds, when deviations are found, yielding fractal scaling exponents, and what causes these deviations. Our mechanistic theory goes beyond KLB and also predicts the upper and lower bounds of the inertial range as well as the energy scaling in the dissipative range. Coherent structures of two different types play a key role in our theory; both correspond to exact solutions of the Euler equation. The first type describes the dynamics of the largest scales acessible to the flow – the so-called condensate arising due to the inverse cascade. The second type describes the dynamics of small-scale filamentary vorticity stretched and folded by the large-scale flow in the inertial range. The physical mechanism represented by these coherent structures describes a continuous, rather than cascading, process by which enstrophy is transferred from large to small scales, where it is eventually dissipated by viscosity in much the same way as passive scalars are stirred by chaotic advection creating filaments that are eventually homogenized via molecular diffusion.

References

[1] Kraichnan, Robert H, (1967): Inertial ranges in two-dimensional turbulence, *The Physics of Fluids*, vol. 10, pp. 1417-1423

[2] Leith, Cecil E, (1968): Diffusion approximation for two-dimensional turbulence, *The Physics of Fluids*, vol. 11, pp. 671-672

[3] Batchelor, George K, (1969): Computation of the energy spectrum in homogeneous two-dimensional turbulence, *The Physics of Fluids*, vol. 12, pp. II-233

New insights in wall-bounded turbulence

S. Hoyas [1], M. Oberlack [2,3]

[1] Instituto Universitario de Matemática Pura y Aplicada, Universitat Politècnica de València, Camino de Vera, 46024 València, Spain
[2] Technical University of Darmstadt, Chair of Fluid Dynamics, Darmstadt, Germany
[3] Technical University of Darmstadt, Centre for Computational Engineering, Darmstadt, Germany

key-words: Wall-bounded turbulence; Symmetry theory

The calculation of turbulence statistics is considered the key unsolved problem of fluid mechanics, i.e., precisely the computation of arbitrary statistical velocity moments from first principles alone. Using symmetry theory, we derived turbulent scaling laws for moments of arbitrary order in two regions of a turbulent channel flow. Besides the classical scaling symmetries of space and time, the key symmetries for the present work reflect the two well-known characteristics of turbulent flows: non-gaussianity and intermittency. We presented the new scaling laws in [1] and the details of the simulation in [2]. We have extended this simulation in two ways. First, we have doubled the simulated time of the flow to get a better quality of the statistics of the high-order moments, in particular for those of U_2 and U_3. Further, we have started a simulation at a friction Reynolds number $Re_\tau = 15000$. Very interesting results are already visible.

Figure 1 shows the wall-normal (U_2) and spanwise (U_3) velocity-moment deficit scaling laws up to order 6 in the channel center for $Re_\tau = 10^4$. The scaling laws are similar to those of U_1 [1]

$$\frac{\overline{U_i^n} - \overline{U_i^n}^{(0)}}{u_\tau^n} = C'_{i,n} \left(\frac{x_2}{h}\right)^{n(\sigma_2-\sigma_1)+2\sigma_1-\sigma_2} \quad \text{with} \quad i = 2,3 \quad \text{and} \quad C'_{i,n} = \alpha'_i \mathrm{e}^{\beta'_i n}. \tag{1}$$

The agreement of symmetry theory and DNS data is excellent, even though $\sigma_1 = 1.95$ and $\sigma_2 = 1.94$ were taken from [1] for the U_1 moments. It follows that the exponents are effectively independent of n, and thus strongly intermittent behavior is evident.

In figure 2, we show the proof of the existence of the second maximum of the root mean square of the streamwise velocity, $u_1'^+$. Notice that this second maximum could lead to new phenomena at the beginning of the logarithmic layer [3]. The maximum is around $y^+ \approx 200$ for $Re_\tau = 15000$. Fitting the data to a logarithmic law, we obtain $d_y u_0'^+ = 0.29 \log Re_\tau - 2.7$, and an approximate critical value of $Re_\tau = 13100$, which is a bit smaller than the one estimated in [2].

References

[1] Oberlack, M., Hoyas, S., Kraheberger, S.V., Alcántara-Ávila, F. Laux, J., (2022). Turbulence statistics of arbitrary moments of wall-bounded shear flows: A symmetry approach. Physical Review Letters, 128(2), p.024502.

[2] Hoyas, S., Oberlack, M., Alcántara-Ávila, F., Kraheberger, S.V., Laux, J., (2022). Wall turbulence at high friction Reynolds numbers. Physical Review Fluids, 7(1), p.014602.

[3] Marusic, I., Mathis, R. and Hutchins, N., 2010. Predictive model for wall-bounded turbulent flow. Science, 329(5988), pp.193-196.

[4] Hoyas, S. and Jiménez, J., (2006). Scaling of the velocity fluctuations in turbulent channels up to Re_τ= 2003. Physics of fluids, 18(1), p.011702.

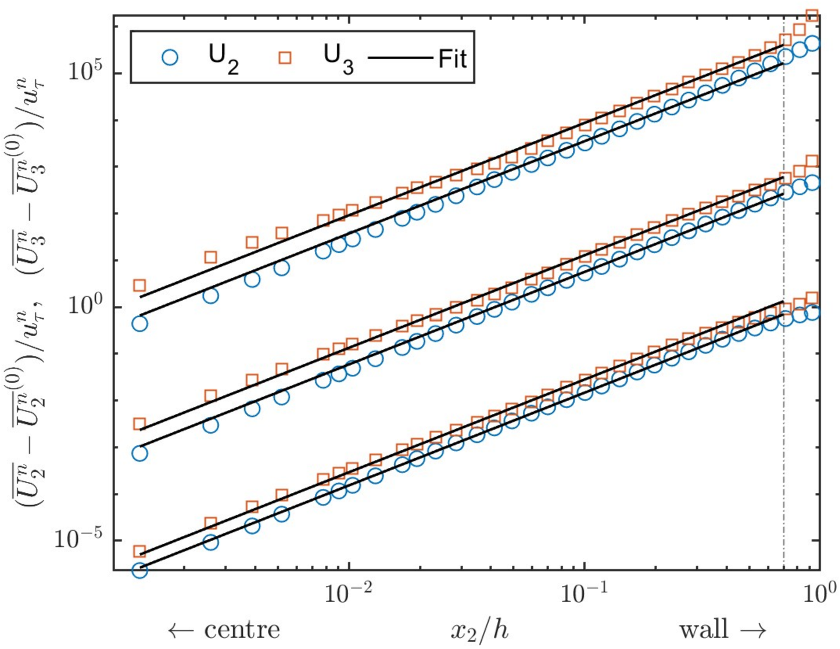

Figure 1: Deficit scaling plotted of the moments of U_2 and U_3 in the channel center for the H-moment orders $n = 2, 4, 6$. Curves are shifted by 10^{n-2}. Lines: scaling laws (1). Squares and circles: new DNS data at $Re_\tau = 10^4$

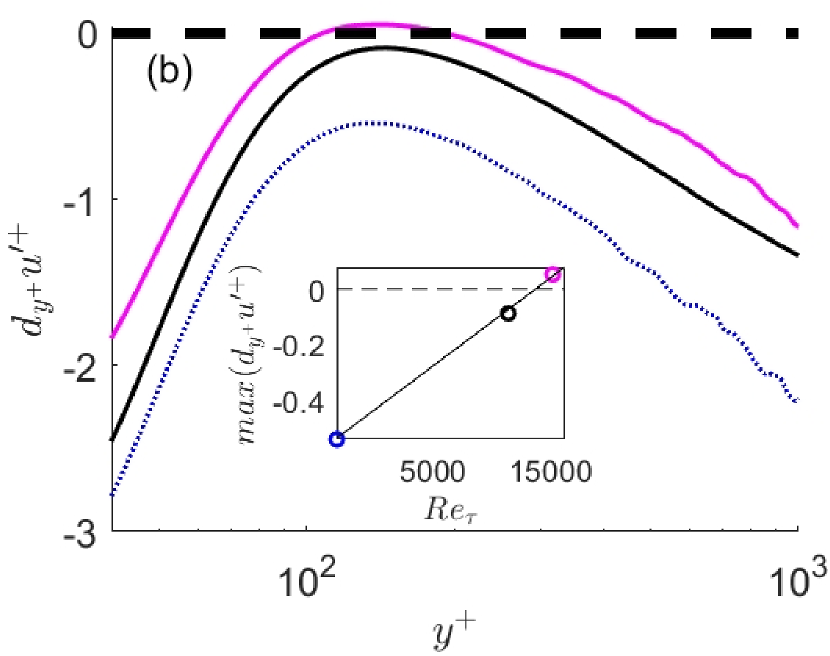

Figure 2: $du'^+/dy^+ = d_{y^+}u'^+$, for y^+ close to the second maximum. The magenta line corresponds to $Re_\tau = 15k$. The first zero is a minimum, and the second one the new maximum. Box: maximum value of $d_{y^+}u'^+$. Blue line [4], Black line [2]

Turbulent flows over heterogeneous rough walls

B. Frohnapfel

Institute of Fluid Mechanics (ISTM), Karlsruhe Institute of Technology (KIT), Germany

key-words: rough wall boundary layers, flow resistance

The full-scale prediction of flow resistance due to drag between fluid and a solid surface is one key aspect in the design of different technological devices, in particular in the transport sector. In this respect, the uncertainty in the drag prediction of turbulent flow over rough surfaces has a strong economic and environmental impact as nicely summarized in the recent review by Chung et al. [1].

Our present predictive capabilities for turbulent drag on rough surfaces rely on Nikuradse or Moody type charts. In those, results of reference experiments are collected for different rough surfaces in the form of a friction coefficient C_f (or similar) versus bulk Reynolds number Re_b. In the so-called fully rough regime the friction coefficient of a rough surface becomes indpependent of Re_b. In this flow regime, any rough surface can be compared against the drag of uniform, close-packed sand grains obtained in the pioneering experiments of Nikuradse. This comparison allows to assign the hydraulic property of an equivalent sand grain height k_s to a rough surface. For engineering predictions k_s is typically translated into the roughness function ΔU^+ which describes the downward shift of the logarithmic region of a velocity profile of wall-bounded shear flows. This quantity is then e.g. inserted into RANS based predictions .

A lot of ongoing research is dedicated to the question of how to indentify a transfer function between the surface topography of a rough surface and the answer of the flow in terms of k_s or ΔU^+ which allows to reduce the present uncertainties in the resulting predictions. All these approaches typically concern evenly distributed, statististically homogeneous rough surfaces. For heterogeneous rough surfaces, which are widely encountered in reality, we have little knowledge at hand. While there are attempts to deal with heterogeonous surface roughness in predictive models [2, 3], there is very little reference data available that allows to validate the model assumptions or dervie alternative modelling suggestions.

The conference talk provides an overview of the research activities at ISTM in this field. Since there are infinite possibilities of heterogeneous roughness arrangements it is reasonable to start with idealized distributions. In our reserach, we focus on streamwise aligend strips of rough surfaces that alternate with smooth surface parts. Experimental and numerical results for turbulent flows over such heterogeneous rough walls will be discussed.

References

[1] D. Chung, N. Hutchins, M.P. Schultz, K.A. Flack (2021), Predicting the Drag of Rough Surfaces, *Annual Review of Fluid Mechanics, vol. 53, pp. 439-471.*

[2] N. Hutchins, B. Ganapathisubramani, M.P. Schultz, D.I. Pullin (2023): Defining an equivalent homogeneous roughness length for turbulent boundary layers developing over patchy or heterogeneous surfaces, *Ocean Engineering, vol, 271, 113454.*

[3] E. Bou-Zeid, C. Meneveau, M.B. Parlange (2004), Large-eddy simulation of neutral atmospheric boundary layer flow over heterogeneous surfaces: Blending height and effective surface roughness, *Water Resour. Res. 40, W02505.*

Assessment of different methods for drag penalty predictions in rough-wall boundary layers

T. Medjnoun[1], M. A. Ferreira[1], R. Reinartz[1], B. Nugroho[2], J. P. Monty[2], N. Hutchins[2] and B. Ganapathisubramani.[1]

[1] AFM Research Group, University of Southampton, Hampshire, SO17 1BJ, UK
[2] Department of Mechanical Engineering, University of Melbourne, Australia.

key-words: Rough-wall turbulence, Experiments.

Abstract:

The skin friction drag is well-established as the most valuable quantity characterising smooth- and rough-wall bounded flows, as it embodies the result of the conversion of the free stream momentum into shear force by means of the boundary layer. Considering the ever-increasing interest in reducing the carbon footprint and the environmental impact of fuel-based systems, accurate measurement and prediction of this quantity remain vital to a whole range of engineering applications. Skin friction is equally crucial in understanding wall-turbulence dynamics due to its scaling capabilities for both the near- and outer-wall regions [1]. Regardless of whether the frictional drag is directly or indirectly measured, the use of similarity laws is required to scale up the information from laboratory measurements and/or numerical simulations to full-scale predictions.

In this study, we examine the use of three methods of estimating the frictional drag: two indirect namely; Townsend's outer-layer similarity (OLS) hypothesis and the Comprehensive Shear Stress (CSS) methods [2, 3], and contrast the results with a direct method using wall-shear stress and velocity profile measurements. The measurements are carried out in a wind tunnel on a turbulent boundary layer over a realistic rough surface (scanned from a fouled ship-hull) to evaluate the impact of these methods with an emphasis on using the outer-layer similarity hypothesis for full-scale drag predictions. Wall-shear stress is measured using an in-house floating-element drag balance (DB) and velocity profiles are obtained using particle image velocimetry (PIV), allowing the evaluation of aerodynamic roughness parameters (equivalent sandgrain roughness height k_s), and the associated wake parameter Π. The results are subsequently scaled up from laboratory to full-scale to assess the impact on high Reynolds numbers using an integral boundary layer evolution method [4].

By assuming the validity of the outer-layer similarity hypothesis and using the Comprehensive shear stress [3] methods, indirect estimates of the aerodynamic parameters have been obtained and compared with results from the direct measurements. The comparison highlighted the limitation of using these flow assumptions, which resulted in underestimating the equivalent sand-grain roughness by 35% and 25% for the OLS and CSS methods, respectively. Using the integral boundary layer evolution method outlined by [4], it is observed that the predicted drag penalty can vary by over 15% among the different methods highlighting the care that should be taken when employing such methods. The current results also showed that at a Reynolds number of $Re_x \approx 10^9$ (equivalent to a Reynolds number of a 50 m long vessel at full-speed), assuming outer-layer similarity underestimated the frictional drag by over 12% while the comprehensive shear stress method resulted in approximately 6% difference.

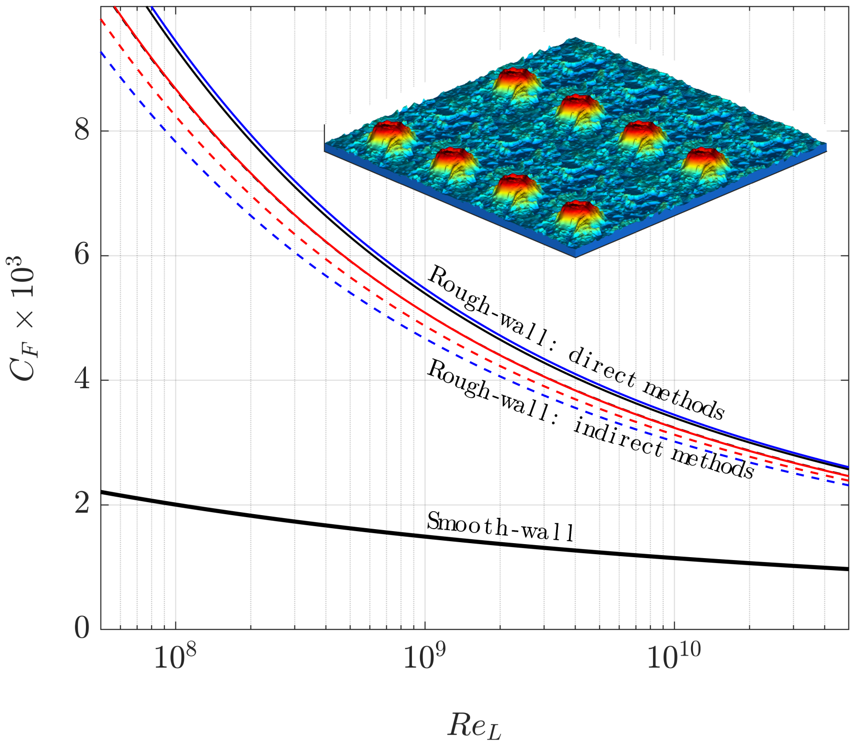

Figure 1: *Evolution of the average skin-friction coefficient C_F as a function of fetch Reynolds number Re_L using the integral method presented by [4], at a unit Reynolds number $U_\infty/\nu \approx 2 \times 10^7$ with $U_\infty \approx 18\ ms^{-1}$ and $\nu \approx 9 \times 10^{-7}\ m^2 s^{-1}$. The figure compares C_F determined using the different methods colour-coded (Black: Direct method. Blue: Outer-layer similarity. Red: Comprehensive shear stress method), compared with the smooth-wall (thick line). The dashed lines represent predictions made with the assumption of smooth-wall wake strength parameter* Π.

References

[1] Chung, D., Hutchins, N., Schultz, M. P. and Flack, K. A. (2021), Predicting the drag of rough surfaces, *Annu Rev Fluid Mech, vol. 53, pp. 439-471*

[2] Townsend, A.A. (1976), *The structure of turbulent shear flow 2nd edition, Cambridge university press*

[3] Womack, K. M., Meneveau, C. and Schultz, M. P., (2019), Comprehensive shear stress analysis of turbulent boundary layer profiles, *J Fluid Mech*

[4] Monty, J. P., Dogan, E., Hanson, R., Scardino, A. J., Ganapathisubramani, B. and Hutchins, N. (2016), An assessment of the ship drag penalty arising from light calcareous tubeworm fouling, *Biofouling, vol. 32, pp. 451-464*

On the instantaneous characteristics of ridge-type induced secondary motions

K. Schäfer [1], B. Frohnapfel [1] and D. Gatti [1]

[1] Institute of Fluid Mechanics (ISTM), Karlsruhe Institute of Technology (KIT), Karlsruhe, Germany

key-words: Secondary motions, turbulent large-scale structures, direct numerical simulations

Abstract:

Heterogeneous surfaces occur in many technical and environmental flows, and in the case of spanwise heterogeneous surfaces turbulent secondary motions can emerge. These appear as counter-rotating vortices in the mean velocity field and can significantly alter the momentum, heat and mass transport of turbulent flows [1]. So far, many studies have focused on the mean characteristics of secondary motions, while only a few recent studies investigated the instantaneous characteristics of secondary motions [2, 4, 3]. It was found that instantaneous secondary motions over alternating rough- and smooth-wall strips share some similarities to large-scale motion (LSM) and very-large-scale motions, which occur naturally over smooth wall conditions [3]. While coexistence between secondary motions and VLSM was found for strip-type surfaces, this was not found for streamwise-aligned ridges in turbulent open-channel flows [4].

The present investigation aims to contribute to a better understanding of the instantaneous characteristics of secondary motions and the relation to turbulent large-scale motions. For this, direct numerical simulations are used to study turbulent open-channel flows at $Re_\tau = 540$ with streamwise-aligned ridges, shown in figure 1. The large domain size of the open-channel ($L_x, L_z = 36\delta, 12\delta$, where δ is the domain height) allows the formation of VLSMs for smooth wall conditions. By introducing Gaussian ridges with ridge height $h_g = 0.1\delta$ secondary motions form in the mean velocity field, which is illustrated in figure 2 for the different ridge spacings S. For $S \geq 2\delta$ the secondary motions have their largest spatial extent, while for smaller S their extent becomes more confined to the near-wall region. The largest ridge spacing $S = 12\delta$ shows an area between the ridges that is not affected by secondary motions, and where the flow homogenizes. In this region, VLSMs can now form with similar properties as those above smooth wall channels, which can be seen in pre-multiplied streamwise velocity spectra in figure 3, where VLSMs appear at large streamwise wavelengths $\lambda_x \geq 18\delta$. For the case $S = 4\delta$, VLSMs can also be observed between the ridges, but they appear in an weakened form compared to $S = 12\delta$ and $S = \infty$. For the ridge spacings $S \leq 2\delta$, which were studied in the recent experiment by [4], no coexistence is found, which is in agreement with their observations. Preliminary results, for which the ridge height h_g is reduced for case $S = 4\delta$, show that VLSMs between the ridges increase in strength with decreasing h_g. Moreover, for the smallest ridge height $h_g = 0.025\delta$ ($h_g^+ = 13.5$) investigated, VLSMs can eventually occur in the vicinity of the ridges, such that the ridges no longer represent a spatial barrier for the occurrence of VLSMs.

Further results examining the instantaneous characteristics of secondary motions will be presented at the conference. For this, the proper orthogonal decomposition is used to detect the dominant flow structures of instantaneous secondary motions for the different ridge heights and spacings. This will shed further light on the similarities and differences between the instantaneous secondary motions and turbulent large-scale motions and hopefully contributing to a better understanding of their formation.

References

[1] Stroh, A., Schäfer, K., Forooghi, P. abd Frohnapfel, B., (2020), Secondary flow and heat transfer in turbulent flow over streamwise ridges, *International Journal of Heat and Fluid Flow, 81*

[2] Vanderwel, C., Stroh, A., Kriegseis, J., Frohnapfel, B. abd Ganapathisubramani, (2019): The instantaneous structure of secondary flows in turbulent boundary layers, *J. Fluid Mech. 862.*

[3] Wangsawijaya, D. D., Baidya, R., Chung, D., Marusic, I. and Hutchins, (2020): The effect of spanwise wavelength of surface heterogeneity on turbulent secondary flows, *J. Fluid Mechanics 894*

[4] Zampiron, A., Cameron, S. abd Nikora, V., (2020): Secondary currents and very-large-scale motions in open-channel flow over streamwise ridges, *J. Fluid Mechanics 887, A17.*

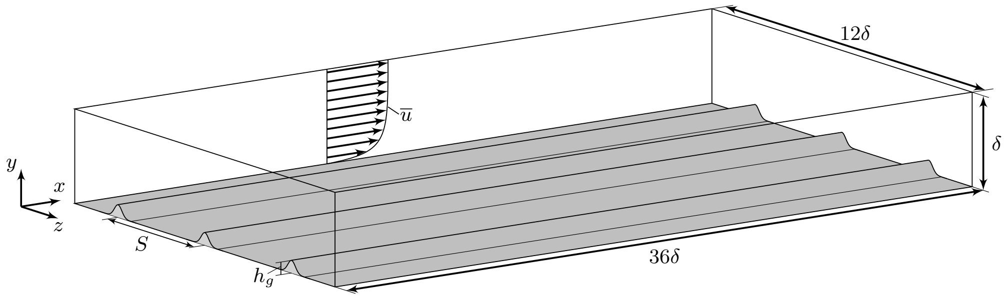

Figure 1: Sketch of the open-channel flow with streamwise-aligned Gaussian ridges at the wall.

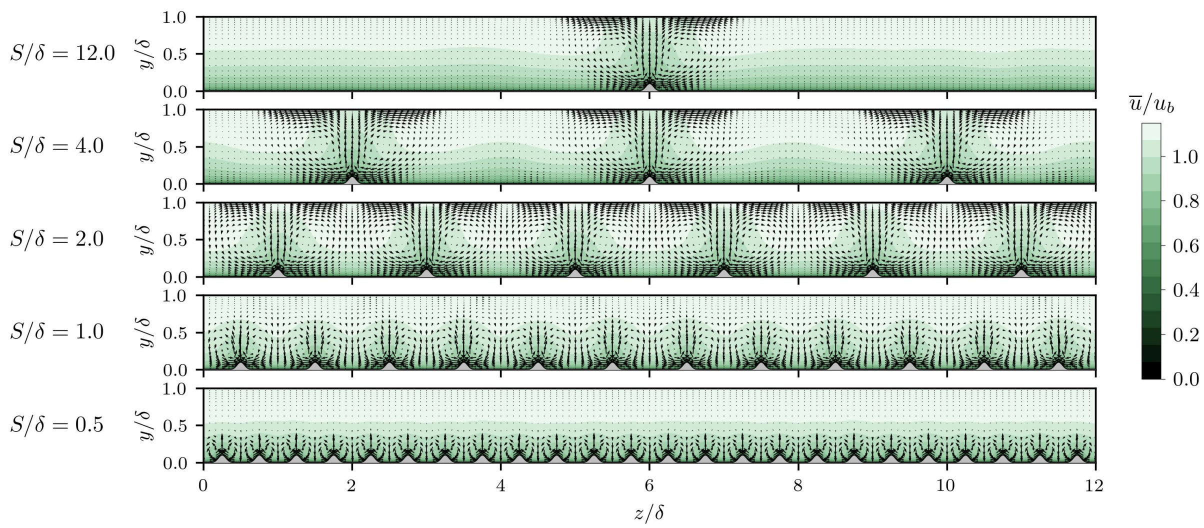

Figure 2: Mean streamwise velocity in cross-sectional plane for different S. The cross-sectional mean velocity components are illustrated by arrows and are scaled by u_b. Ridge height is $h_g = 0.1\delta$.

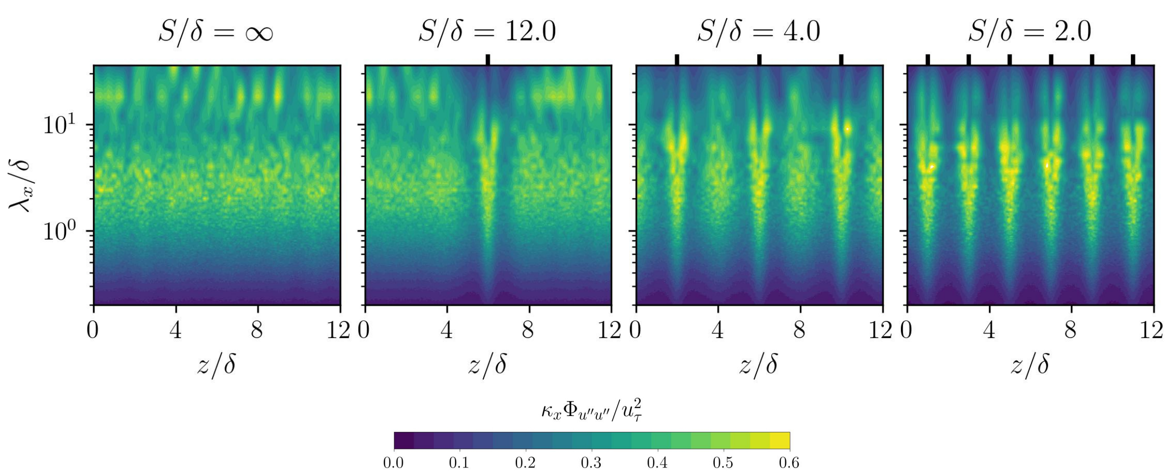

Figure 3: Pre-multiplied spectra $\kappa_x \Phi_{u''u''}(\lambda_x, y = 0.5\delta, z)$. The black vertical lines at the outer top figure frame indicate the spanwise position of the ridges.

Wall pressure fluctuations in the CICLoPE facility

G. Dacome[1], W.J. Baars[1], A. Talamelli[2], L. Lazzarini[2] and G. Bellani[2]

[1] Faculty of Aerospace Engineering, Delft University of Technology, 2629 HS Delft, The Netherlands
[2] Dipartimento di Ingegneria Industriale, Università di Bologna, Forlì, Italy

key-words: Wall-pressure, turbulent pipe flow, high Reynolds number, experiment

High-Reynolds number wall-bounded turbulence, dictating the performance of many engineering systems (i.e. aviation and marine transport), has received an increasing attention over the last decade or so due to the commencement of experimental facilities to simulate such flows. Measurements of the wall-pressure, p_w, can be relatively robust on practical systems and would form a valuable input for flow-control systems. This work presents an experimental campaign on the dynamic wall-pressure within the high-Reynolds number pipe flow facility at CICLoPE. Results will provide insight into (1) measurement and post-processing (filtering) procedures for obtaining the fully-resolved, hydrodynamic wall-pressure fluctuations, (2) Reynolds number scaling of the fully-resolved wall-pressure spectra (addressed in the literature for relatively lower Re_τ [1, 2, 3]), and (3) correlations between wall-pressure and the off-the-wall velocity fluctuations.

Data were acquired in the fully developed turbulent pipe flow facility at CICLoPE, near the end of the 110.9 m-long pipe with an inner diameter of 0.901 m. Several plugs were designed that fit within the pipe's wall, housing pressure-microphones for performing the dynamic wall-pressure measurements. The G.R.A.S. 46BE 1/4 in microphones employed have a sufficient dynamic range and frequency-response for conducting fully-resolved measurements. A pinhole-arrangement was used to increase the spatial resolution of the microphone-diaphragms: the plugs featured four different Helmholtz resonator-cavities (see Fig. 1b for the geometry), with pinhole diameters ranging between $d = 0.18$ mm and 0.40 mm. This allowed for fully-resolved measurements with $d^+ < 16$ for all Re_τ (following [1]). Measurements were performed at a range of friction Reynolds numbers, Re_τ, between 4 800 and 38 000 [4].

Enhancing the spatial resolution of the microphones comes at the expense of Helmholtz resonance of the cavity, in the frequency range of interest. An acoustic calibration of the cavities was performed by simultaneously exciting the pinhole-mounted microphone and a reference one (without cavity) with white noise (Fig. 1a). Linear transfer kernels were generated and compared to a model-fit of a second-order system. Fig. 1c displays the kernel's gain, $|H_L|$, for all four pinhole cavities. With the aid of these kernels, measured wall-pressure signals are corrected in a sequence of post-processing steps, which will be detailed in the full proceedings.

Measurements in the pipe flow facility (Fig. 2a) were performed with the microphone-plugs positioned in different streamwise and azimuthal positions. Post-processing steps of the wall-pressure data will be described in the full paper; these steps remove the (relatively lower-frequency) acoustic pressure-signatures from the hydrodynamic wall-pressure fluctuations. As a preliminary result, Fig. 2b presents the pre-multiplied wall-pressure spectra for three values of Re_τ. Their spectral shape resembles the spectrum obtained from high-Reynolds-number DNS data [5]. Their higher amplitude is expected and the large-wavelength-end of the spectra comprises a larger fraction of the total energy. In the full proceedings we will elaborate upon the measurement resolution, filtering procedures to further remove relatively low-frequency acoustic signatures and the wall-pressure–velocity coupling.

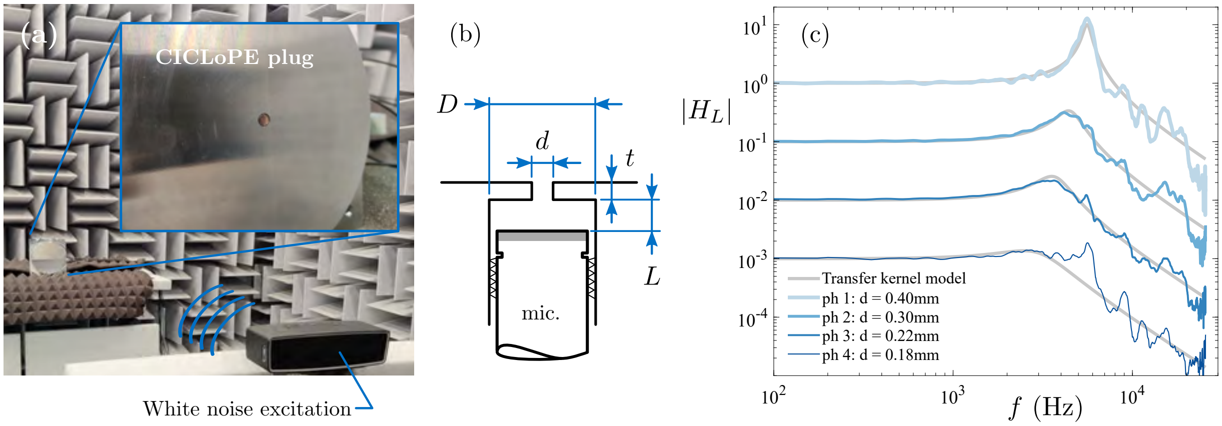

Figure 1: (a) Calibration of the pinhole-microphone arrangement within anechoic facility at the TU Delft. (b) Detail of the pinhole-mounted microphone. (c) Gain of the resonator's transfer kernel: measurements from the acoustic calibration are compared to a fitted model kernel.

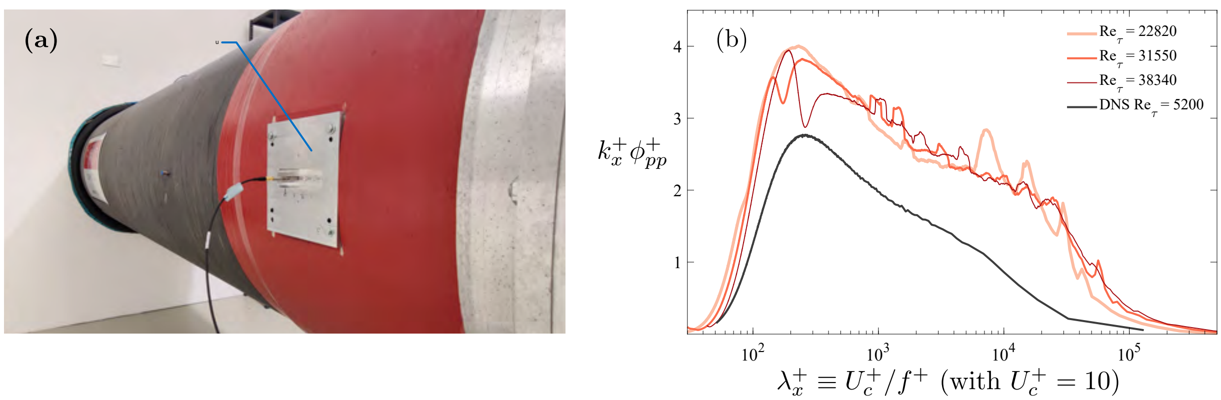

Figure 2: (a) Wall-pressure measurements at CICLoPE. (b) Preliminary result of the pre-multiplied wall-pressure spectra at three Re_τ conditions, in comparison to DNS [5].

References

[1] S. P. Gravante, A. M. Naguib, C. E. Wark, and H. M. Nagib, "Characterization of the pressure fluctuations under a fully developed turbulent boundary layer," *AIAA J.*, vol. 36, no. 10, pp. 1808–1816, 1998.

[2] Y. Tsuji, J. H. M. Fransson, P. H. Alfredsson, and A. V. Johansson, "Pressure statistics and their scaling in high-Reynolds-number turbulent boundary layers," *J. Fluid Mech.*, vol. 585, pp. 1–40, 2007.

[3] J. C. Klewicki, P. J. A. Priyadarshana, and M. M. Metzger, "Statistical structure of the fluctuating wall pressure and its in-plane gradients at high Reynolds number," *J. Fluid Mech.*, vol. 609, pp. 195–220, 2008.

[4] R. Örlü, T. Fiorini, A. Segalini, G. Bellani, A. Talamelli, and P. H. Alfredsson, "Reynolds stress scaling in pipe flow turbulence—first results from CICLoPE," *Phil. Trans. R. Soc. A*, vol. 375, p. 20160187, 2017.

[5] M. Lee and R. D. Moser, "Direct numerical simulation of turbulent channel flow up to $Re_\tau = 5200$," *J. Fluid Mech.*, vol. 774, pp. 395–415, 2015.

Flexible fibers in turbulent channel flow

Cristian Marchioli[1,2], and Davide Di Giusto[1]

[1] DPIA, University of Udine, Udine, Italy
[2] Dept. Fluid Mechanics, CISM, Udine, Italy

key-words: Elongated deformable particles, Turbulence, Direct Numerical Simulation

Abstract:
We numerically investigate the dispersion of slender flexible fibers in turbulent channel flow. In particular, we examine fiber orientation and deformation at varying fiber inertia, aspect ratio and bending stiffness. We use a Euler-Lagrangian approach based on DNS of the flow, combined to a rod-chain pointwise representation of the fibers [1] and accounting for the inter-phase momentum exchange [2]. The simulations are performed exploiting a GPU-accelerated pseudo-spectral solver at shear Reynolds number Re=300, moderate mass fraction (3%) with fibers of aspect ratio r=50, 100, 200, dimensionless length L^+ = 18, 36, 72 (extending up to the inertial range of the turbulent flow) and Stokes number St= 0.1, 0.11, 11. For each combination of parameter values, different fiber rigidity is considered depending on the dimensionless Young modulus: E_Y^+= 0 (no stiffness) and 10^4 (moderate stiffness). Our results show that the fibers in the bulk of the flow orient with the local strain, aligning with the vorticity as also observed in HIT [3] and experience a lower tumbling rate, comparable to that of rigid fibers [4,5]. Near the walls, vorticity orients with the spanwise direction under the action of the mean shear, whereas flexible fibers align with the mean flow. This orthogonality determines a stronger contribution of the flow rotation to the tumbling rate. We classify the possible deformed shapes in a bi-variate probability space, suggesting that two typical deformation patterns exist: 'eyelash' bending and 'compressing' buckling (the latter being suppressed with a finite, albeit moderate, bending stiffness). Flexible fibers in wall turbulence spend a short time in a bent state, before being stretched again by the flow. We find that this time scales with the fiber rotation timescale and exhibits a gamma distribution.

References

[1] D. Dotto, A. Soldati, C.Marchioli. “Deformation of flexible fibers in turbulent channel flow” Meccanica 55 (2020), 343–356
[2] F. Battista, J. P. Mollicone, P. Gualtieri, R. Messina, C. M. Casciola “Exact regularised point particle (ERPP)method for particle-laden wall bounded flows in the two-way coupling regime” J. Fluid Mech. 878 (2019), 420–444
[3] S. Olivieri, A. Mazzino, M.E. Rosti “On the fully coupled dynamics of flexible fibres dispersed in modulated turbulence” J. Fluid Mech. 946 (2022)
[4] T. B. Oehmke, A. D Bordoloi, E. Variano, G. Verhille “Spinning and tumbling of long fibers in isotropic turbulence” Phys. Rev. Fluids 6 (2021), 044610
[5] S. Parsa, G.A. Voth “Inertial range scaling in rotations of long rods in turbulence” Phys. Rev. Lett. 112 (2014), 024501

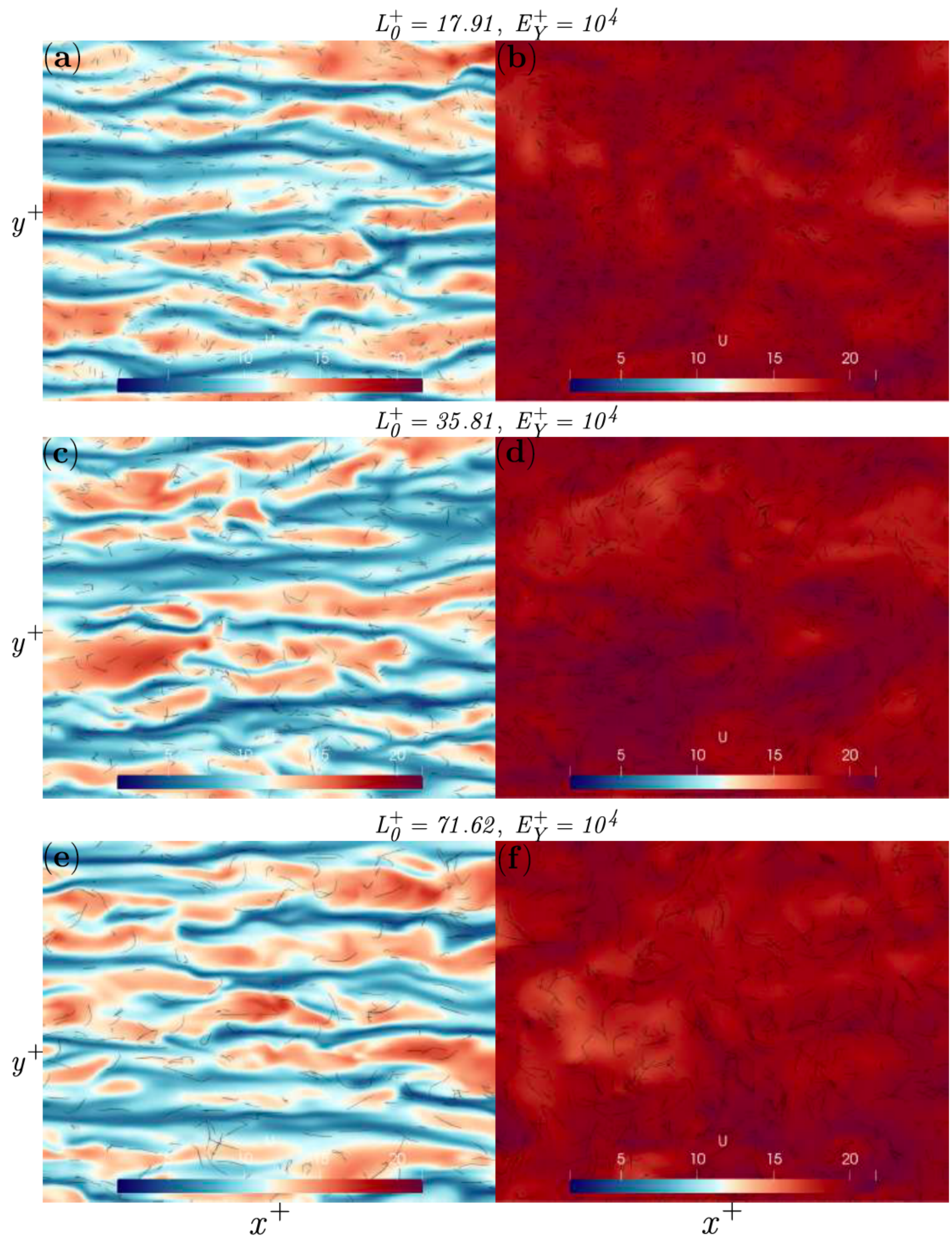

Figure 1: Instantaneous visualization of the fiber-laden turbulent channel flow for stiff ($E_Y^+=10^4$) fibers. Panels display fibers whose center of mass lies within 30 wall units from the wall (left) or the half-height of the channel (right). Panels are colored according to the streamwise fluid velocity, *u*, measured on a plane at $z^+=10$ (left) or $z^+=300$ (right). The size of each panel is $L_x^+= 975$ x $L_y^+= 840$ wall units. Panels: (a), (b) short fibers ($L_0^+=17.91$); (c), (d) intermediate fibers ($L_0^+=35.81$); (e), (f) long fibers ($L_0^+=71.62$).

Evaluation of Turbulence Models in Unsteady Separated Flows

C. Y. MacDougall[1], U. Piomelli[1] and F. Ambrogi[1]

[1]Department of Mechanical and Materials Engineering, Queen's University, Kingston, Canada

key-words: RANS, Unsteady Separation

Abstract:
Separation occurs may be caused by sharp changes in the geometry of an object or by a strong adverse pressure gradient (APGs). The negative effects of separation are well-known, but they may be amplified when the adverse pressure gradient is unsteady. Separation can cause noise and vibrations, resulting in performance reduction or failure of a flow device [1].

The present work aims to evaluate the prediction of unsteady separation by the three most commonly used turbulence models for the Reynolds-Averaged Navier-Stokes equations: Spalart-Allmaras, $k-\varepsilon$, and $k-\omega$ for the prediction of unsteady separations. The equations of motion are solved using second-order accurate finite differences on a staggered grid. Unsteady separation and reattachment are generated by a time-varying distribution of wall-normal velocity V_{top} at the top boundary, with a spatial profile similar to that used in [4]. Two cases are considered; in the first case (Case A), for half of the cycle, a favourable pressure gradient (FPG) is followed by an adverse pressure gradient (APG) with separation, while in the other half, the opposite occurs. In between, there are two phases where a zero pressure gradient (ZPG) is imposed. If T is the period, and $\phi = 360^o \times t/T$ the phase angle, the maximum APG occurs at $\phi = 270^o$, the maximum FPG at 90^o, whereas at $\phi = 0^o$ and 180^o a ZPG is imposed. In the second case (Case B), V_{top} always results in an APG followed by an FPG, but the magnitude of the pressure gradient varies, and separation always occurs. For case A, the data of a well-resolved LES is available (see Ref. [2]) Case B is compared to the DNS, and RANS data by Park et al. [3]. One important feature of Case A is the fact that at this frequency, a recirculation region is formed at $\phi \simeq 252^o$, remains steady until $\phi \simeq 0^o$, and is then advected downstream. In Case B, on the other hand, the recirculation bubble only changes in size but remains centred around the same location.

Figure 1 compares the skin friction coefficient obtained using the turbulence models with those of the high-fidelity simulation. The top two panels show the time-averaged profiles for cases A and B, while the bottom four show the comparison for Case B for the four main phases. In Case A, there is significantly better agreement between the LES and the data than in case B. It is interesting to notice that in Case B the main error is near the separation and reattachment regions, whereas in Case A, it occurs mostly downstream of the recirculation bubble. The average error is 8.1% in case A and 14% in Case B. The reason for this difference is the fact that the cycle in case A goes through two phases where the freestream velocity is nearly uniform. In these ZPG phases, all the models tested are expected to be accurate. This is evident in the lower panels of the Figure, which shows that the error is significantly lower at the ZPG phases than in the FPG and APG regions.

Figure 2 confirms this conjecture by showing the phase dependence of the average error obtained with the three models in Case A. The error is the most significant during phases with strong pressure gradients and the smallest in the ZPG. The intermediate phases with mild or zero pressure gradients act as an 'anchor' that stops the solution from diverging too far from the correct result when the strong pressure gradients are applied. This phenomenon does not occur in Case B, where the APG is always strong enough to cause separation.

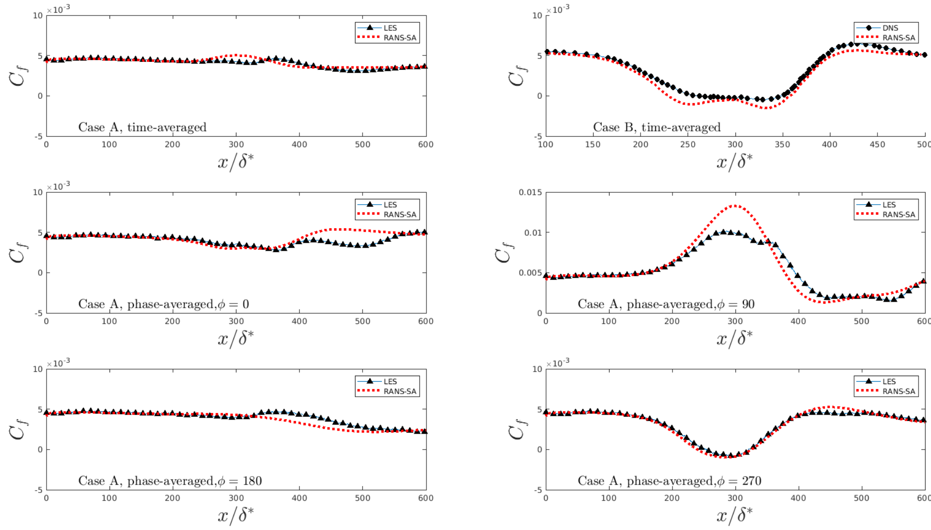

‘

Figure 1: Comparison of RANS prediction of C_f with high fidelity results.

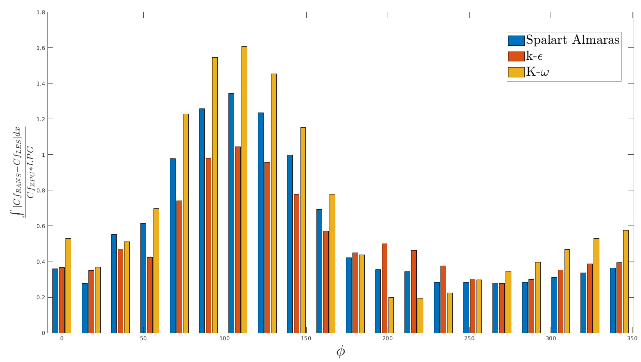

Figure 2: Average difference between C_f predictions from RANS and LES, normalized by C_f at the inflow.)

References

[1] R L Simpson (1989), *Ann. Rev. Fluid Mech.* **21**, pp. 205–232.

[2] Ambrogi, F., Piomelli, U. and Rival, D.E. (2022), *J. Fluid Mech.*, **945**, A10, pp. 1-30.

[3] Park, J. Ha, S. and You, D.(2021), *Phys. Fluids* **33**, 065125.

[4] Y. Na and P. Moin (1998), *J, Fluid Mech*, **3**74, pp. 379–405.

Computationally efficient prediction of turbulence statistics using a Bayesian hierarchical multifidelity model

Saleh Rezaeiravesh [1], Timofey Mukha [2] and Philipp Schlatter [2,3]

[1] Department of Fluids and Environment/MACE, The University of Manchester, Manchester, UK
[2] KTH Engineering Mechanics, Royal Institute of Technology, Stockholm, Sweden
[3] Institute of Fluid Mechanics (LSTM), Friedrich–Alexander Universität Erlangen–Nürnberg, Germany

key-words: Simulation, Data-driven Methods, Turbulence

Abstract:
Despite the need for understanding the complex physics of turbulent flows, conducting high-fidelity experiments and scale-resolving numerical simulations such as large eddy simulation (LES) and direct numerical simulation (DNS) can be prohibitively expensive, particularly at high Reynolds numbers which are relevant to engineering applications. On the other hand, it is necessary to develop accurate yet costeffective models for outer-loop problems involving turbulent flows which include uncertainty quantification (UQ), data fusion, prediction, and robust optimization. A remedy can be using multifidelity models (MFMs) which aim at accurately predicting quantities of interest (QoIs) and their stochastic moments by combining the data obtained from different fidelities. When constructing MFMs, a given finite computational budget is optimally used through running only a few expensive (but accurate) simulations and many more inexpensive (but potentially less accurate) simulations. In recent years, there has been a significant interest in developing and applying MFMs in various fields [1]. For turbulent flows, the main strategies for constructing effective MFMs can be summarized as: i) Co-Kriging models [2], ii) models based on non-intrusive polynomial chaos expansion and stochastic collocation methods, see e.g. [3], and iii) multi-level multifidelity Monte Carlo models.

The present study reports our recent progress on further development and application of a class of Bayesian hierarchical multifidelity models with calibration (HC-MFM) which rely on Gaussian processes. Following Goh et al. [3], at each fidelity level, which can be associated to any of the turbulence simulation approaches, the Kennedy-O'Hagan model [4] is used which allows for considering both model inadequacy and aleatoric uncertainties in the process of data fusion.

Results:
The accuracy and efficiency of the described HC-MFM is evaluated for various problems involving turbulent flows. For instance, Figure 1 shows the prediction (mean and 95interval) of the lift coefficient, C_L, of a wing with a NACA0015 airfoil profile at Reynolds number 1.6×10^6 [5]. The flow angle of attack (AoA) is the design parameter and the data fed into the MFM comprises of: wind-tunnel experiments, detached-eddy simulations (DES) and two-dimensional RANS. According to Figure 1, compared to the experimental data, the MFM is capable of accurately predicting $C_L$over the considered range of AoA.

Our MFM is consistent with the hierarchy of turbulence modeling approaches and can handle various forms of uncertainties. ii) For a fixed number of high-fidelity simulations the HC-MFM prioritizes the prediction of QoIs so that they become as close as possible to the high-fidelity data, while the posterior distributions of the calibrated parameters are found to be accurate only if sufficiently many low-fidelity data are provided.

The conference presentation will include an overview of the theoretical approach behind the present hierearchical multifidelity model, and apply it to a number of test cases with increasing complexity, including the above mentioned case of the airfoil. We will also discuss potential future applications, where an efficient evaluation of the flow for varying parameters is necessary, such as optimisation.

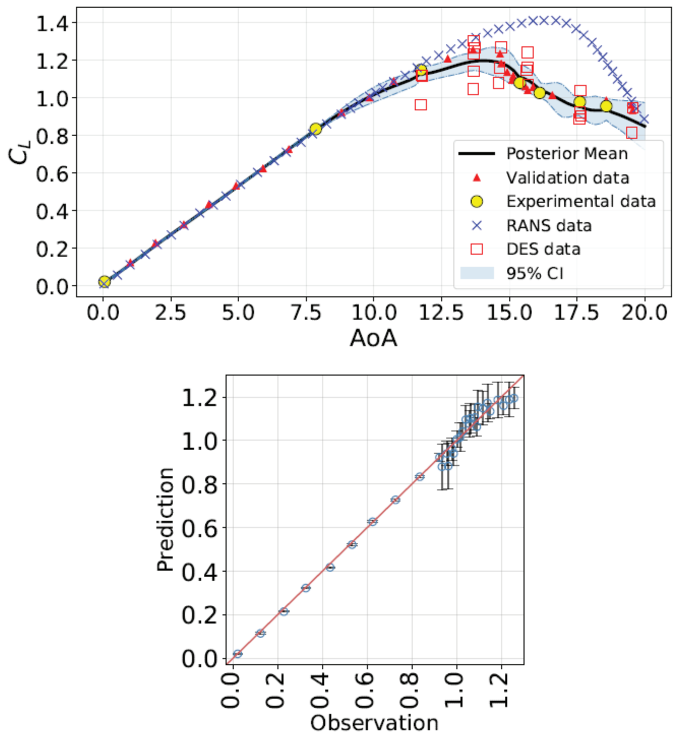

Figure 1: *(Top) Lift coefficient C_L plotted against the angle of attack AoA: the MFM is trained by the experimental data (yellow circles), as well as the DES (squares) and RANS (crosses) data. The DES are performed with the resolved turbulence intensities TI = 0%, 0.1%, 0.5%, 1%, and 2% at the inlet. The validation data (red triangles) are also taken from the experiments. The mean prediction by the MFM is represented by the solid line along with associated 95% confidence interval. (Bottom) predictions by HC-MFM plotted against the validation data. The error bars represent the 95% CI.*

References

[1] B. Peherstorfer, K. Willcox, and M. Gunzburger, "Survey of multifidelity methods in uncertainty propagation, inference, and optimization," SIAM Review, vol. 60, no. 3, pp. 550–591, 2018.

[2] L. J. Voet, R. Ahlfeld, A. Gaymann, S. Laizet, and F. Montomoli, "A hybrid approach combining DNS and RANS simulations to quantify uncertainties in turbulence modelling," Applied Mathematical Modelling, vol. 89, pp. 885 – 906, 2021.

[3] J. Goh, D. Bingham, J. P. Holloway, M. J. Grosskopf, C. C. Kuranz, and E. Rutter, "Prediction and computer model calibration using outputs from multifidelity simulators," Technometrics, vol. 55, no. 4, pp. 501–512, 2013.

[4] M. C. Kennedy and A. O'Hagan, "Bayesian calibration of computer models," Journal of the Royal Statistical Society: Series B (Statistical Methodology), vol. 63, no. 3, pp. 425–464.

[5] S. Rezaeiravesh, R. Vinuesa, and P. Schlatter, "Towards multifidelity models with calibration for turbulent flows," in 14th WCCM-ECCOMAS Congress, CIMNE, 2021.

A multi-timescale wall model for LES and applications to non-equilibrium channel flows

M. Fowler [1], T.A. Zaki [1] and C. Meneveau [1]

[1] Mechanical Engineering, Johns Hopkins University, Baltimore, MD 21218, USA

key-words: LES, wall model, channel flow, non-stationary flows

Abstract:
Wall modeled large eddy simulations (LES) replace the small-scale near-wall dynamics with a reduced order model to avoid the high computational cost required to resolve this flow. However, traditional wall models such as the equilibrium wall model (EQWM) have been shown to under-perform in cases where equilibrium assumptions fail [8, 6, 1]. A recently introduced LES wall model [1], called a Lagrangian relaxation towards equilibrium (LaRTE) wall model, captures unsteady, non-equilibrium wall-stress dynamics through separate modeling of quasi-equilibrium and non-equilibrium contributions. This wall model has since been modified and extended to include additional non-equilibrium wall-stress dynamics and then tested for several challenging non-stationary flows including pulsating and linearly accelerating channel flow [2]. The LaRTE model captures the quasi-equilibrium dynamics through a derived model equation with slow, relaxation dynamics. It is supplemented with a laminar non-equilibrium (lamNEQ) model to capture the wall-stress response to rapid changes in the LES pressure gradient which has been shown to have a laminar-like response due to the turbulence being "frozen" [7, 5, 3, 4]. A turbulent non-equilibrium (turbNEQ) model has been added to capture additional wall-stress contributions caused by near-wall turbulent eddies. The combined LaRTE+lamNEQ+turbNEQ wall model therefore covers a wide range of time scales and is named the multi-timescale (MTS) wall model. Figure 1 schematically shows which time scales are captured by each component of the MTS wall model. The MTS wall model is tested for pulsating and linearly accelerating channel flow over a wide range of non-equilibrium parameter values (the forcing frequency and acceleration/ramp rate, respectively). Results show that the traditional EQWM performs poorly when used under high non-equilibrium conditions whereas the MTS wall model agrees well with the direct numerical simulation (DNS) data over all conditions tested. Finally, a simpler instantaneous-equilibrium limit of the MTS wall model (called the EQMTS wall model) is developed and compared with the parent model, the MTS wall model. This wall model also shows good results at reduced complexity but provides less complete information about the wall-stress physics.

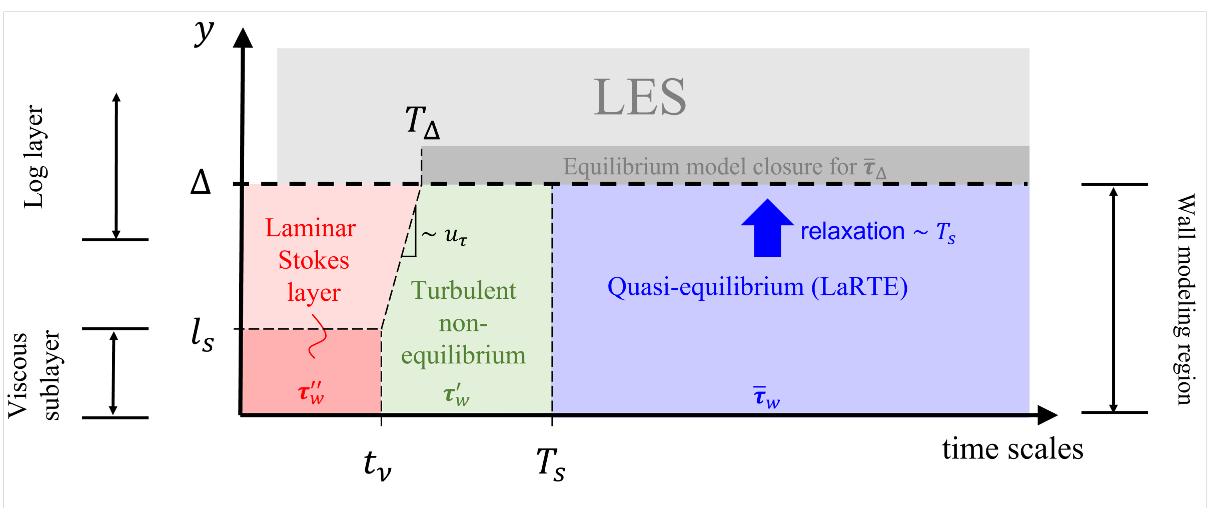

Figure 1: Multi-timescale wall model length and time scales

References

[1] M. Fowler, T. A. Zaki, and C. Meneveau. A lagrangian relaxation towards equilibrium wall model for large eddy simulation. *Journal of Fluid Mechanics*, 934:A44, 2022.

[2] M. Fowler, T. A. Zaki, and C. Meneveau. A multi-timescale wall model for les and applications to non-equilibrium channel flows. *Pre-print (under reveiw)*, 2023.

[3] D. Greenblatt and E. A. Moss. Rapid temporal acceleration of a turbulent pipe flow. *Journal of Fluid Mechanics*, 514:65–75, 2004.

[4] S. He, C. Ariyaratne, and A.E. Vardy. A computational study of wall friction and turbulence dynamics in accelerating pipe flows. *Computers & Fluids*, 37(6):674–689, 2008.

[5] S. He and J. D. Jackson. A study of turbulence under conditions of transient flow in a pipe. *Journal of Fluid Mechanics*, 408:1–38, 2000.

[6] A. Lozano-Durán, M. G. Giometto, G. I. Park, and P. Moin. Non-equilibrium three-dimensional boundary layers at moderate Reynolds numbers. *Journal of Fluid Mechanics*, 883, 2020.

[7] Toshiro Maruyama, Toshiaki Kuribayashi, and Tokuro Mizushina. The structure of the turbulence in transient pipe flows. *Journal of Chemical Engineering of Japan*, 9(6):431–439, 1976.

[8] X. I. A. Yang, J. Sadique, R. Mittal, and C. Meneveau. Integral wall model for large eddy simulations of wall-bounded turbulent flows. *Physics of Fluids*, 27(2):025112, 2015.

Physics-Informed Minimal Error Simulation Methods for Turbulent Flow Predictions

Stefan Heinz [1]

[1] Department of Mathematics and Statistics, University of Wyoming, Laramie, USA

key-words: Theory, Modeling, Simulations

Abstract:

Figure 1 illustrates well known problems of computational simulation methods in regard to reliable and feasible predictions of high Reynolds number (Re) flows that require flow resolution. Large eddy simulation (LES) suffers from its huge computational requirements, especially in regard to simulations of wall-bounded turbulent flows at high Re: LES is inapplicable to many high Re flows that need to be considered. Reynolds-averaged Navier-Stokes (RANS) equations suffer from their inability to reflect the physics of flows that cannot be properly modeled, as is the case for separated turbulent flows. Popular hybrid RANS-LES, too, suffer from RANS-type problems: under conditions where validation data are unavailable, such methods cannot reliably deal with simulations of flows that require flow resolution [1].

A core issue of popular partially and fully resolving simulation methods (including usually applied LES concepts) is the model's inability to account for the amount of resolved motion involved in simulations. The latter has serious consequences. Under conditions of high (low) flow resolution, the model contribution (the modeled viscosity) needs to be relatively small (large). This is needed for a functional RANS-LES "swing", i.e. the model's ability to reliably cover transitional regimes between RANS and LES. The lack of this mechanism effectively adds a random component to flow simulations, which implies random results.

The talk presents continuous eddy simulation (CES) methods, which were introduced to overcome this problem [1–4]. Based on exact mathematics, it is shown how it is possible to design methods involving a functional RANS-LES "swing" in regard to a variety of turbulence model structures and hybridization types. Corresponding minimal error simulation methods represent a relatively minor modification of usual (two-equation) RANS turbulence models. The essential difference to regularly applied simulation methods is that the model applied is properly informed about physics involved (resolved motion).

Figure 2 illustrates the CES performance (the KOKU variant) in regard to periodic hill flow simulations [3]. The core problem is addressed: the functioning of the mode communication to accomplish a proper redistribution of modeled and resolved motions. The expectation is simple: a coarser grid and a higher Re need to imply an increased amount of modeled motion. Re effects are considered in the first row. The experimental data involved do only apply to the $Re = 37K$ case. It may be seen that the mean streamwise velocity $\langle U \rangle / U_b$ tends toward a more uniform spatial distribution. The resolution indicator L_+ (the ratio of modeled to total turbulence length scales) shows the essential model feature. As required, an increased Re leads to higher L_+ values (i.e. a decreased amount of flow resolution). Grid effects are considered in the second and third row. We note that grid effects have little influence: such RANS-type simulations imply $\langle U \rangle / U_b$ profiles that hardly differ from higher resolved cases. The L_+ plots show the required model behavior, L_+ increases (the amount of flow modeling increases) if the grid becomes coarser.

References

[1] Heinz, S., "A review of hybrid RANS-LES methods for turbulent flows: Concepts and applications," *Prog. Aerosp. Sci.*, Vol. 114, 2020, pp. 100597/1–100597/25.

[2] Heinz, S., Mokhtarpoor, R., and Stoellinger, M. K., "Theory-Based Reynolds-Averaged Navier-Stokes Equations with Large Eddy Simulation Capability for Separated Turbulent Flow Simulations," *Phys. Fluids*, Vol. 32, No. 6, 2020, pp. 065102/1–065102/20.

[3] Heinz, S., "Minimal error partially resolving simulation methods for turbulent flows: A dynamic machine learning approach," *Phys. Fluids*, Vol. 34, No. 5, 2022, pp. 051705/1–051705/7.

[4] Heinz, S., "From two-equation turbulence models to minimal error resolving simulation methods for complex turbulent flows," *Fluids*, Vol. 7, No. 12, 2022, pp. 368.

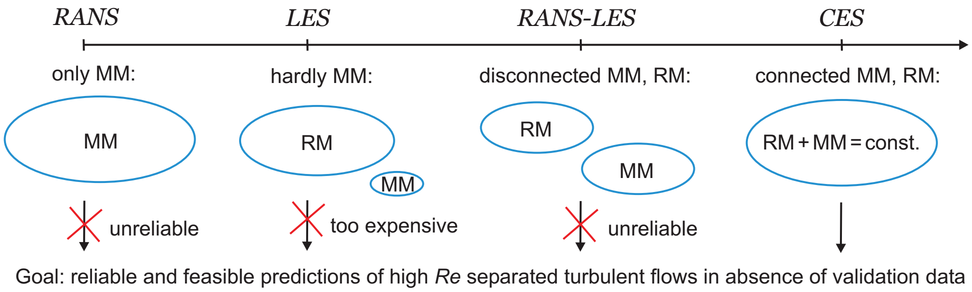

Figure 1: Abilities of computational methods in regard to reliable and feasible predictions of high Re flows that require flow resolution. Here, hybrid RANS-LES refers to popular methods, MM (RM) refers to modeled (resolved) motion. CES refers to continuous eddy simulation.

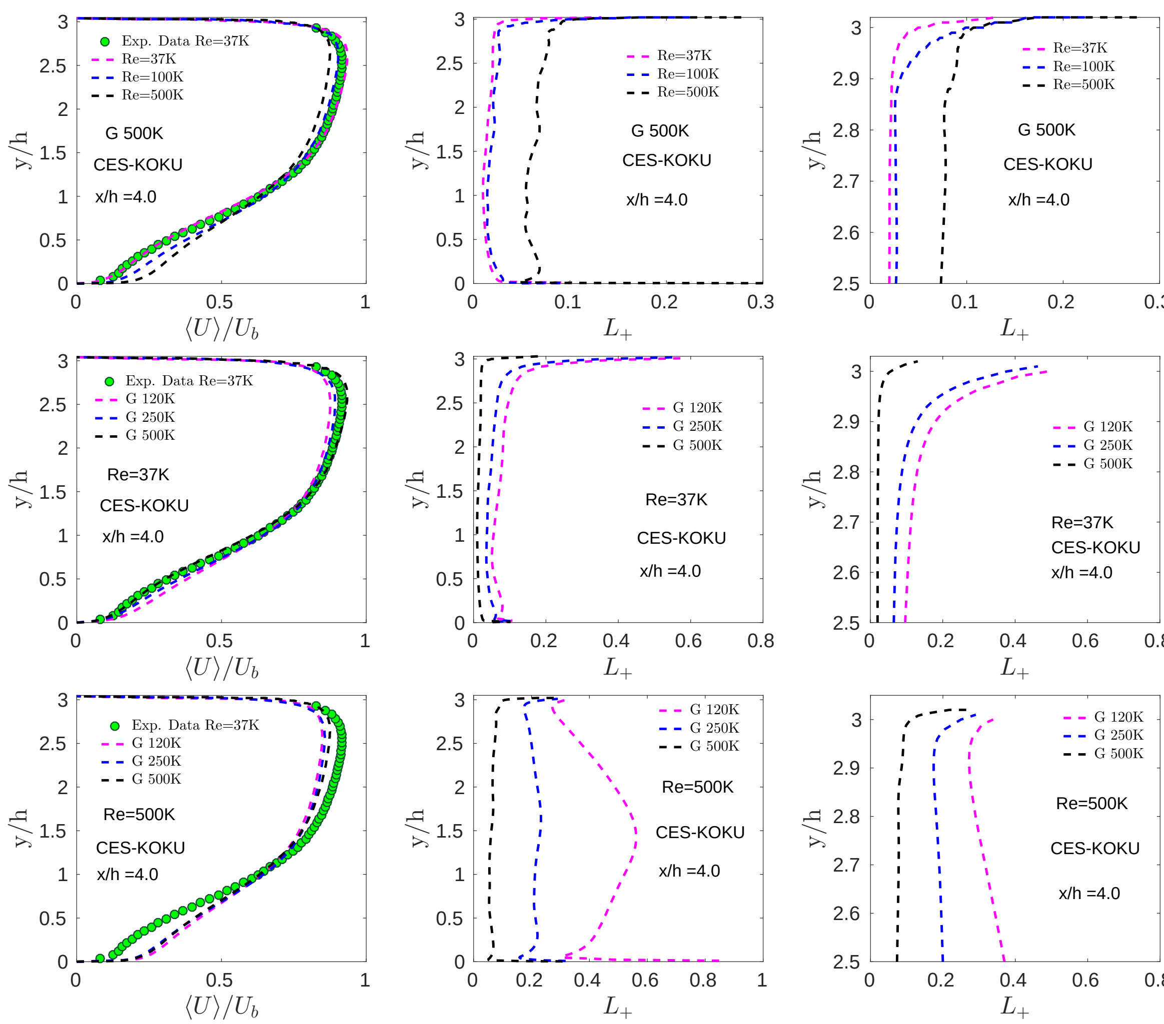

Figure 2: Profiles of the mean streamwise velocity $\langle U\rangle/U_b$, overall and upper wall L_+ obtained by CES-KOKU simulations at $x/h = 4$. Re and grids applied are specified in the plots. First row: Re effects using the $500K$ grid. Second and third row: grid effects for $Re = (37, 500)K$. Reproduced from Heinz et al. [2], with the permission of AIP Publishing.

Towards a clearer understanding of jet and propeller noise: time-frequency analysis and stochastic models

R. Camussi[1]

Dipartimento di Ingegneria Civile, Informatica e delle Tecnologie Aeronautiche, Università Roma Tre, Italia.

key-words: Jet Noise, Wavelet Transform, Propeller Noise

Abstract:
Recent studies tackling aeroacoustics have shown that the physical mechanisms underlying the generation of noise in compressible jets and aeronautical propellers are strictly correlated to turbulence, non-linearities [1] and intermittency [2]. These properties have to be taken into account in order to set up reliable predictive models namely for reproducing far field noise emitted by high speed jets [3]. It is known that wavelet transform is an efficient tool to extract and characterize intermittent events in turbulence and to identify anomalous scalings (see e.g. [4] and [5]). In this lecture it is shown how time-frequency analysis can be useful in identifying noise sources in high-speed jets in free and installed configurations and to set up stochastic models to describe their dynamics. These models provides a probabilistic description of the main properties of the flow structures responsible for the noise emission. A wavelet-based technique providing the separation between acoustic and hydrodynamic pressure is also presented and discussed [6-7]. Examples of application of the method in jet noise as well as in configurations out of free jets are presented. In the field of propeller noise, examples of successful application of wavelet analysis will include the identification of broadband noise components and the description of the so-called haystacking phenomenon observed in installed configurations.

References

[1] Cavalieri A.V.G. and Argaval A., (2014): Coherence decay and its impact on sound radiation by wavepackets, *Journal of Fluid Mechanics*, vol. 748, pp. 399-415.

[2] Camussi R., Bogey C., (2021): Intermittent statistics of the 0-mode pressure fluctuations in the near field of Mach 0.9 circular jets at low and high Reynolds numbers, *Theoretical and Computation Fluid Dynamics*, Vol. 35, pp. 229–247.

[3] Cavalieri A.V.G., Jordan P., Argaval A., Gervais Y., (2011): Jittering wave-packet models for subsonic jet noise, *Journal of Sound and Vibration*, Vol. 330, pp.4474–4492.

[4] Farge, M., (1992): Wavelet transforms and their applications to turbulence, *Annual Review of Fluid Mechanics*, Vol. 24, pp. 395–458.

[5]Meneveau C., (1991): Analysis of turbulence in the orthonormal wavelet representation, *Journal of Fluid Mechanics*. Vol. 232, pp. 469- 479.

[6] Grizzi S:, Camussi R., 2012): Wavelet analysis of Near-Field Pressure Fluctuations Generated by a Subsonic Jet, *Journal of Fluid Mechanics*, Vol. 698, pp. 93-124.

[7] Mancinelli M., Pagliaroli T., Camussi R., Castelain T., (2018): On the hydrodynamic and acoustic nature of pressure POD modes in the near field of a compressible jet, *Journal of Fluid Mechanics*, Vol. 836, pp. 998-1008.

The near– and intermediate–wakes of cylinders under the influence of freestream turbulence

L. Li [1] and R. J. Hearst [1]

[1] Energy and Process Engineering, Norwegian University of Science and Technology, Trondheim, Norway

key-words: cylinder wake, grid turbulence

Abstract:
Wake flows behind cylinders are quite common occurrences found in both nature and engineering applications, where the presence of freestream turbulence is also abundant. Understanding the flow fields around the cylinders under such flow conditions is crucial to engineering designs. The analytical solution to the wake in the self-similar region predicts that the centreline velocity deficit U_s decays as $x_1^{-0.5}$, while the wake half width ℓ grows as $x_1^{0.5}$. Here x_1 denotes the streamwise direction. However, freestream turbulence can have significant effects on the wake velocity fluctuations, the unsteady drag, and the wake geometry (e.g. Surry 1972, Britter et al. 1979, Eames et al. 2011). It is particularly important, for engineering applications, to systematically investigate how freestream turbulence affects the near- and intermediate-wakes behind cylinders of different shapes, which is currently lacking in literature. We seek to address this gap by experimentally investigating the flow behind a circular and a square cylinder under the influence of different freestream turbulence conditions. A total of four inflows were created with the aid of an active grid. The freestream turbulence intensities and integral lengths scales, measured at the cylinder position, ranged from $0.8\% < \langle u_1'^2 \rangle^{0.5}/U_0 < 13.8\%$ and $4.3 < \mathcal{L}/D < 7.9$ respectively. The cylinder was mounted horizontally at $64M$ downstream from the active grid. The circular diameter and the square side length were both $D = 50$ mm, giving $Re_D \approx 35,000$. Particle image velocimetry was used to capture the 2D planar flow field behind the cylinders. The field of view measures $20D \times 7D$, or 991 mm $\times$ 348 mm in physical space.

Figure 1 shows the normalized streamwise velocity U_1/U_0 for all test cases in the near-wake. While the circular cylinder shows negligible effects from the freestream turbulence, the recirculation region behind the square cylinder is noticeably elongated as freestream turbulence intensity increases, effectively giving it a more "streamlined" shape and thus reducing the wake width in the near-wake region. This is more quantitatively shown in figure 2. Moving to the intermediate-wake region ($x_1/D \gtrsim 3$), freestream turbulence appears to induce an earlier onset of self-similar behaviour, as seen by the closer approximations of U_s/U_0 and ℓ/D, in figure 2, to the analytical solution as freestream turbulence intensity increases. In essence, the wake development is artificially "matured". Subsequent analysis will examine intermittency to quantify instantaneous extreme events in the wake, as well as using proper orthogonal decomposition to reveal more insight into the wakes' spatial features.

References

Britter, R., Hunt, J. & Mumford, J. (1979), 'The distortion of turbulence by a circular cylinder', *Journal of Fluid Mechanics* **92**(2), 269–301.

Eames, I., Jonsson, C. & Johnson, P. (2011), 'The growth of a cylinder wake in turbulent flow', *Journal of Turbulence* (12), N39.

Surry, D. (1972), 'Some effects of intense turbulence on the aerodynamics of a circular cylinder at subcritical reynolds number', *Journal of Fluid Mechanics* **52**(3), 543–563.

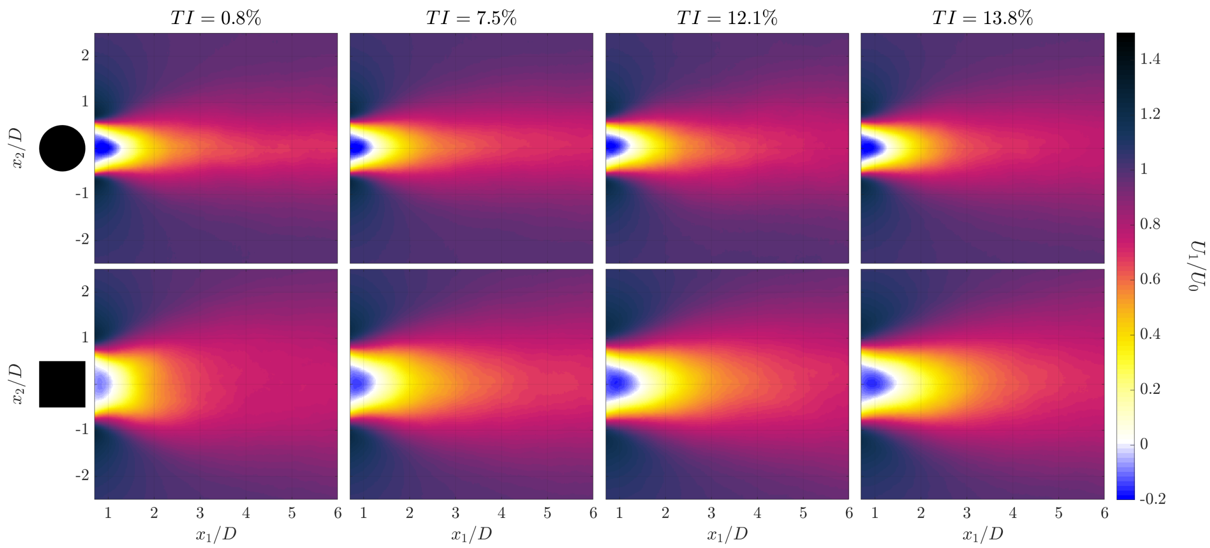

Figure 1: Normalized mean streamwise velocity U_1/U_0 fields in the near-field of the wake, for all test cases.

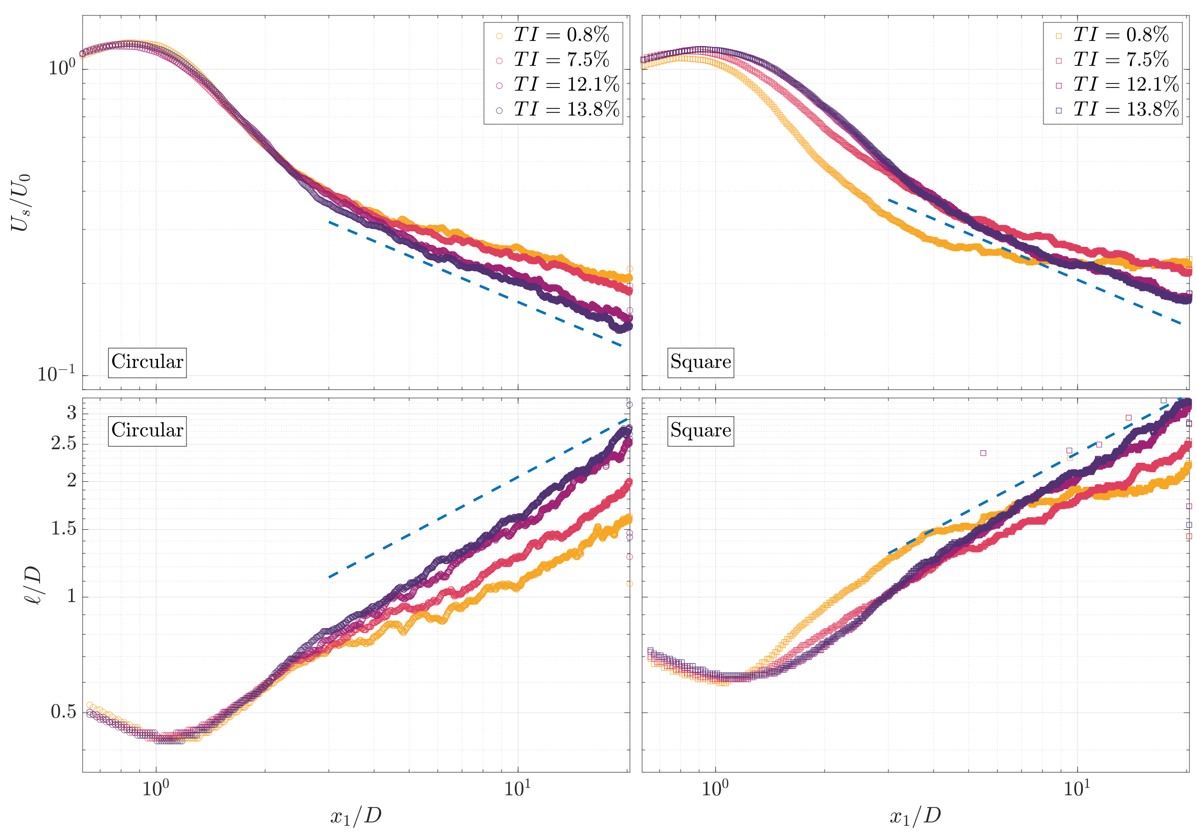

Figure 2: Streamwise profiles for all test cases for U_s/U_0 and ℓ/D. The blue lines in each plot denote the corresponding analytical solutions $U_s/U_0 \propto (x_1/D)^{-0.5}$ and $\ell/D \propto (x_1/D)^{0.5}$.

Spatial evolution of the turbulent/turbulent interface geometry and turbulent momentum entrainment

J. G. Chen [1] and Oliver R. H. Buxton [1]

[1] Department of Aeronautics, Imperial College London, South Kensington Campus, London SW7 2AZ, UK

key-words: Turbulent/turbulent interface, Wake

Abstract:
The spreading of turbulence into previously irrotational fluid depends on viscous diffusion of vorticity across a well-defined thin layer, usually referred to as a turbulent/non-turbulent interface (TNTI), which bounds the turbulent region and separates it from the outer, non-turbulent regions. In contrast to the extensive studies of TNTIs [1], our knowledge of the interface between flow regions with different levels of turbulence intensity, hereinafter referred to as a turbulent/turbulent interface (TTI), remains limited, notwithstanding its prevalence in the physical world. Kankanwadi & Buxton [2, 3] observed that both the turbulence intensity and the integral length scale in the ambient flow correlate to enhanced entrainment in the presence of the large-scale coherent vortices in the near wake of a cylinder, whilst a contrasting result was observed in the far field in which background turbulence was observed to suppress the entrainment rate with the turbulence intensity of the background turbulence playing the dominant role. An immediate question raised by these observations is that how the geometrical and dynamical features of the TTI in a cylinder wake spatially evolve from near to far field with the coherent motions diminishing? This is of central interest to the present study. The turbulent wake was marked with a high-Schmidt-number (Sc) scalar and a planar laser induced fluorescence (PLIF) experiment was carried out to capture the interface between the wake and the ambient flow from $x/d = 5$ to 40 where x is the streamwise coordinate from the centre of the cylinder and d is the cylinder's diameter (figure 1). The cylinder is placed at various downstream distances from various grids which are used to generate the background turbulence [2], such that the parameter space (turbulence intensity TI, integral length scale L_{12}) was explored as widely as possible in order to truly investigate the behaviour of the interface between the wake and the background flow with various "flavours" of turbulence. We conducted experiments for seven cases of (TI, L_{12}) and the distribution of (TI, L_{12}) at $x/d = 20$, i.e. the middle of the field of view, is displayed in figure 2. Figure 3a shows that all the TTI cases have a larger mean value of mean interface position $\overline{y_I}$ than the TNTI case (case 1a) at almost all x/d positions. A transition region of the interfaces' spreading toward the ambient flow is found at $x/d \approx 15$, beyond which the interfaces propagate at a slower rate than upstream and scale with the local wake half-width L_ϕ (figure 3b). It is also found that the location of both the TNTI and TTI have non-Gaussian probability density functions (PDFs) in the near wake because of the influence of the large-scale coherent motions present within the flow. Further downstream, after the large-scale coherent motions have dissipated, the TNTI position PDF does become Gaussian. Finally, the spatial variation from near- to far-wake of the"roughness" of the TTIs is quantified via the fractal dimension. We found that turbulence intensity induces a higher fractal dimension of the interface in the far wake (figure 4a), while the effect of the integral length scale is more appreciable in the near wake region (figure 4b). The evolution of the entrainment of momentum across the various TTIs is also examined in a separate experiment of combined PIV & PLIF measurement and will be discussed in the full paper.

References

[1] da Silva, C. B., Hunt, J. C., Eames, I., and Westerweel, J., (2014), Interfacial layers between regions of different turbulence intensity, *Annual review of fluid mechanics, 46, 567-590.*

[2] Kankanwadi, K. S. and Buxton, O. R. (2020), Turbulent entrainment into a cylinder wake from a turbulent background. *Journal of Fluid Mechanics, 905, A35.*

[3] Kankanwadi, K. S. and Buxton, O. R. (2023), The influence of freestream turbulence on the near-field growth of a turbulent cylinder wake: turbulent entrainment and wake meandering. *arXiv preprint arXiv:2301.10150.*

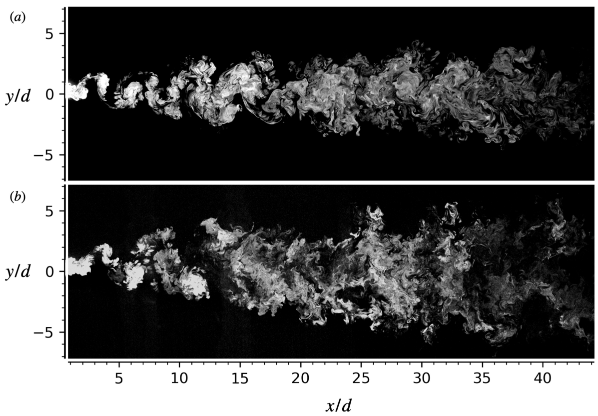

Figure 1: Visualisation of the wake (a) without and (b) with turbulence present in the background flow.

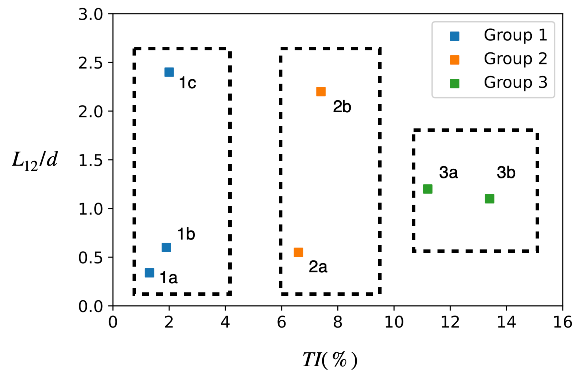

Figure 2: Parameter space (TI, L_{12}) of the background flow in the middle of the field of view at $x/d = 20$.

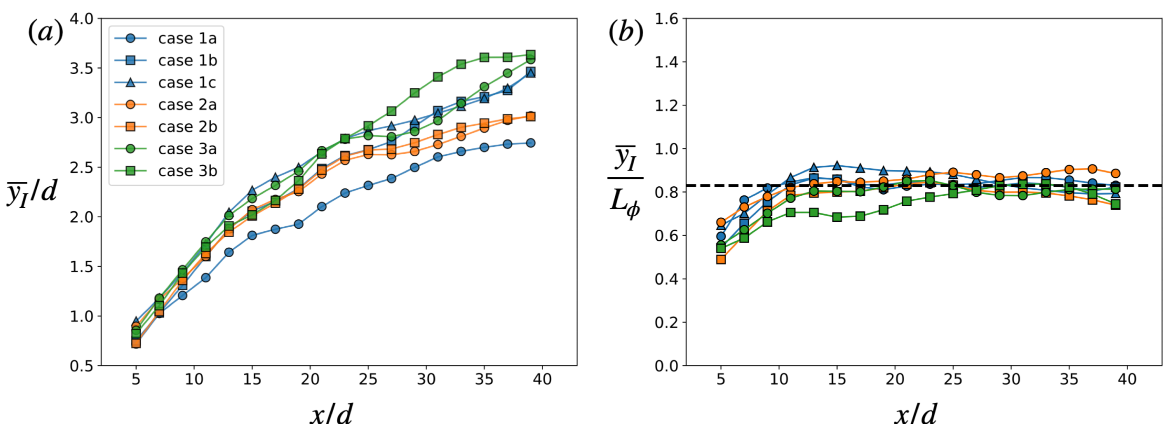

Figure 3: Streamwise distribution of the mean interface position (a) $\overline{y_I}/d$ and (b) $\overline{y_I}/L_\phi$ of all cases.

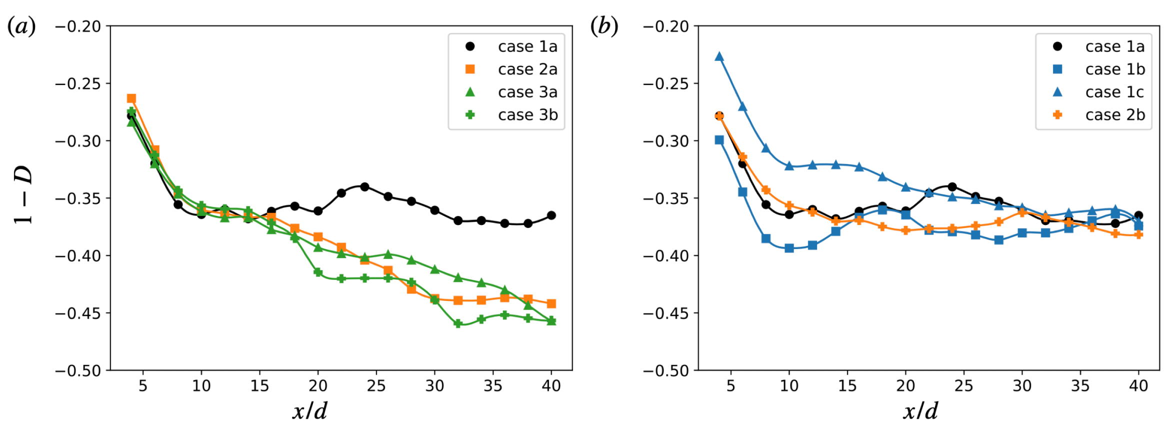

Figure 4: Streamwise distribution of fractal dimensions of TNTI and all TTI cases. (a) Effect of turbulence intensity, and (b) effect of integral length scale.

The beauty of active grids and their infinite possibilities of turbulence generation

Lars Neuhaus, Michael Hölling, Matthias Wächter, and Joachim Peinke

February 2023

Wind tunnel experiments are of major importance for fundamental turbulence research as well as investigation of objects under realistic reproducible conditions. Wind turbines operating in the atmospheric boundary layer are significantly affected by turbulence. These are high Reynolds number flows that are hard to reproduce in experiments. To increase the possibilities of generating turbulent flows, active grids are used. Different approaches to generate turbulent flows – homogeneous, inhomogeneous, and highest Reynolds number flows – will be presented.

Experiments are conducted in the closed test section of the large wind tunnel Oldenburg with a cross section 3x3m^2 and length of 30m. The wind tunnel can be equipped with two different active grids. Both exhibit the same basic design and control. One active grid consists of 80 individually controllable shafts with attached flaps and a mesh width of 0.143m and covers the whole cross section (Fig. 1). The second active grid is a reduced version of the first one (Fig. 2). Only 36 shafts are mounted at the lower half of the wind tunnel and are supported by a bar at roughly 1.22 m. This way the upper half is completely empty and laminar flow is ensured here.

This enables the generation of fundamentally different flows. While with the common active grid flow patterns can be imprinted and highest Reynolds number can be achieved (Fig. 3), the new half active grid enables to generate inhomogeneous flows with strongly varying turbulence parameters (Fig. 4). By this, the observed reduction of turbulence over height, as present in the atmospheric boundary layer can be reproduced. Further, it allows to investigate the turbulent non-turbulent interaction, with a wide range of adjustable turbulence properties at lower heights.

Already plenty different procedures to generate turbulent flows and tailor them the current needs are present. However, there is still a tremendous amount of opportunities to excite new features and further customize the flows, whether by adjusting of the shaft motion or by adaption the active grid design.

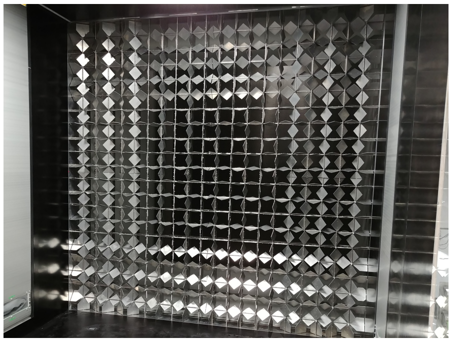

Figure 1: *Common active grid.*

Figure 2: *Half active grid.*

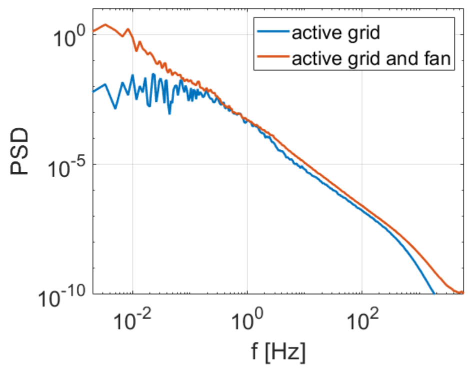

Figure 3: *High Reynolds number flow generated by the active grid.*

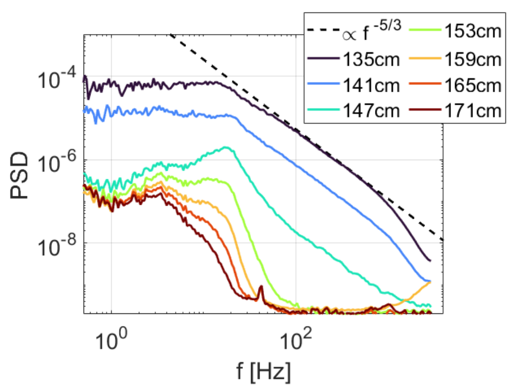

Figure 4: *Turbulent to non-turbulent flow generated by the haf active grid.*

Comparing hot-wire measurements and particle image velocimetry of turbulence fields generated by a flapping active grid

I. Neunaber [1], M. Asadi [1], L. Li[1], and R.J. Hearst [1]

[1] Department of Energy and Process Engineering, Norwegian University of Science and Technology, Trondheim, Norway

key-words: Active grid, Particle Image Velocimetry

Abstract:
The customization of flows by means of active grids has fascinated the experimental turbulence community for decades [1]. Over the years, different philosophies for the excitation of active grids have emerged, for example, randomized spinning and flapping of the wings, synchronized flapping motions, or the creation of flows with controlled flow patterns such as gusts, e.g., [2, 3, 4]. As a consequence, a large variety of parametric studies is available, and usually, hot-wires are used in these experiments to characterize the evolution of small-scale turbulence structures. Therefore, the temporal and spatial turbulence evolution are only looked at statistically, for example, through mean values and energy spectra.

To complement this approach, we study flows generated by an active grid using both particle image velocimetry (PIV) and the traditional hot-wires. The active grid has a mesh length of $M = 10\,\mathrm{cm}$. A total of of six randomized flapping and two synchronized flapping protocols, cf. table 1, were investigated 60 M downstream of the active grid at a mean velocity of $10\,\mathrm{ms}^{-1}$. The PIV set-up has a field of view of 10 M in the streamwise and 2.5 M in the wall-normal directions. This allows for a detailed comparison of the instantaneous behaviour of the velocity field obtained by PIV with the temporally highly resolved hot-wire data. Figure 1 gives two examples of velocities measured by hot-wire, and figure 2 shows instantaneous velocity fields for the same excitation protocols. The fluctuation magnitude of these cases is very different. In table 1 it is evident that the randomized actuation sequences have strong agreement between the measurement methods, while the synchronized sequences have stark differences in the estimated turbulence intensities (order 100%). This naturally begs the question, what is happening in the flow and what method should we rely on? This will be explored further in this study.

References

[1] Makita H., (1991), Realization of a large-scale turbulence field in a small wind tunnel, *Fluid Dyn. Res.* vol. 8, pp. 53.

[2] Hearst R.J., Lavoie P., (2015): The effect of active grid initial conditions on high Reynolds number turbulence. *Exp Fluids* 56, 185.

[3] Kröger L., Frederik J., van Wingerden J.-W., et al. Peinke J., and Hölling M., (2018): Generation of user defined turbulent inflow conditions by an active grid for validation experiments, *J. Phys. Conf. Ser.* 1037, 052002.

[4] Larssen J.V., Devenport W.J., (2011): On the generation of large-scale homogeneous turbulence. *Exp Fluids* 50, 1207–1223.

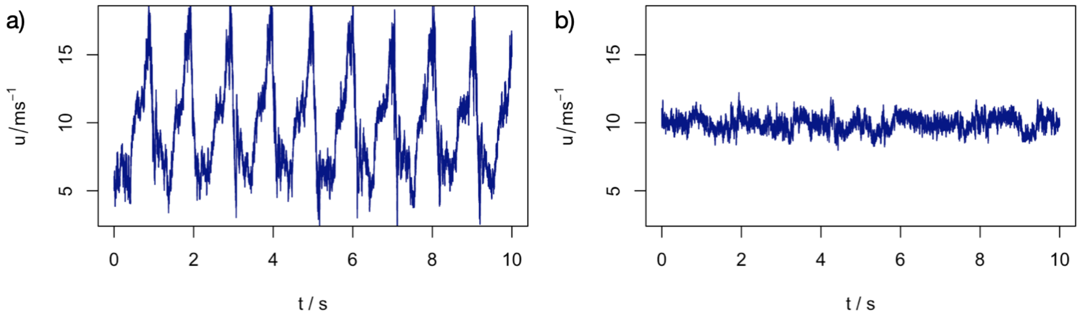

Figure 1: *Examples of hot-wire measurements for case Sync. A (a) and Rand. C (b).*

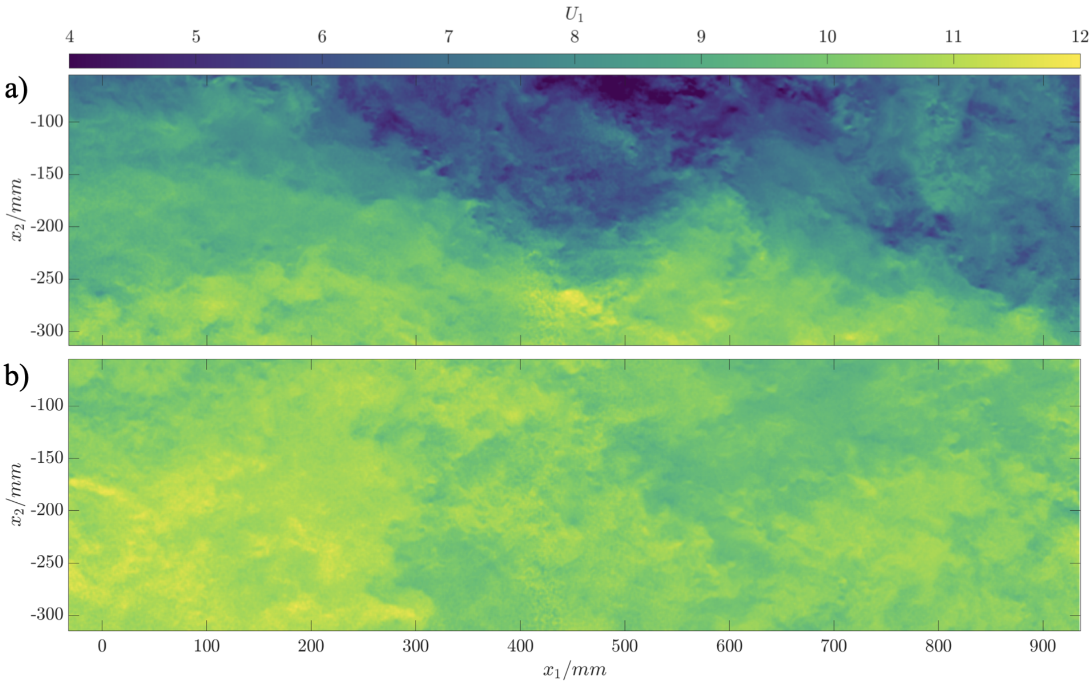

Figure 2: *Examples of instantaneous stream-wise velocity for case Sync. A (a) and Rand. C (b).*

Table 1: Comparison of mean velocities u and turbulence intensities TI obtained by hot-wire and PIV. Sync. abbreviates synchronized flapping and rand. stands for randomized flapping.

	Sync. A	**Sync. B**	**Rand. A**	**Rand. B**	**Rand. C**	**Rand. D**	**Rand. E**	**Rand. F**
$u_{hw}/\,\mathrm{ms}^{-1}$	9.68	9.89	9.93	9.96	9.98	10.04	9.77	9.76
$TI_{hw}/\%$	35	25	3	3	5	5	8	7
$u_{PIV}/\,\mathrm{ms}^{-1}$	9.74	9.72	10.32	10.31	10.20	10.24	10.17	10.19
$TI_{PIV}/\%$	18	15	2	2	5	5	7	6

Study of Dust Devils in a large-scale laboratory experiment

R. du Puits[1] and C. Kaestner[2]

[1] Aerodynamics Group, Technische Universitaet Ilmenau, Germany
[2] Production Technology Group, Technische Universitaet Ilmenau, Germany

key-words: Experimental work, Dust devils, Thermal convection

Abstract:

Intense vortices with vertical axes frequently form in the near surface atmospheric boundary layer (ABL) under dry convective conditions and in flat terrain (see Fig. 1). They are known as Dust Devils and are believed to significantly contribute to the production of continental aerosol. They are extremely difficult to measure in their natural environment, since stationary sensors provide insufficient data and remote sensing methods do not have an appropriate spatial and temporal resolution. In our talk we will present the experimental part of a collaborative project to study Dust Devils, in which meteorologists, physicists and engineers are involved. The core idea of this work is to complement Large-eddy simulations (LES) and Direct numerical simulations (DNS) with experiments in a well-defined laboratory environment. We will introduce an idea, how dust devils can be generated in a laboratory experiment and how processes, which contribute to their formation, can be investigated. We run our experiments in a large-scale Rayleigh-Bénard set-up, which features most of the basic properties of a convective ABL. The facility is known as the "Barrel of Ilmenau" (www.ilmenauer-fass.de, [1]). It reproduces the typical temperature stratification of a convective ABL with a higher temperature at the bottom and a lower temperature at the top. Although, our maximum Rayleigh number in the experiment is not higher than $Ra=10^{12}$ (about 6 decades lower than that of the ABL), dust devil-like structures are expected to evolve even at these low Ra numbers. In order to study these structures, we use the so-called Particle Tracking Velocimetry. We will present a novel variety of this metrology being capable to measure the flow field in the entire volume of our test section of $V\sim100$ m³. We will demonstrate the application of this technology in the "Barrel of Ilmenau" and we will show selected results which will be published soon [2].

Figure 1: Dust Devil in the desert (link: springer.com)

References

[1] du Puits R., Resagk C., and Thess A. (2013). Thermal boundary layers in turbulent Rayleigh-Bénard convection at aspect ratios between 1 and 9. New J. Phys., vol. 15, pp. 013040.

[2] Kaestner C., Schneider J. D., du Puits R. Evolution and Features of Dust Devil-Like Vortices in Turbulent Rayleigh-Bénard Convection - An Experimental Study. JGR: Atmospheres, accepted for publication.

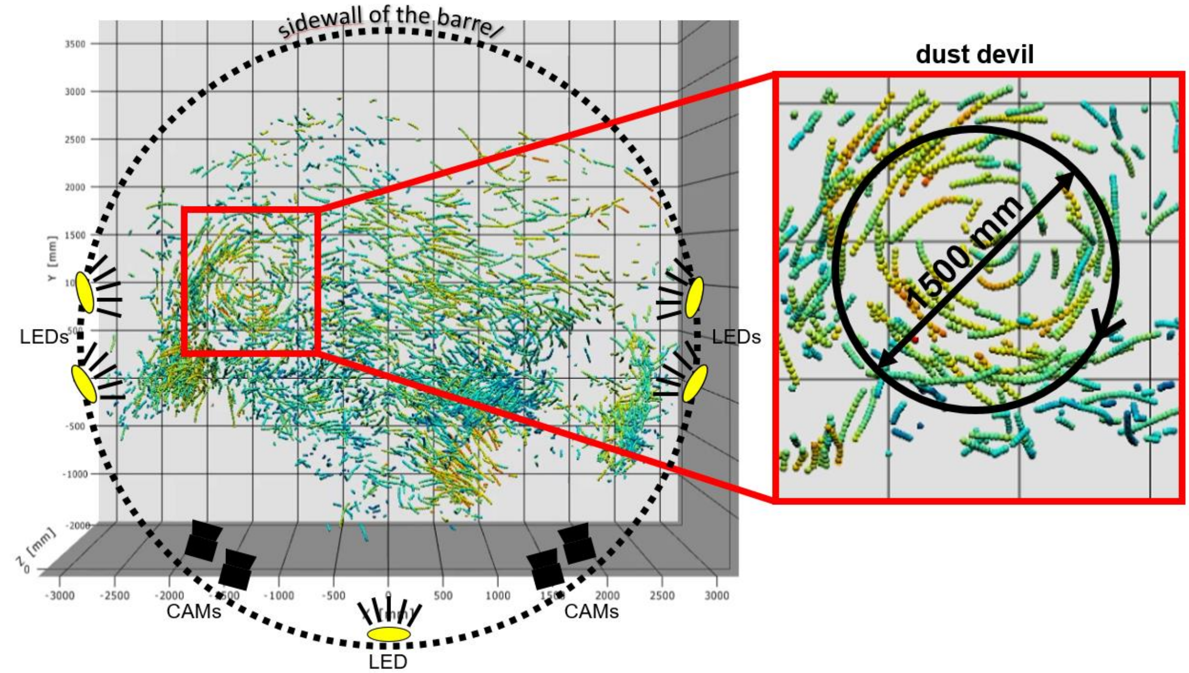

Figure 2: Full-scale reconstructed Lagrangian velocity field at Ra *= 1.5 × 10^{10}, showing a dust devil-like vortex.*

Effect of coherent fluctuation in stellar convection viewed from the non-equilibrium turbulence effect

Nobumitsu Yokoi [1], Youhei Masada [2] and Tomoya Takiwaki [3]

[1] Institute of Industrial Science, University of Tokyo, Tokyo, Japan
[2] Department of Applied Physics, Fukuoka University, Fukuoka, Japan
[3] Science Division, National Astronomical Observatory of Japan, Mitaka, Japan

key-words: stellar convection, plumes, non-equilibrium turbulence, double averaging

Abstract:
The non-equilibrium effect associated with the plume motions in convective turbulent flows is investigated. The surface cooling and resultant down-flowing plumes play a dominant role in the turbulent mixing in the stellar convection. The properties of the turbulent transports such as the turbulent mass, momentum and energy/heat fluxes as well as spatiotemporal field configurations are fairly different between the surface cooling non-locally driven case and the adiabatically locally driven case (Figure 1) [1]. The spatial distribution of the turbulent fluxes in the non-locally driven case cannot be explained by the standard gradient-diffusion type model with the mixing-length theory (Figure 2). In order to extract the effect of plumes, the time–space double averaging procedure is adopted, where a field quantity f is decomposed as

$$f = \overbrace{\langle \overline{f} \rangle + \underbrace{\widetilde{f}}_{\overline{f} - \langle \overline{f} \rangle}}^{\overline{f}} + \underbrace{f''}_{f - \overline{f}} \quad . \tag{1}$$

Here, $\langle \overline{f} \rangle$ is the space average of the time averaged $\overline{f}$, $\widetilde{f}$ is the dispersion part of $\overline{f}$ and is denoted as the *coherent fluctuations*, f'' is the deviation from the time average $\overline{f}$ and is denoted as *incoherent fluctuations*. In this framework, the plumes are regarded as the *coherent fluctuations* represented by $\widetilde{\mathbf{u}}$ (the fluctuation velocity $\mathbf{u}'$ is divided into $\mathbf{u}' = \widetilde{\mathbf{u}} + \mathbf{u}''$). With this time–space double averaging formulation, the energy transfer between the coherent and incoherent fluctuations, $\widetilde{K} \equiv \langle \widetilde{\mathbf{u}}^2 \rangle / 2$ and $K'' \equiv \langle \mathbf{u}''^2 \rangle / 2$, is expressed by the production mechanisms as

$$P_{\tilde{K}} \equiv \left\langle \widetilde{u''^\ell u''^i} \frac{\partial \tilde{u}^i}{\partial x^\ell} \right\rangle = -P_{K''}. \tag{2}$$

This means that, in the presence of the coherent velocity shear, $\nabla \widetilde{\mathbf{u}}$, energy transfer between the coherent and incoherent fluctuation components is occurred mediated by the dispersion part of the random fluctuation velocity correlation, $\widetilde{\mathbf{u}''\mathbf{u}''} (\equiv \overline{\mathbf{u}''\mathbf{u}''} - \langle \overline{\mathbf{u}''\mathbf{u}''} \rangle)$ (Figure 3). On the analogy of the non-equilibrium effect in the Reynolds averaged model, the non-equilibrium effect in the time–space averaging procedure is expressed as [2]

$$\kappa_{\mathrm{NE}} = \begin{cases} \kappa_{\mathrm{E}} \left[1 - C_{\tilde{\tau}} \dfrac{\tilde{\tau}}{\langle \mathbf{u}'^2 \rangle} \tilde{\Gamma}_D \right] & \text{for} \quad \tilde{\Gamma}_D < 0, \\ \kappa_{\mathrm{E}} \left[1 + C_{\tilde{\tau}} \dfrac{\tilde{\tau}}{\langle \mathbf{u}'^2 \rangle} \tilde{\Gamma}_D \right]^{-1} & \text{for} \quad \tilde{\Gamma}_D > 0, \end{cases} \tag{3}$$

with $\widetilde{\Gamma}_D = \langle (\widetilde{\mathbf{u}} \cdot \nabla) \overline{\mathbf{u}'^2} \rangle$, where $\tilde{\tau}$ is the timescale of the coherent fluctuation and $C_{\tilde{\tau}}$ is the model constant. The non-equilibrium effect along the plume motions are represented by $\widetilde{\Gamma}_D$. The turbulent internal-energy flux $\langle e' \mathbf{u}' \rangle$ in the non-locally driven case is plotted in comparison with the DNS (e': internal-energy fluctuation) (Figure 4). The spatial distribution of $\langle e' \mathbf{u}' \rangle$, which cannot be reproduced by the standard gradient-diffusion model with the mixing-length expression, is well reproduced by the non-equilibrium model.

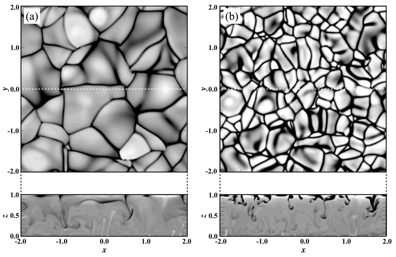

Figure 1: *Entropy distributions in our direct numerical simulations (DNSs) for the locally driven case (a) and the non-locally driven case (b). The horizontal cross-section at the top surface (upper) and the vertical cross-section of the entropy fluctuation.*

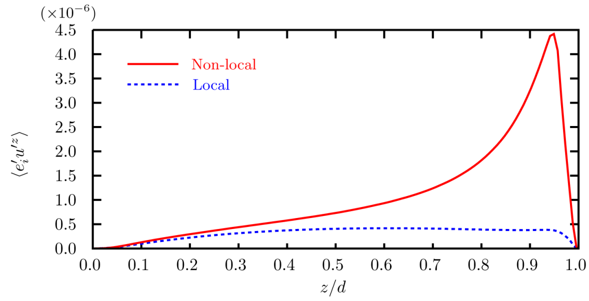

Figure 2: *Spatial profiles of the turbulent internal-energy flux $\langle e' \mathbf{u}' \rangle$ in our DNSs for the locally driven case (dotted line) and non-locally driven case (solid line).*

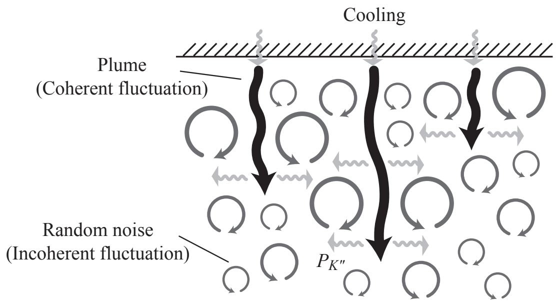

Figure 3: *Schematic picture of the interaction between the coherent and incoherent fluctuations. Plumes (coherent fluctuations, depicted by thick black curved lines) are driven by the surface cooling. The energy of the plume motions are transferred to the energy of the random noise (incoherent fluctuation, depicted by grey circle eddies) by the interaction $P_{K''}$ if $P_{K''} > 0$.*

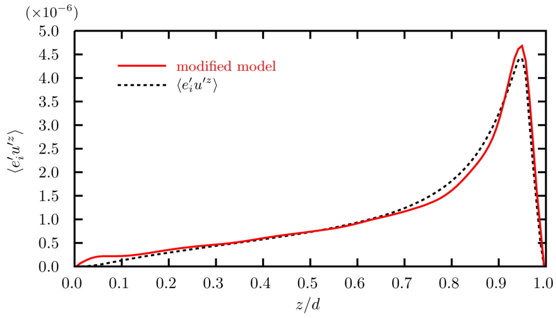

Figure 4: *Spatial profiles of the turbulent internal-energy flux $\langle e' \mathbf{u}' \rangle$ in the non-locally driven case. The results by the DNS (dotted line) and by the non-equilbrium model (solid line).*

References

[1] Cossette J.-F., Rast M. P., (2016), Supergranuration as the largest buoyantly driven convective scale of the Sun, *Astrophysical Journal, vol. 829, pp. L17-1-5.*

[2] Yokoi N., Masada Y. and Takiwaki T., (2022): Modelling stellar convective transport with plumes – I. Non-equilibrium turbulence effect in double-averaging formulation *Monthly Notice of Royal Astronomical Society, vol. 516, pp. 2718-2735.*

Estimation of boundary layer turbulence through non-intrusive sensing of wall-temperature fluctuations

F. Foroozan[1], A. Ianiro[1], S. Discetti[1] and W.J. Baars [2]

[1] Department of Aerospace Engineering, Universidad Carlos III de Madrid, 28911 Leganés, Spain
[2] Faculty of Aerospace Engineering, Delft University of Technology, 2629 HS Delft, The Netherlands

key-words: Turbulent Boundary Layer, Wall Friction, Heat Transfer, Experiment

Abstract:
Wall-attached coherent structures populating Turbulent Boundary Layers (TBLs) are responsible for carrying approximately 60% of the tangential Reynolds stresses. This aspect of coherence has inspired the development of non-intrusive, wall-based measurement methods that are capable of providing an estimation of these structures in wall turbulence. For instance, linear stochastic estimation has been used to predict the velocity field of turbulent channel flow, solely from wall-based observations [1]. Results revealed that the velocity field in the near-wall region can be estimated with reasonable accuracy from its footprint at the wall. An experimental sensor system that measures a flow-quantity at the wall—thus eliminating any form of drag of the system itself—is particularly valuable for realizing real-time, wall-based flow control methodologies that are aimed at, e.g. heat transfer enhancement or turbulent drag reduction [2]. In tandem to the proof-of-concept of such a sensor, the estimation schemes for the off-the-wall velocity field (with the sensor field as input) needs investigation and will demonstrate its applicability for control-sensing.

This work has investigated an experimental arrangement, consisting of a non-intrusive film-based sensor embedded within the wall below a TBL flow, and synchronized flow-field measurements using PIV. The experimental campaign was carried out in an open-loop wind tunnel at the Delft University of Technology, comprising a cross-sectional area of $60 \times 60\,\mathrm{cm}^2$; nominal free-stream velocity settings of $5\,\mathrm{m/s}$ and $10\,\mathrm{m/s}$ were selected. A TBL was generated downstream of an initial trip (P40-grit sandpaper) applied on all four walls, and developed under ZPG conditions having a curved ceiling. Measurements were conducted at two friction Reynolds numbers of 990 and 1800.

Instantaneous flow fields were measured using planar PIV, in a wall-parallel plane at the start of the logarithmic region around $y^+ = 80$. Synchronized convective heat transfer fluctuations on the wall beneath the PIV field-of-view were measured using high-repetition-rate infrared thermography. For this purpose, a non-intrusive and flush-mounted heated-thin-foil sensor [3] was designed, manufactured, and mounted on the bottom wall at the mid-span position. The sensor comprised a thin stainless-steel foil of $10\,\mu$m thickness, and was heated by a direct current that was uniformly applied across the two spanwise leading- and trailing-edge sides of the foil. With data of the input heat flux $\dot{q}_{in}$ (due to the Joule heating) and the foil temperature T_w, the convective heat transfer coefficient between the foil and the flow was estimated through an energy balance on the foil [4]. Finally, instantaneous distributions of the convective heat transfer coefficient are presented in non-dimensional form, in terms of the Nusselt number $Nu \equiv hl/k$ (figure 1 left) along with instantaneous fluctuating velocity fields (figure 1 right).

Previous studies in the water tunnel of Universidad Carlos III de Madrid successfully applied the proposed technique with a water fluid-medium. In this work, it is shown that this arrangement is capable of obtaining simultaneous measurement of flow and heat transfer fluctuations in air. The time-resolved heat transfer measurements captured the instantaneous convective heat transfer coefficient at the wall, which depicts the footprint of the large-scale wall-attached flow structures. Also, the synchronized measurements enable investigating the correlation between the stream-wise velocity fluctuations and the heat transfer fluctuations at the wall. Present results are potentially valuable for flow control methodologies aimed at heat transfer enhancement and drag reduction.

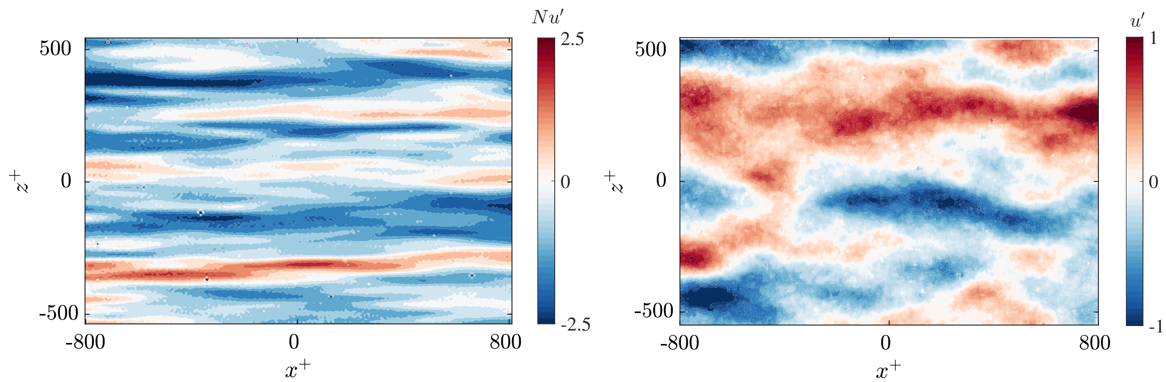

Figure 1: *[Left] An instantaneous fluctuation Nu field captured at the wall. [Right] The stream-wise velocity fluctuation field u' at $y^+ = 80$ captured at the same time instant.*
The coordinate system shows the stream-wise and span-wise directions in viscous units, and flow is from left to right.

Aknowledgement

F. Foroozan, S. Discetti and A. Ianiro have been supported by the project ARTURO, funded by the Spanish State Research Agency. ref. PID2019-109717RBI00/AEI/10.13039/501100011033.

F.Foroozan has been supported by the mobility grant provided by Universidad Carlos III de Madrid.

References

[1] Encinar, M. P., and Jiménez, J., (2019): Logarithmic-layer turbulence: A view from the wall, *Phys. Rev. Fluids*, **4**, 114603.

[2] Jiménez, J., (2018): Coherent structures in wall-bounded turbulence, *J. Fluid Mech.*, **842**, P1.

[3] Carlomagno G. M., and Cardone G., (2010): Infrared thermography for convective heat transfer measurements, *Exp. Fluids*, **49**, pp. 1187–1218

[4] Nakamura, H., (2009): Frequency response and spatial resolution of a thin foil for heat transfer measurements using infrared thermography, *Int. J. Heat Mass Transf.*, **52**, pp. 5040–5045

Enstrophy budgets in a turbulent temporal plume

Lorenzo Campana [1], M. van Reeuwijk [2], E. De Angelis [1,3]

[1] Department of Industrial Engineering, Università of Bologna, Forlí, Italy
[2] Department of Civil and Environmental Engineering, Imperial College, London, UK
[3] School of Engineering, Cardiff University, Cardiff, UK

key-words: Convection, plumes/thermals, turbulent simulation

Abstract:

In turbulent free shear flows such as jets, wakes and plumes, a sharp interface continually deformed over a wide range of scales separates the turbulent from the irrotational flow region: the turbulent/non-turbulent interface (TNTI) [1]. Near the TNTI, the exchanges of mass, momentum, and scalars (temperature) occur across this interface, making its study relevant to many engineering and geophysical flows, e.g., the dynamics near the TNTI govern the entrainment and mixing rates in turbulent reacting jets. Several previous works have focused on the role of vorticity or enstrophy in free shear flows, but they mainly concentrate on jets, wakes or mixing layers, as reviewed in [2]. Among these different flow configurations, a notable exception is the work in [3], which discussed aspects of the TNTI on a plane temporal plume. In line with this investigation, the present study aims to elucidate the role of enstrophy close to the sharp interface that separates the turbulent plume from the non-turbulent surroundings. The flow problem considered here is for a Reynolds number based on the initial conditions $Re = 200$ and Prandtl number $Pr = 1$. The domain is a cuboid of size $144H \times 144H \times 96H$ and has been discretized with $3240 \times 2880 \times 1920$ elements. From the initial conditions, the flow freely evolves in time. The data sets of the velocity fields, pressure and temperature are here analysed at a $t = 40$ where we observe a $\mathrm{Re}_\lambda \approx 89$.

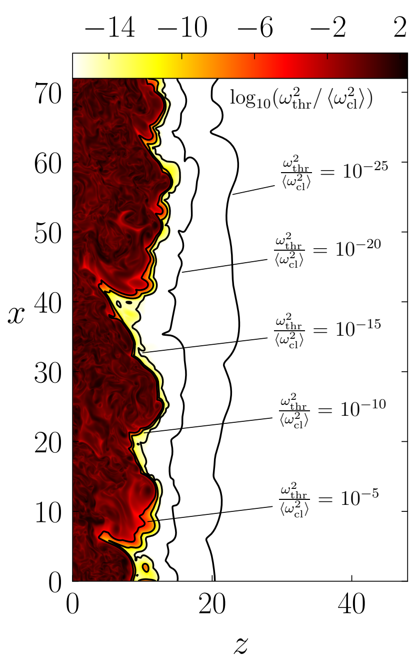

Figure 1: *Cross-section showing logarithmic enstrophy contour normalised by the mean centre-line enstrophy, isolines of fixed threshold values,* $\log_{10}(\omega_{\rm thr}/\langle\omega_{\rm cl}\rangle)$*, are also shown.*

Temporal evolving flows do not show the typical shape of a jet or wake. Here the average interface is flat but instantaneously appears strongly convoluted with bulges and re-entrant zones as in Fig.1. Analysing the flow topology, two main classes of coherent tube-like vorticity structures are observed: the large vorticity structures (LVSs) and the intense vorticity structures (IVSs), consistent with what was observed in [4]. Visually the IVSs, identified by the λ_2-criterion, are smaller than the LVSs and exhibit no preferential orientation as in Fig 2. Conversely, the LVSs tend to be aligned in the spanwise or streamwise direction. Moreover, these structures show a striking correlation with the interface bulges confirming that they define its geometry, see Fig. 3.

Moving to the quantitative analysis of the enstrophy budget, the traditional averaging procedure regarding the global reference frame in the cross-flow direction turned out to be unsuitable for properly studying the enstrophy dynamics close to the interface. Thus, an analysis of the mean enstrophy budget conditioned to the instantaneous position of the TNTI has been performed. The conditional budget confirms that the enstrophy dynamics is dominated by inviscid production and viscous destruction but highlights some interesting results. The viscous diffusion term is fundamental for the enstrophy increase close to the TNTI. Furthermore, in the conditional mean enstrophy budget, the convective term shows a different trend than that observed in jet flows [5]. Lastly, the baroclinic torque is essentially negligible for almost all the cross-flow directions. However, at the interface location, it undergoes a relatively large increase in magnitude that nearly matches what was already observed [3], acquiring 16% of the net enstrophy budget balance.

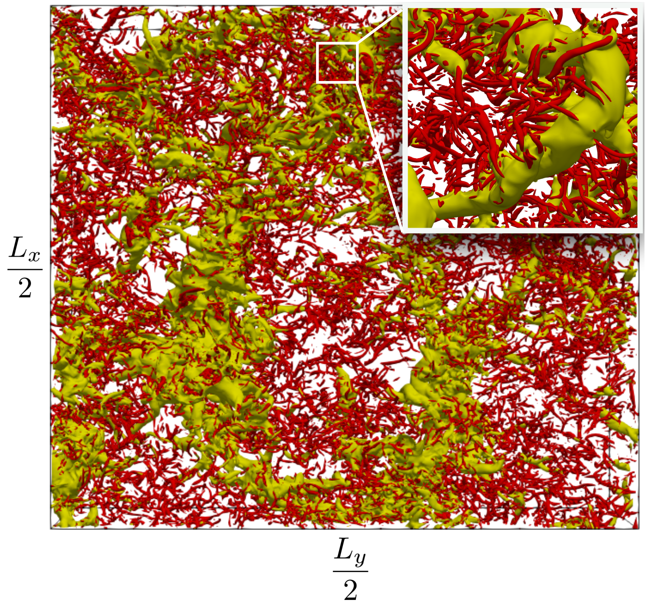

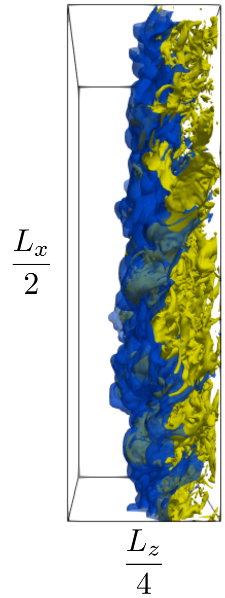

Figure 2: *Large vorticity structures (LVSs) identified by a low pressure iso-surface (yellow) and intense vorticity structures (IVSs) identified by the λ_2-criteria (red).*

Figure 3: *Temporal plume TNTI interface identified by an enstrophy iso-surface (blue) and large vorticity structures (LVSs) identified by a low pressure iso-surface (yellow).*

References

[1] Corrsin S. and Alan L. Kistler A. L., (1955), Free-stream boundaries of turbulent flows., *No. NACA-TR-1244.*

[2] da Silva, C. B. and Hunt J. CR. and Eames I. and Westerweel J., (2014), Interfacial layers between regions of different turbulence intensity., *Annual review of fluid mechanics, Vol. 46 pp. 567-590.*

[3] Krug D., Chung D., Philip J. and Marusic I., (2017) Global and local aspects of entrainment in temporal plumes., *Journal of Fluid Mechanics, Vol. 812, pp. 222–250.*

[4] da Silva C. B. and dos Reis Ricardo J. N., (2011), The role of coherent vortices near the turbulent/non-turbulent interface in a planar jet., *Philosophical Transactions of the Royal Society A: Mathematical, Physical and Engineering Sciences, Vol. 369, pp. 738–753.*

[5] Silva. T. S., Zecchetto M. and da Silva C. B., (2018), The scaling of the turbulent/non-turbulent interface at high Reynolds numbers. *Journal of Fluid Mechanics Vol. 843, pp. 156.*

New Insights on Buoyancy Driven Turbulence

Kiran Bhaganagar

[1] Laboratory of Turbulence, Sensing and Intelligence Systems, Department of Mechanical Engineering, University of Texas, San Antonio, Texas, 78248

key-words: Thermal Convection, Buoyancy-driven Turbulence

Abstract:
Turbulent buoyant plumes are a significant class of geophysical flows that occur whenever a persistent source of buoyancy creates a rising motion in buoyant fluid upward and away from the source. Wildland fire plumes, and atmospheric convective plumes, are examples of geophysical scale plumes, and in which it has been shown that helicity exists. The key mechanism that dominates the vorticity dynamics is stretching by turbulence fluctuations[1]. Studies have demonstrated the intensification of the local vertical vorticity by the stretching mechanisms causes the swirling nature of thermal plumes. Chen and Bhaganagar recently demonstrated that both the velocity and thermodynamic fluctuations contribute in the enhancement of the turbulent kinetic energy[2]
In helical flows, such as thermal wildland fire plumes, both energy, and helicity (scalar product of velocity and vorticity) are the two inviscid invariants of symmetrical three-dimensional Navier–Stokes equations. The direction of the turbulent energy transfer is, thus, given by the net flux of turbulent kinetic energy and helicity In this talk, we present new discoveries on the energy cascading in turbulent buoyant plumes are presented. A high-resolution large eddy simulation is used simulate buoyant gas plumes. The helicity and turbulent kinetic energy spectra reveal consistent trends and demonstrate a deviation from the classical Kolmogorov's inertial spectra at high wave numbers. Turbulent energy transfer is strongly associated with buoyant plume developments. With strong anisotropic structures found inside plumes, the possibility of double energy cascade is explored. And becomes critical to understand geophysical and astrophysical systems. Additional insight into turbulence physics has been confirmed in this study: the forward cascading of energy exists only at higher wavenumbers, whereas the flux of energy and helicity flows from smaller to large-scale structures for the large-scale structures.

In buoyancy-generated flows, the turbulence generated by the active scalar field (e.g. density field in wildland fire smoke or temperature in thermal plumes) interacts non-linearly across multiple scales (See Fig.1). This raises an important scientific question - How does the buoyancy forcing modify the turbulence spectra? and does the forcings at these smaller-scale move the energy to the larger scales ? We investigate these questions.

Spectral analysis of the turbulent structures provides crucial information on the energy transfer processes within plumes. The vertical spectra shows a consistent -3 slope[Fig. 2]. This is a deviation from the Kolmogorov's isotropic slope of $E \sim k^{\{-5/3\}}$ for the inertial regime. One of the possibilities is due the existence of buoyancy waves caused by the variations in density. Several theories have been proposed to explain the spectral slope of -3. This trend has been confirmed for both thermal plumes and buoyancy gas plumes.

Overall, our data present unambiguous evidence of the existence of inverse and forward cascades in both thermal and gas plumes. The new knowledge on the existence of inverse cascades in three-dimensional buoyancy-driven plumes will have an important impact on our fundamental understanding of flows in the atmosphere such as stratified atmospheric flows, compressible high-speed flows, flows with mixing, and flows with heat dissipation effects.

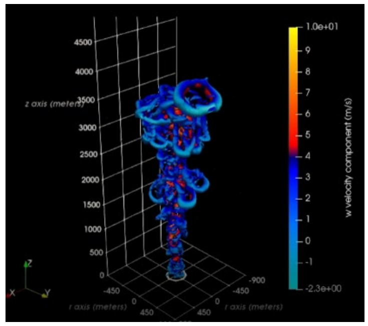

Figure 1: *Spatial evolution of the plume with strong vorticity and helicity*

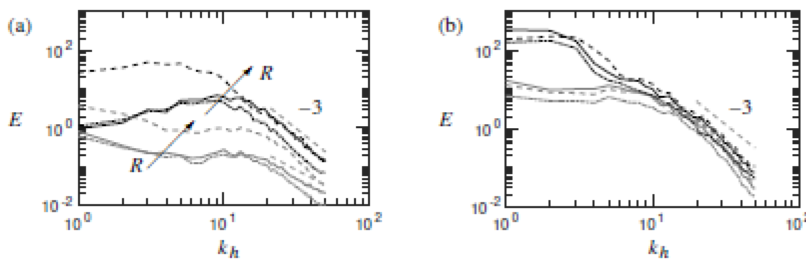

Figure 2: *Turbulent Kinetic Energy spectra (a) Horizontal component (b) Vertical Component*

References

[1] Chen, C. H. & Bhaganagar, K. 2021 New findings in vorticity dynamics of turbulent buoyant plumes. 810 *Phys. Fluids* **33** (11), 115104

[2] Chen , C.H. & Bhaganagar, K, 2023, Energetics of Buoyancy Generated Turbulent flows with active scalar: Pure Buoyant Plume, Journal of Fluid Mechanics , 2023

Detailing history and non-equilibrium effects in adverse pressure gradient turbulent boundary layers

S. Romero [1], S. Zimmerman [2], J. Philip [1], and J. Klewicki [1]

[1] Department of Mechanical Engineering, University of Melbourne, Parkville, Australia
[2] Department of Mechanical Engineering, John Hopkins University, Baltimore, USA

key-words: Adverse Pressure Gradients, Tuburlent Boundary Layers

Abstract:
The criteria of non-equilibrium boundary layers are studied using zero pressure gradient (ZPG) and adverse pressure gradient turbulent boundary layer (APG TBL) data sets over a range of Reynolds number. Although the term "equilibrium" in TBLs takes on a variety of definitions these have been mainly set in terms of self-similarity or via properties of the stresses, e.g. [1, 2]. The latter of these is interrogated herein, as it holds the promise to embrace a more comprehensive framework for characterizing non-equilibrium and flow history effects.

The stress balance for the APG TBL is as follows:

$$\underbrace{\nu\frac{\partial U}{\partial y}}_{\text{VS}} + \underbrace{(-\overline{uv})}_{\text{RS}} + \underbrace{\int_0^y \left[-U\frac{\partial U}{\partial x} - V\frac{\partial U}{\partial y'}\right] dy'}_{\text{MIS}} + \underbrace{(-\frac{y}{\rho}\frac{dP}{dx})}_{\text{PS}} = {u_\tau}^2, \tag{1}$$

where y' is a dummy variable of integration. The viscous stress (VS) reaches unity at the wall (y = 0) and there the Reynolds stress (RS) is zero. Like the ZPG case, the balance includes a non-constant mean inertia stress (MIS) term, and like the channel flow case there is a pressure stress (PS) term dependent on the wall-distance. Unlike the ZPG case, the magnitude of $-\overline{uv}/u_\tau^2$ is no longer bounded by 1. Since it has been previously observed in various APG TBL studies that the friction velocity u_τ is not the characteristic velocity scale for APG TBLs, it is beneficial to look at different velocity scalings. In [3] a velocity scale,

$$u_{hyb}^2 \equiv u_\tau^2 + \frac{y}{\rho}\frac{dP}{dx} \tag{2}$$

exhibited relative success in scaling the Reynolds stress over a range of Clauser pressure gradient parameter, β, and friction Reynolds number.

The stress balance terms from (1) are shown in figure 1. In panels numbered 1-4 the changes in β are small, as seen in figure 2. At these locations the distance between the ${u_{hyb}}^2$ and RS decreases up to the peak in the RS profile, indicating that the VS and MIS terms are negligible in this region. In panels 5-7, however, β is now rapidly changing and the PS and MIS profiles have dropped significantly in the outer region and and the local ${u_{hyb}}^2$ profile no longer behaves similarly to the local RS profile. Instead the ${u_{hyb}}^2$ from panel 4 (plotted as red dashed lines) behaves similarly to the RS profile in panels 5-7. This observation suggests a reconsideration of what is implied by equilibrium. Namely, when the PS and RS terms locally balance, as in panels 1-4, the boundary layer can be considered to be in equilibrium according to this underlying structure. Beyond this point (e.g., panels 5-7), where there is a qualitative change in the stress balance, the flow exhibits non-equilibrium behaviour. As such, in this study we explore the broader hypothesis that the cross-over from equilibrium to non-equilibrium, corresponding in the present scenario to where the MIS transitions from positive to negative, is dynamically characterized by a qualitative change to the internal leading order stress balance.

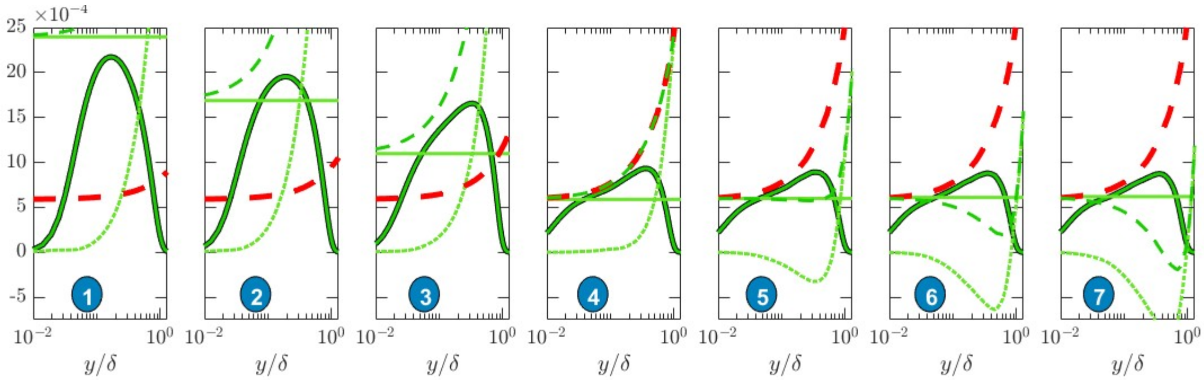

Figure 1: Stress balance. The panels are numbered 1-7, and correspond to the locations indicated in figure 2. Top panels: ═══: local Reynolds shear stress, ⋯⋯: local mean inertia stress, – –: local ${u_{hyb}}^2$, ——: local ${u_\tau}^2$. – –: Profile of ${u_{hyb}}^2$ from panel 4. Data from [4].

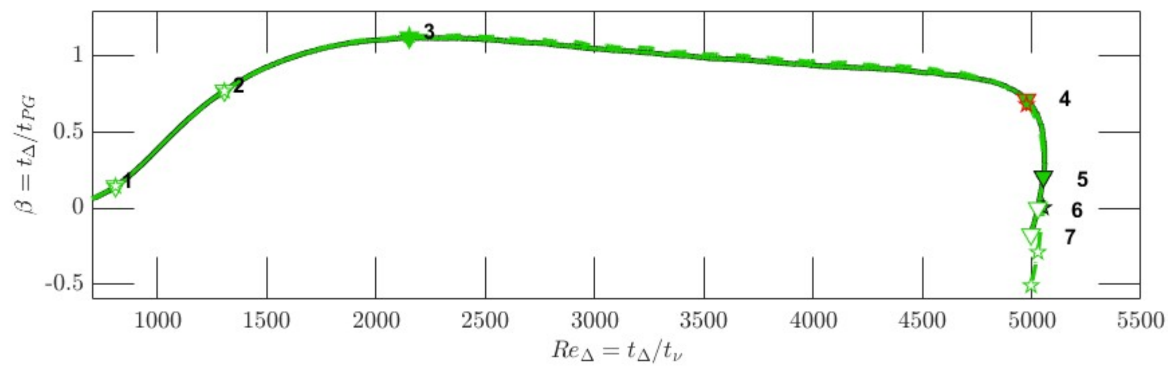

Figure 2: $\beta = t_\Delta/t_{PG}$ plotted as solid lines and markers are plotted as triangles. $\beta = (\delta^*/\tau_w)/(dP/dx)$ at $y/\delta = 0.5$ plotted as dashed lines and markers are plotted as stars. Solid markers indicate the point where the β reaches its maximum along the flow. The markers outlined in red indicate where β begins to rapidly decrease and where the maximum of $-\overline{uv}/u_\tau^2$ of the APG cases matches the maximum of the ZPG case at similar Reynolds number. The markers outlined in black indicate where $\beta = (\delta^*/\tau_w)/(dP/dx)$ at $y/\delta = 0.5$ is equal to 0. Data from [4].

References

[1] Townsend, A., (1956) The structure of turbulent shear flow, *Cambridge University, vol. 15.*

[2] Devenport W., Lowe T., (2022), Equilibrium and non-equilibrium turbulent boundary layers, *Progress in Aerospace Sciences, vol. 131, pp. 100807.*

[3] Romero S., Zimmerman S., Philip J., Klewicki J., (2022), Stress equation based scaling framework for adverse pressure gradient turbulent boundary layers , *Int. J. of Heat and Fluid Flow, vol. 93, pp. 108885.*

[4] Bobke A., Vinuesa R., Örlü R. and Schlatter P., (2017), History effects and near equilibrium in adverse-pressure-gradient turbulent boundary layers, *J. Fluid Mech., vol. 820, pp. 667–692.*

Statistical characteristics of three velocity components in pipe flow at high Reynolds number

M. Ono[1,2], N. Furuichi[1] and Y. Tsuji[2]

[1] National Metrology Institute of Japan, AIST, Tsukuba, Japan
[2] Nagoya University, Nagoya, Japan

key-words: 3 components turbulence statistics, spectrum analysis, High Reynolds number, pipe flow, LDV

Abstract:

To understand turbulence structure at wall-bounded flow in deeply, turbulence statistics for not only streamwise but also wall-normal and spanwise components are essential. Moreover, to investigate universality of a wall-bounded turbulence, high Reynolds number experiment which can identify clearly the inner and outer layer regions is also required. In this study, we report turbulence statistics for three components up to $Re_\tau \approx 20000$ using laser Doppler velocimetry (LDV) at "High Reynolds number actual flow facility (Hi-Reff)". Since the turbulence intensity is generally overestimated at the inner region with large velocity gradient due to the spatial resolution issue in LDV measurement, the measurement data were corrected by the following equation proposed by Durst et al.[1],

$$u'^2_{meas} = u'^2_{cv} + \frac{L^2}{16}\left(\frac{dU_{cv}}{dy}\right)^2 + \frac{L^2}{32}\left(\frac{d^2 u'^2_{cv}}{dy^2}\right) \qquad (1)$$

where U and $u'$are respectively the mean velocity and turbulence intensity. L is the control length, subscript *meas* is the measured value and subscript *cv* is the value at the center of the control length. The results of turbulence intensity profiles for 3 components agree well with the previous DNS data (Fig. 1). Furthermore, in this study, we discuss Reynolds number dependence of the three components turbulence statistics, with comparisons to previous high Reynolds number experimental data by other facilities.

To conduct spectrum analysis, the discrete time series data obtained using LDV were reconstructed into equal time interval data by the Sample and Hold reconstruction method[2]. By verifying the reconstruction method and appropriate sampling rate, the pre-multiplied spectrum (PMS) obtained in this study show nice consistency with previous data using hot wire (Monty et al.[3]), except the high wavenumber at near the wall (Fig. 2). PMS around the overlap region shows a bi-modal distribution constructed by large-scale motion (LSM) and very large-scale motion (VLSM) as reported by Kim and Adrian[4]. VLSM is energetically dominant at more inner region of the overlap region, while the LSM becomes energetically dominant at at more outer region of the overlap region. We report the results of the spectral analysis from $Re_\tau \approx 3000$ to 20000 and discuss the turbulent structures such as attached eddy, VLSM, and LSM from the turbulence statistics and PMS for three components.

References

[1] Durst, F., Jovanović, J., Sender, J., (1995), "*LDA measurements in the near-wall region of a turbulent pipe flow*", J. Fluid Mech.

[2] Adrian, R., Yao, C., (1986), "*Power spectra of fluid velocities measured by laser Doppler velocimetry*", Experiments in Fluids

[3] Monty, J., Hutchins, N., Ng, H.C.H., Marusic, I., Chong, M.S., (2009) "*A comparison of turbulent pipe, channel and boundary layer flows*", J. Fluid Mech.

[4] Kim, K. C., & Adrian, R. J. (1999), "*Very large-scale motion in the outer layer*", Physics of Fluids.

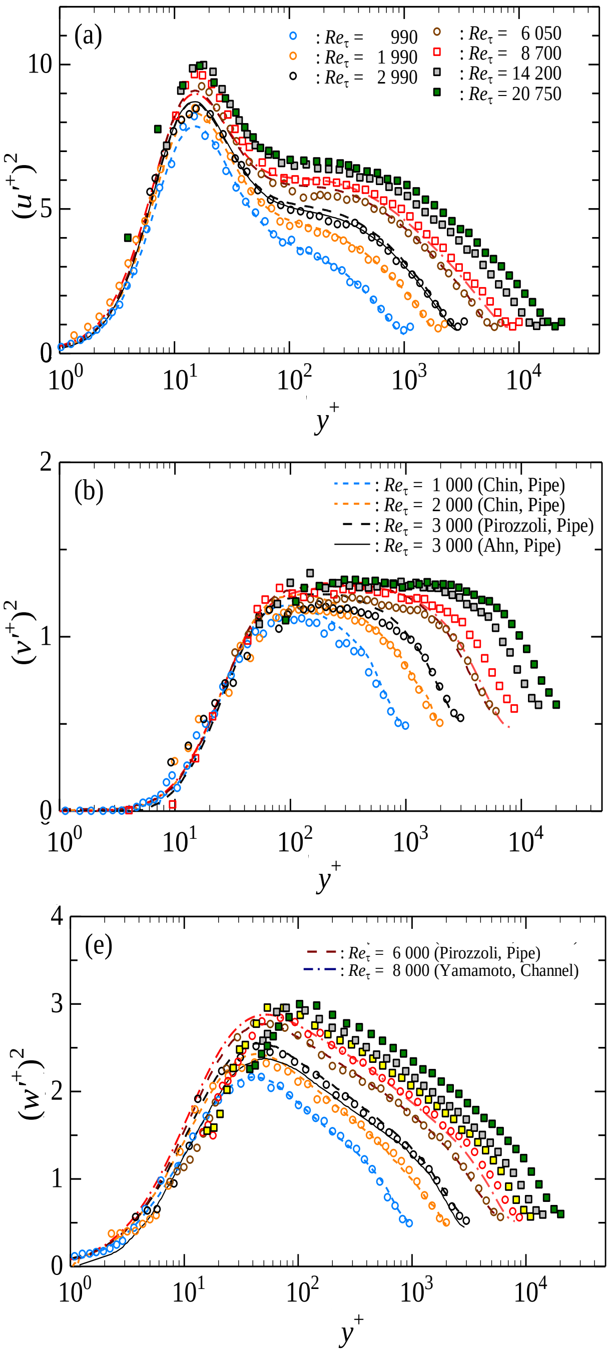

Figure 1. *Turbulence intensity profiles for three components at $Re_\tau \approx 1000$ to 20000.Broken lines are DNS data in previous researches.*

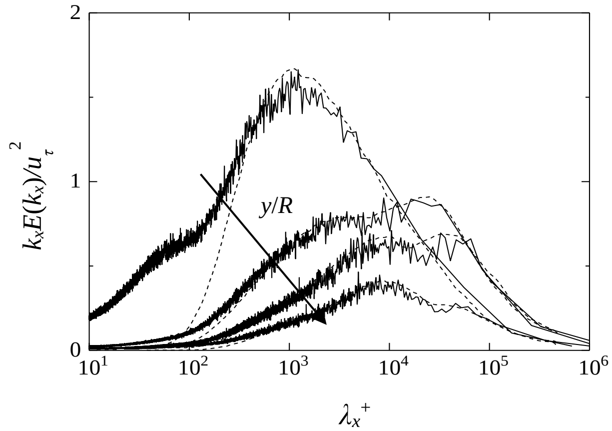

Figure 2. *The comparison of PMS distributions with previous data measured by hot-wire. The black solid lines are present results $y^+ \approx 15$, $y^+ \approx 190$ ($y/R \approx 0.064$), $y^+ \approx 870$ ($y/R \approx 0.293$), $y^+ \approx 1890$ ($y/R \approx 0.638$) at $Re_\tau = 2960$. The broken lines are PMS reported by Monty et al. (2009) at $y^+ \approx 15$, $y^+ \approx 180$ ($y/R \approx 0.060$), $y^+ \approx 800$ ($y/R \approx 0.265$), $y^+ \approx 2000$ ($y/R \approx 2/3$) at $Re_\tau = 3005$.*

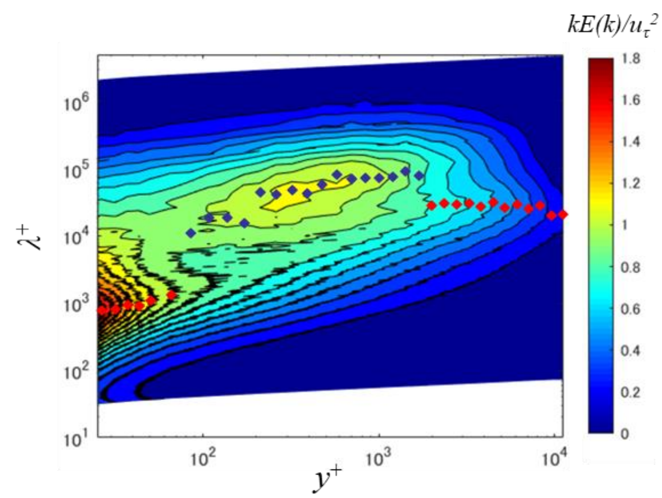

Figure 3. *Contour maps of pre-multiplied spectra with wall distance y^+ at $Re_\tau = 11200$. The red diamonds indicate LSM peaks of PMS and the blue diamonds indicate VLSM peaks.*

Effects of spanwise mean pressure gradient on rotating plane Couette flow

Oaki IIDA[1], Tomohiro KANDA[2]

[1] Department of Mechanical Engineering, Nagoya Institute of Technology, Nagoya 466-8555, Japan

key-words: Fundamentals, Direct Numerical Simulation, Turbulent plane Couette flow, System rotation, Mean pressure gradient

Abstract:

Effects of system rotation have pivotal effects on turbulence in engineering flows, e.g., turbomachinery. Turbulent plane Couette and Poiseuille flows are typical flow configurations for studying the spanwise system rotation on the wall turbulence[1,2]. When the imposed rotation has the opposite sense as the mean vorticity, turbulence is enhanced and secondary flows are generated, which flow configuration is coined as the anticyclonic rotation. The important result of the anticyclonic rotation is the emergence of the linear mean velocity profile, i.e., LMV, in the channel center, and zero absolute vorticity, i.e., ZAV, where mean vorticity related to mean velocity gradient is negatively equal to the imposed rotation frequency, i.e., 2Ω, and hence, the sum of the mean vorticity and 2Ω becomes zero[1,2]. The other important characteristic is reported in the rotating plane Couette flow; under the typical rotation number, the S-shaped mean velocity, i.e., SSMV appears, and the velocity gradient becomes negative in the center of the channel, which is verified in both experimental and numerical studies [3,4,5,6].

In contrast, the above results are on the condition where the direction of the mean flow is always in the streamwise direction, and to the authors' knowledge, the effects of its veering in the spanwise direction, because of the curvature of the wall and pressure gradient, are not studied. Hence, in this study, the effects of the veering in the spanwise directions are numerically studied by imposing an oscillating spanwise mean pressure gradient, which is coined as OSMPG, on the turbulent rotating plane Couette flow. Direct numerical simulations of an incompressible turbulent Couette flow as shown in Fig. 1 are performed with a spectral method, as indicated by our previous study [6].

The Reynolds and rotation numbers are chosen so that the ZAV and SSMV are observed. The sign of the imposed mean pressure gradient is periodically changed, and hence, mean flow in the spanwise direction is almost negligible, when it is averaged over the cycles of the oscillation. The two major effects of the OSMPG are observed. At first, OSMPG disrupts the secondary flow, which results in the significant attenuation of the skin friction coefficients (Fig. 2). Secondly, OSMPG enhances the near-wall turbulence by generating the shear in the spanwise direction; induced spanwise velocity is shown in Fig. 3.

As a result of these effects of imposing OSMPG, we find that in the case where ZAV is observed, the oscillating mean pressure gradient does not affect the mean velocity profile. In contrast, in the case where the SSMV is observed, the mean velocity profiles are significantly changed; SSMV is drastically shifted to the LMV (Fig. 4). These studies indicate that LMV requires sufficiently disturbed regions in the wall vicinity to dissipate the turbulence generated in the wall vicinity, and not to transport them into the region away from the wall.

References

[1] Johnston, J. P., Halleen, R. M., and Lezius, D. K., Effects of spanwise rotation on the structure of two-dimensional fully developed turbulent channel flow, Journal of Fluid Mechanics, Vol. 56 (1972), pp.533-557.

[2] Bech, K. H. and Andersson, H. I., Turbulent plane Couette flow subject to strong system rotation, Journal of Fluid Mechanics, Vol. 347 (1997), pp.289-314.

[3] Kawata, T. and Alfredsson, P. H., Turbulent rotating plane Couette flow: Reynolds and rotation number dependency of flow structure and momentum transport, Physical Review Fluids, Vol. 1 (2016), 034402.
[4] Kawata, T. and Alfredsson, P. H., Scale interactions in turbulent rotating plane Couette flow: insight through the Reynolds stress transport, Journal of Fluid Mechanics, Vol. 879 (2019), pp.255-295.
[5] Salewski, M., and Eckhardt, B., Turbulent states in plane Couette flow with rotation, Physics of Fluids, Vol. 27 (2015), 045109.
[6] Iida, O., Kamiya, K, and Kanda, T., Effects of anticyclonic spanwise rotation on plane Couette flow at small Reynolds number, Journal of Fluids Science and Technology, Vol. 17(2022), No. 21-00239.

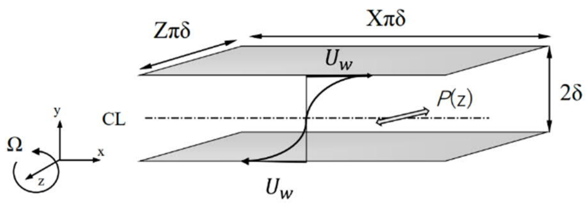

Figure 1: *flow configuration and coordinate system in rotating Couette flow; a flow is driven by moving walls with a constant velocity U_w in the opposite streamwise directions. By assuming the anticyclonic system rotation in the spanwise direction, the flow is dynamically unstable in the entire regions of a channel; X and Z are determined as 15 and 10, respectively, for the sufficient numbers of the secondary flow to be included; the grid points are 256,128, and 128, in the x, y, and z directions, respectively; OSMPG dP(z)/dz is also imposed in the spanwise z direction*

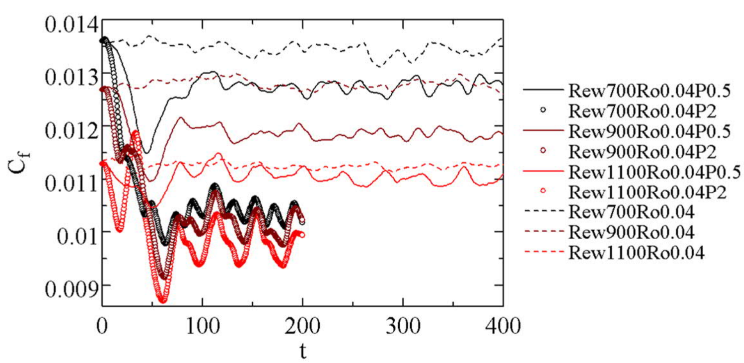

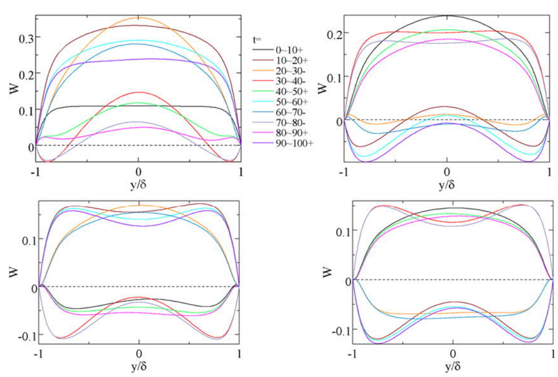

Figure 2 (left): *Time development of streamwise skin friction coefficients;* Rew=$U_w\delta/\nu$, Ro=$2\Omega\delta/U_w$, and P=dP/dx($\delta/u_{\tau 0}^2$), where $u_{\tau 0}$ is friction velocity on the condition not imposing the OSMPG Figure 3 (right): *Time development of spanwise mean velocity profiles in the case of Rew700Ro004P2*

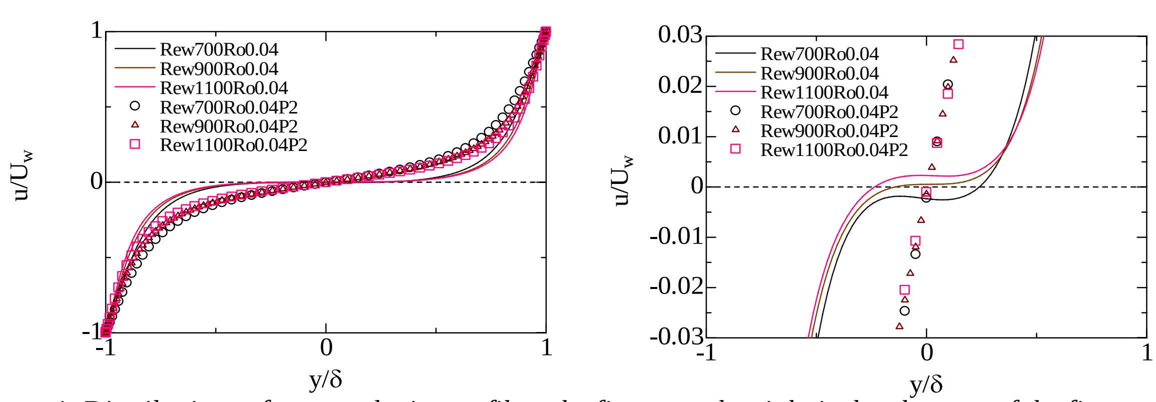

Figure 4: *Distributions of mean velocity profiles; the figure on the right is the close-up of the figure on the left*

Turbulence in spatially accelerating turbulent boundary layers

Matthew Falcone [1†], Shuisheng He [1]

[1] Department of Mechanical Engineering, University of Sheffield, Sheffield, UK

key-words: Boundary layers, simulation

Abstract:
A new understanding of spatially accelerating turbulent boundary layers is proposed to help explain the evolution of turbulence and the emergence of laminarisation in these flows. Spatial acceleration occurs in a range of engineering applications including turbomachinery and modern high-lift aircraft systems [1] where the sudden changes in skin friction and heat transfer coefficients associated with laminarisation can have a significant effect on flow behaviour [2]. Laminarisation has been found to occur for acceleration parameter, $K = \frac{\nu}{U^2}\frac{dU_\infty}{dx} \gtrsim 3 \times 10^{-6}$ and is characterised by the domination of the slowly evolving Reynolds stresses by the pressure gradient [3] with mean flow parameters tending towards values more typical of laminar flows. In this study, we perform direct numerical simulations (DNSs) of spatially accelerating turbulent boundary layers with inflow conditions generated using the recycling-rescaling method [4]. Four cases are presented which cover a range of acceleration parameters and include those that clearly begin the process of laminarisation with $K_{max} > 3 \times 10^{-6}$ (cases 1 & 2) and those that do not (cases 3 & 4).

The results show that all these cases undergo a process of transition similar to that found in temporal acceleration (He and Seddighi [5]). This transition process is characterised initially by a large increase in the near-wall mean shear due to the resistance to the acceleration provided by the wall and viscous effects. This results in the amplification of the near-wall streaks through the lift-up effect without accompanying increases in the transverse components which is reflected by the development of the Reynolds stresses in figure 1. Eventually, these streaks break down forming turbulent spots which spread as they are convected downstream. The formation and growth of turbulent spots for one of the weaker accelerations can be seen in figure 2 with the sudden increase of $\overline{v'v'}$ and $\overline{w'w'}$ at this location clear in figure 1. Key differences are identified between the stronger and weaker accelerations. This includes an absolute reduction of the transverse stresses in cases 1 and 2 whereas cases 3 and 4 do exhibit substantial changes. The present results also identify for the first time important differences between the reduction of v' and w' in the stronger accelerations with the peak of the former found to move away from the wall across the mean streamlines whereas the latter tends to follow the mean streamlines residing closer to the wall as the flow approaches the quasi-laminar state. There are also significant differences in the behaviour of the Reynolds stress budgets between these two components during laminarisation. Work is ongoing to precisely identify the mechanism behind the absolute turbulence reduction observed in the stronger accelerations.

†Email: mfalcone1@sheffield.ac.uk, Presenting and corresponding author.

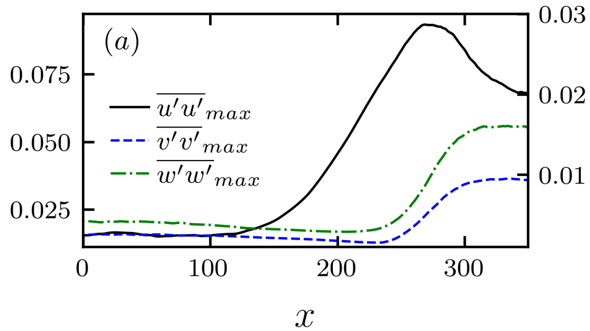

Figure 1: Wall-normal maxima of normal Reynolds stresses. (a): laminarising case, (b) non-laminarising case.

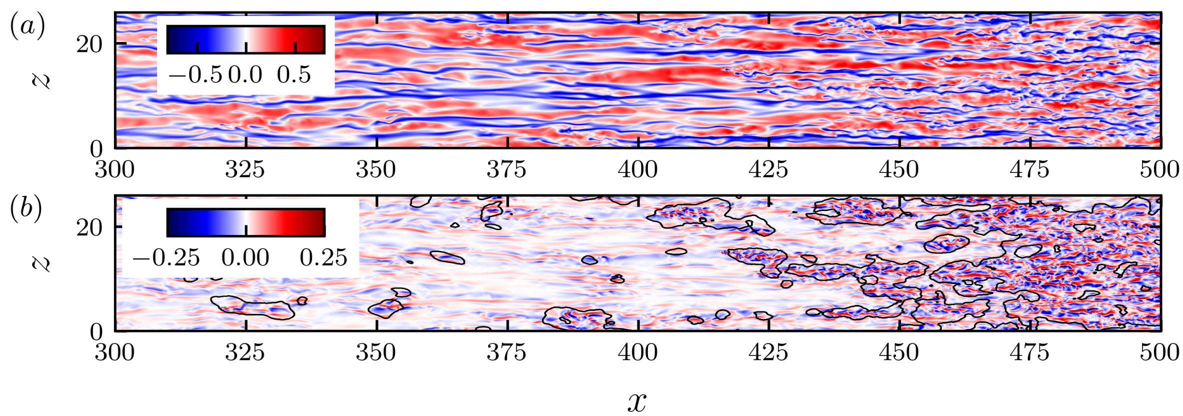

Figure 2: The onset of transition in a non-laminarising spatial acceleration. (a): u', (b): v'.

References

[1] C. P. Van Dam. The aerodynamic design of multi-element high-lift systems for transport airplanes, 2 2002. ISSN 03760421.

[2] P.M. Moretti and W.M. Kays. Heat transfer to a turbulent boundary layer with varying free-stream velocity and varying surface temperature—an experimental study. *International Journal of Heat and Mass Transfer*, 8:1187–1202, 9 1965. ISSN 0017-9310.

[3] R. Narasimha and K. R. Sreenivasan. Relaminarization in highly accelerated turbulent boundary layers. *Journal of Fluid Mechanics*, 61:417–447, 11 1973. ISSN 0022-1120.

[4] Thomas S. Lund, Xiaohua Wu, and Kyle D. Squires. Generation of turbulent inflow data for spatially-developing boundary layer simulations. *Journal of Computational Physics*, 140: 233–258, 1998. ISSN 0021-9991.

[5] S. He and M. Seddighi. Turbulence in transient channel flow. *Journal of Fluid Mechanics*, 715:60–102, 1 2013. ISSN 0022-1120.

iTi Conference on Turbulence X

July 23 - 26, 2023 | Bertinoro, Italy

Poster presentation

Convective heat transfer enhancement in turbulent boundary layers with linear genetic algorithms

Rodrigo Castellanos[1,2], Isaac Robledo[1], Juan Alfaro[1] Andrea Ianiro[1] and Stefano Discetti[1]

[1] Department of Aerospace Engineering, Universidad Carlos III de Madrid, Leganés 28911, Spain
[2] Theoretical and Computational Aerodynamics Branch, Flight Physics Department, Spanish National Institute for Aerospace Technology (INTA), Torrejón de Ardoz, Spain

key-words: Machine learning, Genetic algorithms, Flow control, Pulsed crossflow jets, Turbulent Boundary layers, Convective heat transfer enhancement

Abstract:

The convective heat transfer enhancement in a turbulent boundary layer (TBL) on a flat plate is optimised using an artificial intelligence control based on linear genetic algorithms. The actuation system consists of an array of 6 streamwise-aligned slot jets in crossflow, as shown in figure 1. The jets are divided into two groups, assigning independent control laws, b_1 and b_2 for odd and even jets, respectively. The actuation is achieved by the full-modulation of the jet in crossflow by means of an open-loop optimal periodic forcing defined by the carrier frequency f, the duty cycle DC and the phase difference ϕ between actuators as control parameters ($\Xi = [f_1, f_2, DC_1, DC_2, \phi]$). The considered optimisation framework in this work lies under the definition of Machine Learning Control (MLC) [1], particularly focusing on the integration of linear genetic algorithms. The control laws are optimised with respect to the unperturbed TBL and actuation with a steady jet. The optimisation process is driven by the cost function J, defined as a multi-purpose function that includes wall convective heat transfer and the cost of the actuation. The performance of the controller is quantified by infrared thermography, providing the value of the convective heat transfer coefficient in its dimensionless form, the Nusselt number Nu. The perturbed flow field is characterised with particle image velocimetry measurements to assess the flow topology upon the action of the jets.

The action of the jets considerably alters the flow topology compared to the steady-jet actuation, as illustrated in figure 1. The LGAC controller progressively learns the best set of control parameters for the convective heat transfer enhancement problem (see figure 2). After a few generations, the controller converges to a characteristic actuation frequency and duty cycle, while the rest of the learning process is used to tune the phase between odd and even jets. Interestingly, the preferred frequency found by the machine-learning algorithm coincides with that identified in our previous experimental investigation employing a single jet [2]. It is noted that such frequency is strikingly equal to the inverse of the characteristic travel time of large-scale turbulent structures advected within the near-wall region. The optimal controller yields a slightly asymmetric flow field. The phase difference between multiple jet actuation has shown to be very relevant and the main driver of the flow asymmetry. The results pinpoint the potential of machine learning control in unravelling unexplored controllers within the actuation space. Our study furthermore demonstrates the viability of employing sophisticated measurement techniques together with advanced algorithms in an experimental investigation.

References

[1] Duriez T., Brunton S.L. & Noack B.R. (2017): *Machine Learning Control – Taming Nonlinear Dynamics and Turbulence*, volume 116 of Fluid Mechanics and Its Applications, Springer International Publishing.

[2] Castellanos R., Salih G., Raiola M., Ianiro A. & Discetti S. (2023): Heat transfer enhancement in turbulent boundary layers with a pulsed slot jet in crossflow. *Applied Thermal Engineering*, 219, 119595.

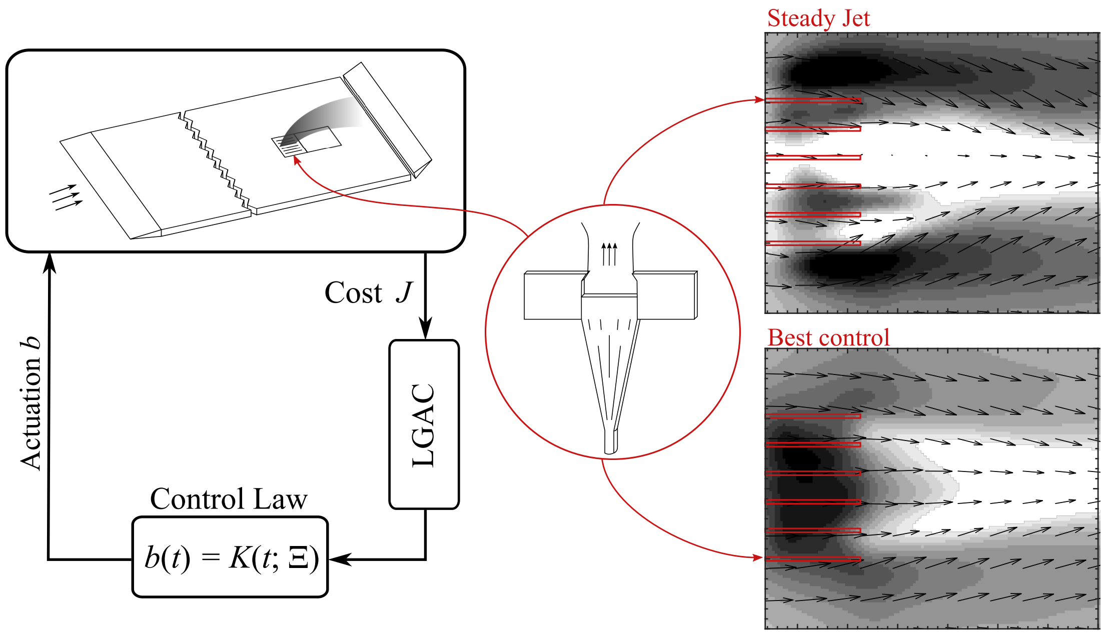

Figure 1: *Schematic of the convective heat transfer control using an array of six slot-jets in crossflow controlled by a linear genetic algorithm control (LGAC) algorithm. On the right, a miniature of the velocity field for the steady jet and the best control is included.*

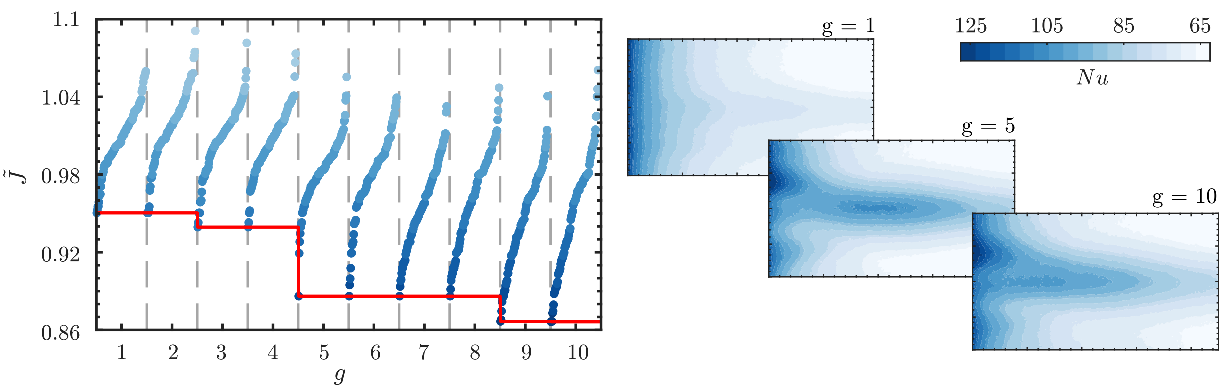

Figure 2: *Optimisation process of the LGAC algorithm. (Left) progress of the cost function J along the generation. (Right) evolution of the Nusselt number distribution downstream the actuators for three selected generations.*

On intermittency in the turbulent asymptotic suction boundary layer

E. Foschi [1,2], R. Örlü [1], A. Talamelli [2], P. Schlatter [1]

[1] KTH Engineering Mechanics, Royal Institute of Technology, 100 44 Stockholm, Sweden
[2] Department of Industrial Engineering, University of Bologna, 40126 Bologna, Italy

key-words: Asymptotic suction boundary layer, turbulent spots, DNS, Intermittency

Abstract:
A series of direct numerical simulations of turbulent asymptotic suction boundary layer (TASBL) is performed in a periodic domain, on which constant suction is applied over a flat plate. "Asymptotic" refers to the regime once the boundary layer has developed spatially and reached a constant boundary-layer thickness. The flow becomes independent of the stream-wise location and the suction rate acts as the only control parameter, writing $Re = U_\infty/V_0 = 1/\Gamma$. The study is performed in order to understand the discrepancy between the results of the numerical simulations in Khapko *et al.* (2016) [1] and the experimental data given by Ferro *et al.* (2021) [2]. The driving idea is that the difference in the statistics for the cases studied in the publications aforementioned is due to the presence of intermittent structures of laminar flow, developing in both temporal and spatial sense. These intermittent laminar regions in the extent of the developed turbulent flow cause lower values of the flow statistics which are appreciable in the data set of the numerical simulation while they appear to not be present in the experiments, evidenced by the higher fluctuation values. This is a clear discrepancy between simulation and experiments. The observation of intermittency is made possible by the application of flow tripping which removes laminar regions, making the turbulence fully developed and increasing the statistics values. The DNS were performed at different suctions rates which correspond to Re above the critical $Re_g = 270$, as stated in [1]. The domain size of temporal simulations is (L_x, L_y, L_z) is $(200, 100, 100)$ and their resolution (N_x, N_y, N_z) is $(128, 257, 128)$. The results of the DNS performed at different suction rates and with the application (or not) of tripping with different amplitudes are shown in Figure 1 with comparison of the results obtained in [1],[2]. The domain size of spatial simulations is (L_x, L_y, L_z) is $(3000, 50, 50)$ and their resolution (N_x, N_y, N_z) is $(960, 121, 64)$. The results of the DNS performed at different suction rates are shown in Figure 2 with comparison of the results obtained in [1], [2]. The statistics taken from the simulations at different stream-wise positions also support the developing character of the flow with increasing intermittency further downstream. Thus, we can conclude that the actual flow state at these marginal Reynolds numbers is indeed an intermittent one, with lower fluctuation values as the experimental data would predict. Thus the issue of long development lengths discussed by Bobke *et al.* (2016) [3] is still relevant.

References

[1] Khapko, T., Schlatter, P., Duguet, Y. & Henningson, D. S., (2016), Turbulence collapse in a suction boundary layer, *J. Fluid Mech.* 795, 356–379

[2] Ferro, M., Fallenius, B.E.G. & Fransson, J.H.M., (2021), Experimental study on turbulent asymptotic suction boundary layers, *J. Fluid Mech.* 915, A80

[3] Bobke, A., Örlü, R. & Schlatter, P., (2016), Simulations of turbulent asymptotic suction boundary layers, *J. Turb.* 17 (2), 157–180

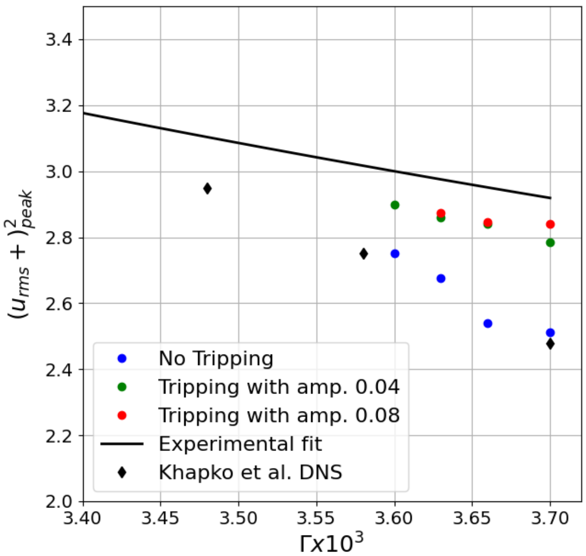

Figure 1: Maximum of velocity variance in inner units. Filled circles, the results of temporal simulations; black diamonds, DNS by Khapko *et al.* (2016) [1]; black line, experimental fit proposed in Ferro *et al.* (2021) [2]

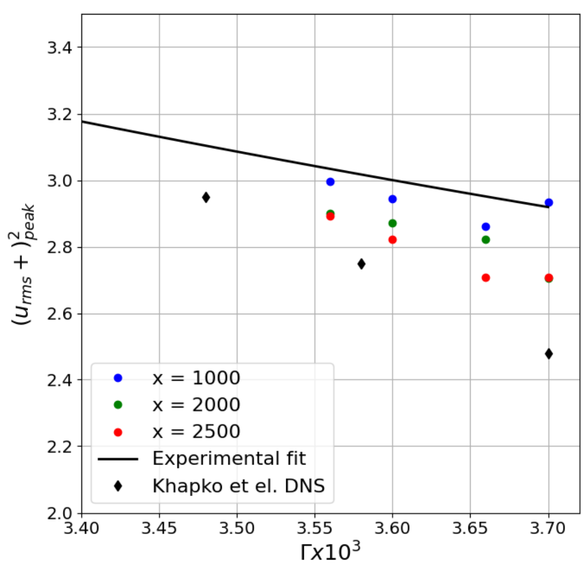

Figure 2: Maximum of velocity variance in inner units. Filled circles, the results of spatial simulations; black diamonds, DNS by Khapko *et al.* (2016) [1]; black line, experimental fit proposed in Ferro *et al.* (2021) [2]

Analysing the large-scale circulation dynamics of a turbulent Rayleigh-Bénard convection in a cubic cell

R. Barta [1,2], C. Wagner [1,2]

[1] Institute of Aerodynamics and Flow Technology, German Aerospace Center (DLR), Göttingen, Germany
[2] Institute of Thermodynamics and Fluid Mechanics, Technische Universität Ilmenau, Ilmenau, Germany

key-words: turbulent Rayleigh-Bénard convection, Particle-Tracking-Velocimetry

Abstract:
We present recent results on the analysis of turbulent flow structures in a cubic Rayleigh-Bénard (RB) convection cell based on measurement data processed by Particle-Tracking-Velocimetry (PTV) techniques. The RB convection is a canonic flow suited to study the principles of turbulent thermal convection because of its geometrically simple configuration, i.e. a cylindrical or rectangular shaped container which is cooled from above and heated from below (Brown and Ahlers, 2006). The latter cause an interplay of warm fluid rising up from the heating plate and cold fluid descending from the cooling plate. The configuration of interest is the cubic RB cell since the dynamics of the flow are guided by meta-stable (Wei, 2021) large scale circulations (LSC). In this case, the LSC are circular flow structures oriented along one of the cell diagonals which are rotating clockwise or counterclockwise along the present cell diagonal. The dynamics of the LSC is meta-stable because its current orientation only lasts for a limited time window. Vasiliev et al. (2016); Bai et al. (2016); Ji and Brown (2020) showed the LSC statistically disorder and then reorder in a different meta-stable configuration due to flow reversal events.
To analyse the flow dynamics leading to the reversal events, we present and discuss optical, non-invasive measurements of a turbulent Rayleigh-Bénard convection in a newly constructed cubic cell. The cell is equipped with an optically transparent cooling plate in order to be able to illuminated the measurement volume from above. This arrangement allows the flow to be observed through the side walls of the cell, which are made of glass, with a viewing angle of up to 360°. The cooling plate is made of sapphire glass and the heating plate is made of aluminium. Both materials allow a homogeneous temperature distribution due to their high thermal conductivity. During the measurement, the cell is filled with water to reach a Prandtl number of Pr ≈ 6.9. A RB convection in the hard turbulence regime is realized by achieving a Rayleigh number of Ra $\approx 3 \cdot 10^8$. Vishnu et al. (2020) suggests that in this regime the time scale to observe a reversal event is about 2 to 3 hours because the LSC contains a lot of turbulent kinetic energy which makes the LSC quite stable against reorientation. To make sure that at least two reversal events fall within the measurement they are extended to up to 8 hours. Thereby, for the flow visualisation high-quality polyamide particles from LaVision with a mean diameter of $60\,\mu$m are seeded in the flow. The particles have a density of $\rho = 1.001\,\rho_{H_2O}$, to ensure buoyancy neutral seeding particles.
In the last years Particle-Tracking-Velocimetry (PTV) became one of the most popular optical, non-invasive flow measurement techniques. PTV reconstructs the 3D path of individual seeding particles in a Lagrangian frame. Therefore, even complicated turbulent flow structures occurring on large as well as on small scales can be observed without interfering the flow. To determine particle trajectories from the measurement data our novel open-source probability-based Particle-Tracking-Velocimetry framework named pyPTV is applied. The framework will be freely available in mid-2023 and is completely written in Python. It allows the user to perform a full PTV routine on a given data set including image-processing, calibration and PTV algorithms including post-processing tools like track repairing and backtracking. Consequently, the pyPTV framework can be used to interpolate Eulerian velocity flow fields on Cartesian coordinates from the processed Lagrangian particle trajectories. An example of the particle trajectories obtained with pyPTV and a section of an instantaneous Eulerian velocity field along the LSC diagonal reconstructed from the particle trajectories is shown in Fig. 1.
At the conference, we want to present the analysis of the LSC dynamics based on Eulerian flow fields extracted from PTV trajectories. Here, the interplay between primary and secondary circulation structures is studied by applying a Proper-Orthogonal-Decomposition (POD). In addition, the dynamics of the LSC inside the cubic RB convection upon observing flow reversal events will be investigated by analysing the turbulent kinetic energy budget of the flow.

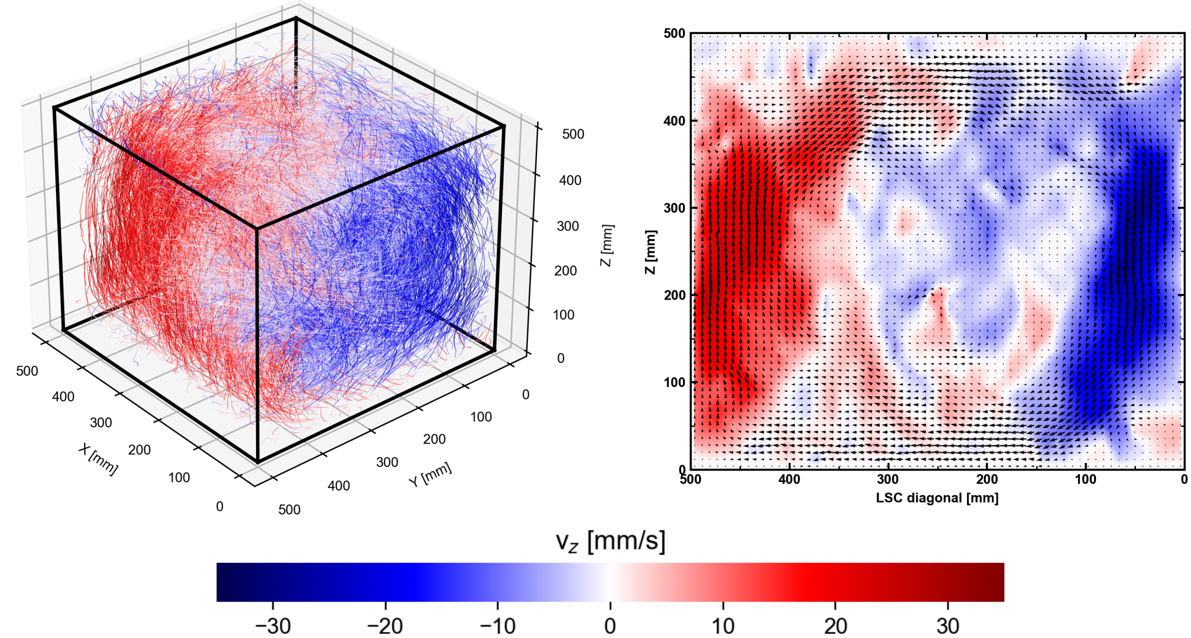

Figure 1: **Left:** reconstructed particle trajectories of an experimental RB convection with Ra $\approx 1 \cdot 10^{10}$ and Pr ≈ 6.9. **Right:** instantaneous Eulerian velocity field along the LSC diagonal ($X = Y$) reconstructed from the particle trajectories. Both plots are color coded by the vertical velocity component v_z.

References

Bai K, Ji D, and Brown E (2016) Ability of a low-dimensional model to predict geometry-dependent dynamics of large-scale coherent structures in turbulence. *Physical Review E* 93:023117

Brown E and Ahlers G (2006) Rotations and cessations of the large-scale circulation in turbulent rayleigh–bénard convection. *Journal of Fluid Mechanics* 568:351–386

Ji D and Brown E (2020) Low-dimensional model of the large-scale circulation of turbulent rayleigh-bénard convection in a cubic container. *Physical Review Fluids* 5:064606

Vasiliev A, Sukhanovskii A, Frick P, Budnikov A, Fomichev V, Bolshukhin M, and Romanov R (2016) High rayleigh number convection in a cubic cell with adiabatic sidewalls. *International Journal of Heat and Mass Transfer* 102:201–212

Vishnu VT, De AK, and Mishra PK (2020) Dynamics of large-scale circulation and energy transfer mechanism in turbulent rayleigh-bénard convection in a cubic cell. *Physics of Fluids* 32:095115

Wei P (2021) The persistence of large-scale circulation in rayleigh–bénard convection. *Journal of Fluid Mechanics* 924

Direct numerical simulation of turbulent open channel flow: Streamwise turbulence intensity scaling and its relation to large-scale coherent motions

C. Bauer [1], Y. Sakai [2] and M. Uhlmann [3]

[1] Institute of Aerodynamics and Flow Technology, German Aerospace Center, Bunsenstraße 10, 37073 Göttingen, Germany

[2] TUM School of Engineering and Design, Technical University of Munich, Arcisstraße 21, 80333 München, Germany

[3] Institute for Hydromechanics, Karlsruhe Institute of Technology, Kaiserstraße 12, 76131 Karlsruhe, Germany

key-words: direct numerical simulation, turbulent open channel flow

Abstract:
The well-known failure of wall scaling of the streamwise turbulent intensity in closed channel flows (CCF) is associated with the appearance of very-large-scale motions (VLSMs, [1]). In turbulent open channel flow (OCF), VLSMs are larger, more energetic and appear at lower Reynolds number than in CCF [2, 3]. Thus, to investigate the scaling of turbulence intensities and its relation to underlying coherent structures in OCF, we carried out direct numerical simulations of both OCF and CCF of friction Reynolds numbers up to $\mathrm{Re}_\tau \approx 900$ in large computational domains ($Lx/h \times L_z/h = 12\pi \times 4\pi$). Figure 1 shows the turbulent intensities normalized by the bulk flow velocity u_b. Unlike CCF, where the streamwise turbulent intensity scales neither in wall nor in bulk units (figure 1b), our data suggests that u_{rms} in OCF scales with the bulk velocity u_b for $\mathrm{Re}_\tau \gtrsim 400$. This difference in scaling behavior of OCF with respect to CCF is presumably caused by contributions from VLSMs as depicted in figure 2(a,b). In OCF, VLSMs are linked to so-called super-streamwise vortices (SSVs), which are statistically difficult to track [6]. However, in figure 2(c,d) we visualize SSVs in terms of the two-point correlation of the streamfunction of the streamwise-averaged, crosssectional velocity components. Similar to VLSMs, SSVs are more intense in OCF than in CCF and they occur much more regularly in the shape of alternating positive and negative vortices. Summarizing, at the conference, we are going to present new evidence of bulk scaling of the streamwise turbulence intensity in OCF and relate it to underlying coherent motions, such as VLSMs and SSVs. In addition, we are going to look at the scaling of the near-surface layers in OCF.

References

[1] Hoyas S. and Jiménez J. (2006), *Phys. Fluids, vol. 18, 11702*
[2] Pinelli M., Herlina H., Wissink J.G. and Uhlmann, M. (2022), *J. Fluid Mech., vol. 933, A49*
[3] Duan Y., Chen Q., Li D. and Zhong Q. (2020), *J. Fluid Mech., vol. 892, A3*
[4] Lee M. and Moser R. D. (2015), *J. Fluid Mech., vol. 774, 395–415*
[5] Oberlack M., Hoyas S., Kraheberger S. V., Alcántara-Ávila F. and Laux J. (2022), *Phys. Rev. Lett., vol. 128, 024502*
[6] Zhong Q., Chen Q., Wang H., Li D. and Wang X. (2016), *Water Resour. Res., vol. 52(5), 3563–3578*

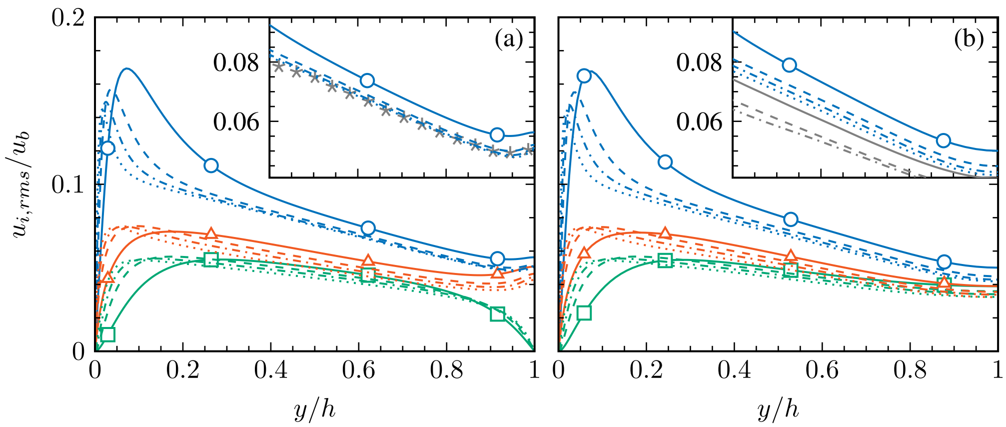

Figure 1: Turbulence intensities normalized by u_b as function of the distance from the wall y/h for OCF (a) and CCF (b): —○—, u_{rms}; —□—, v_{rms}; —△—, w_{rms}. Solid lines, $\mathrm{Re}_\tau \approx 200$; dashed lines, $\mathrm{Re}_\tau \approx 400$; dashed-dotted lines, $\mathrm{Re}_\tau \approx 600$; dotted lines, $\mathrm{Re}_\tau \approx 900$. The insets show a zoom for the streamwise turbulence intensity component. The symbols (*) in (b) indicate a profile from OCF measurements by [3] at $\mathrm{Re}_\tau = 2407$. The gray lines in (d) indicate CCF DNS data at $\mathrm{Re}_\tau = 2003$ (—, [1]), $\mathrm{Re}_\tau = 5186$ (- - -, [4]), $\mathrm{Re}_\tau = 10049$ (- - -, [5]).

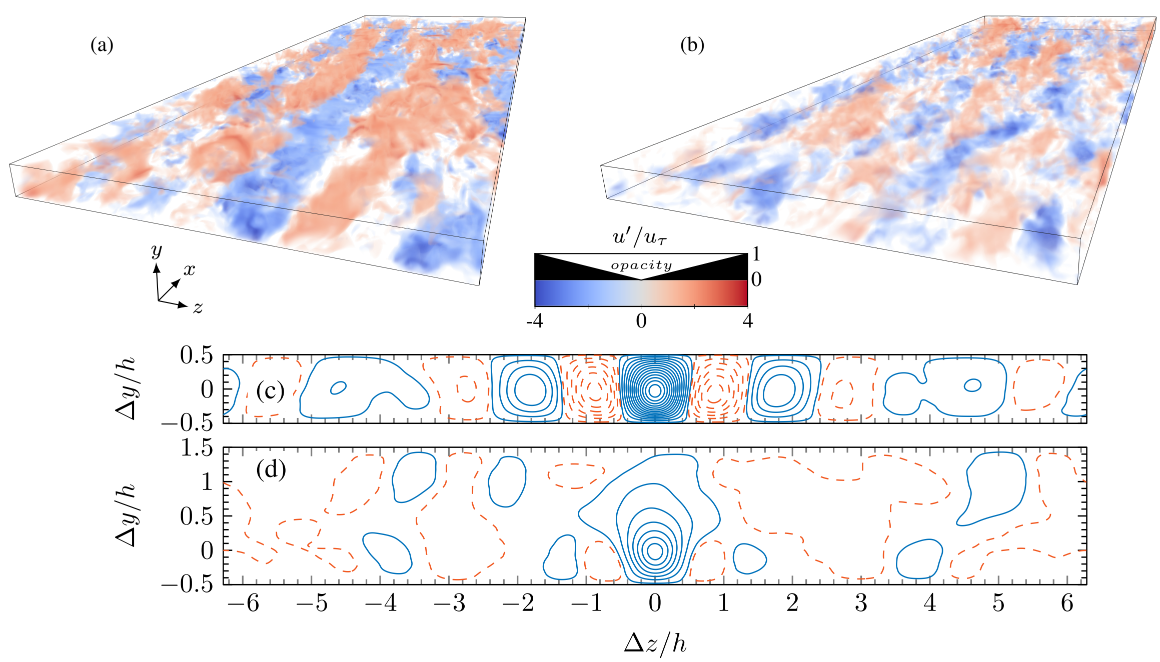

Figure 2: (a,b) Iso-volumes of the streamwise fluctuating velocity u' in OCF (a) and CCF (b) in a subvolume of the flow domain $l_x \times l_z = 4\pi h \times 2\pi h$, $0.5 \leq y/h \leq 1$ for $\mathrm{Re}_\tau \approx 600$. (c,d) Two-point correlation of the streamfunction of the streamwise-averaged, crosssectional velocity components $R_{\psi\psi}$ with $\psi = \psi_{\langle v\rangle_x \langle w\rangle_x}$ in OCF (c) and CCF (d) around $y_0/h = 0.5$ normalized by $(u_\tau h)^2$ for $\mathrm{Re}_\tau \approx 900$; Blue solid (red dashed) iso-contours indicate values of $R_{\psi\psi} = +(-)10^{-5}$ to $+(-)6.6 \cdot 10^{-4}$ with an increment of $5 \cdot 10^{-5}$.

Effect of freestream turbulence on the reattachment length downstream of a backward-facing step

Srikar Yadala, Girish K. Jankee, Leon Li, Nicholas A. Worth and R. Jason Hearst

Department of Energy and Process Engineering, Norwegian University of Science and Technology, Trondheim N-7491, Norway

key-words: Separated flows, grid turbulence

Backward-facing-step (BFS) flows occur when there is a sudden expansion in the geometry. Such configurations give rise to separated flows that eventually reattach, a common occurrence in nature and manufactured systems. The reattachment zone is crucial because it sets the initial conditions for the recovery process downstream and affects properties such as heat and mass transfer, skin friction and drag. Thus, estimating the reattachment length (X_r) is very significant. This length is known to be affected by the step height (h) and incoming boundary layer parameters [1, 2]. However, the relationship between the reattachment length and the incoming flow's turbulent properties is not fully understood, motivating the current study.

The experiments were conducted in a water channel facility and an active grid was used to generate different freestream turbulence conditions. Further details regarding the facility and active grid can be found in reference [3]. Three BFSs with different step heights (45 mm, 35 mm and 18 mm) were each subjected to three different freestream turbulence conditions. An LDV system was used to obtain freestream statistics of the incoming flow and a planar PIV system was employed to measure the velocity fields. Figure 1 shows the mean streamwise velocity fields for the three BFSs corresponding to the most turbulent case. These figures display the recirculation zone, separating shear layer, reattachment, and the recovering boundary layer.

The reattachment length for each test cases was determined by finding the point closest to the bottom surface with zero mean velocity [1]. Preliminary findings indicate that Re_h (Reynolds number based on h, figure 2a) is most influential, causing an increase in the reattachment length. Increasing turbulence intensity ($\mathrm{TI} = u'/U_\infty$) or integral length scale ($L_{u,\infty}$) results in a shorter reattachment length as observed in figures 2b and c, but the magnitude of the change is smaller than the changes induced by varying the step height. Using these measurements, a universal scaling that can predict the reattachment length will be derived. Furthermore, the physical principles that result in the observed trends and the impact of turbulence on the post-reattachment recovery process will be investigated.

References

[1] Armaly B.F., Durst F., Pereira J.C.F. and Schönung B. (1983), Experimental and theoretical investigation of backward-facing step flow, *Journal of Fluid Mechanics, vol. 127, pp 473–496*

[2] Adams E.W. and Johnston J.P., (1988), Effects of the separating shear layer on the reattachment flow structure Part 2: Reattachment length and wall shear stress, *Experiments in Fluids, vol. 6, pp 493–499*

[3] Jooss Y., Li L., Bracchi T. and Hearst R.J., (2021), Spatial development of a turbulent boundary layer subjected to freestream turbulence, *Journal of Fluid Mechanics, vol. 911*

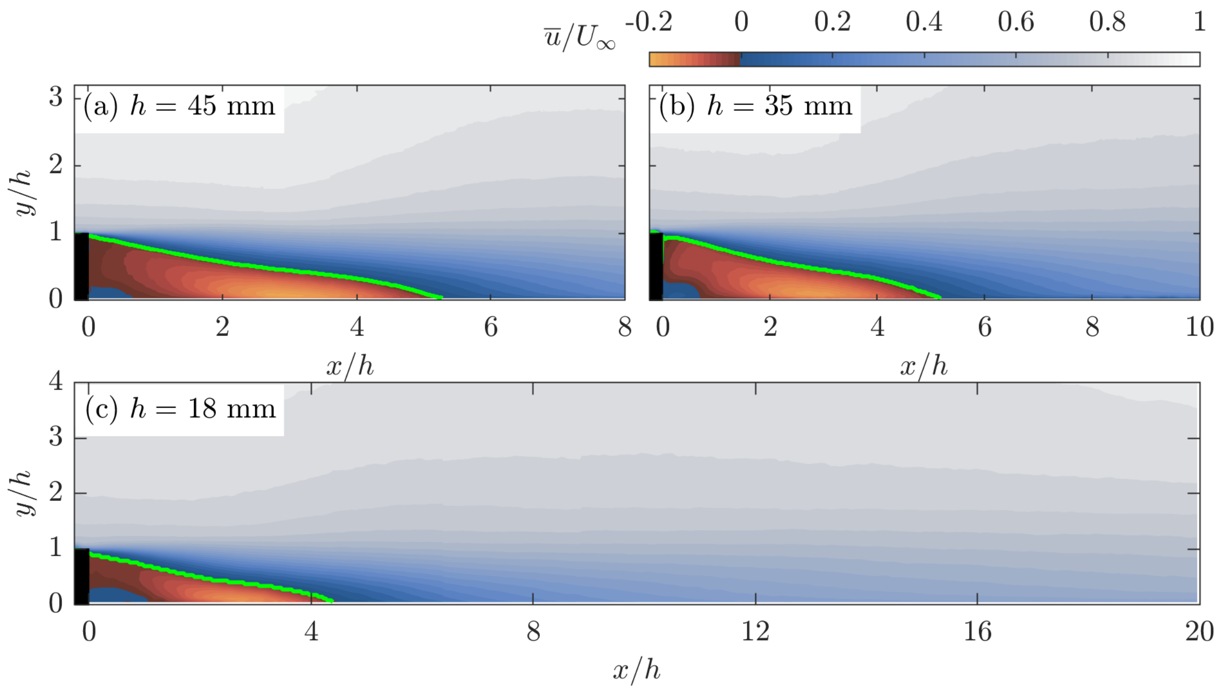

Figure 1: *Mean streamwise velocity fields ($\overline{u}/U_\infty$) for the three BFSs corresponding to the most turbulent case. The black rectangles are the BFSs and the green lines represent $\overline{u}/U_\infty = 0$ trace.*

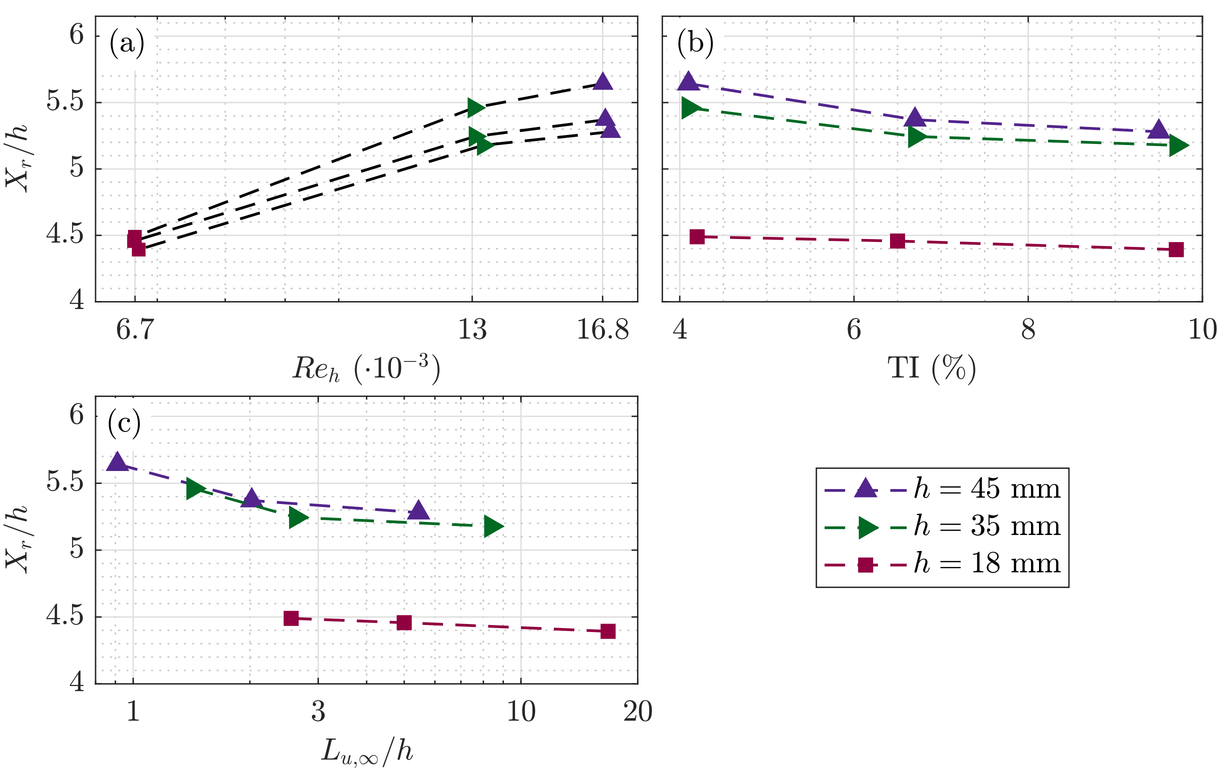

Figure 2: *Variation of reattachment length X_r with (a) Re_h, (b) turbulence intensity ($TI = u'/U_\infty$) and (c) integral length scale ($L_{u,\infty}$).*

Reversible Navier-Stokes equation on logarithmic lattices

Costa Guillaume [1], Barral Amaury [1] and Bérengère Dubrulle [1]

[1] Université Paris-Saclay, CEA, CNRS, SPEC, 91191, Gif-sur-Yvette, France

key-words: Turbulence, numerical simulations, logarithmic lattices, phase transition, reversibility

Abstract:
We study the three-dimensional Reversible Navier-Stokes equations first introduced by [1], [2], in which the energy is kept constant by adjusting the viscosity over time. We perform numerical simulations of these equations using a new framework called log-lattices, to reach extremely large resolutions at a moderate numerical cost. This technique allows us to explore regimes of parameters that were out of reach of the previous direct numerical simulations of [2]. Using the non-dimensionalized forcing as a control parameter, and the square root of enstrophy as the order parameter, we confirm the existence of a second order phase transition well described by a mean field Landau theory. The log-lattices framework allows us to probe the impact of the resolution, highlighting an imperfect transition at small resolutions with exponents differing from the mean field predictions. Our findings are in qualitative agreement with predictions of a 1D non-linear diffusive model, the reversible Leith model of turbulence.

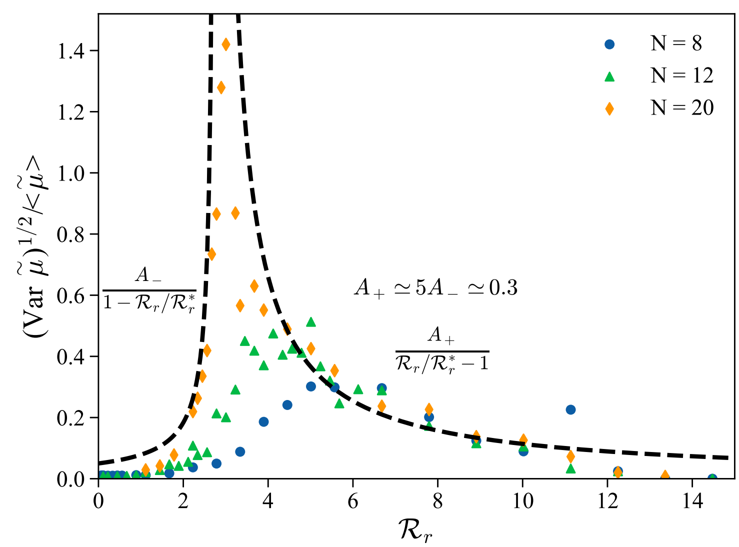

Figure 1: ***Second order transition for Reversible Navier-Stokes on log-lattices.*** *Figure shows the variations of the square-root of the enstrophy as a function of a dimensionless control parameter* $\mathcal{R}_r = \frac{f_0}{E_0 k_f}$. f_0 *being the forcing amplitude,* E_0 *the total, conserved, kinectic energy and* k_f *the injection scale. N corresponds to the number of modes.*

References

[1] G.Gallavotti, (1996): Equivalence of dynamical ensembles and Navier-Stokes equations, *Physics Letters A., 223, 91.*

[2] V.Shukla, B.Dubrulle, S.Nazarenko, G.Krstulovic, S.Thalabard, (2019): Phase transition in time-reversible Navier-Stokes equations *Physics Review E, 100, 043104.*

Dual scaling and the n-thirds law in grid turbulence

S. L. Tang [1], R. A. Antonia [2] and L. Djenidi [3]

[1]Center for Turbulence Control, Harbin Institute of Technology, Shenzhen, 518055, P. R. China
[2]Discipline of Mechanical Engineering, College of Engineering, Science and Environment, University of Newcastle, Newcastle, 2308 NSW, Australia
[3]Department of Mechanical Engineering, Indian Institute of Technology - Bombay, Powai, Mumbai 400076, India

Key-words: Turbulence theory, homogeneous isotropic turbulence

Abstract:

A dual scaling of the turbulent longitudinal velocity structure function $\overline{(\delta u)^n}$, *i.e.* a scaling based on the Kolmogorov scales (u_K, η) and another based on (u', L) representative of the large scale motion, is examined in the context of both the Karman-Howarth equation and experimental grid turbulence data over a significant range of the Taylor microscale Reynolds number Re_λ. Here, u is the longitudinal velocity fluctuation in the direction x, $\delta u = u(x+r) - u(x)$, r being the separation in the direction x; $\eta = (\nu^3/\overline{\varepsilon})^{1/4}$ and $u_K = (\nu\overline{\varepsilon})^{1/4}$ are the Kolmogorov length and velocity scales respectively; L is the integral length scale; $u' \equiv \overline{u^2}^{1/2}$; $Re_\lambda = u'\lambda/\nu$, where $\lambda = u'/(\partial u/\partial x)'$ and ν is the fluid kinematic viscosity. As Re_λ increases, the scaling based on (u', L) extends to increasingly smaller values of r/L while the scaling based on (u_K, η) extends to increasingly larger values of r/η. The implication is that both scalings should eventually overlap in the so-called inertial range as Re_λ continues to increase, thus leading to a power-law relation $\overline{(\delta u)^n} \sim r^{n/3}$ when the inertial range is rigorously established (see for example [1]). The latter is likely to occur only when $Re_\lambda \to \infty$. The use of an empirical model for $\overline{(\delta u)^n}$ [2], viz.

$$\frac{\overline{(\delta u)^n}}{u_K^n} = \frac{1}{15^{n/2}} F_n \frac{(\frac{r}{\eta})^n \left(1 + D_n(\frac{r}{L})\right)^{2C_n - n}}{\left(1 + B_n(\frac{r}{\eta})^2\right)^{C_n}}, \tag{1}$$

where B_n, C_n, D_n and F_n ($\equiv \overline{(\partial u/\partial x)^n}/\overline{(\partial u/\partial x)^2}^2$) are constants, shows that values of Re_λ between 10^4 and 10^5 are required before the distributions of $\overline{(\delta u)^n}$ ($n = 2, 3, 4, 6$) start to exhibit the onset of an inertial range. The model describes adequately the dependence on Re_λ of the available experimental data for $\overline{(\delta u)^n}$ and implies indirectly that the extrapolation of these data to infinitely large Re_λ should comply with $\overline{(\delta u)^n} \sim r^{n/3}$ (figures 1-2).

References

[1] Djenidi, L., Antonia, R. A. & Tang S. Consequences of Dual Scaling on the Velocity Structure Functions. 2022 Australasian Fluid Mechanics Conference, Sydney, Australia. 4-8 December 2022. Paper No: AFMC2022-19.

[2] Kurien, S. & Sreenivasan, K. R. 2000 Anisotropic scaling contributions to high-order structure functions in high-Reynolds-number turbulence. *Phys. Rev. E 62, 2206–2212.*

[3] Kaminsky, J., Birnir, B., Bewley, G. P. & Sinhuber, M. 2020 Reynolds number dependence of the structure functions in homogeneous turbulence. *Journal of Nonlinear Science 30, 1081–1114.*

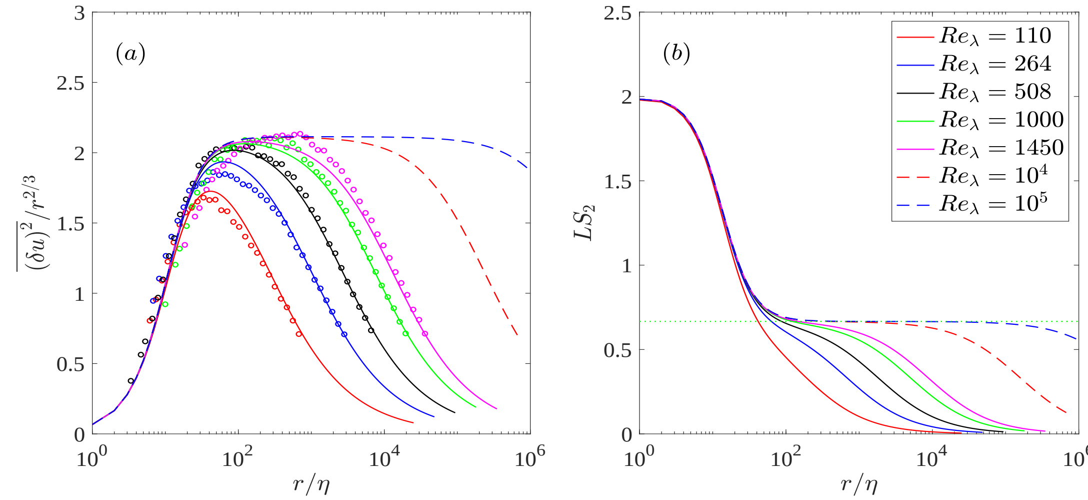

Figure 1: (a) Distributions of $\overline{(\delta u)^2}/(\bar{\epsilon}r)^{2/3}$ based on Eq. (1) at $Re_\lambda = 110$, 264, 508, 1000, 1450, 10^4 and 10^5 respectively. Symbols with the same color are the corresponding grid turbulence data [3]. (b) Local slope ($LS_2 = d\log(\overline{(\delta u)^2})/d\log r$). Dashed horizontal line: 2/3.

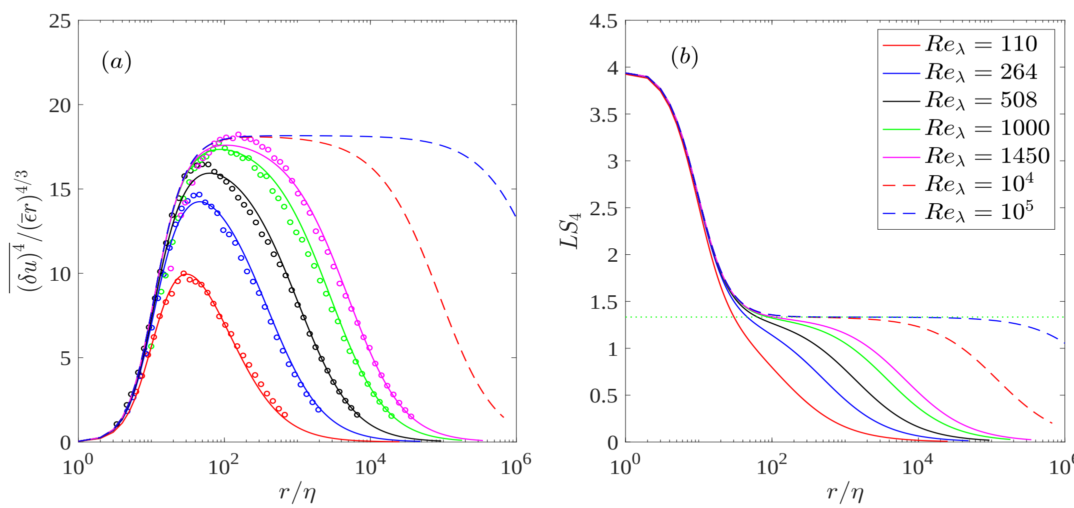

Figure 2: (a) Distributions of $\overline{(\delta u)^4}/(\bar{\epsilon}r)^{4/3}$ based on Eq. (1) at $Re_\lambda = 110$, 264, 508, 1000, 1450, 10^4 and 10^5 respectively. Symbols with the same color are the corresponding grid turbulence data [3]. (b) Local slope ($LS_4 = d\log(\overline{(\delta u)^4})/d\log r$). Dashed horizontal line: 4/3.

On the interface between freestream turbulence and a turbulent boundary layer

Masoud Asadi [1], Pim Bullee [1] and R. Jason Hearst [1]

[1] Department of Energy and Process Engineering, Norwegian University of Science and Technology, Trondheim, Norway

key-words: Turbulent boundary layers, Freestream turbulence

Abstract:
The effect of freestream turbulence (FST) on the statistics of turbulent boundary layers (TBLs) has been the subject of several studies. Identifying the instantaneous freestream (FS) flow and separating it from the instantaneous TBL is a prerequisite for further exploration of the effects. Wu et al. [1] argued that an instantaneous interface should exist that separates the boundary layer flow from the freestream turbulent flow. Using direct numerical simulations of a TBL subjected to homogeneous-isotropic FST, they approached the problem by a scalar marking method, where a constant temperature threshold value was used to demarcate the instantaneous interface. On the other hand, You and Zaki [2] remarked that due to the presence of diffusion on both sides of the interface, a scalar is not a good indicator of the interface position. Instead, they used a step-level approach to separate the FS flow from the TBL. Using particle image velocimetry (PIV), Hearst et al. [3] attempted to identify the upper edge of TBL in the presence of FST by employing a constant kinetic energy deficit threshold. In fact, they opted for the same method previously used to identify the turbulent/non-turbulent interface. Here, we seek to improve the interface detection procedure for experimental data by introducing a new method and to investigate the effect of FST on the interface properties.

An active grid ($M = 10$ cm, where M is the mesh grid length) was placed at the entrance of a water channel ($18M$ width $\times$ $110M$ length) to generate FST, which interacts with a TBL growing beneath it. The channel was filled to a height of $2.2M$. Three different operational sequences were utilized to run the active grid, resulting in three different cases referred to as 'A', 'B', and 'C' in the order of increasing turbulence intensity. Planar PIV measurements were performed in streamwise–wall-normal planes by capturing 3000 image pairs for each test case. Several locations downstream of the grid, i.e., $55M$, $65M$, $72M$, and $85M$, were tested to be able to comment on the streamwise evolution of the interface properties.

Contour lines of constant velocity are commonly used to demarcate the boundaries of uniform momentum zones in TBLs. The method introduced here identifies a constant velocity threshold for each instantaneous field, whose continuous contour line marks the interface between the instantaneous TBL and FST (see figure 1a for an example). Two physical assumptions are employed to identify the velocity thresholds, (1) the interface should pass through regions of high-shear events, (2) the FST and TBL encompass different vortical structures; hence, the spanwise vorticity distributions on both sides of the interface should differ from one another considerably. In the first step, the positive wall-normal gradient of streamwise velocity is conditionally averaged on the contour lines of various constant velocities. Figure 1b shows an example of the conditionally averaged gradient profile. The peaks in this plot are identified as the candidate velocities for the instantaneous threshold value as their contour lines pass through a series of high-shear events. In the next step, beginning from the highest candidate velocity, the vorticity distribution in a region between the contour lines of two consecutive candidate velocities, e.g., R2 in figure 1c, is quantitatively compared to the vorticity distribution in the region above the top contour line, e.g., R1 in figure 1c. If the difference is higher than a threshold, then the top contour line is chosen as the interface, separating the instantaneous FST from TBL. Otherwise, the higher candidate velocity is discarded and the next two are tested. Figure 1d shows the distributions of the vorticity in different regions shown in figure 1c. Although the vorticity distributions in R1 and R2 are almost identical, R3 is considerably different than R1+R2. Thus, the region above the blue contour line in figure 1c is considered the instantaneous FS, while R3 belongs to the instantaneous TBL. This process is repeated for all the instantaneous velocity fields of all cases to identify the instantaneous interfaces, which are field specific.

It is observed that increased FST intensity broadens the distributions of the velocity threshold values, indicating the necessity of the identification of instantaneous threshold values instead of using a constant threshold value. Tracking the location of the interface shows that increased FST intensity generally pushes it toward the wall and increases the jump in the vorticity across the interface (not shown here for brevity).

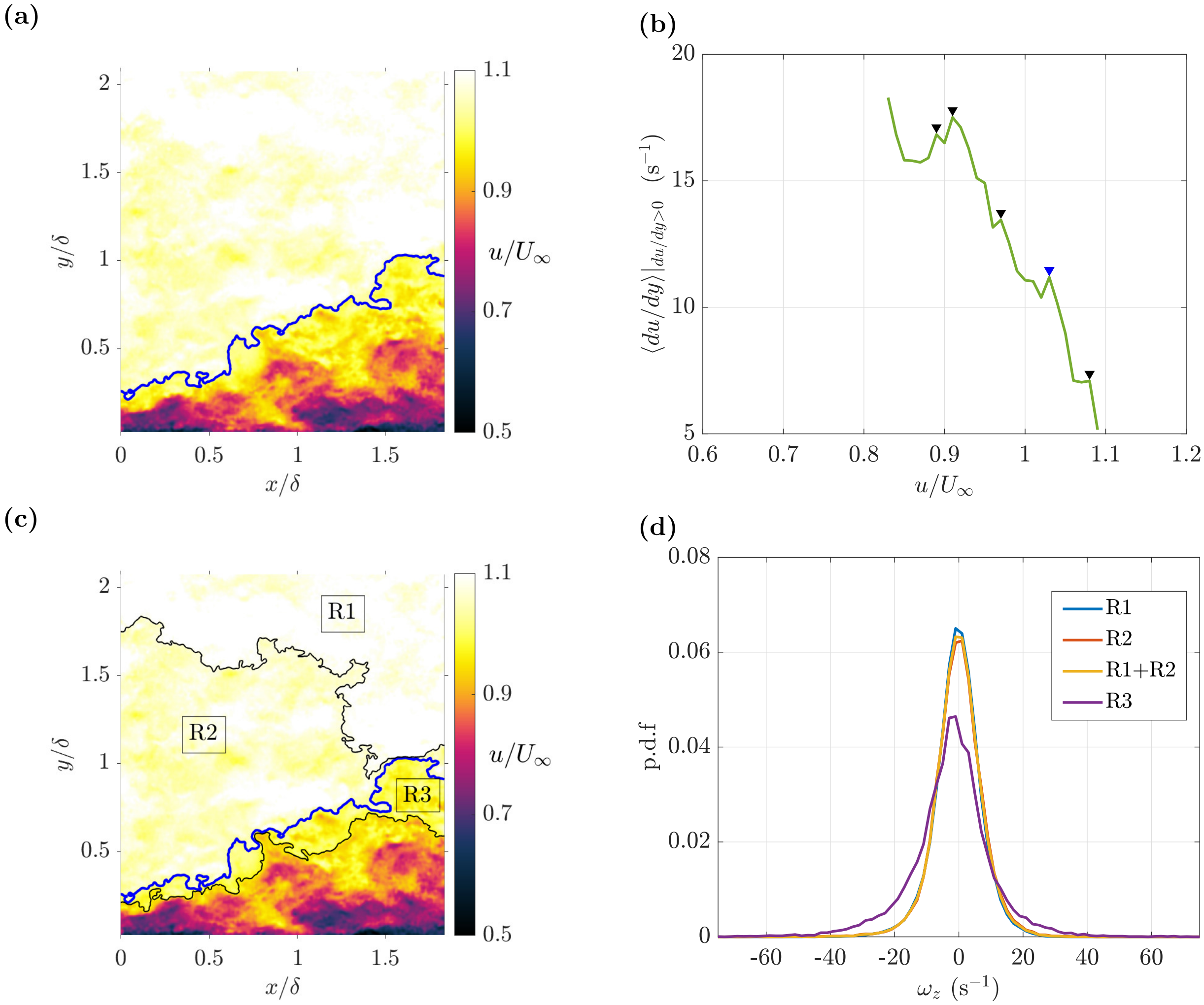

Figure 1: (a) An instantaneous streamwise velocity field of case C with the interface between FST and TBL marked by the contour line of $u_{th}/U_\infty = 1.03$ (the blue line). (b) Candidate velocity threshold values (marked by ▼), identified as peaks in the profile of Wall-normal gradient of streamwise velocity conditionally averaged along the continuous contour lines of constant velocity. (c) the same field as (a) with continuous contour lines of the three highest candidate velocities in (b), i.e., $u/U_\infty = 1.08$, 1.03, and 0.97. R1 indicates the region bounded by the outermost contour line and the top of the field, while R2 and R3 indicate the regions bounded by the consecutive contour lines. (d) Distributions of the vorticity in different regions of (c).

References

[1] Wu X., Wallace J.M. and Hickey J.P., (2019), Boundary layer turbulence and freestream turbulence interface, turbulent spot and freestream turbulence interface, laminar boundary layer and freestream turbulence interface, *Physics of Fluids, vol. 31, p. 045104*

[2] You J. and Zaki T.A., (2019), Conditional statistics and flow structures in turbulent boundary layers buffeted by free-stream disturbances, *Journal of fluid Mechanics, vol. 866, pp. 526-566*

[3] Hearst R.J., de Silva C.M., Dogan E. and Ganapathisubramani, B., (2021), Uniform-momentum zones in a turbulent boundary layer subjected to freestream turbulence, *Journal of fluid Mechanics, vol. 915, p. A109*

Transfer mechanism of a passive scalar in grid turbulence with mean scalar gradient

M. Wang [1], T. Yurikusa [1], K. Iwano [1], Y. Sakai [2], and Y. Ito [1]

[1] Graduate School of Engineering, Nagoya University, Nagoya, Japan
[2] Nagoya Industrial Science Research Institute, Nagoya, Japan

key-words: Grid Turbulence, Numerical Simulation, Scalar Transfer, Structure Function

Scalar diffusion and mixing in turbulence are seen in a wide variety of industrial and environmental flows. Therefore, fundamental understanding of scalar transfer in turbulence is of great importance. In particular, when a scalar is introduced to the flow field under a non-premixed condition, its transport becomes a multi-scale process dominated by the velocity field, which necessitates the multi-scale analysis of scalar field. In this study, we perform DNSs of grid turbulence with mean scalar gradient and conduct scale-by-scale analysis to reveal interscale transfer of passive scalar. Figure 1 (a) shows a schematic view of the computational domain as a rectangular box with dimensions $L_x \times L_y \times L_z = 32M \times 6M \times 6M$, where M is the mesh size of the grid as defined in Fig. 1 (b). Here, x, y, and z represent streamwise, vertical, and spanwise directions, respectively. A uniform flow of $U_0 = 1$ was supplied from the inlet. The initial concentration of a passive scalar was set to $C = C_0 = 1$ for the upper-half layer of the stream and $C = 0$ for the lower-half. The Reynolds number based on M and U_0 was set to $Re_M = 5000$ and 9000.

$$\underbrace{\frac{\partial \delta c^2}{\partial t}}_{4A_{t,c}} + \underbrace{\left(\frac{\langle U_k\rangle + \langle U_k'\rangle}{2}\right)\frac{\partial \delta c^2}{\partial X_k}}_{4A_c} + \underbrace{\frac{\partial \delta u_k \delta c^2}{\partial r_k}}_{4\Pi_c} + \underbrace{\frac{\partial \langle \delta U_k\rangle \delta c^2}{\partial r_k}}_{4\Pi_{U,c}} = \underbrace{-2\delta c \delta u_k \frac{\partial \delta \langle C\rangle}{\partial r_k} - (u_k + u_k')\,\delta c \frac{\partial \delta\langle C\rangle}{\partial X_k}}_{4P_c} \quad (1)$$

$$\underbrace{-\frac{\partial}{\partial X_k}\left(\frac{(u_k + u_k')\,\delta c^2}{2}\right)}_{4T_c} + \kappa[\underbrace{2\frac{\partial^2}{\partial r_k^2}}_{4D_\kappa} + \underbrace{\frac{1}{2}\frac{\partial^2}{\partial X_K^2}}_{4D_{X,\kappa}}]\delta c^2 \underbrace{-2\kappa\left[\left(\frac{\partial c}{\partial x_k}\right)^2 + \left(\frac{\partial c'}{\partial x_k'}\right)^2\right]}_{4\chi}$$

The scale-by-scale scalar(SBSS) equation is derived[1, 2], and employed in the DNS data to evaluate the interscale transfer between two points x_k and x_k' as shown in Eq. (1). The superscript $'$ indicates the values at x_k'. The symbol $\langle \cdots \rangle$ indicates the time average. Moreover, $\delta\langle U_k\rangle = \langle U_k\rangle - \langle U_k'\rangle$, $\delta\langle C\rangle = \langle C\rangle - \langle C'\rangle$, $\delta u_k = u_k - u_k'$, $\delta c = c - c'$, $X_k = (x_k + x_k')/2$, and $r_k = x_k - x_k'$. For clarity, $\langle U_k\rangle$ is the k-th component of the mean velocity vector; $\langle C\rangle$ is the mean scalar; u_k is the k-th component of the fluctuation velocity vector, and c is the scalar fluctuation. Additionally, A_c in Eq. (1) is the advection of δc^2 by the mean flow; Π_c is the nonlinear transfer term; $\Pi_{U,c}$ is the linear transfer term; P_c is the turbulent production term; T_c is the turbulent transport term; D_κ is the molecular diffusion term in the r space; $D_{X,\kappa}$ is the molecular diffusion term along X; χ is the scalar fluctuation dissipation, and $A_{t,c}$ is the residual. The results of circumferentially average terms in the SBSS equation at $x/M = 10, Re_M = 5000$ are shown in Fig. 2 (a). The superscript a means the circumferential average. The axis of abscissa represents the radial position in the spherical coordinates r normalized by λ. Particularly, the nonlinear transfer term Π_c becomes negative at large scales $r/\lambda > 4$(inverse cascade occurs), while it is positive at small scales. The decomposition of the nonlinear transfer term Π_c(Figs. 2 (b)(c)) reveals that the y component, especially the component $\Pi_{c,y2} = \delta v \delta c\,(\partial c/\partial y + \partial c'/\partial y')$ plays a dominant role in this process. Here, $\Pi_{c,y2}$ consists of δv, δc, and $(\partial c'/\partial y' + \partial c/\partial y)$, and all terms can take both positive and negative values. Therefore, to identify the couplings of the terms causing the negative flux of the non-linear term, the probability of each coupling was calculated. Figure 3 (a) shows the probability of couplings between terms consisting of $\Pi_{c,y2}, P(\omega_i)$, where ω_i is the event of each coupling. The first, second, and third signs of each coupling at the axis of abscissa in the figure are the signs for δv, δc, and $(\partial c'/\partial y' + \partial c/\partial y)$, respectively. It is revealed that when the separation distance is large($r/\lambda = 6$), where the interscale scalar transfer is inverse (small to large scales), the direction of the scalar flux is determined by the vertical velocity fluctuation difference between two points $(\partial c/\partial y + \partial c'/\partial y')$ since the mutual sign of the events of coupling $(+--)$ and $(-+-)$ is the third one. The conditional average results based on the event of coupling $(+--)$ (the most significant event of coupling for inverse cascade at large scale) reveal that a negative scalar gradient always appears with the occurrence of the inverse cascade as shown in Fig. 3 (b). Further analysis shows that the existence of fluid mass with an unmixed scalar plays a vital role in the inverse cascade phenomenon.

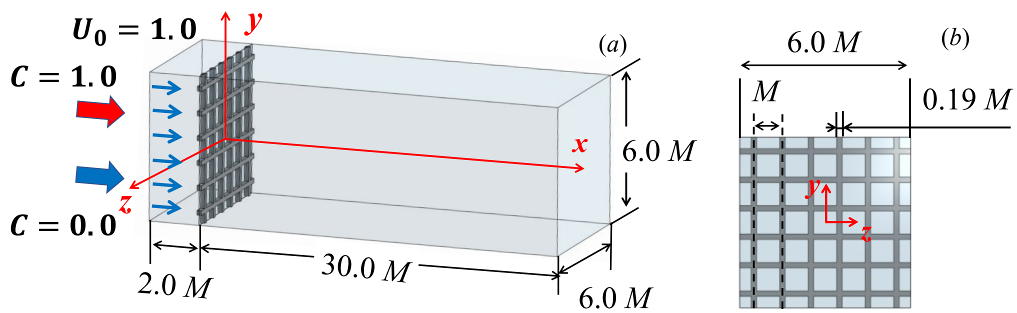

Figure 1: *Schematic view of (a) the computational domain and (b) the turbulence-generating grid.*

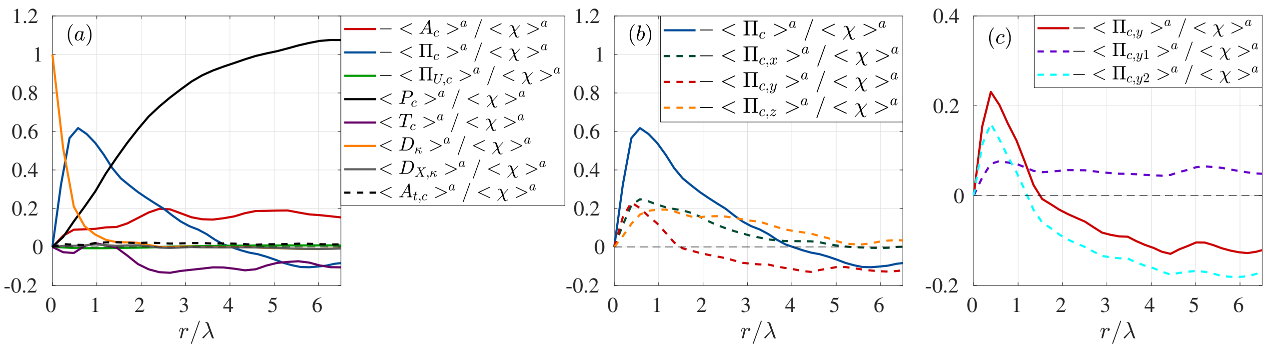

Figure 2: *Circumferentially average of (a) terms in SBSS equation, (b) decomposition of nonlinear transfer term* Π_c *and (c) decomposition of* y *component of the nonlinear transfer term* $\Pi_{c,y}$*, all the results are normalized by scalar dissipation rate* χ *at* $x/M - 10, Re_M = 5000$.

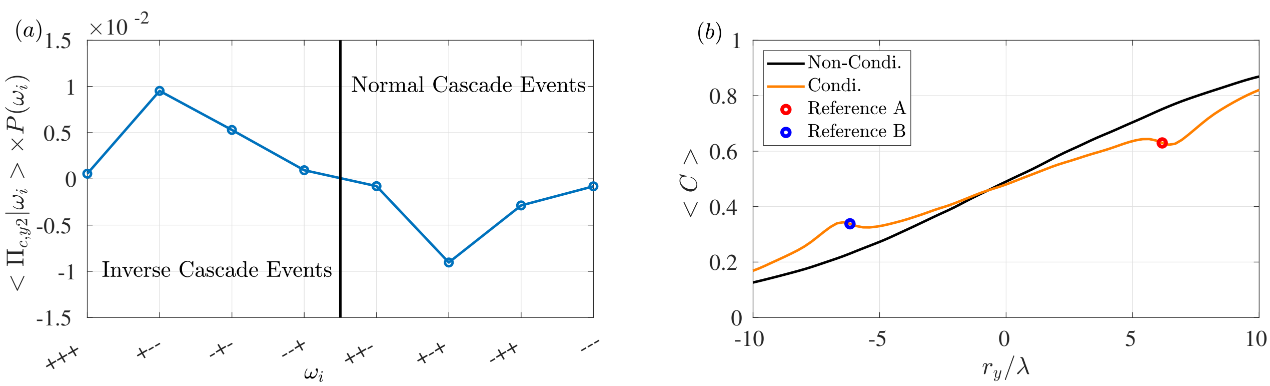

Figure 3: *(a) Conditional average of the component of nonlinear transfer term* $\Pi_{c,y2}$ *and (b) separation dependence of conditional average scalar concentration conditioned on the event* $(+--)$ *at* $r/\lambda = 6$.

References

[1] Hill R.J., (2002), Structure-function equations for scalars, *Physics of fluids, vol. 14, pp. 1745-1756*

[2] Vassilicos J.C., (2015), Dissipation in turbulent flows, *Annual review of fluid mechanic, vol. 47, pp. 95-114*

Phase proper orthogonal decomposition for analysis of spatio-temporal modal dynamics in a co-axial jet

Y. Zhang [1], A. Hodžić [1] and C. M. Velte [1]

[1] Department of Civil and Mechanical Engineering, Technical University of Denmark, Kongens Lyngby, Denmark

key-words: 4D Proper Orthogonal Decomposition, Turbulence, Jet, Experiment, Particle Tracking Velocimetry

Abstract:
Local energy transfer in the fashion suggested by Richardson, i.e., that energy is passed from large to small scales through interactions between scales of similar sizes, forms the basis for the cascade picture of the classical picture of turbulence [1], that is hypothesized to result in turbulence equilibrium [2]. The local energy transfer hypothesis appears to be valid to a good approximation in some turbulent flows (see e.g. [3]), while there is also evidence that non-local interactions exist in other stationary turbulent flows (see e.g. [4, 5]).

To gain more insight into the actual underlying processes of inter-scale energy exchange, we have established an experimental setup to generate stationary and non-stationary turbulent jet flows, see Figure 1 [6, 7]. Seeding micron-sized (air-filled) bubbles into the flow and illuminating them using high-power LEDs, four high-speed high-resolution cameras are used to record and reconstruct the flow field using Particle Tracking Velocimetry (PTV).

To be able to analyze these processes of energy exchange between scales, we have developed a *Phase Proper Orthogonal Decomposition (Phase POD) that can be used to analyze the spatio-temporal modal dynamics in both stationary and non-stationary turbulent flows.* In a non-stationary lid-driven cavity flow simulation [8], we found clear evidence of non-local energy transfer coupled to the non-stationarity in the analyzed flow.

In the current study, the stationary jet will be investigated for different velocity ratios between the inner jet flow and the outer (concentric) jet flow and analyzed using the new Phase POD method. The four-dimensional Phase POD modes will be visualized, and the local and non-local energy transfer results will be shown corresponding to different velocity ratios of the inner jet and the outer jet.

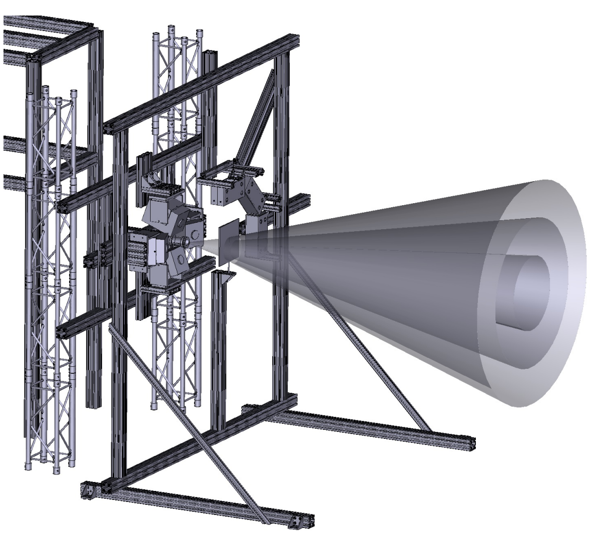

(a)

(b)

Figure 1: The experimental setup

References

[1] P.A. Davidson(2004): Turbulence: An Introduction for Scientists and Engineers, *OXFORD UNIVERSITY PRESS*

[2] Velte, C. M., and Buchhave, P. (2021): Dynamic triad interactions and non-equilibrium turbulence. *In R. Örlü, A. Talamelli, J. Peinke, and M. Oberlack (Eds.), Progress in Turbulence IX: Proceedings of the iTi Conference in Turbulence 2021 (pp. 3-12). Springer. Springer Proceedings in Physics Vol. 267*

[3] Couplet, M., Sagaut, P., and Basdevant, C. (2003): Intermodal energy transfers in a proper orthogonal decomposition–Galerkin representation of a turbulent separated flow, *Journal of Fluid Mechanics, 491, 275-284. doi:10.1017/S0022112003005615*

[4] Rubini, R., Lasagna, D., and Da Ronch, A. (2020): The l1-based sparsification of energy interactions in unsteady lid-driven cavity flow, *Journal of Fluid Mechanics, 905, A15. doi:10.1017/jfm.2020.707*

[5] Rubini, R., Lasagna, D., and Da Ronch, A. (2022): A priori sparsification of Galerkin models, *Journal of Fluid Mechanics, 941, A43. doi:10.1017/jfm.2022.318*

[6] S. L. Ribergaard, Y. Zhang, H. Abitan, J. S. Nielsen, N. S. Jensen, and C. M. Velte (2021): A novel laboratory pushing the limits for optics-based basic turbulence investigations, *14th International Symposium on Particle Image Velocimetry – ISPIV 2021*, Chicago, 137

[7] Y. Zhang, H. Abitan, S. L. Ribergaard, and C. M. Velte (2021): Volumetric velocimetry for small seeding tracers in large volumes, *14th International Symposium on Particle Image Velocimetry – ISPIV 2021*, Chicago, 194

[8] Y. Zhang, A. Hodzic, F. Evrard, B. Van Wachem, and C. M. Velte (2023): Phase proper orthogonal decomposition of non-stationary turbulent flow, *arXiv* https://arxiv.org/abs/2301.10462

Temperature assimilation for convective flows by convolutional neural networks

M. Mommert [1], C. Bauer [1] and C. Wagner [1,2]

[1] Department Ground Vehicles, Institute of Aerodynamics and Flow Technology, German Aerospace Center (DLR), 37073 Göttingen, Germany
[2] Institute of Thermodynamics and Fluid Mechanics, Technische Universität Ilmenau, 98684 Ilmenau, Germany

key-words: convection, assimilation, convolutional neural networks

Abstract:
The transport of heat in convective flows plays an important role in nature and in many technical applications. Precise predictions of such convective flows can be made in Direct Numerical Simulations (DNS), which require a substantial amount computing time and storage space. Thus, DNSs can only be used for predictions over comparatively short time periods and for flow problems, which can usually also be investigated in the laboratory due to their dimensions. A canonical laboratory experiment that is well suited for basic investigations of turbulent, thermal convection flows and the development of models is the so-called turbulent Rayleigh-Bénard convection, which occurs as a result of buoyancy forces in cells heated from below and cooled from above with adiabatic side walls.

Compared to the DNS, measurements can capture the velocity field over long periods of time. However, in order to be able to determine the heat transport in convective flows, additional spatial temperature measurements are typically carried out. Respective combined measurements are also very laborious and therefore only applied scarcely. In order to provide an estimated temperature distribution based on precise velocity field measurements, the assimilation of the temperature field from the velocity vector field is pursued. So far, the approach of extracting temperature fields based on the conservation laws has been explored [1]. At the same time, machine learning provides promising tools for regression tasks such as the one at hand [2].

Figure 1 introduces the approach investigated here: As model, a convolutional neural network with an encoder-decoder architecture is defined. It exploits the structural information of the velocity fields and uses order reduction to cope with noisy inputs. Subsequently, this model is trained with clippings of down-sampled data of a DNS conducted over a short time period, with the velocity components as input and temperatures as output. For validation or inference, the generated clips of the temperature field are joined overlapping each other. Thus, the model can be used to predict temperatures making use of velocity fields measured over long time periods.

As an exemplary result of the overlapping reconstruction, figure 2 displays a vertical center plane of the 3-dimensional Rayleigh-Bénard convection sample used as training example. From left to right, a down-sampled DNS velocity vector field and temperature field from the validation data set as well the respective temperature prediction are shown. The comparison of the temperature fields reveals that the prediction is visually well correlated with the DNS results.

At the conference, we will present a comparison of different design choices for the model to provide a base on which more universal and complex models can built.

References

[1] Bauer C., Schiepel D. and Wagner C., (2022), Assimilation and extension of particle image velocimetry data of turbulent Rayleigh–Bénard convection using direct numerical simulations, *Experiments in Fluids, vol. 63, no. 22*

[2] Brunton S. L., (2021), Applying machine learning to study fluid mechanics, *Acta Mechanica Sinica, vol. 37, pp. 1718-1726*

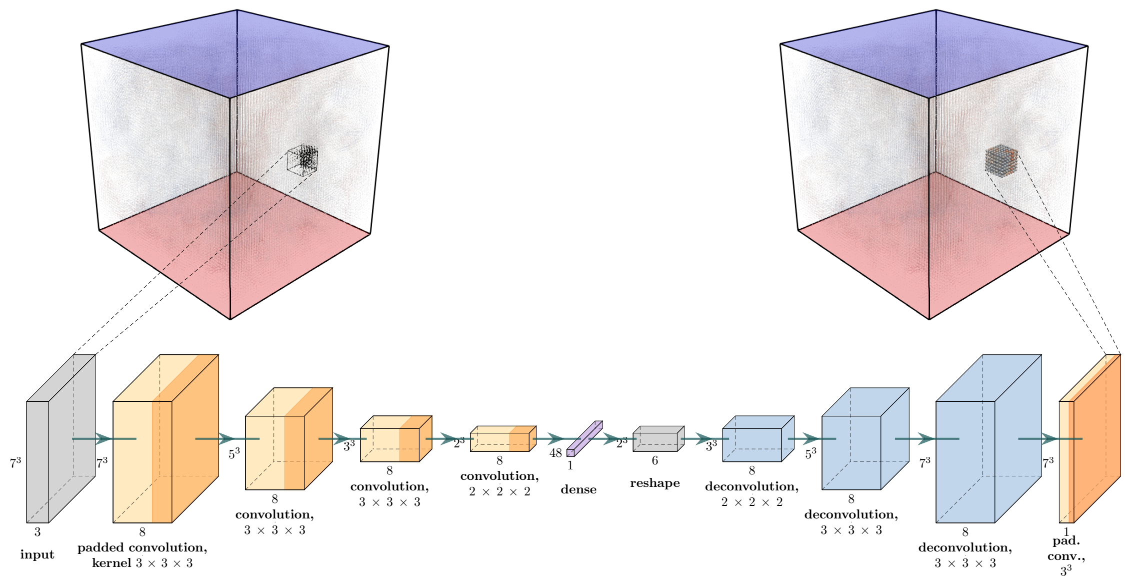

Figure 1: *Architecture of the encoder-decoder neural network, which is fitted to predict temperatures based on velocity information of clippings of the domain (Network visualization with PlotNeuralNet - 10.5281/zenodo.2526396).*

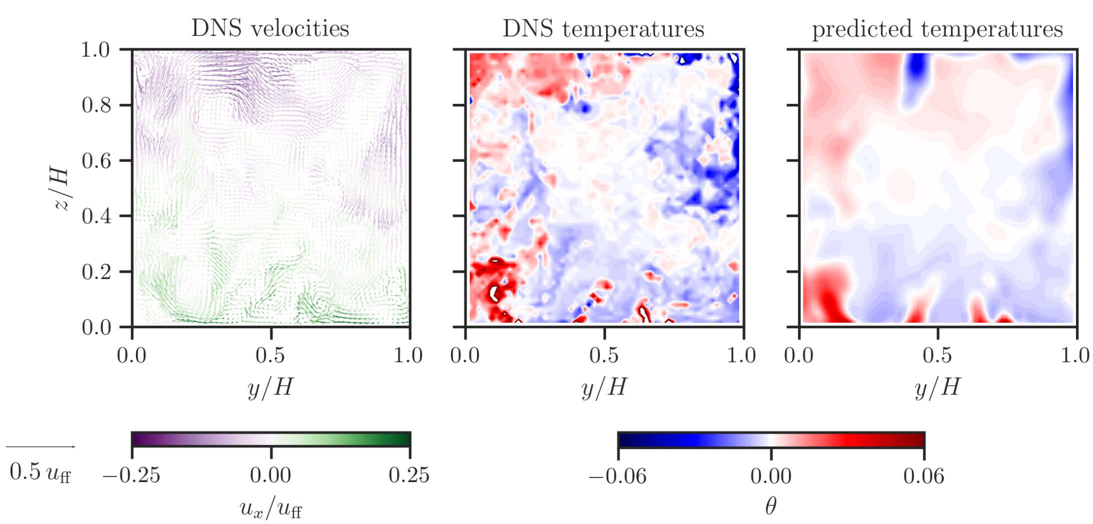

Figure 2: *Instantaneous velocity (left) and temperature (middle) data provided by the down-sampled DNS in a central vertical section of the sample compared to the overlapping reconstruction of the temperatures predicted by the neural network (right). The investigated case is characterized by the Rayleigh number* $Ra = 10^{10}$ *and the Prandtl number* $Pr = 6.9$. u_{ff} *indicates the free-fall velocity and* θ *constitutes the dimensionless temperature ranging from* -0.5 *to* 0.5.

Correlating free-stream turbulence structures to fluctuating loads on a cylinder in a turbulent cross-flow

Francisco J. G. de Oliveira [1], Zahra Sharif Khodaei [1] Oliver R. H. Buxton [1]

[1] Department of Aeronautics, Imperial College London, London, United Kingdom

key-words: turbulent length-scales, load fluctuations

Abstract:

The presence of freestream turbulence can both directly and indirectly induce fluctuating loads /deflections on a bluff body, exposed to a cross-flow; the latter by modifying the vortex shedding process within the bluff body wake [1]. In the present work, we report the correlation between different "flavours" of freestream turbulence and the fluctuating loads/deflections of a circular cylinder. Regardless of the influence of the free-stream turbulence, bluff bodies at sufficiently high Reynolds number produce turbulent wakes, in which several turbulent length/time scales exist concurrently and interact with the body's structure, imprinting these multi-scale physics into the structural response. This analysis will give more insight into the nature of the fluctuating loading acting on these structures imposed by both the conditions upstream and downstream of the structure as depicted in figure 1. A set of experiments is carried out in a water channel, combining simultaneous particle image velocimetry (PIV) measurements, strain measurements, using fibre optic distributed strain sensors (FODS), and load measurements using a 6-axis load cell, similarly to [2]. The cylinder with 50 mm diameter (⌀) is mounted as a cantilever beam, supported at one end, having 95% of its body submerged and exposed to the influence of the flow, as depicted in figure 2. Recent developments in structural health monitoring techniques using FODS [3] allow us to acquire fine details of the structural response of the cylinder to different flow conditions, with a fine spatial sensing distribution, enabling the extraction of the imprinted flow frequencies on the structure. Different "flavours" of background turbulence on the inflow section of the cylinder are produced by a set of turbulence-generating grids placed upstream of the body. The same combination of regular- and space-filling-fractal-grids will be used as in [1]. These were designed to explore a broad range of the TI, L parameter space of the freestream turbulence, where TI is the turbulence intensity and L is the integral length scale. Essentially, two fields of view (FOV1 and FOV2 represented in figure 3) will be used to correlate the influence of L_{12} and L_{13} (see figure 1) to the strain and load signal acquired by the FODS network and load cell. The fluctuations in the load and cylinder deflection signal observed are directly influenced by the impact of freestream turbulence on the structure. Yet the present analysis will allow us to infer the influence of the spanwise de-correlation of vortex shedding modes and the introduced obliqueness of the vortex shedding introduced by the freestream turbulence [1] on the fluctuating loads and deflections on/of the cylinder. Further, we will assess the influence of shedding identity loss events, detailed in [1], on the fluctuating loads/deflections of the cylinder.

References

[1] Krishna S Kankanwadi, Oliver R. H. Buxton, (2023), The influence of freestream turbulence on the near-field growth of a turbulent cylinder wake: turbulent entrainment and wake meandering, `10.48550/ARXIV.2301.10150`

[2] M. M. Cicolin, Oliver R. H. Buxton, G. R. S. Assi, P. W. Bearman, (2021), The role of separation on the forces acting on a circular cylinder with a control rod, *Journal of Fluid Mechanics.*

[3] Cheng Xu, Zahra Sharif Khodaei, (2020): Shape Sensing with Rayleigh Backscattering Fibre Optic Sensor, *Sensors*

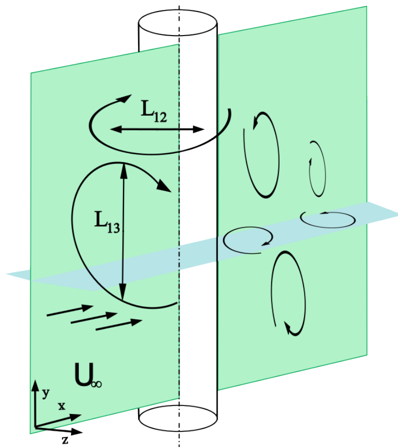

Figure 1: *Representation of multitude of scales present in the upstream section of the flow to analyse their influence on the structure.*

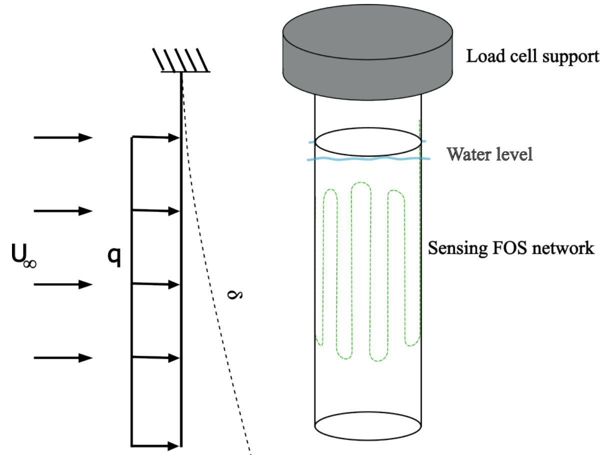

Figure 2: *On the left, representation of deflection, δ, in a simple cantilever test. q corresponds to the fluctuating distributed load acting on the cylinder's submerged surface. On the right, is a representation of the cylinder's distributed sensing network to acquire strain data around the surface of the cylinder.*

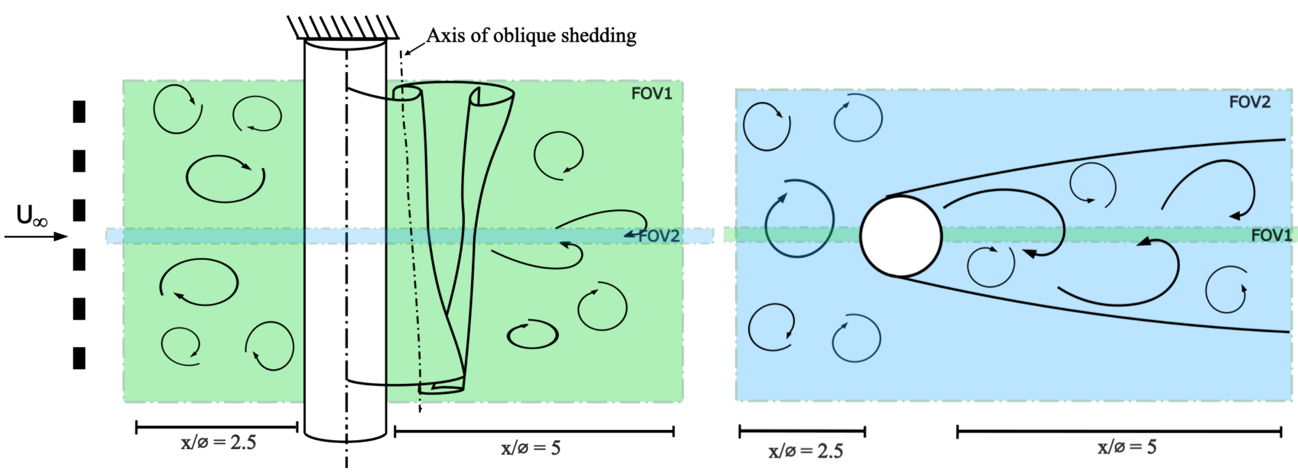

Figure 3: *Representation of the lateral and top plane of PIV data acquisition as well as their extent relative to the cylinder's diameter ⌀, where the acquired turbulent structures related with L_{13} and L_{12} respectively, the oblique vortex shedding (represented in the left figure) and spanwise de-correlation of vortex shedding modes will be correlated to the cylinder's response. Turbulence-generating grid and incoming flow represented on the left hand side of the figure.*

The role of background turbulence on the properties of a turbulent wake generated by different cylinders in a wind tunnel

F. Schmitt [1], M. Hölling [2] and J. Peinke [2] and M. Obligado [1]

[1] LEGI, Grenoble, France
[2] Institute for Physics, Carl-von-Ossietzky University, Oldenburg, Germany

key-words: energy cascade, turbulent wakes, self-similar flows

Abstract:

Wind energy is an important aspect of the renewable energy transition. However, the turbulence and velocity distributions in such wind farms are not only subject to atmospheric processes but also to the wakes of upstream wind turbines. These have in turn an impact both on the power curves and on the loads that act on the blades. In consequence, understanding turbulent wakes in atmospheric conditions is of great importance for the design of wind turbines and the efficiency of wind farms. The far wake of axisymmetric generators (like wind turbines) is usually modelled using the theory developed by Townsend and George [1, 2], that can predict streamwise scalings laws for different averaged quantities of turbulent wakes. It relies on the hypotheses of self-similarity and axisymmetry of averaged quantities and also requires a scaling for the kinetic energy dissipation rate ε. The latter is usually considered to evolve as 1,

$$C_\varepsilon = \frac{\varepsilon\, L}{u'^3}, \tag{1}$$

with u' the rms value of the streamwise fluctuating velocity and L the integral length scale of the flow. The dissipation constant C_ε is expected to be, according to the Richardson-Kolmogorov phenomenology, constant for a given set of boundary conditions and high Reynolds number based on the Taylor scale Re_λ. Nevertheless, it has recently been found that energy cascades at odds with such scalings may be present in turbulent wakes [3, 4]. Such non-equilibrium cascade presents a C_ε that is no longer constant, but evolves proportionally to $\mathrm{Re}_{\mathrm{global}}/\mathrm{Re}_{\mathrm{local}}$ (with $\mathrm{Re}_{\mathrm{global}}$ a Reynolds number that depends on the inlet properties of the flow and $\mathrm{Re}_{\mathrm{local}}$ one that depends on the local, streamwise dependent properties).

C_ε is therefore an important indicator of the properties of the energy cascade within the turbulent flow [4]. Interestingly, it has been found that different dissipation scalings lead to different power laws for the streamwise evolution of the averaged velocity deficit and the wake width. Evidence of both types of scalings has been found in the far wake of axisymmetric turbulent wakes [3, 5]. Nevertheless, most of this studies concern laminar inflows, and little attention has been payed to the properties of the energy cascade for different turbulent inflows.

In this contribution we propose a systematic study on the properties of such energy cascade for different inflows. We will report experimental results obtained using hot-wire anemometry in a wind tunnel using cylinders operated with different grid-generated inflows (using both active and passive grids). We will focus on the following two questions, that arise regarding the role of the turbulent wake within:

1. How does the wake structure (that we will quantify using C_ε, among other averaged quantities) differ under different inflow conditions (turbulence intensity/ integral length scale)?
2. How is the averaged shape of the wake (in terms of velocity deficit and wake width) related to the dissipation scaling for such different inflow conditions?

Three cylinders with different diameters are exposed to several turbulent as well as a laminar inflow. Turbulent inflows are created by a passive and an active grid, whereas the active grid is run in different modes (see figure 1). Due to this different operating conditions, values of turbulence intensity and integral length scales can be set independently within a certain range and mimic certain atmospheric conditions [6]. Given the symmetry present in the averaged wake of a cylinder, transversal profiles taken at different streamwise positions can be used to compute the averaged velocity deficit and the wake width. Measurements are taken in the range between $5\,D$ and $100\,D$. As detailed in previous works [3, 5, 7], such approach allows to test the hypotheses made within the Townsend-George theory, while characterising the averaged streamwise scalings and the energy cascade.

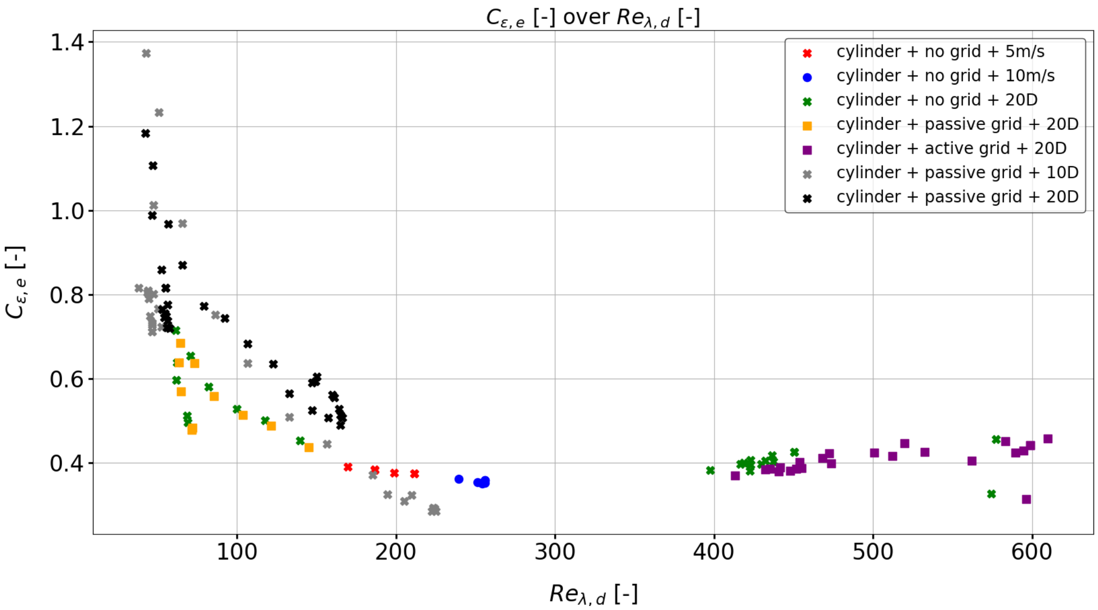

Figure 1: *C_ε as a function of* Re_λ *for the wake of one cylinder and different inflow conditions at different positions both in streamwise and in transversal directions. C_ε is constant for high* Re_λ*, approximately beginning at 200, suggesting the validity of the Richardson-Kolmogorov phenomenology in such conditions.*

References

[1] George W., (1989), Self-preservation of turbulent flows and its relation to initial conditions and coherent structures.

[2] Townsend A. A., (1949), The fully developed turbulent wake of a circular cylinder.

[3] Dairay T., Obligado M. and Vassilicos J. C., (2014), Non-equilibrium scaling laws in axisymmetric turbulent wakes., *Journal of Fluid Mechanics, vol. 781, pp. 166-195*

[4] Vassilicos J. C., (2015), Dissipation in turbulent flows., *Annual Review of Fluid Mechanics, vol. 47, pp. 95-114*

[5] Neunaber I., Peinke J. and Obligado M., (2021), Investigation of the dissipation in the wake of a wind turbine array., *Wind Energy Science, 2021, 13*

[6] Knebel P., Kittel A. and Peinke J., (2011), Atmospheric wind field conditions generated by active grids., *Experimental Fluids, vol. 51, pp. 471-481*

[7] Obligado M., Dairay T. and Vassilicos J. C., (2011), Nonequilibrium scalings of turbulent wakes., *Physical Review Fluids, vol. 1*

Scaling of Turbulent Moments in Compressible Axisymmetric Jets

Kenneth Y.-N. Hinh [1], Robert J. Martinuzzi[1] and Craig T. Johansen[1]

[1] Department of Mechanical and Manufacturing Engineering, University of Calgary, Calgary, Alberta, Canada

Keywords: Turbulent Jets, Self-Preservation, Particle Image Velocimetry (PIV), Compressible Turbulence

The influence of compressibility on turbulence attentuation and self-preservation of axisymmetric turbulent free jets is investigated. Second and third velocity moments containing the streamwise, u and radial velocity fluctuations, v, at Mach 0.3 and Mach 1.25 are obtained using 2-D planar Particle Image Velocimetry (PIV). A schematic of the free jet configuration is provided in figure 1. The third moments provide insights on the Reynolds stress transport. Of particular interest is capturing the influence of compressibility on Reynolds stress anisotropy, which remains an important challenge to the development of reliable turbulence models.

Using the jet half-width, b, and the centerline velocity, U_m, as length and velocity scales, the velocity profile collapses as observed in figure 3a. For self-preserving turbulent axisymmetric jets the Reynolds shear stress scales according to $\overline{uv} \propto U_m^2 db/dx$ [1]. Our recent study [2] have shown that in the compressible axisymmetric jet, the attenuation on the Reynolds shear stress and the shear layer thickness growth rate are proportional and similar to the planar mixing layer - allowing for a collapse of the Reynolds shear stress profiles as shown in figure 3b.

Although there is agreement on the behavior of $\overline{uv}$ [3], the effect of compressibility on other turbulent moments remains unclear. By performing an order-of-magnitude analysis, self-preservation solutions of the Reynolds stress transport equation are investigated. For example, when the density-velocity correlations and the streamwise transport terms are insignificant, the transport equation for $\overline{uv}$ in the jet reduces to,

$$0 = -\left[U\frac{\partial \rho \overline{uv}}{\partial x}\right] - \left[\frac{1}{r}\frac{\partial}{\partial r}(r\rho\overline{uv^2})\right] - \left[\overline{u\frac{\partial p}{\partial r}}\right] - \left[\rho\overline{v^2}\frac{\partial U}{\partial r}\right] \tag{1}$$

where uppercase and overline variables indicate a temporal mean quantity, and lowercase variable indicates a fluctuating quantity. When all turbulent moments are assumed to have self-similar profiles, the reduced transport equation suggests for the second and third moments,

$$\overline{v^2} \propto U_m^2\left(\frac{db}{dx}\right)^2 \qquad\qquad \overline{uv^2} \propto U_m^3\left(\frac{db}{dx}\right)^2 \tag{2}$$

scale with $(db/dx)^2$ instead of db/dx observed in Reynolds shear stress $\overline{uv}$, indicating that compressibility causes anisotropy in the turbulent moments through the spreading rate. As seen in figure 3c and 3d, the profiles of $\overline{v^2}$ and $\overline{uv^2}$ indeed collapse when scaled with $(db/dx)^2$. An analysis of the remaining turbulent transport equations will show that the attenuation of turbulent moments scales with $(db/dx)^n$, where n is an integer, providing insights into the anisotropy of the Reynolds stresses and third moments, especially $\overline{u^2}$ which differs from the behavior observed in the mixing layer [4]. Moreover, the analysis allows for the inference of the effect of pressure-strain correlations as related to compressibility. Comparisons between the supersonic and subsonic cases will be provided to highlight the influence of compressibility.

References

[1] George, W.K., (1988), *Advances in Turbulence, pp. 39-73*

[2] Hinh K. Y-N., Martinuzzi R.J., and Johansen C., (2022), *Proceedings of TSFP12, Osaka, Japan*

[3] Dimotakis, P.E., (1991), *Progress in Astronautics and Aeronautics, pp. 265-340*

[4] Freund, J.B., Lele S.K., Moin P. (2000), *Journal of Fluid Mechanics, vol. 421, pp. 229-267*

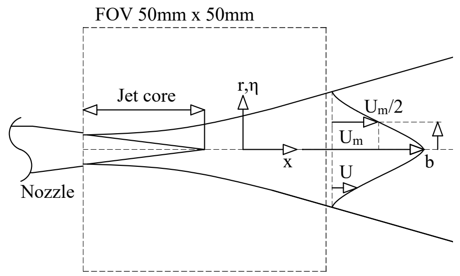

Figure 1: Schematic of Free Jet. Not to scale.

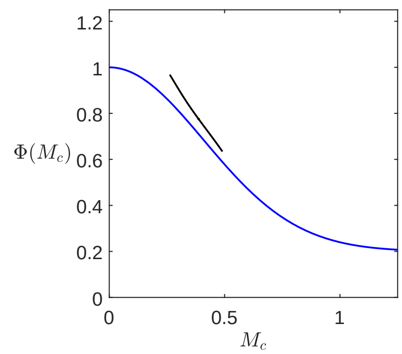

Figure 2: Spreading rate due to compressibility $\Phi(M_c) = b'/b'_0$ where b'_0 is the incompressible rate. Current study (—) and literature (—) [3].

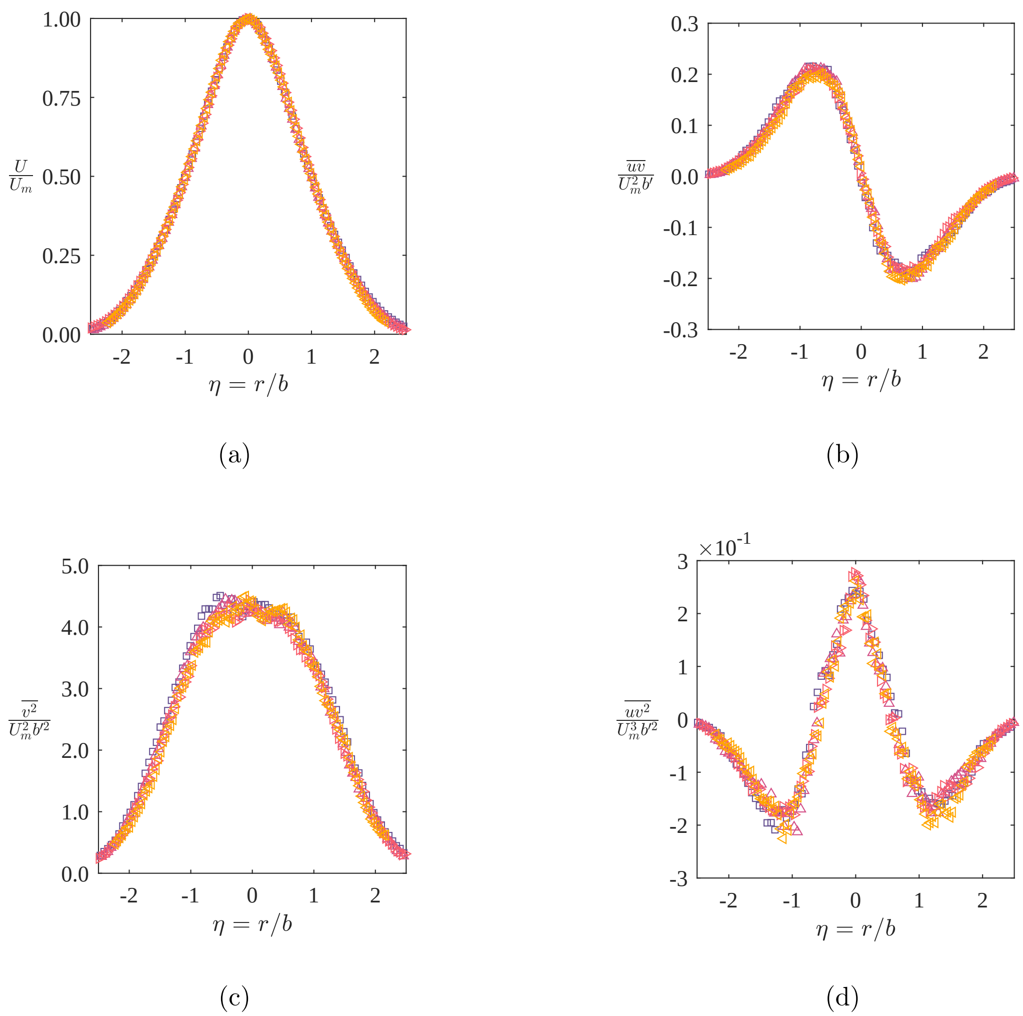

Figure 3: Mach 1.25 Jet. Axial positions x/d = 17.5 (□); 20.0 (△); 22.5 (◁); 25.0 (▷). Where b' db/dx. Every third point is shown for clarity.

Spectral analysis of the spatially evolving turbulent channel flow

Ezhilsabareesh Kannadasan [1], Callum Atkinson [1] and Julio Soria [1]

[1] Laboratory for Turbulence Research in Aerospace and Combustion (LTRAC),
Department of Mechanical and Aerospace Engineering, Monash University,
Melbourne, Victoria 3800, Australia.

key-words: Turbulence simulation, Turbulence theory

Abstract:

The elementary structures of wall turbulence that carry most of the kinetic energy and momentum are typically reffered to as energy-containing eddies (energy-eddies). Despite the general agreement that energy-eddies can sustain themselves at all relevant length scales [1, 2, 3], their exact genesis and spatial evolution are still not well-understood. In this study, energy-eddies at the inflow of a turbulent channel flow direct numerical simulation (DNS) are quenched and the spatial development of these eddies is studied. Two synchronised DNSs are used in the current study: one is a fully resolved streamwise periodic channel flow, which is subsequently denoted by PCH-DNS, while the other is a fully resolved channel flow DNS with inflow–outflow boundary conditions, which will be denoted by IOCH-DNS. In the IOCH-DNS the inlet boundary condition is an inflow velocity field, which is a filtered version of the inflow of the PCH-DNS, with a convective outflow boundary condition applied at the domain exit [4]. The results demonstrates that energy-eddies are essential to maintain the eddies involved in the energy cascade. The streamwise velocity spectra of the developing flow begin to recover at a spanwise wavelength of $\lambda_z^+ \simeq 100$, which is equal to the near-wall spacing of the streaks in the buffer layer at $y^+ \simeq 15$, whereas there are no active vortical motions in the streamwise vorticity spectra until the energy at the wall-normal streak location of $y^+ \simeq 15$ is re-established. This is consistent with the qualitative observation from the iso-surface of an instantaneous field shown in figure 1. It is evident from this visualisation that the energy-eddies, which are a combination of the streaks and streamwise vortices, are removed from the neighbourhood of the inflow of the IOCH-DNS, with the energy-cascade eddies at the inflow initially decaying in the streamwise direction. There is no evidence of the streaks or active vortical motions until $x > 3h$, where streaks start to reappear, while vortical motions only start to become active for $x > 12h$. Hence, the spectral analysis of velocity and vorticity in the present study demonstrates that in a spatially evolving flow, the formation of near-wall streaks is the primary process necessary in the recovery of energy-eddies in a turbulent channel flow.

References

[1] Flores, O., and Jimenez, J ., (2006), Effect of wall-boundary disturbances on turbulent channel flows, *J. Fluid Mech., 566, 357-376.*

[2] Flores, O., and Jimenez, J ., (2007), Vorticity organization in the outer layer of turbulent channels with disturbed walls flows, *J. Fluid Mech., 591, 145-154.*

[3] Hwang, Y., and Cossu, C., (2010), Self-sustained process at large scales in turbulent channel flow, *Phys. Rev. Lett. 105 (4), 044505.*

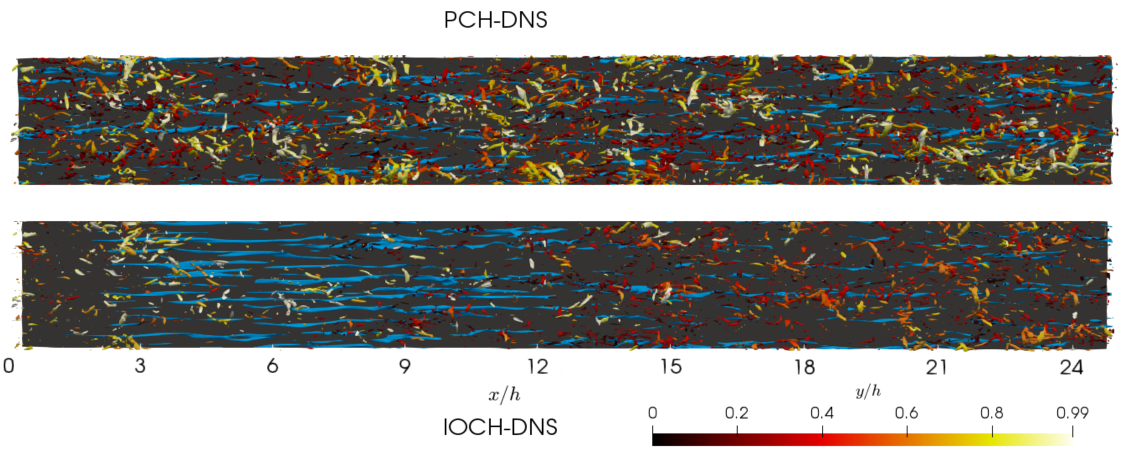

Figure 1: Vortices and low-speed structures visualised by the iso-surfaces of the second invariant of the velocity gradient tensor, $Q_A/\langle Q_W \rangle = 3$, the colour represents the distance from the wall, and the streamwise fluctuating velocity, $u^+ = -0.5$ in blue, respectively. The flow is from left to right.

[4] Kannadasan, E., Atkinson, C., and Soria, J., (2023), Spectral analysis of the evolution of energy-containing eddies, *J. Fluid Mech., 955, R1.*

Characterisation of multi-scale rough surfaces for turbulent drag prediction

A. Ramani [1], L. Schilt[1], B. Nugroho[1], A. Busse[2], T.O. Jelly[1], J.P. Monty[1], N. Hutchins[1],

[1] Department of Mechanical Engineering, University of Melbourne, Parkville, Victoria, Australia
[2] James Watt School of Engineering, University of Glasgow, Glasgow, U.K.

key-words: Turbulent Boundary Layers, Roughness

Abstract:

The presence of surface roughness on walls adjacent to turbulent boundary-layers incurs a drag penalty. Predicting this penalty directly from the measurable properties of the roughness topography is highly desirable as it avoids the need for costly experiments or simulations. One such property is Effective Slope (ES) which is the mean streamwise gradient of the topography. Many studies have shown that ES is a key metric for drag prediction in both the transitionally and fully rough regimes of the flow [1]. However, when it comes to practical multi-scale surfaces, ES can display an unbounded behaviour. This is shown by an example surface (Fig. 1a) that obeys a power-law relationship (exponent of -1.64), which is typical for many naturally occurring surfaces [2]. At different resolutions, Δx, the fractal like nature of this surface results in an almost unbounded value of ES even as other measures converge (Fig. 1b). This is because of the integrated effect of small-scale, high-slope roughness features, which results in artificially high values of ES and leads to erroneous drag prediction. Thus, to reliably use ES, some flow based filtering of the surface, perhaps based on the viscous length scale (ν/U_τ), is required. To this end, experiments were carried out using a set of rough surfaces derived from a single numerically generated height map (multi-scale, Gaussian roughness with $ES \approx 0.13$) shown in Fig. 2a. From this height map, physical surfaces are machined using a CNC router. By systematically increasing the step-over distance of the ball-nosed tool, the ES is increased over the underlying numerical case via the increase in the heights of the machining artefacts known as 'scallops' (Fig. 2d). The benchmark case (machined with the smallest step-over) is nearly identical to the numerical surface (Fig. 2b), with a maximum scallop height $k_{\text{scallop}} \sim 0.4\nu/U_\tau$. For the other cases, k_{scallop} ranges from $0.4 \lessapprox \nu/U_\tau \lessapprox 13$. The relative increase in the drag penalty (ΔC_f) for each case over the benchmark case is shown in Fig. 2e. Despite an increase in the measured ES, the drag curves are seen to follow the benchmark case up to a certain Re, and only show an increase in drag when $k_{\text{scallop}} \gtrapprox 2\nu/U_\tau$ (Fig. 2f). Further, even when the small steep scales exceed this threshold, they do not contribute to the drag penalty in the same manner as the large steep features. These findings suggest that for the reliable use of ES for drag prediction over multi-scale surfaces, some flow dependant filtering of the topography is required.

References

[1] Napoli E., Armenio V. and De Marchis M., (2008), The effect of the slope of irregularly distributed roughness elements on turbulent wall-bounded flows, *J. Fluid Mech., vol. 613, pp. 358-394*

[2] Anderson W. and Meneveau C., (2011), Dynamic roughness model for large-eddy simulation of turbulent flow over multiscale, fractal-like rough surfaces, *J. Fluid Mech., vol. 679, pp. 288-314*

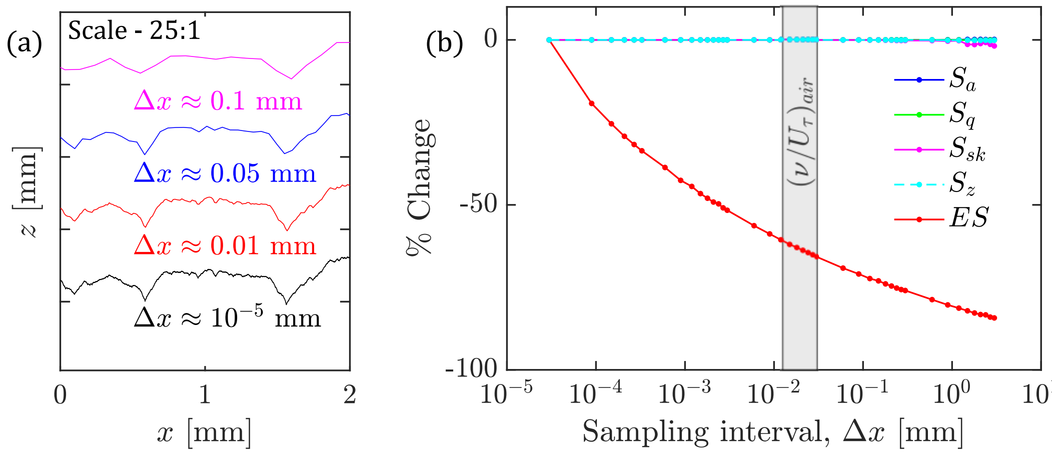

Figure 1: *(a) A synthetically generated roughness profile, z(x), plotted with various sampling intervals,* Δx *(offset to enable comparison). (b) Relative change in the various roughness statistics from the value computed at the smallest* Δx*. The shaded patch indicates the typical extents of the viscous length scale for air in experimental facilities.*

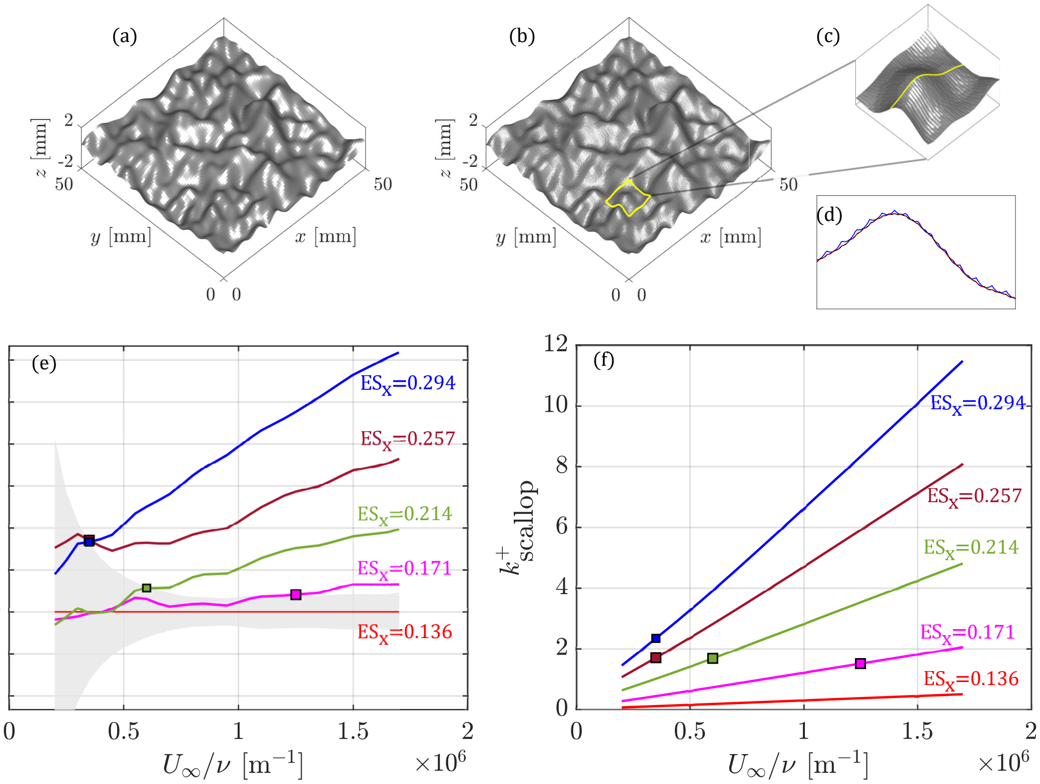

Figure 2: *(a) Sample of the numerically generated surface; (b) The machined benchmark case; (c) Scallops on the machined surface; (d) Roughness profile along the line marked in (c) for step-over distances of 0.25 mm (black) and 0.5 mm (blue); (e) Relative increase in* $\overline{C}_f$ *over the benchmark case* ($ES_x = 0.136$)*. The gray area is the measurement uncertainty for the benchmark case and the square symbols mark the point where each case exceeds this uncertainty; (f) Viscous scaled scallop height* ($k^+_{\text{scallop}} \equiv k_{\text{scallop}} U_\tau/\nu$) *for each case. The square symbols correspond to those in (e).*

Jet flow feature estimation with snapshot PIV and fast probes

L. Franceschelli*, , M. Raiola, S. Discetti

Department of Aerospace Engineering, Universidad Carlos III de Madrid, Av. de la Universidad 30, Leganés, 28911, Spain

key-words: Flow estimation, Jet flows, Data-driven techniques, Low-order modeling

Abstract:
Time-resolved Particle Image Velocimetry (PIV) measurements are often difficult to obtain due to hardware limitations and cost. A cheap alternative, proposed in recent years, is to enhance the temporal resolution of snapshot (i.e. non-time-resolved) PIV with point-wise high-repetition-rate probes. In this sense, Extended Proper Orthogonal Decomposition (EPOD) demonstrated to be a valuable approach for turbulent flow field estimation [1]. EPOD establishes the correlation between two simultaneous measurements in a reduced-order domain, thus focusing on the most significant features measured by PIV and by the probes. The flow fields are reconstructed estimating the POD mode time coefficients through the correlation with the temporal modes of the point measurements. This approach has been applied in several configurations, including wall-bounded flows and high-Reynolds number pipe flow [2]. In the last decade, machine-learning-based methods have been also tested, providing even better results, fostered by the capability to model non-linear relations between probes and flow field features [3].

In this work, we aim to exploit this principle to estimate the most significant flow features in a jet flows. The application of this technique to free-shear flows is made difficult by the complexity of embedding the history in the estimation process and by the probe intrusiveness. Furthermore, the spectral richness of fully-turbulent flows represents a great challenge for flow field estimation based on a limited number of probes. Our objective is to explore different probe arrangements for flow field estimation, including hot-wire probes and microphones, as well as different estimation schemes, including EPOD and nonlinear methods, such as neural networks. In the following, the experiment is briefly described, with some preliminary results from the synchronized measurements.

The experiment is performed in the jet-flow facility of Universidad Carlos III de Madrid, installed inside an anechoic chamber. The jet is issued by a 3D-printed nozzle with an exit section diameter $D = 10$ mm. The bulk velocity is set equal to $V_b = 35$ m/s, providing a jet-flow with Reynolds Number $Re_d \simeq 23000$. Fig. 1 shows the experimental setup in two configurations, one with microphones and the other with hot-wire sensors.
In the first one, 3 pre-amplified electret microphones have been located in the jet-flow longitudinal mid-plane. In the second one instead, a wing-shaped rake of hot-wires is located $8D$ downstream the exit section of the nozzle in the jet-flow longitudinal mid-plane. In this preliminary experiment we are using 2 Dantec 55P11 hot-wires, while for the final conference contribution we are targeting the use of at least 5 probes. In both configurations, a planar non-time resolved PIV is performed.

Preliminary results in form of correlation maps of the hot-wire probes with the flow fields are reported in Fig. 2. It can be shown that the near-axis probe has a sharp correlation peak, thus suggesting that flow features can be estimated only to a limited extent in that region. The second probe, located in the shear layer, shows a wider correlation peak, thus suggesting the possibility to estimate flow features in the shear layer also well upstream of the probe location. In the conference contribution, we will include a study of the performance in estimating flow fields using hot-wire and microphones in different configurations and with different estimation algorithms.

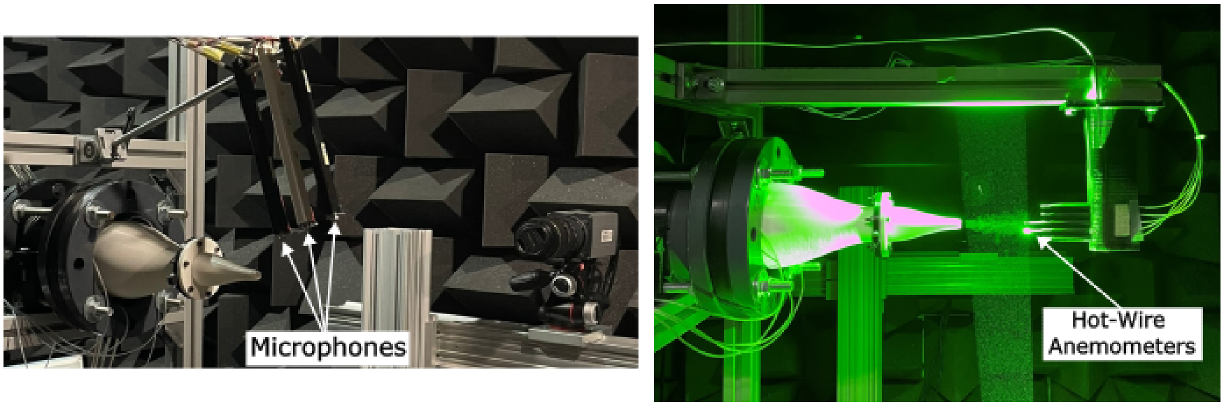

Figure 1: The two tested experimental configurations: on the left, the acquisition using three microphones; on the right, the one using two Hot-Wire Anemometers

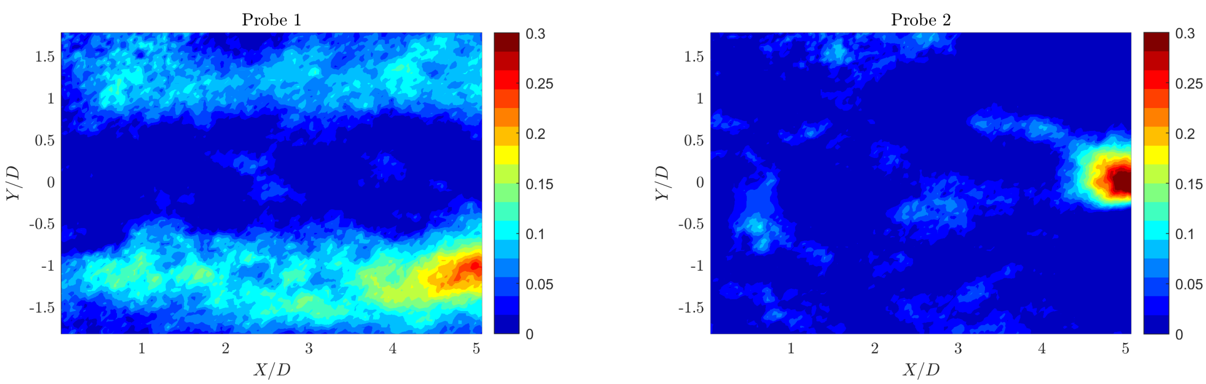

Figure 2: Correlation map between the snapshot PIV flow field and the Hot Wires measurements.

Acknowledgments
This project has received funding from the European Research Council (ERC) under the European Union's Horizon 2020 research and innovation program (grant agreement No 949085).

References

[1] J. Borée, (2003) Extended proper orthogonal decomposition: a tool to analyse correlated events in turbulent flows, *Experiments in Fluids, 35, 188-192, 2003*

[2] S. Discetti, G. Bellani, R. Örlü, J. Serpieri, C.S. Vila, M. Raiola, X. Zheng, L. Mascotelli, A. Talamelli, A. Ianiro, (2019), Characterization of very-large-scale motions in high-Re pipe flows, *Experimental Thermal and Fluid Science, 104, 1-8, 2019.*

[3] X. Jin, S. Laima, W. Chen and H. Li (2020), Time-resolved reconstruction of flow field around a circular cylinder by recurrent neural networks based on non-time-resolved particle image velocimetry measurements, *Experiments in Fluids, 61, 1-23, 2020*, Springer

Effects of sinusoidal riblets on turbulent boundary layer flow structures

G. Cafiero[1] , E. Amico[1], J. Serpieri[1] and G. Iuso[1]

[1] Department of Mechanical and Aerospace Engineering, Politecnico di Torino, Turin, Italy

key-words: 3D Riblets, PIV measurements, Turbulent boundary layer, Coherent structures

Abstract:
We experimentally investigate the effects of sinusoidal microgrooves on the flow structures developing in a zero pressure gradient turbulent boundary layer. The sinusoidal, or 3D riblets, have been found to be more effective than the widely investigated straight riblets [1, 2].

Particle image velocimetry measurements carried out in the streamwise-wall normal plane allow us to infer on the effect of sinusoidal riblets on the near-wall structures, such as hairpin vortices, along with their vorticity and wall distance. In addition to the proposed uplift mechanism induced by the straight grooves, the sinusoidal pattern is expected to introduce a further share of wall normal displacement, in agreement with the further share of drag reduction. Implementing a vortex detection method based on the second invariant of the velocity gradient tensor, we provide statistical evidence for this further uplift, in the case of the sinusoidal groove. Furthermore, the available data suggest that the spanwise vorticity associated to these structures is attenuated as an effect of the groove profile.

Starting from the PIV images acquired in the x-y plane, the identification of the vortical structures can be performed using several approaches ([3], [4]). In this case, it is carried out applying the Q-criterion, where Q corresponds to the second invariant of the velocity gradient tensor, defined as $Q = \frac{1}{2}(||\Omega||^2 - ||S||^2)$, and $||S||$ and $||\Omega||$ represent the traces of the symmetric and anti-symmetric components of the velocity gradient.

A representative snapshot of the smooth case is reported in figure 1 as colormap of the Q values with overlaid velocity vectors. As expected, the majority of the turbulence activity occurs near the wall, and in particular at values of $y/\delta < 0.1$. To statistically characterize the location of the near wall structures, a threshold is applied to the colormaps of Q. Only values of $Q > 1.5$ are considered as belonging to the vortex. Each vortex is then isolated and its centroid is therefore calculated, along with the vorticity values within its core.

The probability density function of the wall normal location is reported in figure 2a. The data show that the riblet geometry has an effect on the displacement of the near wall structures. In particular, the RLong case shows a displacement of the peak towards larger values of y/δ. Nevertheless, the greatest differences are evidenced by the RS1 case. While the Smooth and RLong cases are characterized by three separated peaks of the pdf, the RS1 shows that the majority of the structures are located at $y/\delta \approx 0.065$, thus evidencing a strong modification of the near wall structure of the boundary layer.

It is also interesting to notice that the RS2 case is instead characterized by a behaviour that is similar to the Smooth one, with the exception of the peak nearest to the wall. Indeed, the RS2 only features two peaks in the pdf, one at $y/\delta \approx 0.04$ and a second one at $y/\delta \approx 0.65$. This might suggest the existence of an optimal value of the riblet amplitude such that the structures are effectively uplifted. A larger parametric space is however needed as to investigate this aspect further.

Similarly, the pdf of the spanwise vorticity calculated across the identified vortices is reported in figure 2b. It is shown that, the sinusoidal riblet cases are in general characterized by attenuated vorticity values. This suggests that the sinusoidal riblet, differently from the longitudinal one, does not act only with an uplift mechanism; it also weakens the near wall structures in terms of the spanwise vorticity.

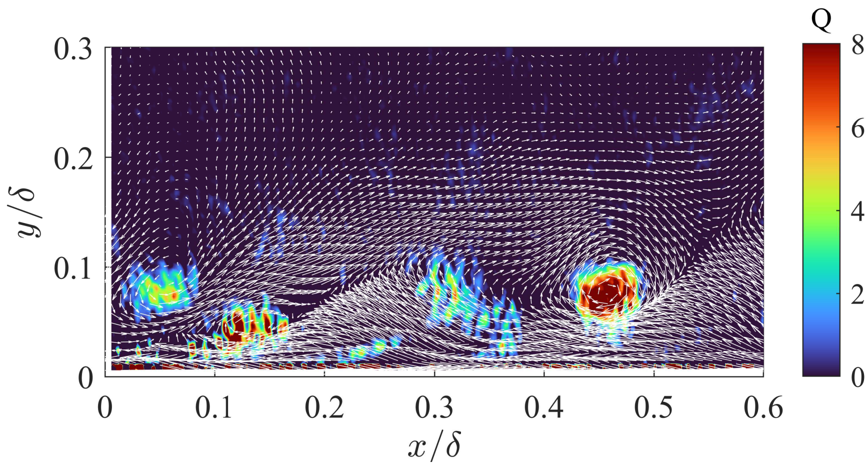

Figure 1: Colormap of the Q values with overlaid fluctuating velocity field measured in the Smooth case. To improve the readability of the plot, one each four vectors is reported.

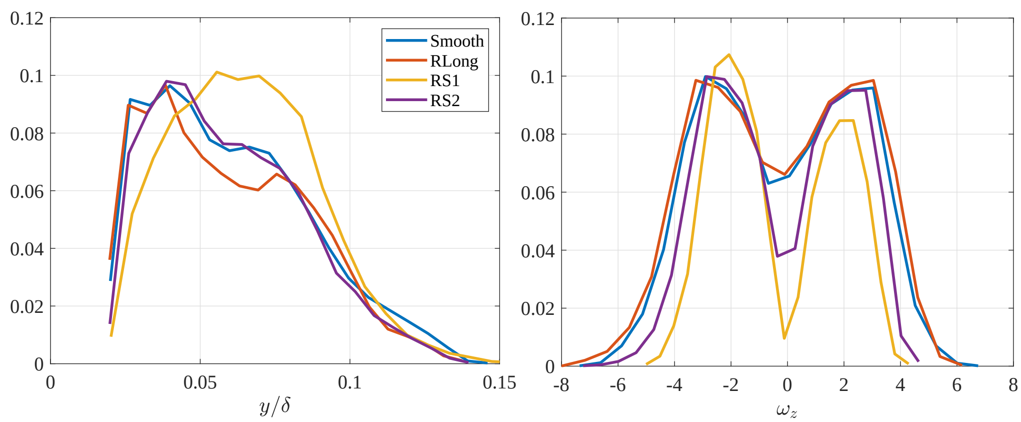

(a) (b)

Figure 2: Pdf of the wall normal distance of the vortices identified with the Q-criterion (a) and pdf of the spanwise vorticity (ω_z) calculated for the identified vorticies (b).

References

[1] Gioacchino Cafiero and Gaetano Iuso, (2022), Drag reduction in a turbulent boundary layer with sinusoidal riblets, *Experimental Thermal and Fluid Science, vol. 139, 110723*

[2] Yulia Peet and Pierre Sagaut, (2009), Theoretical prediction of turbulent skin friction on geometrically complex surfaces, *Physics of Fluids, vol. 21 (10), 10.1063/1.3241993*

[3] Jinhee Jeong and Fazle Hussain, (1995), On the identification of a vortex, *Journal of Fluid Mechanics, vol. 285, pp. 69-94*

[4] Fabrizio De Gregorio and Antonio Visingardi and Gaetano Iuso, (2021), An Experimental-Numerical Investigation of the Wake Structure of a Hovering Rotor by PIV Combined with a Γ2 Vortex Detection Criterion, *Energies, vol. 14, 2613*

Isolated roughness effect on boundary layer topology

Vitalii Yanovych [1], Daniel Duda [1], Václav Uruba [1,2] and Vasyl Sokolenko [3]

[1] University of West Bohemia, Pilsen, Czech Republic
[2] Institute of Thermomechanics, Czech Academy of Sciences, Prague, Czech Republic
[3] Czestochowa University of Technology, Czestochowa, Poland

key-words: Boundary layer, Isolated roughness, Shear layer, Topology of turbulence, Hot-wire anemometry

Abstract:
Currently, there is an increased focus on investigating the patterns of the boundary layer evolution above various surface roughness. This area of research encompasses numerous experimental, theoretical, and numerical studies. The size and roughness configuration significantly affect the evolution and topology of the boundary layer. For example, high roughness created perturbation of the flow, which leads to increased turbulence and boundary layer thickness. While slight roughness can contribute to a thinner and more stable boundary layer formation. Furthermore, the spatial distribution of roughness elements strongly influences the generation of turbulent eddies.

This study aims to investigate the boundary layer's topology under different densities of isolated roughness with zero pressure gradient. For this purpose, we employed three different surface conditions of roughness consisting of rectangular elements with uniform height arranged in staggered rows, covering the entire floor of the wind tunnel. The frontal and plan solidity for each roughness case varied. Additionally, we applied a smooth surface for comparison. During the experiment, the measuring cross-sections were positioned at varying distances from the inlet, while the free flow velocity remained stable $U = 5\, m{\cdot}s^{-1}$. It is noteworthy that, in all cases, the measuring position was located midway between the roughness elements (Fig. 1e). To determine the topology of the boundary layer in streamwise directions, we employed a 55P14 miniature hot-wire probe. The data obtained allowed us to estimate the patterns of mean velocity and turbulence intensity profiles for the various surface conditions.

The data collected clearly indicated that the presence of isolated roughness causes a significant distortion in the velocity profile (Fig. 1a). Furthermore, this trend intensifies as the distance between the roughness elements increases. This is especially noticeable in the area of roughness height. Moreover, there is a significant flow disturbance close to roughness height, as evidenced by the peaks of the turbulence intensity distribution (Fig. 1b).

This atypicality of the obtained data can be caused by presence of isolated roughness elements significantly influencing the character of the boundary layer flow. Once the fluid stream reaches the upstream side of such elements, the flow separates, giving rise to a recirculation zone in the wake (Fig. 1f). Subsequently, the separated flow reattaches downstream, creating a turbulent wake. This, in turn, leads to the formation of a shear layer, which is characterized by a significant velocity gradient and exhibits increased levels of turbulence intensity.

By considering turbulent vortices within shear layers to be large-scale, we employed autocorrelation analysis to estimate their integral length scale (Fig. 1d). Our results indicate a distinct enhancement in the size of the vortices, as evidenced by a sharp increase in data, immediately following the apex of the roughness in the direction of the free flow. Moreover, it can be assumed that growing the distance between isolated rough elements increases the velocity gradient. Because, as the velocity gradient across the shear layer increases, the size and energy of the vortices in the flow start to be higher, leading to an increase in the integral length scale. Thus, formed eddies are often referred to as the "shear-layer eddies" and are typically the largest and most energetic contained. As they approach the edge of the shear layer, they can become unstable and breakdown into the free stream. The reliability of the above is confirmed by comparative analysis between the integral length scale and streamwise skewness distribution, where the lowest skewness is usually associated with the vortex breakdown point. Consequently, the obtained data for rough surfaces show that the maximum of the integral length scale (Fig.1d) and the minimum of the skewness (Fig.1c) clearly coincide.

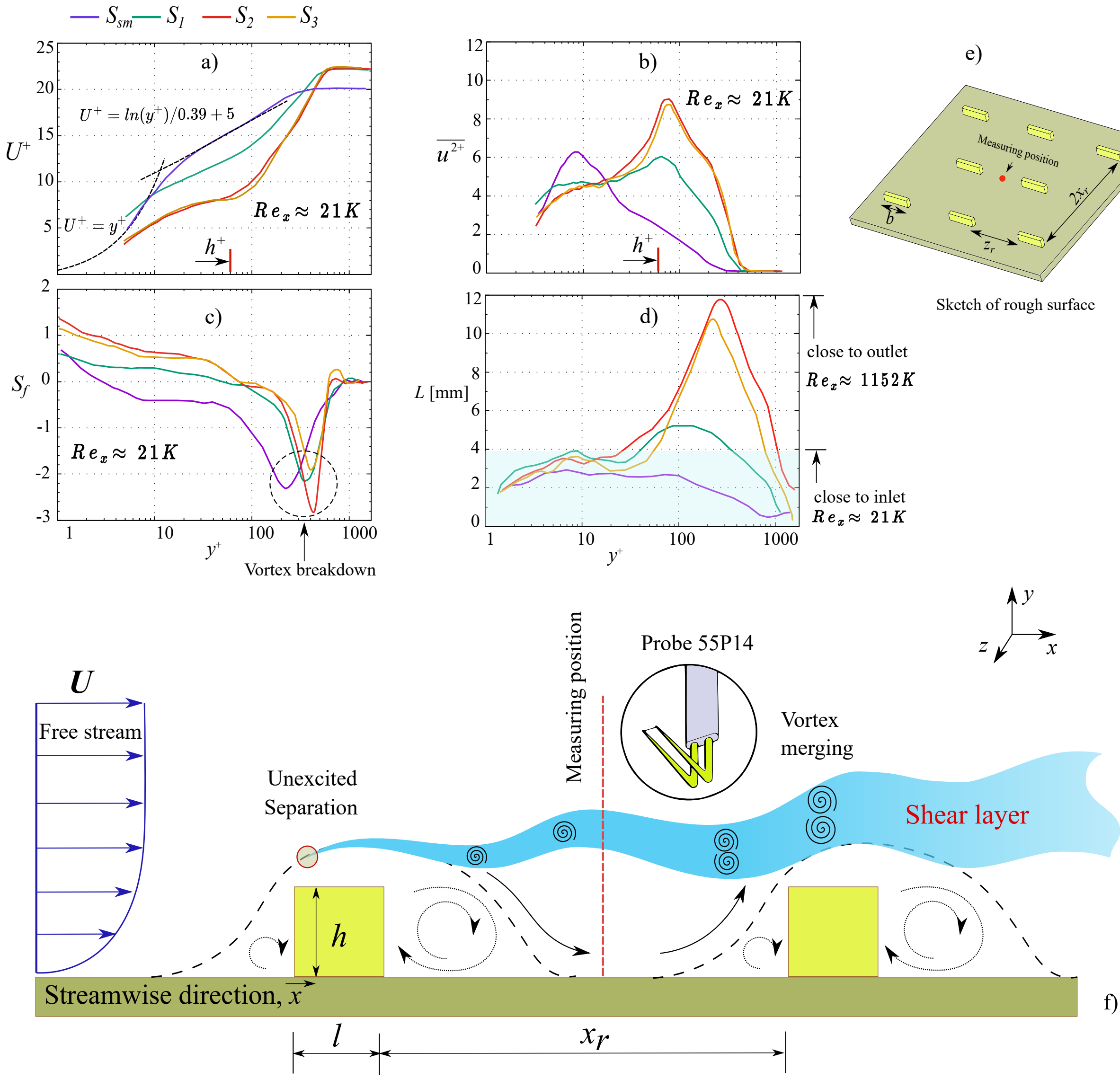

Figure 1: *(a) Mean velocity profiles of experimental turbulent flows. (b) Streamwise turbulence intensity measurements in different rough boundary layers. (c) Skewness factor distribution for vary roughness surfaces. (d) Dependence of integral length scales for different roughnesses on distances. The Reynolds number Re_x is based on the distance from the inlet x, thus at a constant flow stream velocity U it reflects the measuring position. (e) Features of the location of the measurement site. (f) Sketch of boundary layer formation over isolated rough elements. S_i displayed the type of roughness.*

New Experiments on High Reynolds Number Turbulent Pipe Flow Using Spatially Resolved Laser Doppler Velocimeter

F. Heitmann[1], M. Juling[1], M. Ono[2] and N. Furuichi[2]

[1] Physikalisch-Technische Bundesanstalt (PTB), Berlin, Germany
[2] National Metrology Institute of Japan (NMIJ), AIST, Tsukuba, Japan

key-words: Turbulent pipe flow, Turbulence statistics, Friction factor, Laser Doppler Velocimetry

Abstract:
To further the progress in turbulence research, an existing pipe flow facility fitted with a sophisticated experimental setup is qualified for its suitability to generate experimental data at high Reynolds numbers. The experimental campaign will be carried out in collaboration with the National Metrology Institute of Japan (NMIJ), where extensive turbulence research has taken place [1][2]. For the proposed experiments, the Gravimetric Thermal Energy Standard (GraTESt) at the Physikalisch-Technische Bundesanstalt, Berlin will generate flow rates up to 1000 m³/h with water at up to 90 °C in DN 200 honed stainless steel pipes (Ra < 0,2 µm) with self-aligning, low tolerance flange connections. Downstream of a flow straightener, at least 60 D of straight, high-quality piping will be available for the flow development before the experimental section. By using the gravimetric method, i.e., by weighing of the water that passes through the test section, the volumetric flow rate will be determined with an extended uncertainty of 0.04 % (k=2). The maximum Reynolds number is $Re_\tau = 87 \cdot 10^3$.
Talamelli et al. [3] derive two requirements for an experimental setup to be suitable for the investigation of the underlying scaling laws of wall-bounded turbulent flow. They are an attainable Reynolds number of $Re_\tau = 40 \cdot 10^3$ and a sensor probe length of $l_S \leq 10 \cdot l^*$, where l^* is the viscous length scale. Figure 1 is adapted from Talamelli et al. [3] and depicts the ranges of several flow facilities regarding these two criteria. The horizontal line indicates the viscous length scale at $Re_\tau = 40 \cdot 10^3$ at GraTESt to be 2.6 µm. To satisfy the requirement $l_S \leq 10 \cdot l^*$, a probe resolution of 26 µm should be attained. This can be achieved by employing a spatially resolved laser Doppler velocimeter (LDV) [4]. This will allow for the measurement of the axial, wall-normal and tangential velocities and their corresponding turbulence statistics inside a precision glass pipe. As a first experiment, to determine the friction factor over a wide Reynolds number range, the pressure gradient along the honed DN 200 pipes will be measured. Furthermore, the experiments will be carried out in DN 100 pipe and with various components, allowing for the generation of robust data on high Reynolds number turbulent pipe flow.

References

[1] Furuichi N., Terao Y., Wada Y. and Tsuji Y., (2015): Friction factor and mean velocity profile for pipe flow at high Reynolds numbers, Phys. Fluids **27**, 095108

[2] Furuichi N., Terao Y., Wada Y. and Tsuji Y., (2018): Further experiments for mean velocity profile of pipe flow at high Reynolds number, Phys. Fluids **30**, 055101

[3] Talamelli A., Persiani F., Fransson J.H.M., Alfredsson P.H., Johansson A.V., Nagib H.M., Rüedi J., Sreenivasan K.R. and Monkewitz P.A., (2009): CICLoPE—a response to the need for high Reynolds number experiments, Fluid Dyn. Res. **41**, 021407

[4] Juling M., Steinbock J., Kraume M. and Lederer T., (2016): LDA volume flow rate standard for water using high spatial resolution LDA for traceable measurements in power plants, Proceedings of FLOMEKO 2016, Sydney, Australia

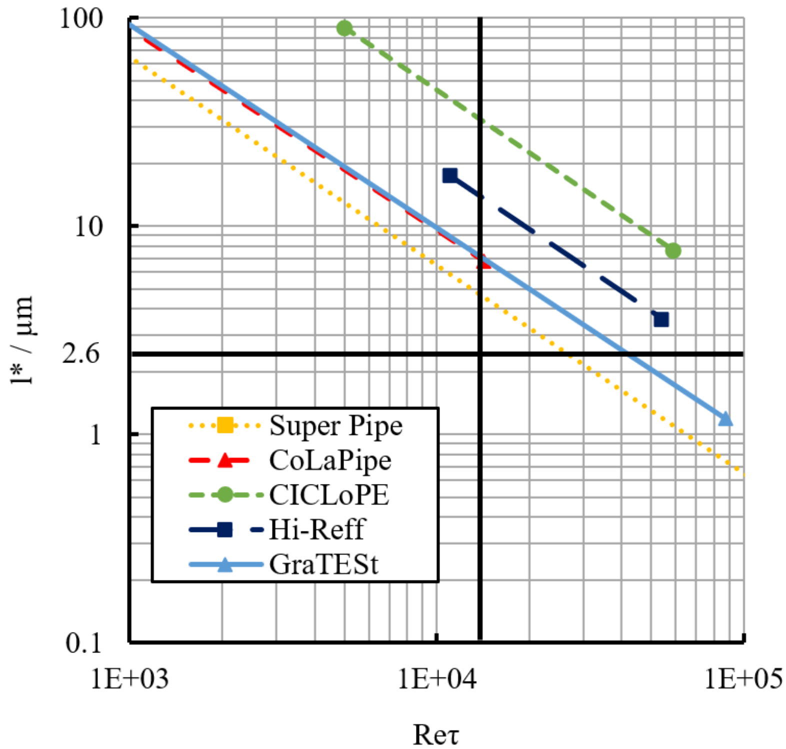

Figure 1: *Viscous length scale and Reynolds number ranges of high Reynolds number pipe flow facilities, adapted from Talamelli et al [3].*

Mixed convection in a particle-laden channel flow: effect of particles in one and two-way coupling regimes

D. Zaza and M. Iovieno

Dipartimento di Ingegneria Meccanica e Aerospaziale, Politecnico di Torino, Torino, Italy

key-words: turbulent channel flow, particle-laden flow, direct numerical simulaton, mixed convection, unstable stratification, two-way coupling.

Abstract:
Particle-laden turbulent flows occur in many engineering applications and natural phenomena. The most representative examples are the evolution of droplet clouds, volcanic clouds, sandstorms, soil erosion processes, sediment transport in watercourses, combustion in solid propellant endoreactors and liquid metal flows in cooling systems. The importance of detailed investigations of such flows for modeling purposes is indisputable, and Direct Numerical Simulations (DNS), more than any other approach, have proven to be essential to provide new physical insights into them, especially when the interaction between the two phases is considered. For isotropic turbulence, particle volume fractions larger than 10^{-6} are effective in modulating turbulence, enhancing turbulent kinetic energy production, or conversely dissipation, depending on the particle Stokes number [1], i. e. the ratio between the particle momentum relaxation time and the fluid time scale. Despite the amount of works on the topic, the understanding of particle-laden flows is however still incomplete when additional physical phenomena play a role, such as in the presence of gravity and buoyancy, or heat exchange and mass transfer (droplet condensation/evaporation), chemical reactions, or even acoustic waves. In the present work, by means of Eulerian-Lagrangian DNSs within the point-particle approach [2], we have studied the modulation of the fluid and particle temperature fields in the channel flow operated by the momentum and energy transfer between the continuous phase and the dispersed one, when also natural convection is taken into account. The incompressible Navier-Stokes equations, coupled by the Boussinesq approximation with an advection-diffusion equation for the temperature, are solved pseudo-spectrally over a domain of $2\pi h \times 2h \times 2\pi h$, where h is the channel half-height. Periodic boundary conditions are imposed in streamwise and spanwise directions, while no-slip conditions are enforced on the walls. The two isothermal walls are kept at different temperatures in order to induce an unstable stratification [3]. A phase consisting of small (sub-Kolmogorov), heavy, spherical particles is suspended in the fluid. Their dynamics is described by the Maxey-Riley equations in which only the terms representing the Stokes drag force and the heat exchanged are retained. We have simulated a single friction Reynolds number $\mathrm{Re}_\tau = 180$, with a particle volume fraction $\varphi_p = 4 \times 10^{-5}$, while we varied the Rayleigh number from 10^2 to 10^7 and Stokes number between 0.6 and 160. The Prandtl number is $\mathrm{Pr} = 0.71$. The ratio between the thermal Stokes number St_ϑ^+ and the Stokes number St^+ is kept constant and equal to 4.4, while the non-dimensional particle radius is $r_p/h = 4 \times 10^{-4}$, leading to a number of particles close to 12 million. We will show the combined effect of forced and free convection in modifying the flow structures and promoting turbulent exchanges for sufficiently high Rayleigh numbers through the formation of a network of rollers and travelling plumes which enhance convective transport in the wall-normal direction. Particle-related features for different Stokes numbers are then presented, highlighting the role of particle clustering near the walls, and the effect of their feedback on the thermal budget will be discussed.

References

[1] Elghobashi S., (1994), On Predicting Particle-Laden Turbulent Flows, *Appl. Sci. Res., vol. 52, pp. 309-329*

[2] Kuerten J. G. M., (2016), Point-Particle DNS and LES of Particle-Laden Turbulent flow - a state-of-the-art review, *Flow Turbulence Combust, vol. 97, pp. 689-713*

[3] Sid S., Dubief Y. and Terrapon V.E., (2015): Direct Numerical Simulation of Mixed Convection in Turbulent Channel Flow: On the Reynolds number dependency of momentum and heat transfer under unstable stratification, *Proc.* 8^{th} *ICCHMT*, Instanbul, p. 190

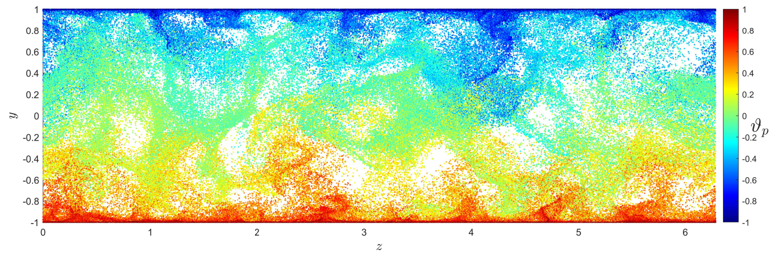

Figure 1: *Visualization of particles with* $\mathrm{St}^+ = 60$ *in a transversal (wall-normal/spanwise) plane in the two-way coupling regime on momentum and temperature (2WM - 2WT). Particles - shown out of scale - are colored according to their non-dimensional temperature* ϑ_p*. The bulk Rayleigh number is* 10^5.

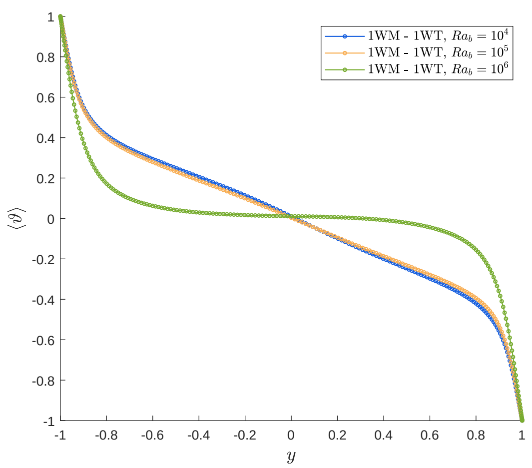

Figure 2: *Fluid mean temperature* $\langle \vartheta \rangle$ *dependence on the Rayleigh number in the one-way coupling regime.*

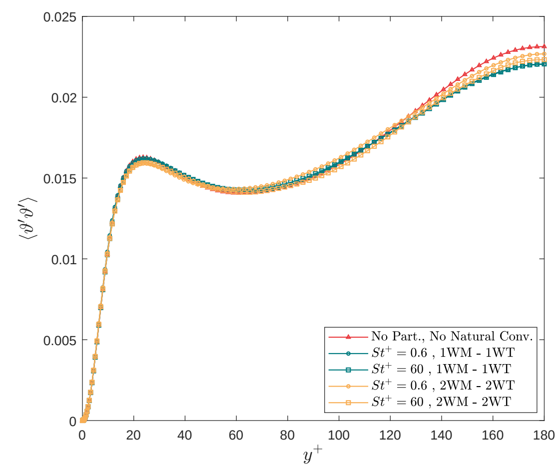

Figure 3: *Fluid temperature variance* $\langle \vartheta' \vartheta' \rangle$ *for* $\mathrm{Ra}_b = 10^5$ *and different Stokes numbers in one and two-way coupling regimes.*

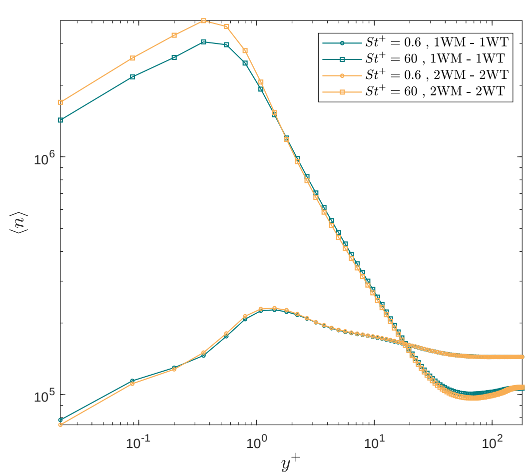

Figure 4: *Mean particle concentration* $\langle n \rangle$ *for* $\mathrm{Ra}_b = 10^5$ *and different Stokes numbers in one and two-way coupling regimes.*

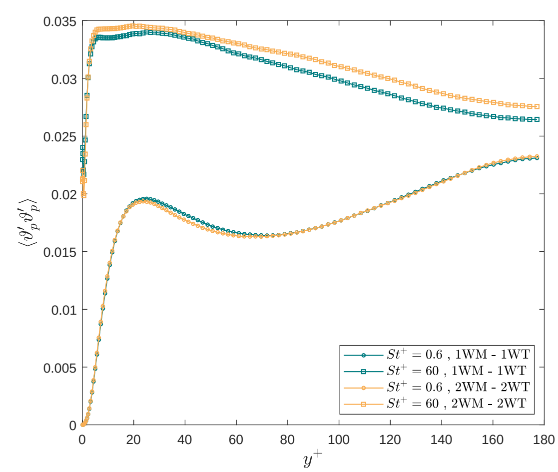

Figure 5: *Particle temperature variance* $\langle \vartheta'_p \vartheta'_p \rangle$ *for* $\mathrm{Ra}_b = 10^5$ *and different Stokes numbers in one and two-way coupling regimes.*

Reynolds number effects on secondary flows over ridge-type surfaces

Mattias Nilsson-Takeuchi [1], B. Ganapathisubramani [1]

[1] Department of Aeronautics and Astronautics Engineering, University of Southampton, Southampton, United Kingdom

key-words: Secondary flows, surface heterogeneity

Secondary flows are formed over spanwise heterogeneous surfaces due to spatial anisotropy in Reynolds shear stresses, and are therefore Prandtl's secondary flows of the second kind. These flows appear in many natural and engineering applications where they impose an additional surface drag penalising such surfaces (see for example [1, 2]). In research applications, these surfaces are commonly divided into ridge-type surfaces (spanwise variation in height) and strip-type surfaces (spanwise variation in skin friction).

Several recent studies have looked into the flow structure that determine the nature and strength of the generated secondary currents over both of these surface types (for example [3, 4]). However, information on the variation of global friction as well as the nature of these secondary flows across a range of Reynolds numbers is scarce.

In this study we investigate secondary flows generated by two ridge-type surfaces in a $L \approx 130H$ long water channel facility with a rectangular cross-section $W/H \approx 8$. The ridge width $W_p \approx 0.8\delta$, the spanwise centre-to-centre spacings are $S \approx 1.6\delta$ and $S \approx 3.2\delta$, and the ridge height $h/\delta \approx 0.1$, where $\delta = H/2$ is the channel half-height. The channel centerline pressure gradient is measured starting from $L \approx 65H$ to the channel outlet. Stereoscopic PIV in a spanwise—wall-normal plane $L \approx 110H$ downstream of the channel inlet is used to obtain the three-component velocity field. In this talk we present results of skin-friction against bulk Reynolds number and explore the structure of the produced secondary flows over a range of bulk Reynolds numbers $Re_m = U_b H/\nu$, where the bulk velocity $U_b = Q/A$ is determined by measuring the channel flow rate Q over the test section area $A = W \cdot H$.

References

[1] Mejia-Alvarez R., Christensen K. T.(2013), Wall-parallel stereo particle-image velocimetry measurements in the roughness sublayer of turbulent flow overlying highly irregular roughness., *Physics of Fluids, 25.*

[2] Schultz M. P., (2007): *Effects of coating roughness and biofouling on ship resistance and powering., Biofouling, 23(5). pp. 331 — 341*

[3] Medjnoun, T., Vanderwel, C. Ganapathisubramani, B. (2020): *Effects of heterogeneous surface geometry on secondary flows in turbulent boundary layers., Journal of Fluid Mechanics, 886*

[4] Wangsawijaya, D. D., Baidya, R., Chung, D., Marusic, I. Hutchins, N. (2020): *The effect of spanwise wavelength of surface heterogeneity on turbulent secondary flows., Journal of Fluid Mechanics, 894*

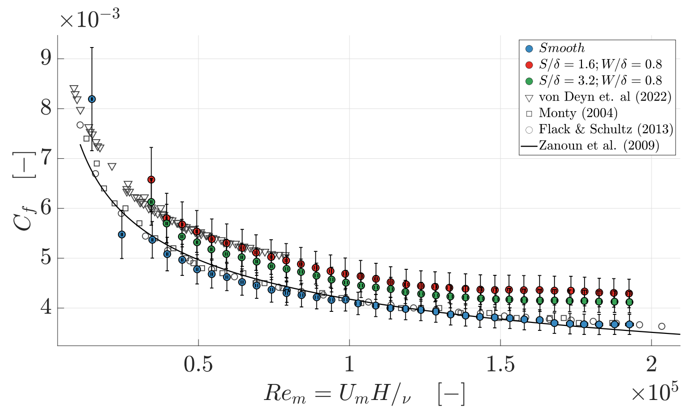

Figure 1: *Variation of global skin friction coefficient versus bulk Reynolds number for the different surfaces*

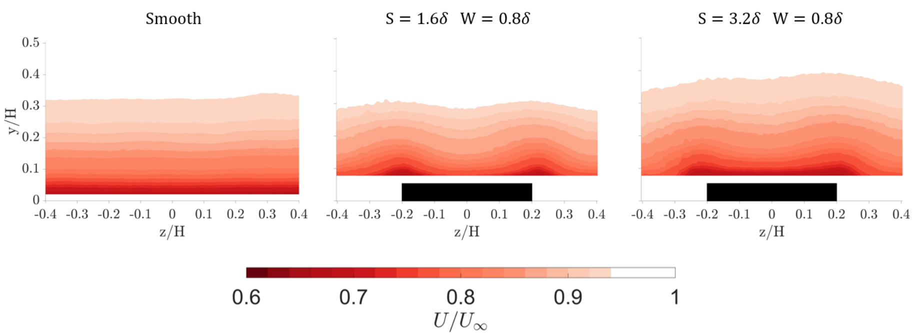

Figure 2: *Average streamwise velocity contours showing appearance of high momentum and low momentum pathways.* $Re_m = 120k$.

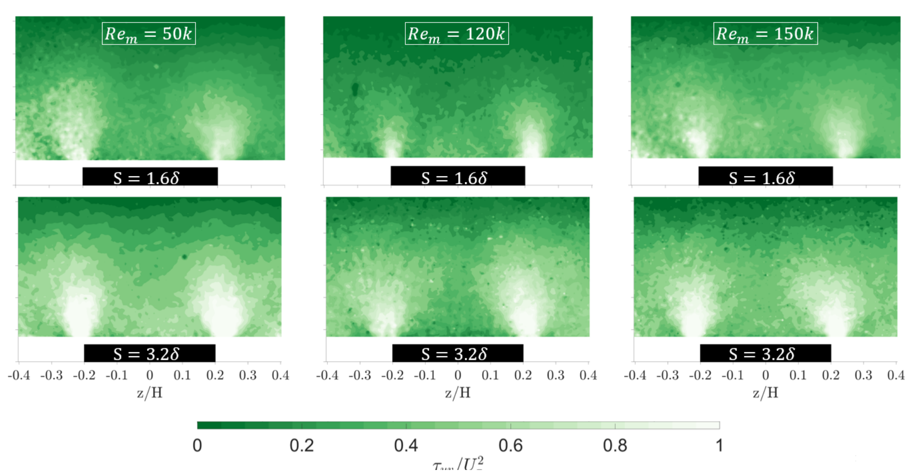

Figure 3: *Contours of total stress* $\tau_{uv} = -(\overline{u'v'} + \overline{\tilde{u}\tilde{v}})$ *for both ridge surfaces at different bulk Reynolds numbers.*

From wall measurements to three-dimensional turbulent-flow fields

A. Cuéllar Martín [1], A. Ianiro [1], R. Vinuesa [2], O. Flores [1] and S. Discetti [1]

[1] Aerospace Engineering Research Group, Universidad Carlos III de Madrid, Leganés, Spain
[2] FLOW, Engineering Mechanics, KTH Royal Institute of Technology, Stockholm, Sweden

key-words: Turbulence, Simulation

Linear methods have successfully reconstructed turbulent flow fields in channel flows using wall measurements up to the logarithmic region [1]. However, deep neural networks have been developed more recently to incorporate non-linear effects, leading to improved accuracy. In particular, generative adversarial neural networks (GANs) have recently outperformed standard convolutional neural networks in this task [2, 3, 4]. Accurately estimating turbulent flow fields from wall-embedded sensors is crucial for implementing boundary-layer flow control, and deep neural networks improve modeling of the non-linear relationship between wall and flow data.

The aim of this research is to use (GANs) to directly estimate 3D turbulent channel flows from wall-shear stress and pressure measurements. This work builds on previous research on the estimation of wall-parallel planes (which requires separate training for each plane) and extends it to full one-shot 3D estimation. Despite being computationally more demanding, we show that a similar network with a moderate increase in training parameters can provide accurate 3D predictions at a comparable cost to previous 2D implementations. The goal of this research is to pave the way for a more efficient flow estimation from wall sensors.

GANs consist of two networks that compete against each other during the training process. With an analogous implementation to that found in [4], the generator network takes wall measurements of pressure and wall-shear stress as input to generate the 3D velocity field, while the discriminator network is trained to determine if a given flow field is original or if it was created by the generator. In this study, the GANs used 3D convolutional layers to address this specific setup, and the main components of the generator network were the residual blocks which included these convolutional layers.

The dataset used was generated by a direct numerical simulation (DNS) of a turbulent open-channel flow at friction-based Reynolds number of 200 with dimensions of πh in the streamwise direction, $\pi/2h$ in the spanwise direction and $2h$ in the wall-normal direction, with 64, 64 and 128 grid points respectively.

The network can predict the flow field with a slightly higher error level if compared to the 2D single-plane estimation, but with the added advantage of being able to predict many wall-parallel layers at once, which makes the process more efficient. As expected, the velocity fluctuations are estimated with a high accuracy in the viscous layer, then the estimation worsens progressively through the buffer and logarithmic layers. This limitation is also observed in 2D GANs and linear methods, and is attributed to the physical limitation of small-scale structures having a limited impact on the wall measurements.

For one of the test cases used in this work, the volume of the DNS domain up to $y^+ = 40$ was predicted using the first 32 wall-normal layers of the DNS simulation, starting from the wall. Although the mean squared error (MSE) of the prediction 1 is slightly higher than the results in reference [4], the 3D GANs architecture used in this study has a relatively smaller number of parameters (9 million) when compared to the increase in output size, as it predicts 32 layers at once instead of one (1 million).

The figures 2 and 3 present the prediction of the flow field at two different distances from the wall. The network can predict the patterns and structures in the flow field, and its capability to make predictions is better close to the wall than in the center of the channel. This is due to the reduction in the intensity of the structures and the filtering of smaller scales as the distance from the wall increases. The smaller scales cannot be reconstructed beyond a certain point, which depends on the distance from the wall and the patterns present in the wall measurements.

ACKNOWLEDGEMENTS

This contribution has received funding from the Spanish Ministry of Universities under the *Formación de Profesorado Universitario (FPU) 2020* programme, and from the European Research Council (ERC) under the European Union's Horizon 2020 research and innovation programme (grant agreement No 949085, NEXTFLOW).

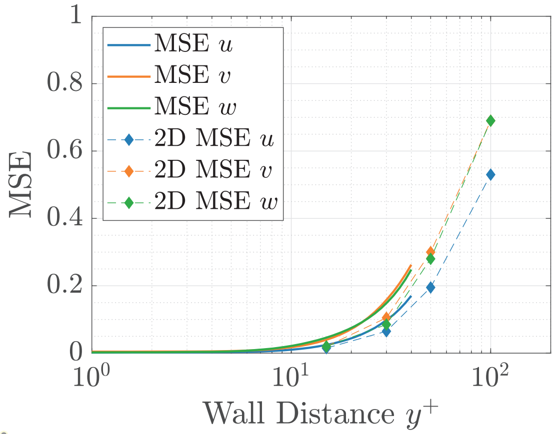

Figure 1: MSE of the prediction of the three components of the velocity fluctuations as a function of the inner-scaled wall-normal coordinate y^+. The 3D prediction (solid lines), and the 2D prediction from the Ref. [4] (dotted lines) at $y^+ = [15, 30, 60, 100]$.

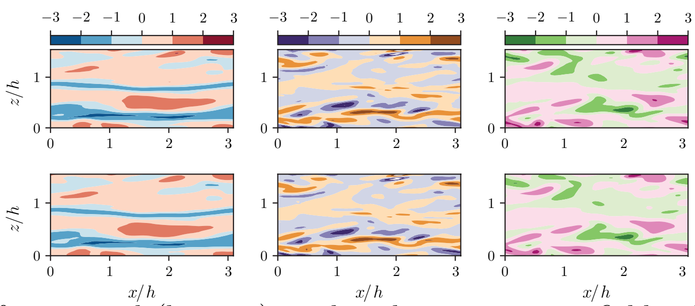

Figure 2: (Top) Reference and (bottom) predicted instantaneous fields of (left) u, (middle) v and (right) w, for $y^+ = 10$.

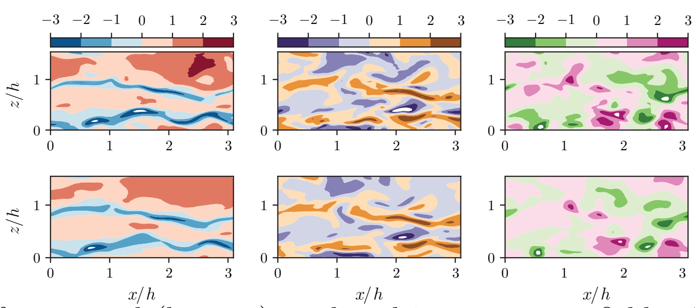

Figure 3: (Top) Reference and (bottom) predicted instantaneous fields of (left) u, (middle) v and (right) w, for $y^+ = 40$.

References

[1] Encinar M. P. and Jiménez J., (2019), Logarithmic-layer turbulence: A view from the wall, *Physical Review Fluids, vol. 4, no. 11, pp. 114603*

[2] Güemes A. et al, (2019), Sensing the turbulent large-scale motions with their wall signature, *Physics of Fluids, vol. 31, no. 12, pp. 125112*

[3] Guastoni L. et al, (2021), Convolutional-network models to predict wall-bounded turbulence from wall quantities, *Journal of Fluid Mechanics, vol. 928*

[4] Güemes A. et al, (2021), From coarse wall measurements to turbulent velocity fields through deep learning, *Physics of Fluids, vol. 33, no. 7, pp. 075121*

On the development of turbulent flow over a porous medium

Thomas Hunter[1], Francesco Avallone[2], Anh Khoa Doan[1] and Daniele Ragni[1]

[1] FPT Department, Delft University of Technology, Delft, The Netherlands
[2] DIMEAS, Politecnico di Torino, Torino, Italy

keywords: porous medium, turbulent flow, aeroacoustics

Abstract:

Turbulent boundary layer trailing edge noise is the dominant or amongst the dominant noise sources in many fields such as wind energy [1] and aviation. Porous materials [2] represent a potential solution to reduce this noise source because they achieve larger noise reduction than the state-of-the-art solution represented by trailing-edge serrations [3].
High-fidelity numerical simulations have been used to optimize the porous medium [4] or to describe the relevant noise reduction mechanisms [5]. It has been shown that, when applied to the trailing edge of an airfoil, most of the noise reduction is achieved when the thickness of the porous medium is smaller or comparable to the boundary layer thickness. In this case, there is unsteady interaction between the suction and pressure side of the airfoil, which mitigates the unsteady pressure mismatch at the trailing edge. This mechanism was named pressure-release[4]. Even if porous material reduce noise, they cause an increase in drag which can prevent their application in aviation [5].
In order understand how the interaction takes place, with the aim of designing innovative meta-materials with minimum drag, it is necessary to describe how the flow interacts between the two sides of the airfoil and how this is affected by the thickness of the material relative to the boundary layer thickness (δ). To this end a numerical experiment is carried out. The proposed numerical setup consists in two vertically stacked spatially developing turbulent channels ($20\delta \times 2\delta+t \times 4\delta$), which is solved by performing lattice-Boltzmann very large eddy simulations using the commercial solver 3DS PowerFLOW. The two channel flows communicate through a fully resolved porous medium. In this work, the porous medium is a 75% porous Schwarz' P triply periodic minimal surface [6]. Results show spanwise coherent turbulent structures on both sides of the porous medium, which is consistent with noncommunicating turbulent channels over streamwise preferential porous media. However, the communication between both turbulent boundary layers leads to the coherence between these span-wise structures in the top and bottom channels. This can affect the pressure release mechanism and therefore impact the overall noise reduction.

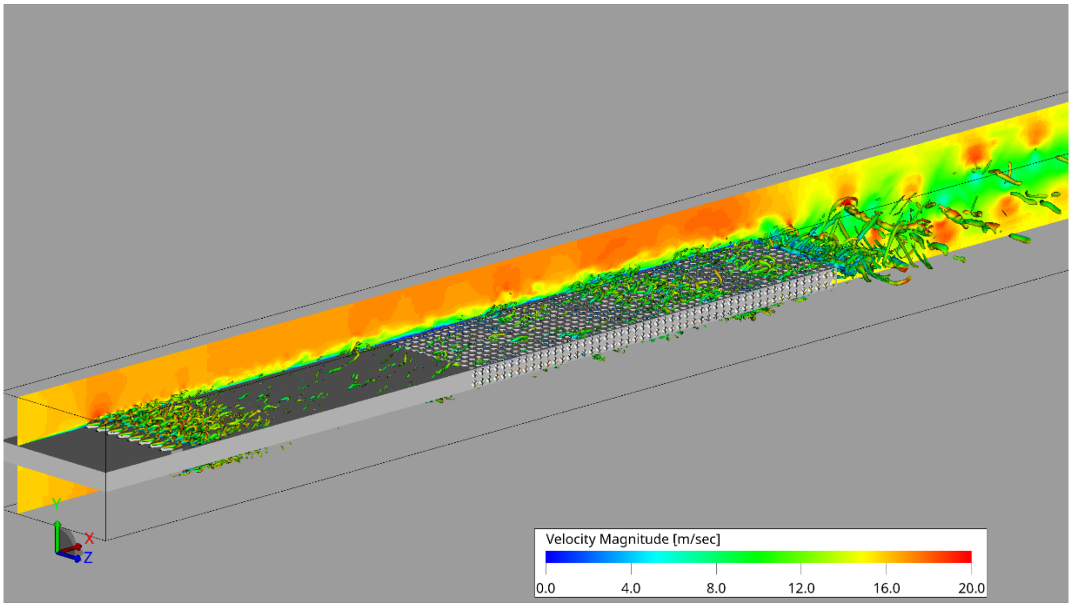

Figure 1. Iso-contours of λ_2=-5x10^7 m^2/sec^2, coloured with the velocity magnitude

References

[1] S. Oerlemans, "Reduction of wind turbine noise using blade trailing edge devices," in *22nd AIAA/CEAS Aeroacoustics Conference*, May 2016, pp. 1–18. doi: 10.2514/6.2016-3018.

[2] A. Rubio Carpio *et al.*, "Experimental characterization of the turbulent boundary layer over a porous trailing edge for noise abatement," *J Sound Vib*, vol. 443, pp. 537–558, Mar. 2019, doi: 10.1016/J.JSV.2018.12.010.

[3] F. Avallone, W. C. P. van der Velden, D. Ragni, and D. Casalino, "Noise reduction mechanisms of sawtooth and combed-sawtooth trailing-edge serrations," *J Fluid Mech*, vol. 848, 2018, doi: 10.1017/jfm.2018.377.

[4] L. Rossian, R. Ewert, and J. W. Delfs, "Prediction of airfoil trailing edge noise reduction by application of complex porous material," *Notes on Numerical Fluid Mechanics and Multidisciplinary Design*, vol. 136, pp. 647–657, 2018, doi: 10.1007/978-3-319-64519-3_58.

[5] C. Teruna, F. Avallone, D. Ragni, A. Rubio-Carpio, and D. Casalino, "Numerical analysis of a 3-D printed porous trailing edge for broadband noise reduction," *J Fluid Mech*, vol. 926, p. 17, 2021, doi: 10.1017/JFM.2021.704.

[6] Y. Jung and S. Torquato, "Fluid permeabilities of triply periodic minimal surfaces," *Phys Rev E Stat Nonlin Soft Matter Phys*, vol. 72, no. 5, p. 056319, Nov. 2005, doi: 10.1103/PHYSREVE.72.056319/FIGURES/9/MEDIUM.

Effect of uniform blowing on the large-scale structures and 'bursting' events of a turbulent boundary layer

G. Hasanuzzaman [1], S. Merbold [1] and Ch. Egbers [1]

[1] Department of Aerodynamics and Fluid Mechanics, Brandenburg University of Technology, Cottbus-Senftenberg, Germany

key-words: flow control, turbulent boundary layer, friction drag, large-scale structures, SPIV

Abstract:

Numerous aerodynamic applications, including aircraft and mechanical transports, operate within the turbulent boundary layer (TBL) regime. In this regime, a significant portion of the total drag is influenced by geometry, skin roughness, and Reynolds number. This relationship leads to a substantial contribution to fuel consumption and operating costs. While streamlining the geometry can reduce form drag, friction drag resulting from surface roughness still accounts for almost half of the total drag. The large-scale coherent structures and associated turbulence process, also known as the "bursting phenomenon," play a vital role in the production of skin friction drag. Hasanuzzaman et al. (2021) [1] presented a concise hypothesis indicating that intermittent turbulent bursts, known as *sweeps* and *ejections*, take place at the boundary of the inner layer. These bursts are believed to be responsible for turbulent production, which ultimately leads to the formation of friction drag footprints on the surface of the wall.

Active flow control techniques, such as "uniform blowing (UB)," significantly influence various characteristics of the bursting phenomenon, including the rate of burst occurrence, Reynolds stresses, and average velocity. As a result, UB is capable of effectively manipulating the bursting phenomenon. High Reynolds number experiments reported in Hasanuzzaman et al. (2020) [2] show a strong dependency of the turbulent statistics at various blowing ratios (BR). BR is defined as the ratio of the vertical blowing velocity to the free stream velocity (U_∞) expressed as a percentage. Additionally, energy spectra of velocity data also indicate a strong dependency on the blowing magnitude. Furthermore, pre-multiplied turbulent kinetic energy is observed to increase with increased BR. Among its many purposes, uniform blowing is utilized to reduce friction drag, manipulate flow separation, and enhance turbulence.

This abstract reports on experiments aimed at studying the influence of wall-normal blowing on large-scale coherent structures. The measurements were conducted using non-intrusive, time-resolved Stereo Particle Image Velocimetry (SPIV) at different BR. The measurements were taken over a range of shear Reynolds numbers, specifically $Re_\tau = u_\tau \delta/\nu = 0.4 \times 10^3$ and $Re_\theta = U_\infty \theta/\nu = 7500$, at the wind tunnel facility located at University Lille [3]. The results were presented using the Variable-Time-Interval-Averaging (VITA) method, and the porous surface used for blowing and measurement techniques were described in detail in previous works [4]. Applying Taylor's frozen turbulence hypothesis [5] to the time-resolved SPIV data, as shown in Figure-1, indicates strong coherence and vorticity in the outer layer turbulent structures.

Acknowledgments:

This research received funding from the European Union's research and innovation funding program, FP7-INFRASTRUCTURES-2012-1, under the European High performance Infrastructures in Turbulence (EuHIT) Grant Agreement Number 312778. The authors would like to express their gratitude to Prof. Jean-Marc Foucaut and Prof. Christophe Cuvier for their generous provision of access to the LMFL wind tunnel.

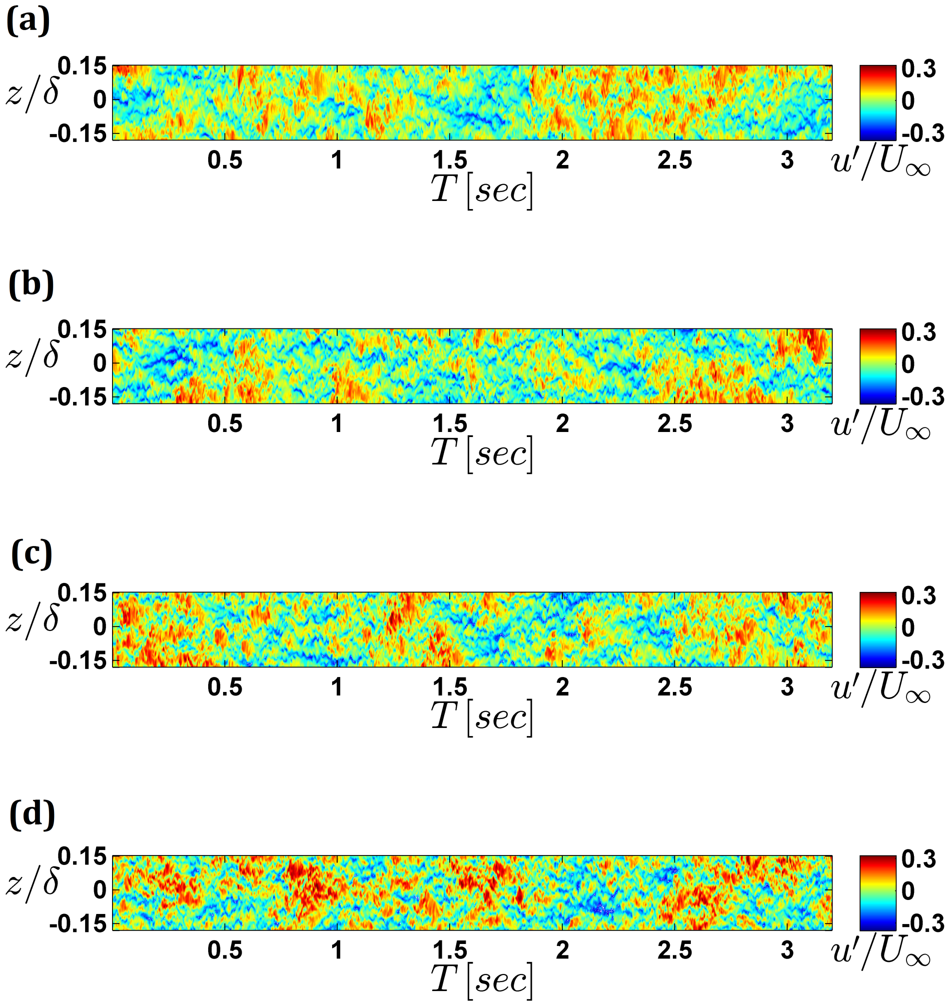

Figure 1: Contour plots of streamwise velocity fluctuations normalized with U_∞ over perforated surface at $Re_{\theta,SBL} = 7500$, distance from the wall $y/\delta = 1.62e-06$ ($y^+_{,SBL} \approx 36$). (a), (b), (c) and (d) presents different blowing ratios, $BR = 0$, 1, 3 and 6 % respectively. Flow is coming from left to right with the readers reference point [1].

References

[1] Hasanuzzaman, G., (2021), Experimental investigation of turbulent boundary layer with uniform blowing at moderate and high Reynolds numbers (1st ed.), *Cuvillier Verlag*

[2] Hasanuzzaman, G., Merbold, S., Cuvier, C., Motuz, V., Foucaut, J.-M., and Egbers, Ch.,(2020), Experimental investigation of turbulent boundary layers at high Reynolds number with uniform blowing, part I: statistics, *Jour. Turb., 21(3), pp. 129 – 165*

[3] Hassanuzzaman G., Merbold S., Motuz V., Egbers Ch., Cuvier C. and Foucaut J-M. (2018), Experimental investigation of active control in turbulent boundary layer using uniform blowing, *ICEFM, Munich, Germany, 2. - 4. July, 2018, pp. 1 – 6*

[4] Hassanuzzaman G., Merbold S., Motuz V., Egbers Ch., (2016), Experimental Investigation of Turbulent Structures and their Control in Boundary Layer Flow, *GALA Fachtagung Experimentelle Strömungsmechanik, 6. - 8. September, Dresden, Germany, pp. 64:1 – 6*

[5] Taylor G., I., (1971), A Model for the Boundary Condition of a Porous Material, Part-1, *Jour. Fluid Mech., vol.49, pp.319 – 336.*

Experiments and simulations on the accelerating/decelerating flow on a square cylinder

G. Lunghi [1], S. Brusco [2,3], A. Mariotti [1], G. Piccardo [3], M.V. Salvetti [1]

[1] Dipartimento di Ingegneria Civile e Industriale, University of Pisa, Italy
[2] Faculty of Engineering, Western University, London, Canada
[3] Dipartimento di Ingegneria Civile, Chimica e Ambientale, Polythecnic School, University of Genoa, Italy

Key-words: square cylinder, Gaussian-type acceleration, LES, wind-tunnel tests

Abstract:
We investigate the high-Reynolds accelerating/decelerating flow around a square cross-sectional cylinder. The square cross-section is a classic shape for wind-engineering applications, e.g. high-rise buildings and towers. The flow is characterized by shear-layer separation at the upstream edges. The separated shear layers undergo Kelvin-Helmholtz instability, but they do not lose coherence until they form the von Karman vortex street in the wake. The flow around a square cylinder has been well characterized when the inflow is steady. Much less is known when the inflow is accelerating or decelerating. These conditions are relevant, e.g., for civil structures in thunderstorms. This work may be considered a first step toward the characterization of the wind loads on civil buildings due to variable wind conditions and to a better appraisal of the limits of the wind-load predictions obtained under the assumption of steady-wind conditions.

We perform high-fidelity Large-Eddy Simulations (LES), using the same numerical set-up described for rectangular cylinders in [1], to investigate the effect of Gaussian-type inflow accelerations and decelerations in the Reynolds range $Re = 1.720 \times 10^4$ - 6.536×10^4 (see Fig. 1 for the accelerations). Numerical results are compared and validated with the experiments in [2], and an excellent agreement is found. In particular, the same discrete changes in the vortex-shedding frequency as in the experiments in [2] are found in the numerical simulations, with the presence of constant-frequency time cells (see Fig. 2). The behavior of the time cells is characterized by using a time-frequency analysis based on the wavelet transform. For the accelerating flow, the vortex-shedding Strouhal number witnesses a decrease within the time cells, followed by a sudden increase between the cells, pointing out the presence of discontinuities in an even more glaring way. The opposite for the decelerating flow. The vortex-shedding Strouhal number is always inside the range $0.10 \leq St \leq 0.14$. In addition, we perform a parametric study by considering different acceleration/deceleration intensities to reproduce conditions similar to full-scale thunderstorm outflows. Constant-frequency time cells are again found in the vortex shedding from the cylinder for all the investigated acceleration/deceleration levels. The increasing intensity of the flow variation reduces the time length of the time cells, and it decreases the vortex-shedding Strouhal number inside each cell, but a similar behavior of St with Reynolds number is found.

References

[1] Mariotti A., Siconolfi L. and Salvetti, M.V. (2017), Stochastic sensitivity analysis of large-eddy simulation predictions of the flow around a 5:1 rectangular cylinder, *Eur. J. Mech. B/Fluids, vol. 62, pp. 149-165.*

[2] Brusco S., Buresti G., Lo Y. L. and Piccardo G. (2022), Constant-frequency time cells in the vortex-shedding from a square cylinder in accelerating flows, *J. Wind Eng. Ind. Aerod., vol. 230, 105182.*

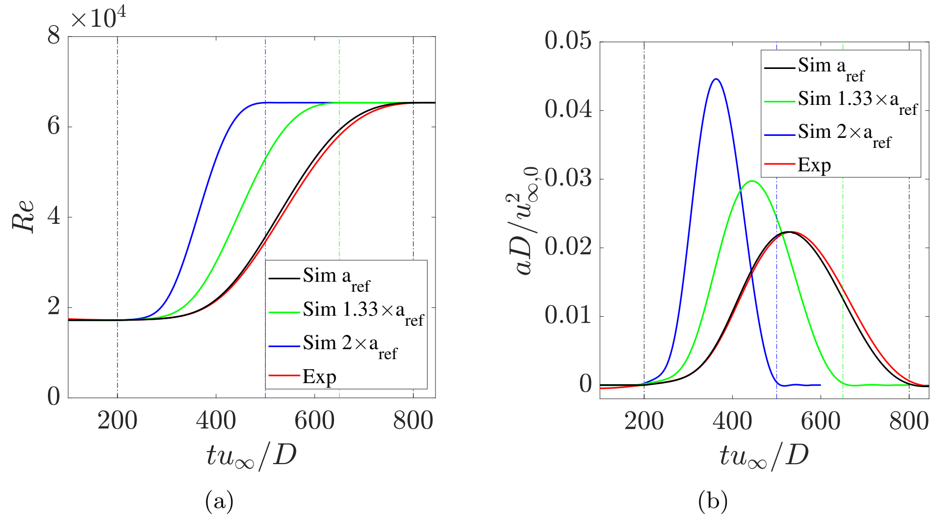

Figure 1: *Time behavior of (a) the inflow Reynolds number and (b) the acceleration.*

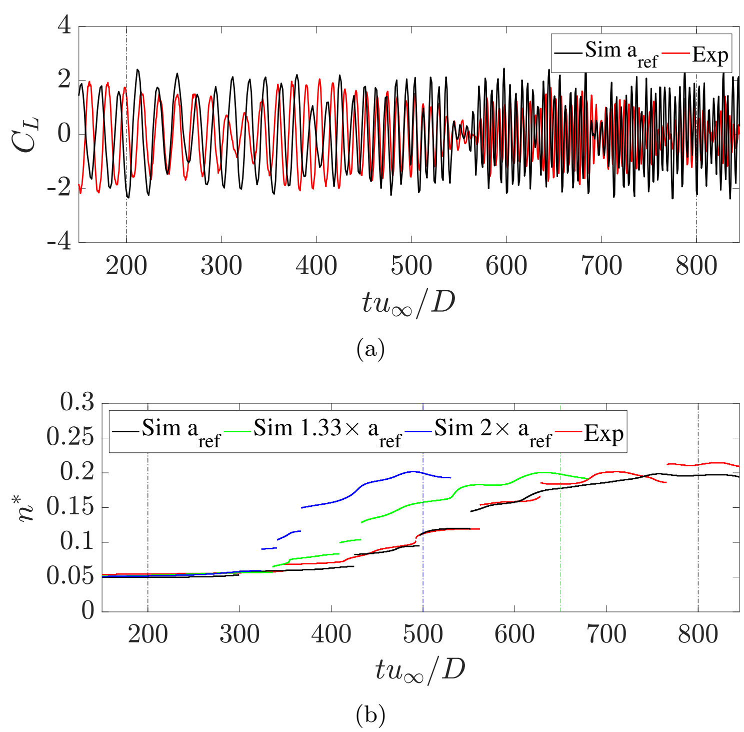

Figure 2: *Time behavior (a) of the lateral-force coefficient, C_L, for a_{ref} and (b) of the vortex-shedding frequency, n^*, during the accelerating flow.*

Simulation of massively separated flows using an intermittency-based hybrid model

F. Miralles[1], S. Wornom[1], B. Koobus [1] and A. Dervieux [2,3]

[1] IMAG, Univ. Montpellier, CNRS, France
[2] INRIA, Sophia-Antipolis, France
[3] Société technologique LEMMA, Sophia-Antipolis, France

Key-words: Intermittency model, Variational multiscale model, Hybrid approach, Massively separated flow

Abstract:
In this work, a hybrid turbulence approach is evaluated on the simulation of the flow around a circular cylinder from subcritical to super-critical Reynolds numbers. The proposed hybrid strategy [1] combines a dynamic variational multiscale (DVMS) large-eddy simulation model with a RANS model possibly equipped with an intermittency transport equation based on the work of Akhter et al. [2] and Menter et al. [3] for representing laminar to turbulent boundary layer transition. The $k-\varepsilon$ model proposed in Goldberg et al. [4] is used as the RANS component for its ability to properly predict separated flows with adverse pressure gradients, and the DVMS approach is the one proposed in [5]. In this approach, the variational multiscale model, aiming to limit the effects of the subgrid-scale (SGS) model to the smallest resolved scales, is combined with the dynamic procedure which provides a tuning of the SGS dissipation in space and time, so that the resulting DVMS model enjoys synergistic effects. Results are compared to those of other numerical simulations in the literature and with experimental data. They highlight the overall good prediction capabilities of the proposed hybrid approach when the laminar-turbulent transition model is activated (figure 1), even with the use of rather coarse unstructured meshes. In particular, the intermittency-based hybrid model was found to be able to predict the drag crisis of a circular cylinder, unlike the equivalent hybrid approach when no transition model is introduced (figure 2). Simulations of the flow over an airfoil in incidence are also in progress.

References

[1] Moussaed, C., Salvetti, M.V., Wornom S., Koobus, B. and Dervieux, A., (2014), Simulation of the flow past a circular cylinder in the supercritical regime by blending RANS and variational-multiscale LES models, *Journal of Fluids and Structures*, **47**, 114-123.

[2] Akhter, M. N., Ali, M., and Funazaki, K.I., (2015), Numerical simulation of heat transfer coefficient on turbine blade using intermittency factor equation. *Procedia Engineering*, **105**, 495-503, The 6th BSME International Conference on Thermal Engineering.

[3] Menter, F.R., Langtry, R., Völker, S., (2006), Transition Modelling for General Purpose CFD Codes. *Flow, Turbulence and Combustion*, **77**, 277-303.

[4] Goldberg, U., Peroomian, O. and Chakravarthy, S., (1998), A wall-distance-free $k-\varepsilon$ model with Enhanced Near-Wall Treatment, *Journal of Fluids Engineering*, **120**, 457–462.

[5] Moussaed, C., Wornom, S., Salvetti, M.V., Koobus, B. and Dervieux, A., (2014), Impact of dynamic subgrid-scale modeling in variational multiscale large-eddy simulation of bluff body flows, *Acta Mechanica*, **225**, 3309-3323.

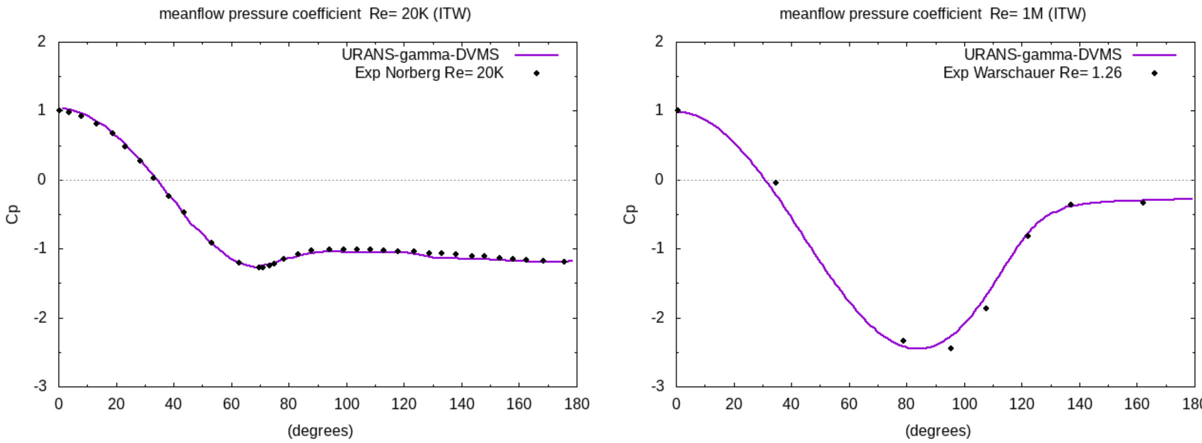

Figure 1: *Pressure distribution on the surface of the cylinder with the intermittency-based hybrid model: Reynolds number 20000 (left) and Reynolds number 1 million (right)*

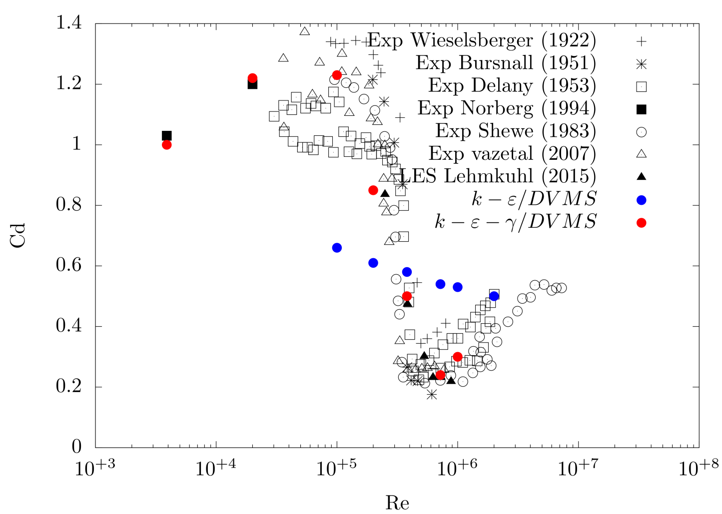

Figure 2: *Flow around a cylinder: impact of the intermittency model (in red) on the drag crisis prediction, in contrast with the same hybrid model without intermittency (in blue)*

Tomo-PIV of turbulence structure in a rapid contraction

Abdullah A. Alhareth[1,2], Vivek Mugundhan[2,3], Kenneth R. Langley[2], Nathan B. Speirs[2] and S. T. Thoroddsen[2]

[1] Center of Excellence for Aeronautics and Astronautics (CEAA), King Abdulaziz City for Science and Technology (KACST), Riyadh 12354, Saudi Arabia
[2] Division of Physical Sciences and Engineering, King Abdullah University of Science and Technology (KAUST), Thuwal, 23955-6900, Saudi Arabia
[3] Mechanical Engineering, Amrita School of Engineering Coimbatore, Amrita Vishwa Vidyapeetham, India

key-words: High-Speed Particle Tracking Velocimetry, Turbulence Structure, Contraction.

Abstract:
Following the study of Mugundhan *et al.* [1], we use Shake-The-Box PTV measurements to examine 3-D vortical features in turbulent flow through a more rapid 4:1 and 16:1 contraction. The flow facility and the active grid are shown in Fig 1 (a). It has a constant-head vertical water tunnel, with active grid to achieve turbulent Reynolds numbers $Re_\lambda \simeq 220$. The grid flaps are rotated in either synchronous or random mode. Most previous studies in similar configurations have used hot-wires for point-wise time-series, while we obtain 50,000 time-resolved volumetric velocity and vorticity fields tracking up to 100,000 particles. This enables us to compare the development of the rms fluctuations to previous observations, as well as examine the alignment and amplification of coherent vortical structures reacting to the strong extensional strain of these contractions. Individual vorticity structures are also monitored to see how they stretch/compress and change orientation over time. Figure 1(b) depicts a typical vorticity field on the centerline of a contraction when it enters the 2-D contraction. The elongated vertical structures strained by the strongest 3-D contraction at its exit is shown in Fig. 1(c).

References

[1] Mugundhan, V., Pugazenthi, R., Speirs, N., Samtaney, R. & Thoroddsen, S. T., (2020), The alignment of vortical structures in turbulent flow through a contraction, *J. Fluid Mech.*, **884, A5.**

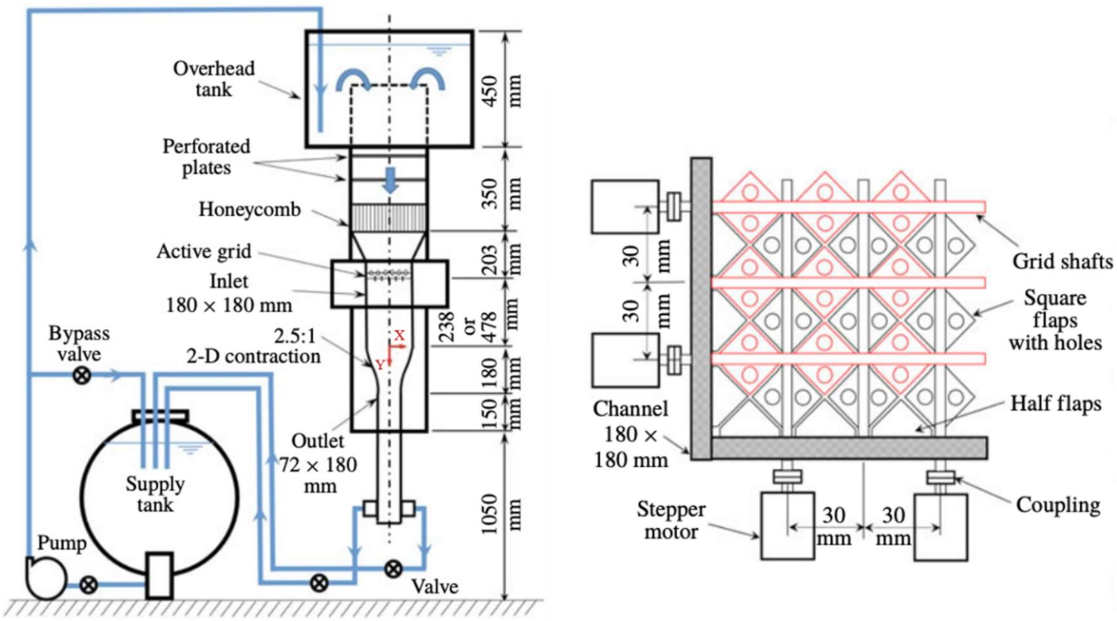

(a)

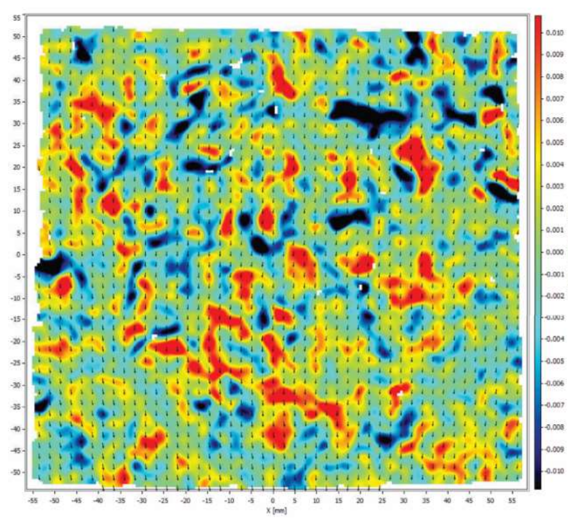

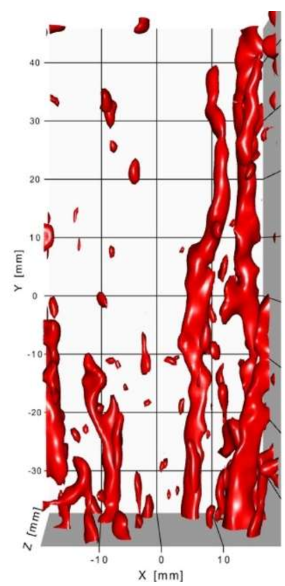

(b) (c)

Figure 1: (a) Flow facility used to study turbulent flow through a rapid contraction and the active grid. (b) Typical plane of vorticity at contraction centerline, with converging walls at 10°, (c) Isosurface of vorticity magnitude ($|\omega|=35\ s^{-1}$) showing instantaneous structure at the exit of a 3D Contraction.

Observation of the alternation of large-scale structures in low Reynolds number two-dimensional turbulent channel flow by two-point correlation of velocity fluctuations

Takeo Anada [1],Ryo Takai [1], Yuya Tanada [1], Kentaro Kato [1], Nobuhiko Henmi [1], and Masaharu Matsubara [1]

[1] Mechanical Systems Engineering, Shinshu University, 4-17-1, Wakasato, Nagano, 380-8553, Japan

key-words: Channel flow, Large-scale structure, cross spectra, two-point correlation

Abstract:
In two-dimensional turbulent channel flow, very large-scale structures that are 10 times longer than the channel width are known to exist. Monty et al.[1] measured two-dimensional channel flow at the very high Reynolds number of $Re = 144000$ (Re is based on channel width d and bulk velocity U_b) using a rake hot-wire probe and found a large-scale structure of a low-velocity steak whose streamwise length is 10 times larger than the channel width. On the other hand, Seki et al.[2] investigated transitional channel flow and reported a spectral peak of the streamwise velocity fluctuations corresponding to more than 10 times the channel width even at $Re = 2660$, which is just above the transition to turbulent flow. Matsubara et al.[3] also observed spectral peaks corresponding to almost the same length scale up to $Re = 4000$, suggesting existence of very large-scale structures. In this study, we investigated the streamwise and spanwise sizes of very large-scale structures appearing at low Reynolds numbers in two-dimensional turbulent channel flow, evaluating the correlation between the streamwise velocity fluctuations at two points separated in the spanwise direction. The channel apparatus consists of two flat plates of 1 m height and 17.35 m length with a channel width $d = 25$ mm. To obtain the correlation between the velocity fluctuations at two points, two hot-wire probes were used, and one of them was traversed in the spanwise direction.

Contour maps of the cross-spectra normalized with the standard deviation of each frequency are shown in Fig. 1. The streamwise length λ_x is defined as $\lambda_x = U_b/fd$, using the frequency f of the velocity fluctuation spectra. Negative minima are observed around $\Delta Z = 4$ and $\lambda_x = 30$ in (a) $Re = 3000$ and (b) $Re = 3400$ of Fig. 1. These minima indicate structures with streamwise and spanwise length scales about $30d$ and $8d$, respectively. This streamwise length corresponds to the spectra peaks by Matsubara et al.[3]. The other negative regions around $\Delta Z = 0.5$ and $\lambda_x = 2$ are considered to be small eddy motions of wall-shear turbulence. As shown in (b) to (d), the negative region of the large scales becomes unclear with increasing Re. On the other hand, the other negative region of the small scale extends to the larger streamwise scale with increasing Re, and it exceeds $\lambda_x = 20$ at $Re = 5000$. The corresponding streamwise and spanwise length scales of this negative region are about $30d$ and $1.6d$, respectively. These scales are close to those of the large-scale structure observed by Monty et al.[1]. Figure 2 shows the correlation coefficient at $\lambda_x = 20$. With increasing Re, a negative valley of correlation coefficient around $\Delta Z = 3.8$ at $Re = 3000$ becomes shallower, while the depth of a valley around $\Delta Z = 0.5$, which appears at $Re = 3700$, increases. This alternation of the peaks is clearly observed when the correlation coefficients at $\Delta Z = 3.8$ and $\Delta Z = 0.8$ plotted as functions of Re as shown in Fig. 3. The estimated threshold value at which the peaks alternate is about Re=3700. From the results mentioned above, there exist two types of the very-large structures in the channel flow; one has the wide width and the other is a streaky structure with the narrow width. The streamwise and spanwise scales of the wide structures appearing are close to the turbulent patches of transitional channel flow observed by Yimprasert et al. (2021)[4], suggesting that the patch-like structures remain even at Re higher than the transition range. As seen in Fig. 3, these two types of very large structures do not seem to coexist. Although the reason for this is unresolved, it is possible that the patch-like structures destroy the long streaky structures that appear at the high Re.

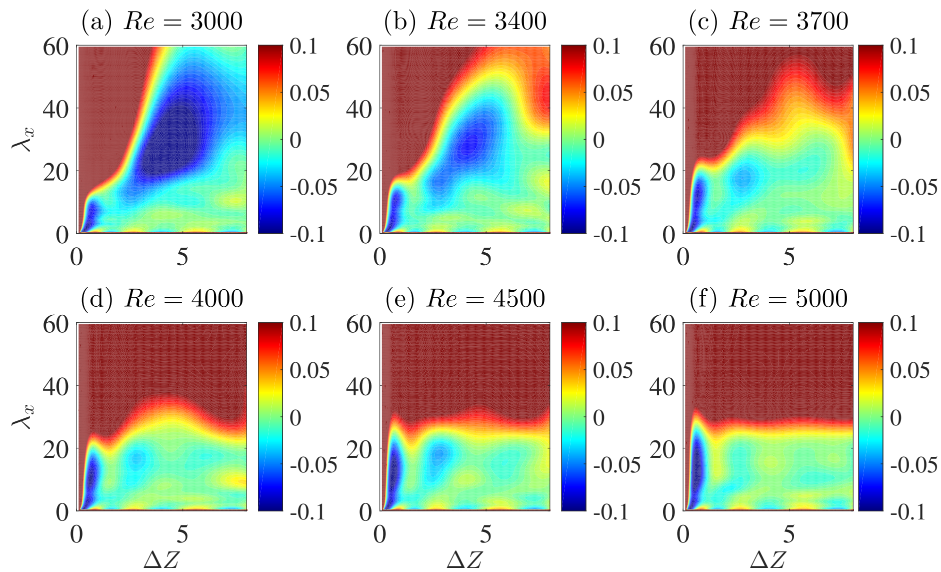

Figure 1: *Contour maps of cross-correlation coefficient of the streamwise velocity fluctuations.*

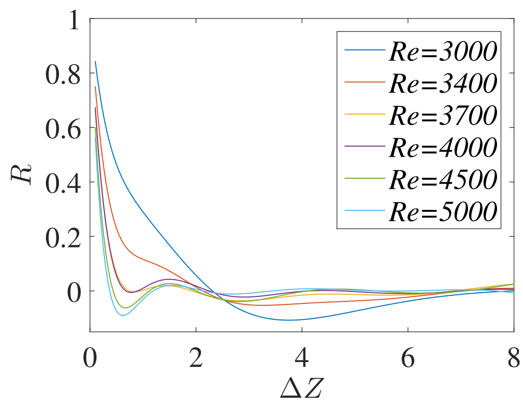

Figure 2: *Coefficients of two-point correlation R at $\lambda_x = 20$.*

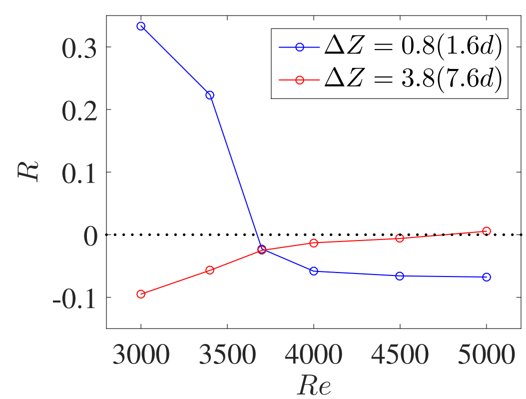

Figure 3: *Dependence of R at $\lambda_x = 20$ on Re.*

References

[1] Monty, J.P., Stewart, J. A., Williams, R.C. and Chong, M.S., (2007), Large-scale features in turbulent pipe and channel flows, *J. Fluid Mech., 589, pp. 147-156.*

[2] Seki, D., and Matsubara, M., (2012), Experimental investigation of relaminarizing and transitional channel flows *Phys. Fluids, 24, 124102.*

[3] Matsubara, M., Horii, S., Sagawa, S., Takahashi Y. and Saito D., (2016), Very-large-scale fluctuations in turbulent channel flow at low Reynolds number *International Journal of Heat and Fluid Flow, 62, Part B, pp. 593-597.*

[4] Yimprasert, S., Kvick, M., Alfredsson, P.H. and Matsubara, M., (2021), Flow visualization and skin friction determination in transitional channel flow. *Exp. Fluids, 62, 31.*

A New Temperature- and Entropy- Concept for Turbulence

Joachim Peinke [1], A. Fuchs [1] and T. T. B. Wester [1]

[1] Institute of Physics and ForWind, University of Oldenburg, Oldenburg, Germany

key-words: Fundamentals

Abstract:

The complexity of the disorder of turbulence has led many researchers to combine turbulence with thermodynamic quantities. Of particular attractiveness is the concept of entropy, as it is supposed to characterize disorder. If the development of systems is considered, entropy can show which direction a system is going to evolve. For non-equilibrium systems it is of interest to look at fluctuations of thermodynamic quantities of microscopic subsystems. In particular for systems out of equilibrium a new second law could be derived for the fluctuations of the entropy production along stochastic trajectories. This law is the so-called integral fluctuation theorem which determines a balance between positive and negative entropy events [2].

In this contribution we consider developed turbulence and in particular the often discussed cascade [1]. This picture of a cascade tries to explain how coarse grained features of turbulence on large scales are related to corresponding features on smaller scales. The interesting features of turbulence are found for a range scales r with $L > r > \eta$, which is limited by the integral length scale L and the dissipation length scale η.

For the cascade we consider the evolution of two quantities, the velocity increment $\xi_i := \xi(x_N, r_i) = u(x_N) - u(x_N - r_i)$ and the energy $\epsilon_i(x_N, r_i) \propto \int_{r_i} (\partial_j u_j|_{x_N})^2 dx$. (Here we use and index i to address a selected scale r_i and N to address a selected point x_N in the flow. Homogeneity allows to investigate ensemble averages over x_N.)

The scale dependence of ξ and ϵ allows to define cascade trajectories at different points x_N, which we denote as $\xi(\cdot)$ and $\epsilon(\cdot)$. The transition probabilities $p(\xi, \epsilon|\xi_i, \epsilon_i)$ from $(\xi(x_N, r_i), \epsilon(x_N, r)_i)$ to $(\xi(x_N, r), \epsilon(x_N, r))$ with $r < r_i$ describes the evolution downwards the cascade and can be described by a Fokker-Planck equation. It is important to note that the explicit form of the Fokker-Planck equation can be estimated directly from data (an open source software is described [3]). Knowing the stochastic process equations the entropy production, ΔS, along the trajectories can be defined [2, 3].

For the step r to $r - \delta$ an entropy change $\delta s(r)$ can be defined as well as the change of energy $\delta\epsilon(r)$ what allows to define a fluctuating temperature

$$\delta T(r) := \left(\frac{\partial \epsilon}{\partial s}\right)_{\xi_{const}} \approx \left(\frac{\delta\epsilon(r)}{\delta s(r)}\right)_{\xi_{const}} \tag{1}$$

where we interpret $\epsilon(r)$ as an inner energy of the system at scale r.

The strength of this approach is that the thermodynamics quantities seem to be related to turbulent structures, as shown as negative entropy structures calculated from PIV measurements in figure 1. These negative entropy events are related to intermittency and are now subject to the strict law of the integral fluctuation theorem [5, 4], which fixes the probability of negative entropy events. Here we see a new way to combine a statistical approach to turbulence with often discussed structures of turbulence.

References

[1] Frisch, U. (1995): *Turbulence: the legacy of AN Kolmogorov*, Cambridge university press.

[2] Seifert, U. (2005). Entropy production along a stochastic trajectory and an integral fluctuation theorem. *Physical review letters, 95(4), 040602.*

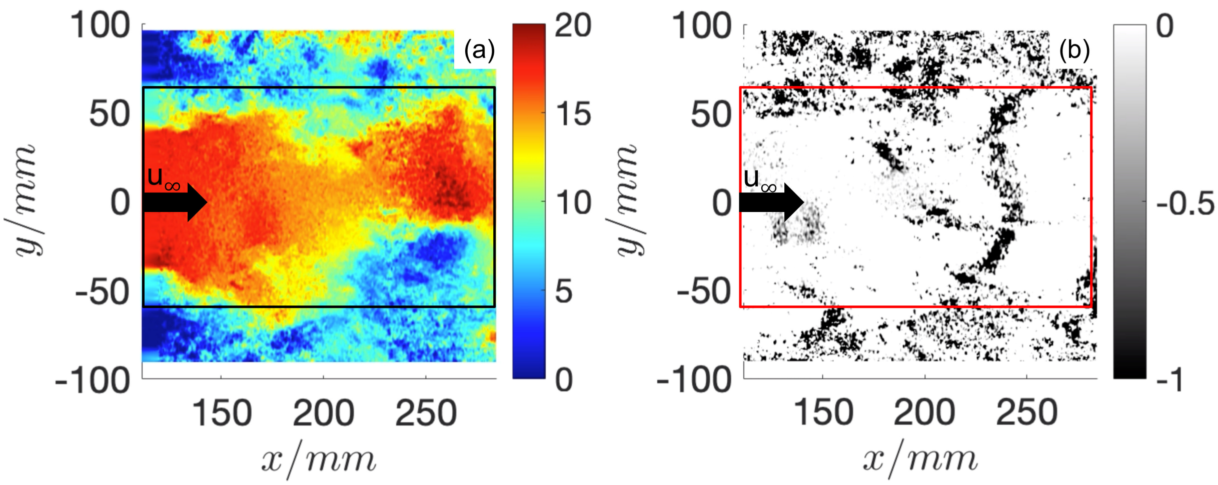

Figure 1: *(a) Velocity magnitude of flow behind a fractal grid measured by PIV in [ms^{-1}]. (b) Normalized Entropy structures calculated from PIV measurements using IFT - black negative entropy events.*

[3] Fuchs, A., Kharche, S., Patil, A., Friedrich, J., Wächter, M., & Peinke, J. (2022). An open source package to perform basic and advanced statistical analysis of turbulence data and other complex systems. *Physics of Fluids, 34(10), 101801.*

[4] Fuchs, A., Herbert, C., Rolland, J., Wächter, M., Bouchet, F., & Peinke, J. (2022). Instantons and the path to intermittency in turbulent flows. *Physical Review Letters, 129(3), 034502.*

[5] Fuchs, A., Queirós, S. M. D., Lind, P. G., Girard, A., Bouchet, F., Wächter, M., & Peinke, J. (2020). Small scale structures of turbulence in terms of entropy and fluctuation theorems. *Physical Review Fluids, 5(3), 034602.*

[6] Renner C, Peinke J, Friedrich R. 2002. On the interaction between velocity increment and energy dissipation in the turbulent cascade *arXiv:physics/0211121* .

Flow Sensitivity Analysis for the Feedback Loop Phenomenon of Subsonic Jet Noise Generation

Shota Morita[1,2], Aiko Yakeno[2], Christophe Bogey[3] and Shigeru Obayashi[2]

[1] Department of Aerospace Engineering, Tohoku University, Sendai, Japan
[2] Institute of Fluid Science, Tohoku University, Sendai, Japan
[3] École Centrale de Lyon, Lyon, France

key-words: subsonic jet noise, flow sensitivity analysis, feedback mechanism

Abstract:

We investigated the receptivity of the shear layer to upstream-propagating waves near the nozzle exit of a subsonic jet, flow sensitivity analysis. Recent studies for the subsonic jet noise generation suggested that the shear layer near the exit of the subsonic jet is influenced by the pressure wave generated by the interaction of the vortices at the end of the potential core, and promoting the upstream transition, thereby amplifying the sound. That is explained as a feedback loop phenomenon [1][2]. This study was conducted to supplement that explanation.

In this study, we analyze the response of a point source oscillation at the end of the potential core. We operate direct numerical simulation (DNS) of the compressible Navier-Stokes (NS) equations with a local body forcing starting from the time-averaged base flow $(\bar{\rho}, \bar{u}, \bar{v}, \bar{w}, \bar{p})$. We compare the temporal behavior of the kinetic energy k of velocity fluctuations (u', v', w') as described in Eqs. (1).

$$k = \frac{1}{2}\rho(u'^2 + v'^2 + w'^2), \qquad (1)$$
$$u' = \bar{u} - u, v' = \bar{v} - v, w' = \bar{w} - w.$$

The point source mimics the upstream-propagating pressure wave generated by the interaction of the vortices. Here we apply the Volume Penalization (VP) method [3], one of the immersed boundary methods, so that a point source oscillates at an arbitrary frequency. In this study, as the first step, we focused on the two-dimensional inflection point instability of the free shear layer and carried out by two-dimensional computation. We observed the responses to 20 frequency cases ranging from diameter based Strauhal number $\mathrm{St_D} = 0.1$to $\mathrm{St_D} = 2.0$ for the jet of Re = 3125 and M = 0.9 computed by Bogey(2019)[4].

We show the kinetic energy amplification with a point source oscillation in Fig. 1. The kinetic energy and time are non-dimensionalized by the sound velocity. Initially, there is not much difference between the frequencies. After T = 35 up to T = 60, the values increase in the case of $\mathrm{St_D}$= 0.2. After that, there is a tendency that the higher the frequency, the larger the energy value. After T = 75, the behavior becomes the more complicated. Fig. 2 (a), (b), and (c) show the absolute values of vorticity at T = 52 without, and with point source of $\mathrm{St_D}$= 0.2, and $\mathrm{St_D}$ = 2.0, respectively. White line in figures shows the streamwise position of the potential core end. In these figures, the case with $\mathrm{St_D}$ = 0.2 has the highest sensitivity to the upstream-propagating wave, because the vortices due to the Kelvin-Helmholtz instability appears more clearly than in the other cases (see the red squared region of Figure 2 (b) and (c)).

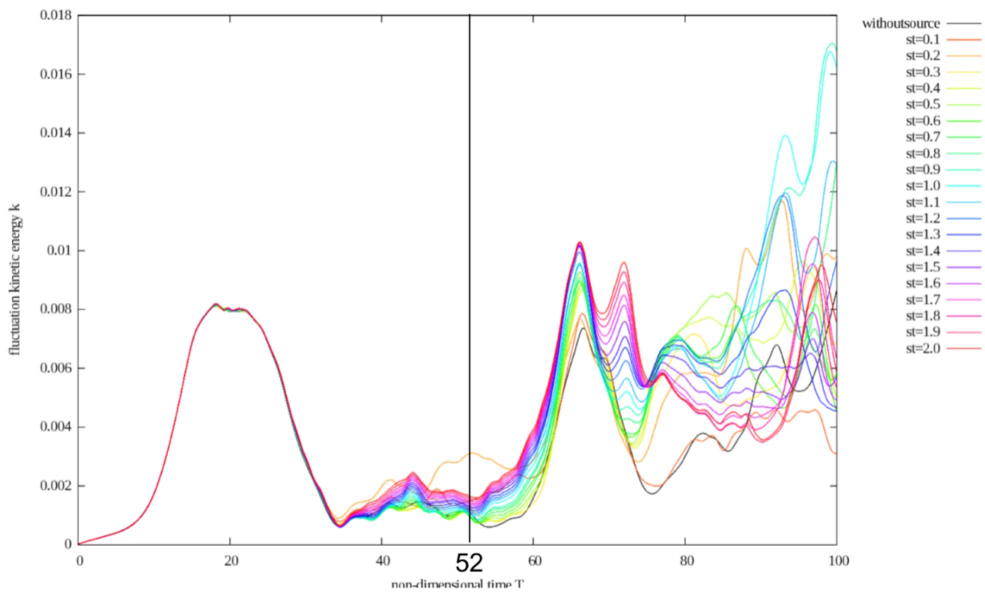

Fig.1 Response in the kinetic energy amplification of the velocity fluctuation added to the time-averaged base flow of a subsonic jet.

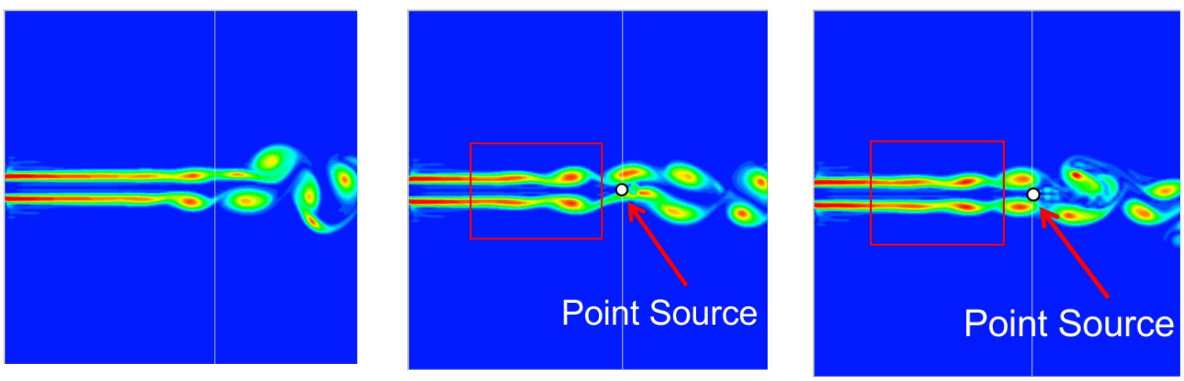

(a) without oscillation (b) $\mathrm{St_D} = 0.2$ (c) $\mathrm{St_D} = 2.0$

Fig.2. Absolute values of vorticity at T = 52 (a) without, and with point source of (b) $\mathrm{St_D} = 0.2$, and (c) $\mathrm{St_D}$= 2.0. The contour ranges from 0 to 3, from blue to red. White line indicates the streamwise position of the end of the potential core and a white point on the white line shows the location of a point source.

References

[1] J. Laufer and P. Monkewitz, On turbulent jet flows-a new perspective, in 6th Aeroacoustics Conference, 1980, p. 962

[2] C. Bogey. Acoustic tones in the near-nozzle region of jets: characteristics and variations between mach numbers 0.5 and 2. *J. Fluid Mech*., 2021, 921:A3.

[3] Q. Liu. and O. V. Vasilyev. A brinkman penalization method for compressible flows in complex geometries. *J. Comput. Phys*., 2007, 227(2):946–966.

[4] C. Bogey. Two-dimensional features of correlations in the flow and near pressure fields of Mach number 0.9 jets, AIAA SciTech Forum, 2019, 2019-0806.

Reynolds number induced growth of large-scale rolls in plane Couette flow and invariant scaling laws for added wall-transpiration using resolvent analysis

Toni Dokoza [1], and Martin Oberlack [1 2]

[1] Technical University of Darmstadt, Chair of Fluid Dynamics, Department of Mechanical Engineering, 64287 Darmstadt, Germany
[2] Technical University of Darmstadt, Centre for Computational Engineering, 64293 Darmstadt, Germany

key-words: Coherent/vortical structures

ABSTRACT

In DNS of turbulent Couette flow the observation has been made, that the long streamwise rolls increase in length with the Reynolds number [1]. For its understanding we employ the resolvent analysis emphasising the high Reynolds number ($Re \to \infty$) and small streamwise wavenumbers ($\alpha \to 0$) limit imposing the distinguished limit $Re_\alpha = Re \cdot \alpha = O(1)$ as done in [2] for the linear stability analysis of the asymptotic suction boundary layer flow, since structures are only significantly amplified for high Reynolds number plane Couette flow, which admit very weak streamwise variation. We find that Re_α acts as a local invariant in the behaviour of the energy of the system characterised through the first singular value σ_1 of the resolvent operator within the investigated asymptotic limit, where the behaviour of σ_1 over both Re and α respectively stays invariant within a certain Re_α-range. In order to obtain constant streamwise structures for increasing Reynolds numbers, the respective streamwise wavenumber has to decrease, which can be seen by the fact that the coherent structures in (a) and (d), (b) and (e), and (c) and (f) in Figure 1 are identical, which verifies the observations from DNS studies of an increasing length of the streamwise structures with the Reynolds number.

The conducted analysis is expanded on the plane Couette flow with constant wall-transpiration velocity V_0 and wall velocity U_w with emphasis on the effect of V_0 on the coherent structures. For this flow setting, the first singular value σ_1 for a constant ratio of the wall-transpiration and streamwise Reynolds numbers $\gamma = \frac{Re_{V_0}}{Re} = \frac{V_0}{U_w}$ is the largest for an invariant relationship $Re \cdot \gamma^a = C$. Figure 2 shows the behaviour of σ_1 over the streamwise Reynoldsnumber for various γ-ratios, where σ_1 reaches a peak value for a certain Re for each γ characterised through the aforementioned invariant relationship. The influence of the wall-transpiration Reynolds number Re_{V0} on the streamwise structures is analysed, where it is shown that the streamwise structures not only move closer to the upper wall, but also become more confined in both the wall-normal and spanwise direction for an increasing Re_{V0}, while keeping the streamwise Reynolds number Re constant.

References

[1] Lee M. and Moser R., (2018), Extreme-scale motions in turbulent plane Couette flows, *Journal of Fluid Mechanics, 842, 128-145*

[2] Yalcin A., Turkac Y. and Oberlack M., (2021), On the temporal linear stability of the asymptotic suction boundary layer, *Physics of Fluids, 33*

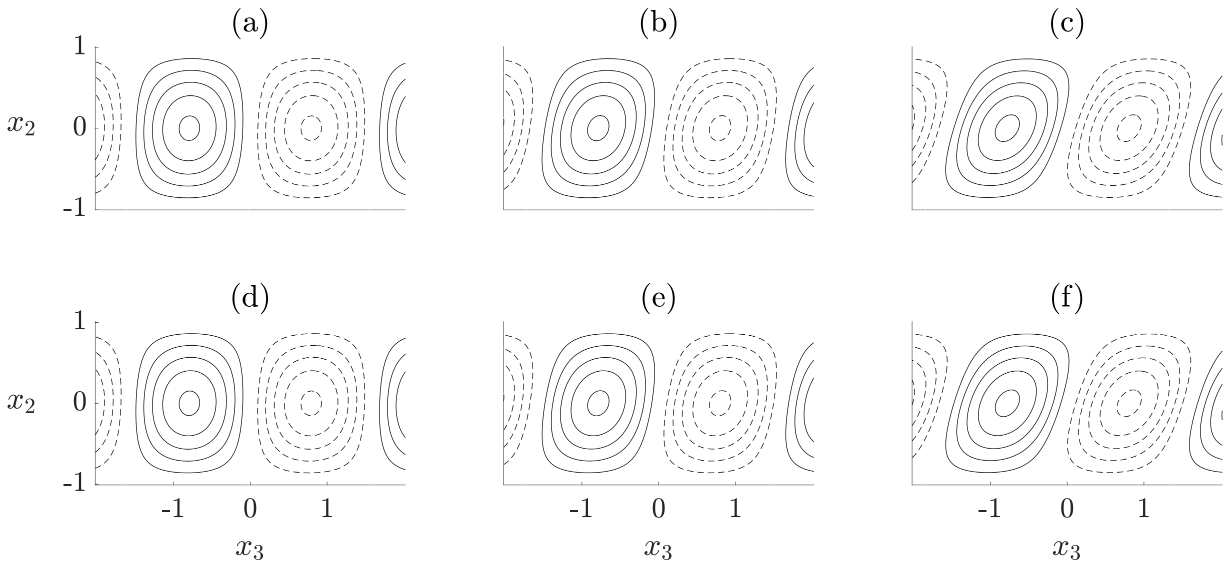

Figure 1: Streamwise structures are shown over the spanwise direction x_3 and wall-normal direction x_2 for (a) $\omega = 0$, $\beta = 2$, $Re_\alpha = 1$, $\alpha = 0.0001$, (b) $\omega = 0$, $\beta = 2$, $Re_\alpha = 5$, $\alpha = 0.0005$, (c) $\omega = 0$, $\beta = 2$, $Re_\alpha = 10$, $\alpha = 0.001$, (d) $\omega = 0$, $\beta = 2$, $Re_\alpha = 1$, $Re = 10000$, (e) $\omega = 0$, $\beta = 2$, $Re_\alpha = 5$, $Re = 50000$, (f) $\omega = 0$, $\beta = 2$, $Re_\alpha = 10$, $Re = 100000$. Solid lines represent fluctuations with a positive sign, while dashed lines represent fluctuations with a negative sign.

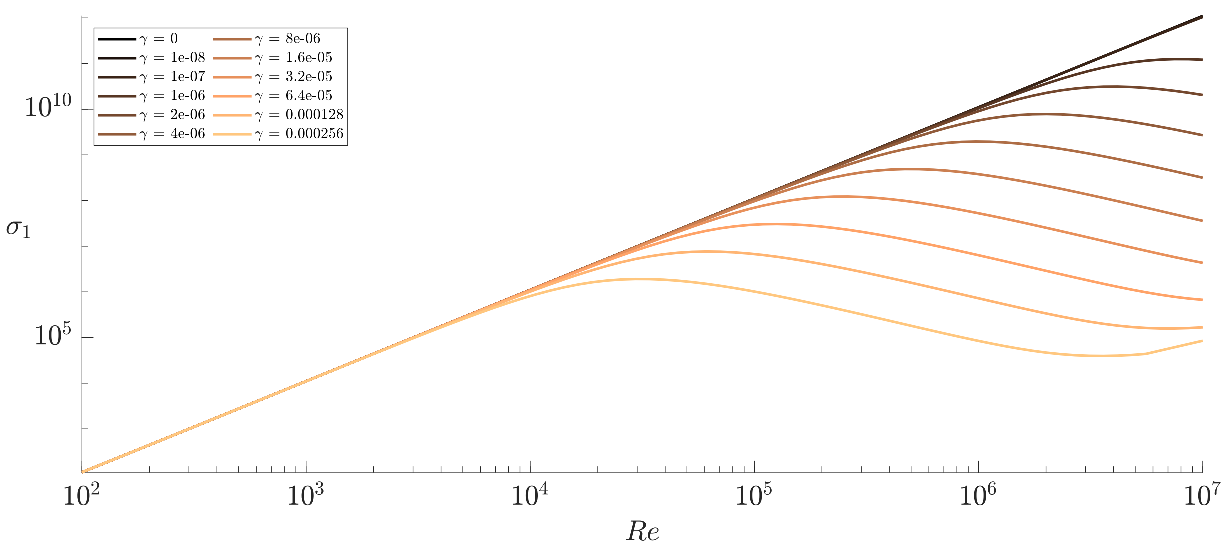

Figure 2: σ_1 is shown over the Reynolds number Re for$\beta = 2, \omega = 0$, $\alpha = 0$ and
$\gamma = [0, 10^{-8}, 10^{-7}, 10^{-6}, 2{\cdot}10^{-6}, 4{\cdot}10^{-6}, 8{\cdot}10^{-6}, 1.6{\cdot}10^{-5}, 3.2{\cdot}10^{-5}, 6.4{\cdot}10^{-5}, 1.28{\cdot}10^{-4}, 2.56{\cdot}10^{-4}]$.

Symmetry-based turbulent scaling laws of a spatially evolving turbulent round jet

Cat Tuong Nguyen [1], and Martin Oberlack [1,2]

[1] Chair of Fluid Dynamics, TU Darmstadt, 64287 Darmstadt, Germany
[2] Centre for Computational Engineering, TU Darmstadt, 64293 Darmstadt, Germany

key-words: Lie-symmetry-analysis, DNS

Abstract:
In most experiments as well as numerical simulations of turbulent round jets, self-similarity is observed primarily for the mean velocity. Here, using symmetry methods, we calculate similarity-type scaling laws for arbitrarily high moments of velocity from the infinite set of multi-point moment equations. Most centrally, symmetry theory provides moments based on instantaneous rather than fluctuation velocities. To prove its validity, a large-scale direct numerical simulation (DNS) of a turbulent jet flow was conducted at a Reynolds number of $Re = 3500$ and a box length of $z/D = 75$. A cross section of q-criterion isosurfaces can been seen in Fig. 1. As an inlet, we utilize a fully turbulent pipe flow to obtain self-similarity at small z, and we calculate almost 200 washouts for a very good statistical convergence of high moments.
Virtually perfect similarity compared to symmetry theory is observed in the $z/D = 25-65$ range and this is especially true for U_z-moments up to order $n = 10$ (see Fig. 2 and Fig. 3). In matching theory and DNS data, we observe that statistical symmetries are negligible for turbulent jets, and this is very different to near-wall turbulence where they are significant for high moment scaling laws [see Oberlack et al., 2022]. In this work, prefactors of near-wall high order moment scaling-laws were found to scale exponentially with order n and this is also observed presently. Additionally, the U_z-moments show Gaussian-like curves that get increasingly narrower with n. Transforming the governing equations with the symmetry-based scaling laws and assuming a Gaussian for the U_z-moments allows us to find an expression for the instantaneous $\overline{U_r U_z}$ correlation which compares well with the DNS data in Fig. 4.
Finally, converting the instantaneous moments to those of fluctuations is straightforward, but will be omitted as it was shown in Oberlack et al. [2023] that uncertainty grows exponentially for $n > 2$ and a sensible interpretation is therefore lost.

References

M. Oberlack, S. Hoyas, S. V. Kraheberger, F. Alcántara-Ávila, and J. Laux. Turbulence statistics of arbitrary moments of wall-bounded shear flows: A symmetry approach. *Phys. Rev. Lett.*, 128(2): 024502, 2022. doi: 10.1103/PhysRevLett.128.024502. URL `https://link.aps.org/doi/10.1103/PhysRevLett.128.024502`.

M. Oberlack, S. Hoyas, J. Laux, and D. Klingenberg. Reply to comments lnk1134 and lpk1133 on "turbulence statistics of arbitrary moments of wall-bounded shear flows: A symmetry approach". *in print with Phys. Rev. Lett.*, 2023.

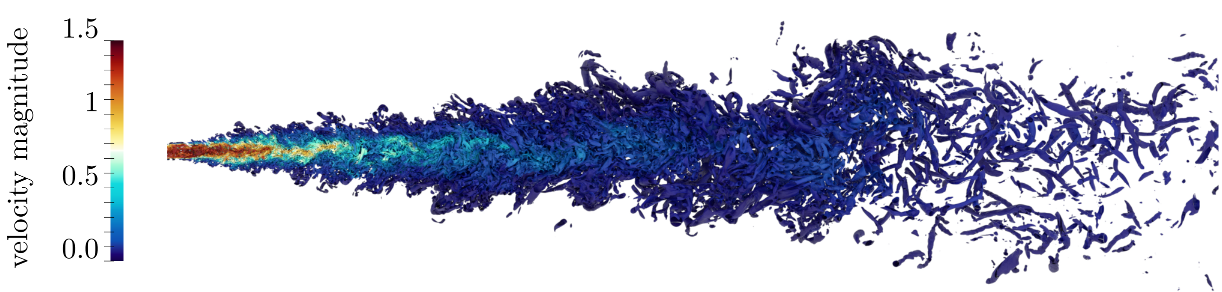

Figure 1: A cross section of q-criterion isosurfaces of the conducted jet DNS colored with the velocity magnitude.

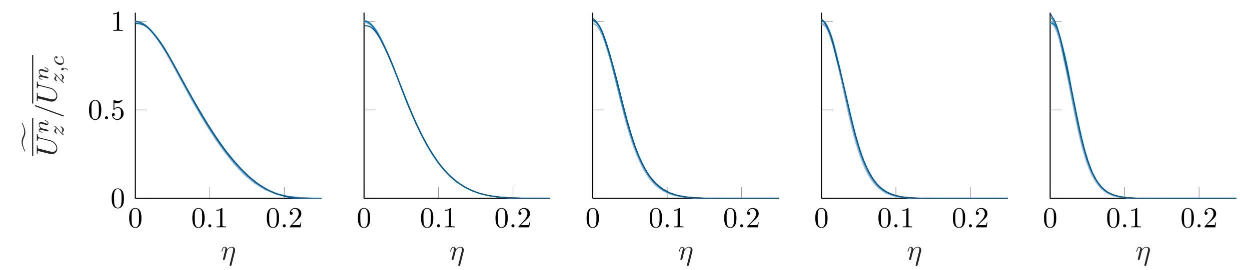

(a) $n = 1$ (b) $n = 2$ (c) $n = 5$ (d) $n = 7$ (e) $n = 10$

Figure 2: The radial profiles of the n^{th} axial moment normalized with the scaling laws at different distances from the orifice: $z = 25$ (——), $z = 35$ (——), $z = 45$ (——), $z = 55$ (——), $z = 65$ (——).

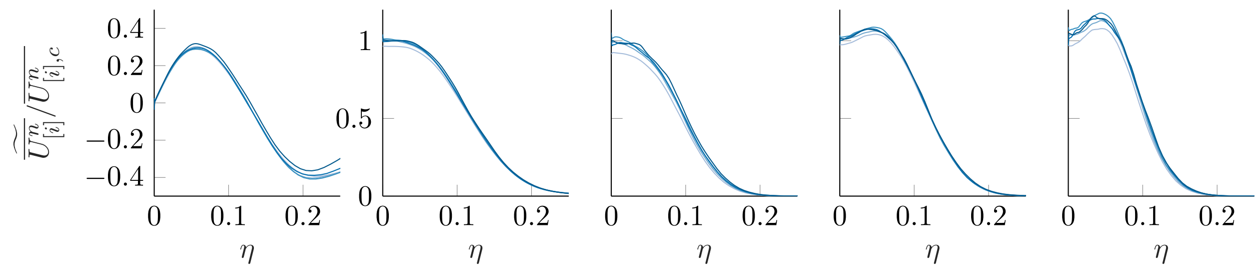

(a) $[i] = r$, $n = 1$ (b) $[i] = r$, $n = 2$ (c) $[i] = r$, $n = 4$ (d) $[i] = \varphi$, $n = 2$ (e) $[i] = \varphi$, $n = 4$

Figure 3: The radial profiles of the n^{th} radial and azimuthal moments normalized with the scaling laws at different distances from the orifice: $z = 25$ (——), $z = 35$ (——), $z = 45$ (——), $z = 55$ (——), $z = 65$ (——).

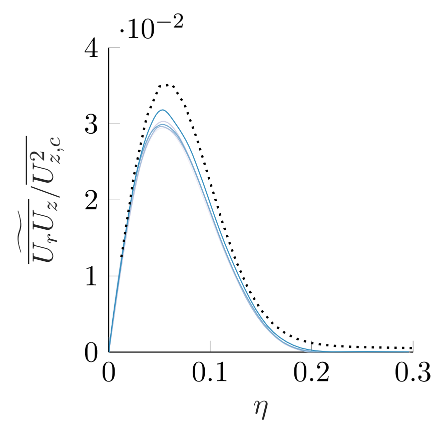

Figure 4: The radial profiles of the $\overline{U_r U_z}$ correlation at different distances z from the orifice compared to the expression found in the governing equations (······): $z = 25$ (——), $z = 35$ (——), $z = 45$ (——), $z = 55$ (——), $z = 65$ (——).

Study of the upstream influence of the diffuser of CICLoPE "long pipe" using oil film interferometry

L. Lazzarini[1], G. Bellani[1] and A. Talamelli[1]

[1] Department on industrial engineering, Alma mater Studiorum – University of Bologna, Via Fontanelle 40, Forlì, Italy; email: lorenzo.lazzarini7@unibo.it

keywords: Experimental aerodynamics, Wall shear stress measurements.

Abstract:
Wall-bounded turbulence is an extremely relevant topic for engineering and natural science application and yet many aspects of this physics are not clear. Due to the relevance of these flows, in recent times several facilities were developed to investigate turbulent flows at high-Reynolds number under fully developed conditions [1],[2] and [3]. In particular, the "long pipe" of CICLoPE is a 111.5m full carbon fiber pipe with a diameter of 0.9m minimizing spatial and temporal filtering issues, a common problem that arises as the Reynolds number increases. Several measurements documenting fully developed conditions in this facility have been previously reported [4], [5]. However, the aim of the present study is to specifically investigate if these conditions are met in the last 1.5 diameters of CICLoPE. A detailed investigation of this location is particularly important for two main reasons: first because this is the location of the test section where measurements are typically performed; moreover, this section is placed before the diffuser, so it is important to verify that there is not upstream influence on the test section. While previous work reported on the invariance of the velocity profiles in the near-wall region, in this work we focus on the centerline velocity and the local wall-shear stress.

In pipe flow typically wall shear stress is obtained through static pressure drop, allowing us to calculate a global wall shear stress value through an "indirect" measurement (i.e., static pressure evolution throughout a pipe section). On the other and, oil film interferometry [6] [7], is a technique that allows us to obtain a localized value of the wall shear stress, which can be inferred from the spreading rate of an oil drop at the wall as shown in figure 2.
In this work we present a collection of centerline velocity and wall shear stress measurements obtained at several streamwise locations. Local values of the wall shear stresses are measured using oil film interferometry or hot wire anemometry, these values are then compared with static pressure drop acquisition. Centerline velocity is measured with a pitot tube placed at the centerline within the last 10 diameters of the pipe. In figure 1 we show the centerline velocity in two different positions normalized with respect to a reference position placed 5 diameters upstream with respect to the test section. The results show a substantial invariance of the centerline velocity. To complete the evaluation, we will present a collection of experiments using oil film interferometry and hot wire anemometry spanning in a range of friction Reynolds number from 5000 to 47000, partially overlapping with the latest DNS available [8], [9].

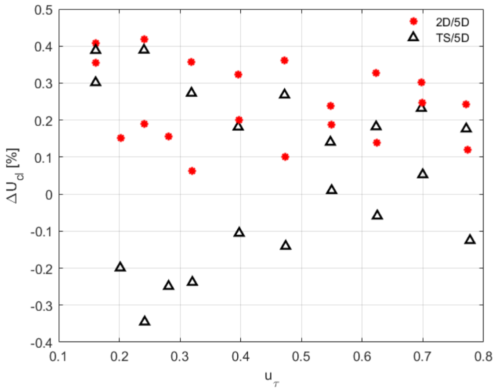

Figure 1: *Variation of the centerline velocity of the "long pipe" with respect to a reference value 5 diameter upstream the test section as function of friction velocity; red dot refers to the 2 diameters upstream normalized with 5d; black upwards triangle refers to the test section normalized with 5 diameters upstream.*

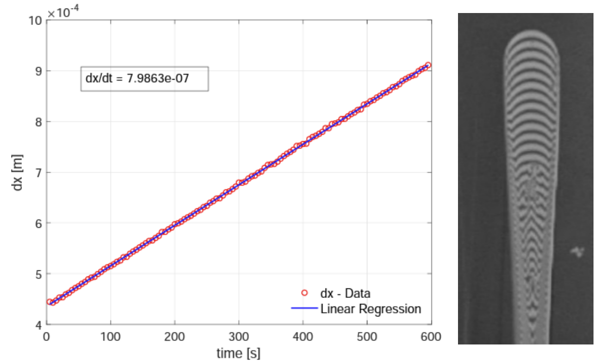

Figure 2: *linear interpolation of the wavelength values of the signal as function of time, red dot represents experimental samples of each fringes dimension, blue line represents the linear regression of the whole dataset.*

References

[1] Furuichi,N. and Terao,Y. and Wada,Y. and Tsuji,Y., Friction factor and mean velocity profile for pipe flow at high Reynolds numbers, Physics of Fluids, 27, 2015
[2] Hultmark, M. and Vallikivi, M. and Bailey, S. C. C. and Smits, A. J., Turbulent Pipe Flow at Extreme Reynolds Numbers, Phys. Rev. Lett., 108, 2012
[3] Talamelli, A. et al. (2009). "CICLoPE - A response to the need for high Reynolds number experiments". In: Fluid Dynamics Research 41.2.
[4] Fiorini, T. 2017 Turbulent pipe flow - high resolution measurements in ciclope. PhD thesis, School of Engineering and Architecture, University of Bologna.
[5] Mascotelli, L. 2020, High Reynolds Number Experiments in the Long Pipe at CICLoPE. PhD thesis, School of Engineering and Architecture, University of Bologna
[6] H.C.H. Ng, I. Marusic, J.P. Monty, N. Hutchins and M.S. Chong, "Oil film interferometry in high Reynolds number turbulent boundary layers", 16th Australasian Fluid Mechanics Conference Crown Plaza, Gold Coast, Australia, 2-7 December 2007.
[7] R. Vinuesa, R. Orlu, "Measurement of Wall Shear Stress", Experimental Aerodynamics, Chapter 12, pp.393-429
[8] S. Pirozzoli, J. Romero, M. Fatica, R. Verzicco, P. Orlandi, "One-point statistics for turbolent pipe flow up to Reτ ≈ 6000", Journal of Fluid Mechanics, 2021, vol.926, A28
[9] J. Yao, S. Rezaeiravesh, P. Schlatter, F. Hussain, "Direct numerical simulations of turbulent pipe flow up to Reτ ≈ 5200", Journal of Fluid Mechanics, 956, A18.